



**HAL**  
open science

# State-plane analysis and optimization of the CLLC resonant converter for bidirectional EV charger

Mohsen Rezayati

► **To cite this version:**

Mohsen Rezayati. State-plane analysis and optimization of the CLLC resonant converter for bidirectional EV charger. Electric power. Université Grenoble Alpes [2020-..]; Sharif University of Technology (Tehran), 2023. English. NNT: 2023GRALT007 . tel-04094415

**HAL Id: tel-04094415**

**<https://theses.hal.science/tel-04094415>**

Submitted on 11 May 2023

**HAL** is a multi-disciplinary open access archive for the deposit and dissemination of scientific research documents, whether they are published or not. The documents may come from teaching and research institutions in France or abroad, or from public or private research centers.

L'archive ouverte pluridisciplinaire **HAL**, est destinée au dépôt et à la diffusion de documents scientifiques de niveau recherche, publiés ou non, émanant des établissements d'enseignement et de recherche français ou étrangers, des laboratoires publics ou privés.



## THÈSE

Pour obtenir le grade de

### DOCTEUR DE L'UNIVERSITÉ GRENOBLE ALPES et de Sharif University of Technology

École doctorale : EEATS  
Spécialité : Génie Electrique  
Unité de recherche : G2ELab – UMR 5269

### Analyse par le plan de phase et optimisation d'un convertisseur résonant CLLC pour chargeur de véhicule bidirectionnel

### State Plane Analysis and Optimization of CLLC Resonant Converter for Bidirectional EV Charger

Présentée par :

**Mohsen REZAYATI**

Direction de thèse :

**Jean-Luc SCHANEN**

Prof, G-INP UGA

Directeur de thèse

**Farzad TAHAMI**

Ass. Prof., Sharif Univ. of Technology

Co-Directeur de thèse

Rapporteurs :

**Sebastien MARIETHOZ**

Prof., Bern Univ. Appl. Sciences

**Mohammad TAVAKOLI-BINA**

Prof., K.N.Toosi Univ. of Technology

Thèse soutenue publiquement le 08 février 2023, devant le jury composé de :

**Forouhar FARZANEH**

Prof., Sharif Univ. of Technology

Président

**Sebastien MARIETHOZ**

Prof., Bern Univ. Appl. Sciences

Rapporteur

**Mohammad TAVAKOLI-BINA**

Prof., K.N.Toosi Univ. of Technology

Rapporteur

**Yves LEMBEYE**

Prof., Univ. Grenoble Alpes

Examineur

**Jean-Luc SCHANEN**

Prof, G-INP UGA

Directeur de thèse

**Farzad TAHAMI**

Ass. Prof., Sharif Univ. of Technology

Co-Directeur de thèse

Invités :

**Mohammadreza ZOLGHADRI**

Ass. Prof., Sharif Univ. of Technology

**Shahriar KABOLI**

Prof., Sharif Univ. of Technology



**Titre:** Analyse par le plan de phase et optimisation d'un convertisseur résonant CLLC pour chargeur de véhicule bidirectionnel

**Mots clés:** Chargeur EV bidirectionnel; Conception de composants magnétiques; Plusieurs points de fonctionnement; Optimisation; Modélisation des pertes; Convertisseur résonant; Programmation quadratique séquentielle; Commutation douce; Analyse par le plan de phase.

**Résumé:** Le convertisseur résonant CLLC est un candidat prometteur pour les applications de transfert d'énergie bidirectionnelle à haute efficacité telles que le chargeur embarqué véhicule-réseau (V2G). Usuellement, il est étudié via l'approximation du premier harmonique (FHA), qui a une faible précision. Dans cette thèse, une méthode d'analyse de circuit basée sur un changement de variables est présentée qui décrit les équations d'état au moyen de deux jeux d'équations découplées, puis les résultats sont reconstruits dans le référentiel d'origine. La méthode proposée est utilisée pour analyser en profondeur le convertisseur résonant CLLC, ainsi que dans son processus d'optimisation. La charge d'une batterie lithium-ion comporte une large gamme de tensions et de courants, par conséquent, le chargeur doit être conçu et optimisé pour faire face à de multiples points de fonctionnement. Dans cette thèse, une méthodologie d'optimisation prenant en compte un ensemble multiple de points de fonctionnement est présentée. L'algorithme de programmation quadratique séquentielle (SQP) est utilisé lors de l'optimisation, ce qui impose à l'ensemble des paramètres et des modèles d'être dérivables. On raisonne donc dans un espace imaginaire, puisque tous les paramètres ne sont pas physiquement implémentables. Une fois l'optimum obtenu, le retour au monde réel (discrétisé et physiquement implémentable) est proposé, en sélectionnant les valeurs discrètes inférieures et supérieures. On obtient ainsi 24 convertisseurs physiquement réalisables, au sein duquel on sélectionne le meilleur. Pour vérifier cette méthodologie, deux prototypes expérimentaux sont mis en œuvre: un convertisseur résonant CLLC optimal de 3,3 kW et un convertisseur résonant CLLC de plus petite taille. Il est montré que le convertisseur optimal répond aux contraintes des points de fonctionnement multiples avec une puissance de 3,3kW et un rendement moyen de 98%, alors qu'il n'est pas possible pour le plus petit convertisseur d'atteindre la puissance de 3,3kW et de répondre à toutes les contraintes.

**Title:** State Plane Analysis and Optimization of CLLC Resonant Converter for Bidirectional EV Charger

**Keywords:** Bidirectional EV charger; Magnetic components design; Multiple operating points; Optimization; Power loss modeling; Resonant converter; Sequential quadratic programming; Soft switching; State-plane analysis.

**Abstract:** The CLLC resonant converter is a promising candidate for high efficient, bidirectional power transfer applications such as vehicle-to-grid (V2G) on-board charger. Its analysis is usually performed using the first harmonic approximation (FHA) method, which has low accuracy. In this thesis, a circuit analysis method based on change of variables is presented that maps the state space equations into two decoupled sets of equations and then the results are mapped onto the original region. The proposed method is then used to thoroughly analyze the CLLC resonant converter, as well as in its optimization process. The charging process of a Lithium-ion battery contains a wide range of voltages and currents. Therefore, the charger must be designed and optimized for these multiple operating points. In this thesis, a methodology for multiple operating points optimization is presented. The sequential quadratic programming (SQP) algorithm is adopted to find the optimum results, which imposes models and parameters to be derivable. The space of solution is thus called "Imaginary world", due to the fact that these parameters are not physically implementable. After optimization, a process is set up to come back to real world (i.e. with physically implementable parameters). In each step, the discrete parameters will be fixed with floor and ceiling, which finally generates 24 possible converters. The best of them is finally selected. To verify the proposed methodology, two experimental prototypes have been implemented, a 3.3kW optimum CLLC resonant converter and a smaller-in-size CLLC resonant converter. It has been shown that the optimal converter meets the constraints of the multiple operating points with the power rating of 3.3kW and average efficiency of 98%, whereas it is not possible for the smaller converter to reach the power of 3.3kW and meet all the constraints.

# **State Plane Analysis and Optimization of CLLC Resonant Converter for Bidirectional EV Charger**

Mohsen Rezayati

Dissertation submitted to the Faculties of the  
Sharif University of Technology

and

University of Grenoble Alpes

in partial fulfillment of the requirements for the degree of

**Doctor of Philosophy**

In

**Electrical Engineering**

Farzad Tahami

Jean-Luc Schanen

Copyright 2023, Mohsen Rezayati

# Abstract

As more renewables step in, the ongoing change will be drastic for the electrical grid. The energy sector must find new ways to balance energy production and consumption. Electric vehicle (EV) batteries are by far the most cost-efficient form of energy storage since they require no additional investments in hardware. A bidirectional EV charger is a new technology that enables energy to be pushed back to the power grid and auxiliary loads from the battery. The electrical requirements of the EV charger are examined in detail to find an appropriate power electronics converter to meet all the requirements.

The CLLC resonant converter is a promising candidate for high efficient, bidirectional power transfer applications such as vehicle-to-grid (V2G) on-board chargers and hybrid vehicle DC-DC converters. The fundamentals of the bidirectional EV charger based on the CLLC resonant converter and its main components including the transformer, resonant inductors, resonant capacitors, inverter and rectifier parts, etc. are studied in depth, where the advantages and disadvantages of the CLLC resonant converter and possible candidates are highlighted.

A global design methodology including transformer design, inductor design, capacitor design, semiconductor losses, diode losses, magnetic core losses, and capacitor losses is studied to define an optimization problem corresponding to the objective function and constraints. An interpolation-based method is proposed for the GaN transistor switching losses with the different voltage and current levels, gate driver circuits, junction temperature, parasitic capacitors, etc. A conduction loss model is also presented based on the datasheet of GaN transistors. The objective function can be considered as maximizing efficiency and power density, as well as, minimizing mass, volume, and losses. The constraints are also highlighted, which are the battery charger operating region, maximum temperature, maximum RMS current of resonant elements, maximum voltage, soft-switching condition, and operating in continuous conduction mode (CCM). Most of these constraints and the CLLC resonant converter analysis have been calculated by the first harmonic approximation (FHA) method, which has low accuracy. Therefore, the analysis of CLLC still remains challenging because of its complex multi-resonant nature and several storage elements.

In this dissertation, a circuit analysis method based on the change of variables is presented that maps the state space equations into two decoupled sets of equations. The analyses are carried out in two state-plane coordinate systems, then the results are mapped onto the original region. Two decoupled sets of equations are similar to the series resonant converter. The

proposed method is then used to thoroughly analyze the CLLC resonant converter operating in the CCM and discontinuous conduction mode (DCM). The voltage and current stresses of components, zero voltage switching condition, output voltage gain, output characteristic diagram, and mode boundary of CCM/DCM are then obtained. The accuracy of the proposed approach is verified by the simulation on a 3.3 kW bidirectional CLLC resonant converter with GaN transistors as the primary and secondary side switches. The results confirm the accuracy of the proposed state-plane analysis of the CLLC resonant converter operating in either direction of power transfer.

By completing the exact analysis of the CLLC resonant converter, the second aim of this dissertation is relative to the optimization of the CLLC resonant converter. The *CADES* Software is used as the platform of optimization and the state plane analysis is implemented on it using C++. Furthermore, the accuracy of the implemented method is verified by Maxwell simulation to be able to be used in the optimization process and check the value of magnetic components, saturation of magnetic material, etc.

The common optimization of a resonant converter has been based on the single operating point. The selection of a single operating point leads the designed converter not to meet all the constraints when the converter operates in a different operating point. Based on the charging process of a Lithium-Ion battery, its operating region contains a wide range of voltages and currents. Therefore, there exist multiple operating points for a bidirectional EV charger. In this dissertation, a new algorithm for multiple operating points optimization is presented. The Sequential Quadratic Programming (SQP) algorithm is adopted to find the optimum results, where the second derivative of the objective functions must be available. However, there are some discrete parameters for optimizing a bidirectional EV charger, such as core sizes, number of turns, and number of turns in each layer. Therefore, in the proposed method, all the discrete parameters are considered as continuous parameters for the availability of the derivatives. This set of parameters is entitled to the *imaginary world* due to the fact that these parameters are not physically implementable. The proposed method optimizes the CLLC resonant converter in the *imaginary world* and with some steps tries to find the optimum solution in the *real world* (i.e. the physically implementable parameters). In each step, the discrete parameters will be fixed by putting a floor under them and setting a ceiling on them. At the end of the steps, the optimum charger is selected between 24 samples.

Finally, the two aims of this dissertation, i.e. analysis and optimization, are verified by the experimental tests and comparison with the simulation results and FHA-based results. The

accuracy of the proposed state-plane analysis is verified by the experiments on a 3.3 kW bidirectional CLLC resonant converter with GaN transistors as the primary and secondary side switches. The results confirm the accuracy of the proposed state-plane analysis of the CLLC resonant converter operating in either direction of power transfer. The optimization algorithm is also verified using two experimental setups, i.e. the optimum converter and a smaller in-size converter.

# Résumé

À mesure que de plus en plus d'énergies renouvelables entrent en scène, le changement en cours sera radical pour le réseau électrique. Le secteur de l'énergie doit trouver de nouvelles façons d'équilibrer la production et la consommation d'énergie. Les batteries de véhicules électriques (EV) sont de loin la forme de stockage d'énergie la plus rentable car elles ne nécessitent aucun investissement supplémentaire en matériel. Un chargeur EV bidirectionnel est une nouvelle technologie qui permet de renvoyer l'énergie vers le réseau électrique et les charges auxiliaires depuis la batterie. Les exigences électriques du chargeur EV sont examinées en détail pour trouver un convertisseur d'électronique de puissance approprié pour répondre à toutes les exigences.

Le convertisseur résonant CLLC est un candidat prometteur pour les applications de transfert de puissance bidirectionnelle à haut rendement telles que les chargeurs embarqués véhicule-réseau (V2G) et les convertisseurs CC-CC de véhicules hybrides. Les principes fondamentaux du chargeur EV bidirectionnel basé sur le convertisseur résonant CLLC et ses principaux composants, y compris le transformateur, les inductances résonantes, les condensateurs résonants, la partie onduleur et redresseur, etc. sont étudiés en profondeur, où les avantages et les inconvénients du convertisseur résonant CLLC et les candidats possibles sont mis en évidence.

Une méthodologie de conception globale comprenant la conception des transformateurs, la conception des inductances, la conception des condensateurs, les pertes des semi-conducteurs, les pertes des diodes, les pertes du noyau magnétique et les pertes des condensateurs est étudiée pour définir un problème d'optimisation correspondant à la fonction objectif et aux contraintes. Une méthode basée sur l'interpolation est proposée pour les pertes de commutation du transistor GaN avec les différents niveaux de tension et de courant, les circuits de commande de grille, la température de jonction, les condensateurs parasites, etc. Un modèle de perte de conduction est également présenté sur la base de la fiche technique des transistors GaN. La fonction objectif peut être considérée comme maximisant l'efficacité et la densité de puissance, ou minimisant la masse, le volume et les pertes. Les contraintes sont également mises en évidence, qui sont la région de fonctionnement du chargeur de batterie, la température maximale, le courant RMS maximal des éléments résonants, la tension maximale, la condition de commutation douce et le fonctionnement en mode de conduction continue (CCM). Dans de nombreux travaux, la plupart de ces contraintes et l'analyse du convertisseur résonant CLLC sont calculées par la méthode



d'approximation du premier harmonique (FHA), qui a une faible précision. Par conséquent, l'analyse de CLLC reste difficile en raison de sa nature multi-résonnante complexe et de plusieurs éléments de stockage.

Dans cette thèse, une méthode d'analyse de circuit basée sur le changement de variables est présentée qui représente les équations de l'espace d'état en deux ensembles découplés d'équations. Les analyses sont effectuées dans deux systèmes de coordonnées de plan d'état, puis les résultats sont reprojétés sur la région d'origine. Les deux jeux d'équations découplés sont similaires aux celles de deux convertisseurs à résonance série. La méthode proposée est ensuite utilisée pour analyser en profondeur le convertisseur résonant CLLC fonctionnant en mode de conduction continue (CCM) et discontinue (DCM). Les contraintes de tension et de courant des composants, la condition de commutation de tension nulle, le gain de tension de sortie, le diagramme de caractéristique de sortie et la limite de mode de CCM/DCM sont ensuite obtenus. La précision de l'approche proposée est vérifiée par la simulation sur un convertisseur résonant CLLC bidirectionnel de 3,3 kW avec des transistors GaN comme commutateurs côté primaire et secondaire. Les résultats confirment la précision de l'analyse du plan d'état proposée du convertisseur résonant CLLC fonctionnant dans les deux sens de transfert de puissance.

En complétant l'analyse exacte du convertisseur résonant CLLC, le deuxième objectif de cette thèse est relatif à l'optimisation du convertisseur résonant CLLC. Le logiciel CADES est utilisé comme plate-forme d'optimisation et l'analyse du plan déphase  $\gamma$  est implémentée à l'aide de C++. De plus, la précision de la méthode mise en œuvre est vérifiée par la simulation éléments finis Maxwell pour pouvoir être utilisée dans le processus d'optimisation et vérifier la valeur des composants magnétiques, la saturation du matériau magnétique, etc.

L'optimisation d'un convertisseur résonant a été basée sur le point de fonctionnement unique. La sélection d'un point de fonctionnement unique conduit le convertisseur conçu à ne pas respecter toutes les contraintes lorsque le convertisseur fonctionne pour un point de fonctionnement différent. Basé sur le processus de charge d'une batterie lithium-ion, sa région de fonctionnement contient une large gamme de tensions et de courants. Par conséquent, il existe plusieurs points de fonctionnement pour un chargeur de VE bidirectionnel. Dans cette thèse, un nouvel algorithme d'optimisation de points de fonctionnement multiples est présenté. L'algorithme de programmation quadratique séquentielle (SQP) est adopté pour trouver les résultats optimaux, où la dérivée seconde des fonctions objectives doit être disponible. Cependant, il existe certains paramètres discrets pour optimiser un chargeur EV bidirectionnel, tels que la taille des noyaux magnétiques, le nombre de tours et le nombre de tours dans chaque

couche. Par conséquent, dans la méthode proposée, tous les paramètres discrets sont considérés comme des paramètres continus pour calculer des dérivées. Ceci correspond à raisonner dans un monde "imaginaire" du fait que ces paramètres ne sont pas physiquement implémentables. La méthode proposée optimise le convertisseur résonnant CLLC dans ce monde imaginaire et avec quelques étapes tente de trouver la solution optimale dans le monde réel (c'est-à-dire les paramètres physiquement implémentables). À chaque étape, les paramètres discrets seront continus en mettant un plancher sous eux et en leur fixant un plafond. A la fin des étapes, le chargeur optimal entre 24 possibilités discrètes est sélectionné.

Enfin, les deux objectifs de cette thèse, à savoir l'analyse et l'optimisation, sont vérifiés par les tests expérimentaux et la comparaison avec les résultats de simulation et les résultats basés sur la FHA. La précision de l'analyse du plan d'état proposée est vérifiée par les expériences sur un convertisseur résonant CLLC bidirectionnel de 3,3 kW avec des transistors GaN comme interrupteurs au primaire et au secondaire. Les résultats confirment la précision de l'analyse du plan d'état proposée du convertisseur résonant CLLC fonctionnant dans les deux sens de transfert de puissance. L'algorithme d'optimisation est également vérifié à l'aide de deux configurations expérimentales, à savoir le convertisseur optimal et un convertisseur de plus petite taille.

# Acknowledgments

Firstly, I would like to express my sincerest gratitude to my supervisors, Dr. Farzad Tahami and Prof. Jean-Luc Schanen, for their consistent supervision, guidance, patience, and support throughout my study. It has been quite a tough and rewarding journey since my dual-degree PhD program started. They have given me the freedom to explore research directions and supported me to build different experimental setups. They taught me a lot not only in the technical and scientific aspects but also in the human aspects of being a researcher. I honestly believe I could not have better supervisors for doing this PhD.

This thesis was funded by Embassy of France in Tehran with the Bourse of French Government, supported in part by the French National Program, and in part by the Iranian National Science Foundation. Many thanks to the people who help me in this way.

I must express my gratitude to the jury members for their useful and productive questions and discussions. I thank Prof. Forouhar Farzaneh for being the president of the jury. Many thanks to Prof. Sébastien Mariethoz and Prof. Mohammad Tavakoli-Bina for all the time and effort that they put on carefully reading the thesis and writing an accurate and detailed report. Special thanks to Prof. Yves Lembeye, Dr. Mohammadreza Zolghadri, and Prof. Shahriar Kaboli for their constructive comments on the examination of my thesis.

I would like to thank G2ELab, the administrative team and human resources especially Ms. Nadine Michel, and the technical team especially Benoit Sarrazin, for providing me hardware prototype, design and practice. Additionally, all the professors Laurent Gerbaud, David Frey, Mahmoud Fotouhi, Yvan Avenas, Seddik Bacha.

During the period of working in G2ELab and Sharif University, I got to know many great people. I would like to thanks all my friends in power electronics and other teams for the wonderful times we had: Morteza, Soleiman, Reza, Ali, Mahdi, Baoling, Alexis, Yousra, Adrien, Andre, Bakr, Blazej, Damien, Lucas, Nisith, Nicolas, Nasreddin, and many others.

Lastly, I'd like to thank my wife Zahra, who has been very supportive, lending an ear and cheerfully and efficiently picking up extra tasks I've missed during the long hours required to complete this effort. I would especially like to thank my parents Mahmoud and Roghayyah, my brother Milad, and my sister Zahra for placing such a consistent and relentless emphasis on the importance of education from our earliest years, for enabling the educational goals of my siblings and me, and for keeping us all on track.

# Table of contents

- LIST OF FIGURES..... XIV**
- LIST OF TABLES.....XX**
- LIST OF ABBREVIATIONS.....XXIII**
- LIST OF SYMBOLS.....XXV**
- 1. INTRODUCTION..... 1**
  - 1.1. BACKGROUND ..... 1
  - 1.2. PROBLEM STATEMENT AND CHALLENGES ..... 7
  - 1.3. RESEARCH SCOPES AND OBJECTIVES ..... 11
    - 1.3.1. *Analysis* ..... 11
    - 1.3.2. *Optimization* ..... 13
  - 1.4. THESIS OUTLINE ..... 15
- 2. LITERATURE REVIEW ..... 17**
- 3. FIRST HARMONIC APPROXIMATION MODEL OF CLLC RESONANT CONVERTER  
32**
  - 3.1. INTRODUCTION ..... 32
  - 3.2. FHA METHOD..... 32
  - 3.3. FHA MODEL FOR THE CLLC RESONANT CONVERTER ..... 35
  - 3.4. EVALUATION OF ELECTRICAL CONSTRAINTS ..... 36
    - 3.4.1. *Current Evaluation based on FHA*..... 37
    - 3.4.2. *Voltage Evaluation based on FHA*..... 38
    - 3.4.3. *ZVS Evaluation based on FHA*..... 40
  - 3.5. SUMMARY ..... 41
- 4. GLOBAL DESIGN METHODOLOGY..... 43**
  - 4.1. INTRODUCTION ..... 43
  - 4.2. OPTIMIZATION PROBLEM DEFINITION..... 44
  - 4.3. OPTIMIZATION ALGORITHMS ..... 45
    - 4.3.1. *Stochastic Algorithms*..... 45
    - 4.3.2. *Deterministic Algorithms*..... 46
  - 4.4. SEQUENTIAL QUADRATIC PROGRAMMING (SQP)..... 47
  - 4.5. CONTINUOUS MODELING OF DISCRETE PARAMETERS ..... 47
    - 4.5.1. *Standard core sizes*..... 47
      - 4.1.1. *The number of turns*..... 49
  - 4.2. DESIGN METHODOLOGY AND MODELS ..... 50
    - 4.2.1. *Semiconductor Losses* ..... 50
      - Proposed Switching Losses Calculation for GaN transistors ..... 50
      - Proposed Conduction Losses Calculation for GaN transistors..... 58
      - Diode Losses..... 60
    - 4.2.2. *Core Losses in Magnetic Components* ..... 60
    - 4.2.3. *Copper Losses in wires*..... 61
    - 4.2.4. *Capacitor Losses* ..... 63
    - 4.2.5. *Inductor Design*..... 63

4.2.6.	<i>Transformer Design</i> .....	66
	Core Selection.....	68
	Number of Turns.....	69
4.2.7.	<i>Selection of Resonant Capacitor</i> .....	70
4.2.8.	<i>Objective Functions Evaluation</i> .....	70
4.2.9.	<i>Constraints Discussion</i> .....	71
	Operating Region.....	72
	Maximum Temperature.....	73
	Maximum RMS Current for resonant capacitors and inductors.....	76
	Maximum Voltage .....	77
	ZVS Condition .....	77
	CCM Condition.....	78
4.3.	REQUIREMENTS OF EV CHARGERS .....	78
4.3.1.	<i>Electrical Requirements</i> .....	78
4.3.2.	<i>Placement Requirements</i> .....	79
4.3.3.	<i>Environmental Requirements</i> .....	80
4.3.4.	<i>Safety Requirements</i> .....	80
4.4.	SIMULATION VERIFICATION OF SWITCHING AND CONDUCTION LOSSES MODEL .....	81
4.4.1.	<i>Verifying the Switching Power Loss Model</i> .....	81
4.4.2.	<i>Verifying the Conduction Power Loss Model</i> .....	82
4.5.	MAXWELL VERIFICATIONS OF THE MAGNETIC DESIGN.....	83
4.6.	SUMMARY .....	85
<b>5.</b>	<b>PROPOSED STATE PLANE ANALYSIS .....</b>	<b>87</b>
5.1.	INTRODUCTION .....	87
5.2.	OPERATING MODES OF THE CLLC RESONANT CONVERTER .....	87
5.3.	PROPOSED NEW STATE-PLANE ANALYSIS OF THE CLLC RESONANT CONVERTER .....	91
5.3.1.	<i>Stresses of Components</i> .....	97
	Current Stresses .....	97
	Voltage Stresses .....	100
5.3.2.	<i>Soft Switching Conditions</i> .....	102
5.3.3.	<i>Output Characteristic</i> .....	104
5.3.4.	<i>Control Plane Characteristics</i> .....	105
5.3.5.	<i>Constant stresses of the resonant components</i> .....	106
5.4.	PROPOSED DCM ANALYSIS FOR CLLC RESONANT CONVERTER.....	107
5.4.1.	<i>DCM state-plane diagram</i> .....	107
5.4.2.	<i>Current stress in DCM</i> .....	110
5.4.3.	<i>Voltage stress in DCM</i> .....	111
5.5.	BOUNDARY CONDITION BETWEEN CCM AND DCM.....	111
5.6.	SIMULATION VERIFICATION .....	114
5.7.	EXPERIMENTAL VERIFICATION .....	115
5.7.1.	<i>Specification of the experimental set up</i> .....	115
5.7.2.	<i>Semiconductors</i> .....	116
5.7.3.	<i>Gate driver circuit</i> .....	117
5.7.4.	<i>Input signals and dead-time circuit</i> .....	118
5.7.5.	<i>Resonant tank</i> .....	119
5.7.6.	<i>PCB</i> .....	122
5.7.7.	<i>Main Waveforms and Comparisons</i> .....	123
5.7.8.	<i>State-plane Analysis Experimental Verifications</i> .....	123
	Output and Control Plane Characteristics .....	123
	Maximum Current and Voltage of Resonant Elements.....	125
	Soft Switching Condition.....	128

Boundary and DCM Operating .....	129
5.7.9. <i>General Comparisons</i> .....	130
5.8. SUMMARY.....	132
<b>6. PROPOSED MULTI OPERATING POINTS TWO-STAGE OPTIMIZATION METHOD</b>	
<b>133</b>	
6.1. INTRODUCTION.....	133
6.2. SOFTWARE ENVIRONMENT.....	133
6.3. OPTIMIZATION PARAMETERS .....	134
6.3.1. <i>Objective function</i> .....	135
6.3.2. <i>Input Parameters</i> .....	138
Electrical input parameters.....	138
Geometrical input parameters .....	140
Coefficient of operating points and G2V probability.....	141
6.3.3. <i>Constraints</i> .....	141
ZVS constraint .....	141
CCM constraint.....	142
Maximum junction temperature.....	143
Minimum efficiency.....	143
Transformer saturation checking.....	143
Horizontally fit in the core .....	144
Vertically fit in the core .....	144
Maximum voltage of the resonant capacitors .....	144
6.3.4. <i>Output parameters</i> .....	145
6.4. SINGLE OPERATING POINT OPTIMIZATION.....	146
6.5. THE PROPOSED MULTI OPERATING POINTS OPTIMIZATION (ALGORITHMS AND TRANSFERRING FROM THE IMAGINARY WORLD TO THE REAL WORLD) .....	148
6.6. NUMERICAL CLARIFICATION OF THE PROPOSED OPTIMIZATION PROCESS.....	151
6.7. COMPARISON BETWEEN THE OPTIMIZATION RESULTS .....	160
6.8. EXPERIMENTAL VERIFICATION .....	162
6.8.1. <i>Specifications of the Experimental Prototype</i> .....	163
6.8.2. <i>Resonant tank</i> .....	164
6.8.3. <i>Considering a Lower Size than the Optimum Setup</i> .....	166
6.8.4. <i>Considering the Optimum Setup</i> .....	169
6.9. SUMMARY.....	172
<b>7. CONCLUSIONS AND FUTURE WORK.....</b>	<b>174</b>
7.1. CONCLUSIONS.....	174
7.2. FUTURE WORK .....	177
<b>REFERENCES .....</b>	<b>178</b>
<b>APPENDIX I.....</b>	<b>191</b>
<b>APPENDIX II .....</b>	<b>192</b>
<b>APPENDIX III.....</b>	<b>200</b>
<b>APPENDIX IV.....</b>	<b>202</b>

# List of Figures

Fig. 1-1: Annual CO <sub>2</sub> emission from fossil fuels and industry. Source: Global Carbon Project [3] .....	1
Fig. 1-2: EV sales in the world from 2012 to 2021 [8] .....	2
Fig. 1-3: The main parts of an all-electric vehicle or battery electric vehicle. *Source: www.afdc.energy.gov .....	4
Fig. 1-4: Number of charging stations installed in France from 2012 to 2021 [18].....	5
Fig. 1-5: General comparison between Si, SiC, and GaN semiconductors [19] .....	5
Fig. 1-6: The conceptual diagram of power flow direction for G2V, V2G, and V2H applications .....	6
Fig. 1-7: Different operating points to reach the global or local maximum. ....	9
Fig. 2-1: Basic concept of an Off-board charger (left side) and On-board charger (right side). ....	17
Fig. 2-2: Basic concept of a wired charger (left side) and wireless charger (right side). ....	18
Fig. 2-3: Conceptual diagram of a bidirectional charger for V2G applications .....	18
Fig. 2-4: Typical structure of a two-stage charger.....	19
Fig. 2-5: Basic structure of a full-bridge resonant converter.....	20
Fig. 2-6: Schematic diagram of a full bridge series resonant converter (SRC).....	21
Fig. 2-7: Schematic diagram of a full bridge parallel resonant converter (PRC).....	21
Fig. 2-8: Schematic diagram of a full bridge LCC resonant converter. ....	21
Fig. 2-9: Schematic diagram of a dual-active bridge converter (DAB). ....	22
Fig. 2-10: Schematic diagram of a full bridge LLC resonant converter.....	22
Fig. 2-11: The applied voltages to the resonant tank of an LLC resonant converter. ....	23
Fig. 2-12: Schematic diagram of a bidirectional full-bridge CLLC resonant converter.....	24
Fig. 2-13: Charging process of a lithium-ion cell in constant current (CC) and constant voltage (CV) processes.....	25
Fig. 3-1: The before and after voltages of the primary side (top) and secondary side (bottom) .....	33
Fig. 3-2: the fundamental harmonic of a square voltage .....	33

Fig. 3-3: FHA model of the full-bridge inverter.....	34
Fig. 3-4: FHA model of the full-bridge rectifier .....	35
Fig. 3-5: FHA model of the full-bridge CLLC resonant converter .....	35
Fig. 3-6: The current of $L_1$ (top) and $L_2$ (bottom) (red curves) and their FHA model (blue curves) .....	37
Fig. 3-7: The voltage of $C_1$ (top) and $C_2$ (bottom) (red curves) and their FHA model (blue curves).....	39
Fig. 3-8: The switching instance for $L_m=58.9\mu\text{H}$ : switch voltage (brown), switch current (green), and gate-to-source voltages (red and blue) .....	40
Fig. 3-9: The switching instance for $L_m=1.5\text{mH}$ : switch voltage (brown), switch current (green), and gate-to-source voltages (red and blue) .....	41
Fig. 4-1: The operating region and constraint of a single-variable objective function.....	44
Fig. 4-2: Geometrical diagram of E-shape core .....	47
Fig. 4-3: Continuous models for some variables using interpolation for parameter X (a); parameter C (b); and the volume of the core (c). .....	49
Fig. 4-4: The circuit test for switching loss calculation of a GaN transistor based on the datasheet information.....	52
Fig. 4-5: Switching losses based on the variation of junction temperature and drain-to-source current for a GaN transistor operating at the base values.....	54
Fig. 4-6: Switching losses based on considering the type II parameters for a GaN transistor operating at the base value. Variation of drain-to-source voltage from 50V to 650V (a), the gate resistor for OFF state (b), the gate resistor for ON state (c), the gate-to-source voltage for OFF condition (d), the gate-to-source voltage for ON condition (e), the parasitic inductor for a gate pin with considering internal gate inductance (f), $C_{iss}$ (g), $C_{oss}$ (h), and $C_{rss}$ (i) capacitors effects consideration for switching losses. The red line, blue line, and black line are OFF switching loss, ON switching loss, and total switching loss, respectively. ....	56
Fig. 4-7: Cross-section area of a circular wire and its skin depth .....	62
Fig. 4-8: Typical structure of a conventional EE core.....	64
Fig. 4-9: The flowchart for core selection .....	65
Fig. 4-10: Minimum dead-time versus the magnetizing inductance .....	67
Fig. 4-11: Effect of magnetizing inductance on (A) maximum current of the primary side; (B) maximum current of the secondary side; (C) maximum voltage of $C_1$ ; (D) maximum voltage of $C_2$ . .....	67
Fig. 4-12: Effect of magnetizing inductance on the J-M curve .....	68
Fig. 4-13: Effect of different constraints on J-M curve: (a) voltage; (b) current; (c) power; (d) the complete operating region.....	72



Fig. 4-14: Thermal modeling of a semiconductor .....	73
Fig. 4-15: Effect of temperature on different materials 3C90 (left circuit) [152], and 3F4 (right circuit) [153]. .....	75
Fig. 4-16: The DC bias characteristic of the CGA6N1C0G3A822J230AE capacitor * Source: product.tdk.com.....	77
Fig. 4-17: Complete structure of an on-board charger. ....	79
Fig. 4-18: 2-D Maxwell implementation of a transformer with 8 turns .....	83
Fig. 4-19: Maxwell simulation result for leakage inductance measuring.....	83
Fig. 4-20: Maxwell simulation results of magnetizing inductance .....	84
Fig. 4-21: 3-D Maxwell implementation of the planar transformer with 8 turns .....	84
Fig. 4-22: 3-D flux density distribution obtained by Maxwell simulation.....	85
Fig. 5-1: Schematic diagram of the full-bridge bidirectional CLLC resonant converter. The red and blue signs are corresponding to the forward and the reverse power conversion, respectively.....	88
Fig. 5-2: Typical CLLC resonant converter waveforms for the above resonant frequency in the forward power transfer mode.....	89
Fig. 5-3: Equivalent circuit of CLLC resonant converter in subinterval 1 (a), subinterval 2 (b), subinterval 3 (c), and subinterval 4 (d).....	90
Fig. 5-4: Equivalent circuit for SRC-P (a) and SRC-N (b). ....	93
Fig. 5-5: State plane diagram of Subinterval 1 for SRC-P (left) and SRC-N (right) .....	94
Fig. 5-6: State plane diagram of Subinterval 2 for SRC-P (left) and SRC-N (right) .....	94
Fig. 5-7: State plane diagram of Subinterval 3 for SRC-P (left) and SRC-N (right) .....	95
Fig. 5-8: State plane diagram of Subinterval 4 for SRC-P (left) and SRC-N (right) .....	95
Fig. 5-9: State-plane diagram of the CLLC resonant converter operating on CCM, for SRC-P (top) and SRC-N (bottom). ....	96
Fig. 5-10: Maximum currents of the primary and the secondary sides in SRC-P and SRC-N state-plane diagrams for; $\beta_P < \pi/2$ (a), $\pi/2 < \beta_P < \pi/2 + \theta_0$ (b), and $\beta_P > \pi/2 + \theta_0$ (c).....	98
Fig. 5-11: The jLP-jLN state-plane trajectory for calculating $v_{C1max}$ . ....	101
Fig. 5-12: Circuit condition between subintervals 1 and 2 for the ZVS analysis. ....	102
Fig. 5-13: The ZVS operating region as a function of voltage gain and dead-time equivalent angle. ....	104
Fig. 5-14: Output characteristics of the CLLC resonant converter for different normalized switching frequencies. ....	105

Fig. 5-15: Constant stresses diagram based on the different resonant elements. (a) $j_{L1}$ and $j_{L2}$ are fixed; (b) $j_{L1}$ and $m_{C1}$ are fixed; (c) $m_{C1}$ and $m_{C2}$ are fixed; (d) $j_{L2}$ and $m_{C2}$ are fixed. ....	106
Fig. 5-16: Typical CLLC resonant converter operation in the discontinuous conduction mode during a half switching period.....	107
Fig. 5-17: The subinterval of III for DCM operating .....	108
Fig. 5-18: The resonant tank model in subinterval III of DCM operating .....	108
Fig. 5-19: The complete state-plane analysis of the CLLC resonant converter in DCM operating. (a) SRC-P and (b) SRC-N.....	110
Fig. 5-20: The circuit diagram of the resonant tank for the DCM condition.....	112
Fig. 5-21: Control plane diagram (M-F) with CCM/DCM boundaries for different values of Q. ....	113
Fig. 5-22: State-plane analysis of SRC-P and SRC-N in the boundary condition. ....	113
Fig. 5-23: The time domain waveform obtained by the state plane analysis of $i_{L1}$ (a), and the state plane analysis of SRC-P (b), and SRC-N (c). ....	114
Fig. 5-24: A comparison for $i_{L1max}$ based on the state plane analysis (a) and simulation with PSIM (b). ....	115
Fig. 5-25: The 3.3kW bidirectional EV charger experimental set up.....	116
Fig. 5-26: The -3V and +6V circuit diagram using PES1-S5-S9-M-TR to supply gate driver.....	118
Fig. 5-27: The SI8271GB-IS gate driver circuit diagram.....	118
Fig. 5-28: The dead-time circuit using 74VHC132MTCX NAND IC and RC circuits.....	119
Fig. 5-29: The magnetic transformers (left figure) and impedance analyzer to measure leakage inductance and magnetizing inductance.....	120
Fig. 5-30: Short circuit test (top) and open circuit test (bottom) to measure the leakage inductance and magnetizing inductance.....	120
Fig. 5-31: Physical implementation of the transformer, primary inductor (L1), and secondary inductor (L2) obtained by the initial design. ....	121
Fig. 5-32 : The resonant capacitor for the resonant capacitors.....	121
Fig. 5-33: The top layer (a) and bottom layer (b) of the final PCB of the dual active full-bridge for using as the inverting and rectifying parts .....	122
Fig. 5-34: Experimental waveforms of CLLC resonant converter in CCM for (a) $F = 1$ , $P_{out} = 1.2$ kW, (b) $F = 1.5$ , $P_{out} = 960$ W, (c) $F = 2$ , $P_{out} = 790$ W, and (d) $F = 3$ , $P_{out} = 570$ W. ....	124
Fig. 5-35: M-F diagram of the CLLC resonant converter. ....	124
Fig. 5-36: M-J diagram of the CLLC resonant converter.....	125

Fig. 5-37 : Current and voltage of the resonant elements for the forward power transferring at: (a) $\pi/2 < \beta_P$ at $P_{out} = 700 \text{ W}$ , $V_{out} = 254 \text{ V}$ , $f_{sw} = 250 \text{ kHz}$ , (b) $\pi/2 < \beta_P < \theta_0$ at $P_{out} = 1 \text{ kW}$ , $V_{out} = 307 \text{ V}$ , $f_{sw} = 170 \text{ kHz}$ , and (c) $\beta_P > \pi/2 + \theta_0$ at $P_{out} = 1.4 \text{ kW}$ , $V_{out} = 360 \text{ V}$ , $f_{sw} = 120 \text{ kHz}$ .	126
Fig. 5-38: Current and voltage waveforms of the resonant elements for the reverse power transfer mode under different conditions: (a) $P_{out} = 3025 \text{ W}$ , $V_{out} = 385 \text{ V}$ , $f_{sw} = 100 \text{ kHz}$ , (b) $P_{out} = 918 \text{ W}$ , $V_{out} = 212.5 \text{ V}$ , $f_{sw} = 200 \text{ kHz}$ .	127
Fig. 5-39: Waveforms corresponding to minimum dead-time that ensures ZVS and ZCS on the rectifier.	128
Fig. 5-40: Simulation of minimum dead-time (boundary condition) for gate pulses and the switch voltage to ensure ZVS.	128
Fig. 5-41: The secondary side current in the boundary condition by; (a) simulation, and (b) state-plane analysis.	129
Fig. 5-42: Experimental test in the DCM operating.	129
Fig. 5-43: Error comparison of the different parameters based on simulation, SPA, and FHA method in comparison with the experimental results for (a) $P_{OUT}=1281\text{W}$ and $P_{OUT}=527\text{W}$	131
Fig. 5-44: Efficiency for the forward and reverse power transferring.	131
Fig. 6-1: The diagram of CADES Software	133
Fig. 6-2: The default environment of the CADES software.	134
Fig. 6-3: The probability of operating in G2V and V2G in the EV's lifespan.	135
Fig. 6-4: Displaying the required voltages for CCM checking	142
Fig. 6-5: Selection of 4 operating points based on the lithium battery charging process.	146
Fig. 6-6: The proposed optimization algorithm for multi operating point optimization in EV charging applications.	149
Fig. 6-7: Horizontal and vertical arrangements of the turns.	150
Fig. 6-8: Two experimental prototypes. Case I is the optimum set up and Case II is the set up with a lower mass.	163
Fig. 6-9: The magnetic transformers (left figure) and impedance analyzer to measure leakage inductance and magnetizing inductance	164
Fig. 6-10: Physical implementation of the transformer, primary inductor (L1), and secondary inductor (L2) obtained by the initial design.	165
Fig. 6-11: The resonant capacitors for two experiments, (a) for the set up with lower size, and (b) for the optimum set up	166
Fig. 6-12: Resonant tank of the experimental set up with a lower size	166

Fig. 6-13: The output current ( $I_{out}$ ) versus the output voltage ( $V_{out}$ ) of the smaller experimental set up ..... 167

Fig. 6-14: M-F curve of the smaller experimental set up ..... 167

Fig. 6-15: The junction temperature of GaN transistors of the primary side (left curve), and the primary resonant inductor (right curve). ..... 168

Fig. 6-16: The primary inductor current (red), the secondary inductor current (green), the primary capacitor voltage (blue), and the secondary capacitor voltage (orange) for the smaller in-size experimental set up..... 168

Fig. 6-17: Some important experimental results at  $F=1$ : (a) temperature distribution in a thermal diagram, (b) location of the components for better investigation of the thermal diagram, (c) voltage of resonant capacitors and current of resonant inductors, (d) drain-to-source and gate-to-source voltages of GaN transistor, and voltage and current of SiC diode. .... 169

Fig. 6-18: Some important experimental results at  $F=2$ : (a) temperature distribution in a thermal diagram, (b) location of the components for better investigation of the thermal diagram, (c) voltage of resonant capacitors and current of resonant inductors, (d) drain-to-source and gate-to-source voltages of GaN transistor, and voltage and current of SiC diode. .... 170

Fig. 6-19: Some important experimental results at  $F=3$ : (a) temperature distribution in a thermal diagram, (b) location of the components for better investigation of the thermal diagram, (c) voltage of resonant capacitors and current of resonant inductors, (d) drain-to-source and gate-to-source voltages of GaN transistor, and voltage and current of SiC diode. .... 171

# List of Tables

Table 1-1: Different standards voltage and current levels [13] .....	3
Table 2-1: Basic comparisons between analyzing methods .....	28
Table 2-2: Previous methods and parameters done for CLLC resonant converter.....	30
Table 3-1: Electrical specifications of the prototype converter.....	37
Table 3-2: The maximum and RMS values of $i_{L1}$ and $i_{L2}$ obtained by the PSIM simulation and FHA model.....	38
Table 3-3: The maximum and RMS values of $i_{L1}$ and $i_{L2}$ obtained by the PSIM simulation and FHA model.....	39
Table 3-4: FHA method and PSIM simulation comparisons for two different output powers .....	42
Table 4-1: The main properties of some optimization algorithms [114].....	46
Table 4-2: Important dimensional of the conventional E cores and planar E cores .....	48
Table 4-3: Continuous equations for the core sizes of conventional and planar E cores .....	50
Table 4-4: Based values of the proposed model for switching loss calculation.....	52
Table 4-5: List of coefficients for the proposed method for switching loss calculation, Type I (Eq. (4.5)) and Type II (Eq. (4.6)) Variables .....	55
Table 4-6: Two values of temperatures and resistance mentioned in the GaN transistors datasheet ....	59
Table 4-7: Thermal resistance of some semiconductors .....	74
Table 4-8: Specifications of the GaN transistors.....	81
Table 4-9: Scenarios for the Accuracy Verification of Proposed Method for the Switching Losses Calculation .....	81
Table 4-10: ON Resistance Comparison with the Proposed Model and LTSPICE Simulation.....	82
Table 5-1: Parameters exchanging for forward and reverse modes for using a symmetrical method for both.....	88
Table 5-2: Base values for the parameters of SRC-P and SRC-N.....	93
Table 5-3: Radius (r) and center (O) of the SRC-P and SRC-N arcs .....	96
Table 5-4: Some angles for the state-plane diagrams of SRC-P and SRC-N in CCM.....	97

Table 5-5: Some angles for the state-plane diagrams of SRC-P and SRC-N in DCM.....	111
Table 5-6: Components of the Experimental CLLC Resonant Converter.....	115
Table 5-7: Electrical characteristics of GS66508B transistor .....	117
Table 5-8: Comparison of the Measurement (Meas.), PSIM Simulation (Sim.), State-Plane Analysis (SPA), and First Harmonic Approximation (FHA) Results for Forward Power Transfer and two output powers. ....	130
Table 5-9: Comparison of the Measurement (Meas.), PSIM Simulation (Sim.), State-Plane Analysis (SPA), and First Harmonic Approximation (FHA) Results for Reverse Power Transfer and two output powers. ....	130
Table 6-1: Electrical input parameters for optimization.....	139
Table 6-2: Geometrical input parameters for optimization .....	140
Table 6-3: Optimization parameters, which are the coefficients of operating points and G2V probability .....	141
Table 6-4: Some important output parameters .....	145
Table 6-5: Single operating point optimization results in the imaginary world, by considering a different operating point and checking the objective function and constraints on all points.....	147
Table 6-6: The optimization results in step 2, when all the discrete parameters are in the imaginary world .....	152
Table 6-7: Input parameters for optimization in step 4 when one of the discrete parameters in step3 is transferred into the real world as a fixed parameter .....	153
Table 6-8: The optimization results in step 4, when one of the parameters was in the real world and two of them were in the imaginary world .....	154
Table 6-9: Input parameters for optimization in step 6 when two discrete parameters in step5 are transferred into the real world as a fixed parameter and only one parameter is free.....	155
Table 6-10: The optimization results in step 6, when two parameters were in the real world and one of them was in the imaginary world .....	155
Table 6-11: Input parameters for optimization in step 8 when all the three discrete parameters in step 6 are transferred into the real world .....	157
Table 6-12: The last optimization results (step 8), when all the three parameters were in the real world .....	158
Table 6-13: Number of parameters and running time comparison for two optimization process .....	160
Table 6-14: four operating points optimizations based on FHA and SPA methods.....	161
Table 6-15: Optimization results based on the genetic algorithm (GA) and sequential quadratic programming (SQP) for 4 operating points optimizations .....	162

Table 6-16: Specifications of two experimental prototypes .....	164
Table 6-17: General comparisons between some references and the proposed method .....	172
Table 0-1: Single operating point optimization results in the imaginary world when the maximum power density is selected for the objective function .....	200
Table 0-1: Single operating point optimization results in the real world when a lower size is selected for the magnetic parts, by considering a different operating point and checking the objective function and constraints on all points .....	202
Table 0-2: Single operating point optimization results in the real world when a higher size is selected for the magnetic parts, by considering a different operating point and checking the objective function and constraints on all points.....	203

# List of Abbreviations

<b>BC</b>	Bee Colony
<b>BEV</b>	Battery Electric Vehicle
<b>BMS</b>	Battery Management System
<b>CADES</b>	Component Architecture for Design of Engineering Systems
<b>CC</b>	Constant Current
<b>CV</b>	Constant Voltage
<b>CCM</b>	Continuous Conduction Mode
<b>DAB</b>	Dual Active Bridge
<b>DCM</b>	Discontinuous Conduction Mode
<b>DG</b>	Distributed Generation
<b>EIA</b>	Energy Information Administration
<b>EMC</b>	Electromagnetic Compatibility
<b>EMI</b>	Electromagnetic Interference
<b>ESR</b>	Equivalent Series Resistor
<b>EV</b>	Electric Vehicle
<b>FEM</b>	Finite Element Method
<b>FHA</b>	First Harmonic Approximation
<b>G2V</b>	Grid-to-Vehicle
<b>GA</b>	Genetic Algorithm
<b>GaN</b>	Gallium Nitride
<b>IC</b>	Integrated Circuit
<b>LP</b>	Linear programming
<b>MLCC</b>	Multilayer Ceramic Capacitor
<b>NLP</b>	Non-linear programming
<b>OF</b>	Objective Function
<b>PCB</b>	Printed Circuit Board
<b>PFC</b>	Power Factor Correction
<b>PRC</b>	Parallel Resonant Converter
<b>PSO</b>	Particle Swarm Optimization
<b>RMSE</b>	Root-Mean-Square Error
<b>SA</b>	Simulated Annealing
<b>SHC</b>	Stochastic Hill Climbing
<b>SML</b>	System Modeling Language
<b>SOC</b>	State-of-the-Charge
<b>SPA</b>	State Plane Analysis
<b>SPDT</b>	Single Pole Double Through
<b>SQP</b>	Sequential Quadratic Programming



<b>SRC</b>	Series Resonant Converter
<b>SRC-N</b>	N-type series resonant converter
<b>SRC-P</b>	P-type series resonant converter
<b>SSA</b>	State Space Analysis
<b>T2A</b>	Traction-to-Auxiliary
<b>TDA</b>	Time Domain Analysis
<b>THD</b>	Total Harmonic Distortion
<b>UPS</b>	Uninterruptable Power Supply
<b>V2G</b>	Vehicle-to-Grid
<b>V2H</b>	Vehicle-to-Home
<b>V2L</b>	Vehicle-to-Load
<b>WBG</b>	Wide Band Gap
<b>ZCS</b>	Zero Current Switching
<b>ZVS</b>	Zero Voltage Switching

# List of Symbols

$\alpha$	Duration of subinterval 2
$\alpha_N$	Duration of subinterval 2 for SRC-N circuit
$\alpha_P$	Duration of subinterval 2 for SRC-P circuit
$B$	Duration of subinterval 1
$\beta_N$	Duration of subinterval 1 for SRC-N circuit
$\beta_P$	Duration of subinterval 1 for SRC-P circuit
$\varphi$	Phase shift between voltage and current
$\theta_0$	The angle of between zero crossing of $i_{L1}$ and $i_{L2}$
$\delta$	Skin depth of a wire
$\delta_N$	The defined angle in Fig. 5-9 for SRC-N diagram
$\delta_P$	The defined angle in Fig. 5-9 for SRC-P diagram
$\lambda_C$	Optimization coefficient for G2V operating
$\lambda_D$	Optimization coefficient for V2G operating
$\lambda_N$	The defined angle in Fig. 5-9 for SRC-N diagram
$\lambda_P$	The defined angle in Fig. 5-9 for SRC-P diagram
$\eta$	Efficiency of the converter ( $=P_{OUT}/P_{IN}$ )
$\mu_0$	Permeability of free space
$\mu_r$	Magnetic permeability of the magnetic material
$\mathfrak{R}_c$	Reluctance of a portion of a magnetic core
$\mathfrak{R}_g$	Reluctance of an air gap
$\mathfrak{R}_{L1}$	Reluctance of $L_1$
$\mathfrak{R}_{L2}$	Reluctance of $L_2$
$\mathfrak{R}_T$	Reluctance of transformer
$\mathfrak{R}_{total}$	Equivalent reluctance of a magnetic core
$\omega$	Angular frequency
$\omega_0$	Base value of angular frequency
$\rho$	Specific resistance
$A_c$	Area of a magnetic core
$A_{eff}$	Effective area of a conductor
$A_g$	Area of an air gap
$a_N$	A circuit parameter defined in (5.5)
$A_N$	A circuit parameter defined in (5.12)
$a_P$	A circuit parameter defined in (5.5)
$A_P$	A circuit parameter defined in (5.12)
$B$	Maximum flux density of a magnetic core
$B_{max\_L1}$	Maximum flux density of inductor $L_1$
$B_{max\_L2}$	Maximum flux density of inductor $L_2$

$B_{max\_T}$	Maximum flux density of transformer
$B_N$	A circuit parameter defined in (5.12)
$B_P$	A circuit parameter defined in (5.12)
$C_1$	Resonant capacitor of primary side
$C_2$	Resonant capacitor of secondary side
$C'_2$	Transferred capacitor $C_2$ to the primary side
$CCM_{CHECKER}$	A parameter to check CCM condition
$C_F$	Output filter capacitor
$C_{ds}$	Drain-to-source capacitor
$C_{gd}$	Gate-to-drain capacitor
$C_{gs}$	Gate-to-source capacitor
$CheckB_{max\_L1}$	A parameter to check the saturation of inductor $L_1$
$CheckB_{max\_L2}$	A parameter to check the saturation of inductor $L_2$
$CheckB_{max\_T}$	A parameter to check the saturation of transformer
$C_{iss}$	GaN input capacitor
$C_N$	Resonant capacitor of SRC-N circuit
$C_o$	Output capacitor
$C_{oss}$	GaN output capacitor
$C_P$	Resonant capacitor of SRC-P circuit
$C_{rss}$	GaN reverse capacitor
$C_{SS}$	Parasitic capacitance of GaN transistor
$d$	Defined angle in Fig. 5-11 ( $=\tan^{-1}(I_{base,N}/I_{base,P})$ )
$E_{Loss}$	Switching loss energy
$e_N$	A circuit parameter defined in (5.5)
$e_P$	A circuit parameter defined in (5.5)
$E_{SW}$	Switching energy
$F$	Normalized switching frequency ( $=f_{sw}/f_0$ )
$f_0$	Base frequency of SRC-P and SRC-N circuits
$Fit\_H$	A parameter to check horizontal fitting of the turns
$Fit\_V$	A parameter to check vertical fitting of the turns
$f_{res}$	Resonant frequency
$f_{sw}$	Switching frequency
$f_{s,max}$	Maximum switching frequency
$I_{base,N}$	Base current for SRC-N circuit
$I_{base,P}$	Base current for SRC-P circuit
$I_{C,RMS}$	RMS current of a capacitor
$I_D$	Drain current
$I_{L1}$	First harmonic of $L_1$ current
$i_{L1}$	Current of inductor $L_1$
$i_{L1,max}$	Maximum current of inductor $L_1$
$I_{L2}$	First harmonic of $L_2$ current
$i_{L2}$	Current of inductor $L_2$
$i_{L2,max}$	Maximum current of inductor $L_2$
$i_{LN}$	Inductor current of SRC-N circuit

$i_{LP}$	Inductor current of SRC-P circuit
$I_{OUT}$	Output current
$I_{RMS}$	Root mean square current of GaN transistor
$J$	Normalized output current ( $=I_{OUT}/I_{base}$ )
$j_{L1}$	Normalized current of $L_1$ inductance
$j_{L2}$	Normalized current of $L_2$ inductance
$j_{LN}$	Normalized current of $L_N$ inductance
$j_{LP}$	Normalized current of $L_P$ inductance
$J_{LPN}$	Maximum current of SRC-N diagram
$J_{LPN\_i_{L1}}$	Maximum current of $i_{L1}$ in SRC-N diagram
$J_{LPN\_i_{L2}}$	Maximum current of $i_{L2}$ in SRC-N diagram
$J_{LPP}$	Maximum current of SRC-P diagram
$J_{LPP\_i_{L1}}$	Maximum current of $i_{L1}$ in SRC-P diagram
$J_{LPP\_i_{L2}}$	Maximum current of $i_{L2}$ in SRC-P diagram
$j_{Lx0}$	Normalized inductor initial current for $x \in \{P, N\}$
$J_{SC}$	Normalized output current in short circuit condition
$K$	Ratio of resonant capacitors ( $=C_2/C_1$ )
$K_{LM}$	Ratio of $L_m/L_1$
$L_1$	Resonant inductor of primary side
$L_2$	Resonant inductor of secondary side
$L'_2$	Transferred inductor $L_2$ to the primary side
$l_c$	Length of a magnetic core
$l_{eff}$	Effective length of a conductor
$L_{ex}$	Source extra inductance of GaN transistor
$l_g$	Air gap of a magnetic core
$L_{Gate}$	Gate inductance of GaN transistor
$L_{Load}$	Load inductance
$L_m$	Magnetizing inductance of transformer
$L_N$	Resonant inductor of SRC-N circuit
$L_{OC}$	The value of inductance in open circuit test
$L_P$	Resonant inductor of SRC-P circuit
$L_{SC}$	The value of inductance in short circuit test
$M$	Normalized output voltage ( $=V_{OUT}/V_{IN}$ )
$m_{C1}$	Normalized voltage of $C_1$ capacitor
$m_{C2}$	Normalized voltage of $C_2$ capacitor
$m_{CN}$	Normalized voltage of $C_N$ capacitor
$m_{CP}$	Normalized voltage of $C_P$ capacitor
$m_{CP,N}$	Maximum voltage of SRC-N diagram
$m_{CP,P}$	Maximum voltage of SRC-P diagram
$m_{CX0}$	Normalized capacitor initial voltage for $x \in \{P, N\}$
$m_{L1}$	Number of layers for inductor $L_1$
$m_{L2}$	Number of layers for inductor $L_2$
$m_T$	Number of layers for transformer
$m_{XN}$	Normalized voltage of SRC-N diagram in Fig. 5-11

$m_{XP}$	Normalized voltage of SRC-P diagram in Fig. 5-11
$n$	Transformer turn ratio
$N$	Number of turns of a magnetic core
$N_1$	Number of turns of the primary side
$N_2$	Number of turns of the secondary side
$NL1$	Number of turns of $L_1$
$nL1$	Number of turns in each layer for $L_1$
$NL2$	Number of turns of $L_2$
$nL2$	Number of turns in each layer for $L_2$
$NT$	Number of turns of transformer
$nT$	Number of turns in each layer for transformer
$O$	Centre of circles of SRC-P and SRC-N diagrams
$OF$	Objective function for an optimization problem
$OP$	Operating point
$P$	Probability of operating in G2V during EV's life
$P_{capacitor}$	Capacitor loss
$P_{cond.}$	Conduction power loss
$P_{copper}$	Copper loss
$P_{core}$	Core loss of magnetic part
$PD\_M$	Nominal output power divided by mass (W/g)
$PD\_Mass$	Efficiency divided by total mass (100%/g)
$PD\_V$	Nominal output power divided by volume (W/cm <sup>3</sup> )
$PD\_Vol$	Efficiency divided by total volume (100%/cm <sup>3</sup> )
$P_{diode}$	Diode power loss
$P_{SW}$	Switching power loss of a GaN transistor
$Q$	Normalized conductance
$R$	Resistive load
$R_{0,N}$	Base impedance of SRC-N circuit
$R_{0,P}$	Base impedance of SRC-P circuit
$R_1$	Value of ON resistance at temperature $T_1$
$r_{1N}$	Radius of SRC-N in subintervals 1 and 3
$r_{1P}$	Radius of SRC-P in subintervals 1 and 3
$R_2$	Value of ON resistance at temperature $T_2$
$r_{2N}$	Radius of SRC-N in subintervals 2 and 4
$r_{2P}$	Radius of SRC-P in subintervals 2 and 4
$R_{AC}$	AC resistance of a wire
$R_{DC}$	DC resistance of a wire
$R_e$	Effective resistance of FHA method
$R_G$	Gate resistance of GaN transistor
$RgOff$	Gate Resistor for OFF state
$RgOn$	Gate Resistor for ON state
$R_{JA}$	Junction-to-ambient thermal resistance
$R_{ON}$	ON resistance of a GaN transistor
$R_{th,JA}$	Core-to-ambient thermal resistance

$r_w$	Radius of a wire
$S$	Space between turns
$S_1$	Space between the ending turn and core
<b>SRC-N</b>	N-type series resonant converter
<b>SRC-P</b>	P-type series resonant converter
$t_{dt}$	Dead-time
$T_A$	Ambient temperature
$T_J$	Junction temperature
$T_s$	Period duration time
<b>V_C1_Checker</b>	A parameter to check maximum voltage across $C_1$
<b>V_C2_Checker</b>	A parameter to check maximum voltage across $C_2$
$V_{base,N}$	Base voltage for SRC-N circuit
$V_{base,P}$	Base voltage for SRC-P circuit
$V_{battery}$	Battery's voltage
$V_{C1}$	First harmonic of $C_1$ voltage
$v_{C1}$	Voltage of capacitor $C_1$
$v_{C1,max}$	Maximum voltage of capacitor $C_1$
$V_{C2}$	First harmonic of $C_2$ voltage
$v_{C2}$	Voltage of capacitor $C_2$
$v_{C2,max}$	Maximum voltage of capacitor $C_2$
$v_{CN}$	Capacitor voltage of SRC-N circuit
$V_{core}$	Volume of the magnetic core
$v_{CP}$	Capacitor voltage of SRC-P circuit
<b>VDDH</b>	+6V voltage for turning-ON the GaN transistor
<b>VEEH</b>	-3V voltage for turning-OFF the GaN transistor
$V_{drop}$	Voltage dropout of diode
$V_{DS}$	Drain-to-source voltage
$V_g$	Input voltage
$V_{gNeg}$	Negative Gate-Source Voltage
$V_{gPos}$	Positive Gate-Source Voltage
$V_{IN}$	Input voltage
$V_O$	Output voltage
$V_{OUT}$	Output voltage
$V'_{OUT}$	Output voltage transferred to the primary side
<b>X</b>	Defined parameter for continuous model
<b>XL1</b>	The core size of $L_1$ in the continuous model
<b>XL2</b>	The core size of $L_2$ in the continuous model
<b>XT</b>	The core size of transformer in the continuous model
<b>ZVSCHECKER</b>	A parameter to check ZVS condition

# 1. Introduction

## 1.1. Background

Fossil fuels have been the main source of energy supply in the world [1]. With the development in the transportation industries, as well as the increase in energy consumption, the consumption of fossil fuels has increased even more [2]. It causes more environmental pollution and a reduction in fossil fuel resources. CO<sub>2</sub> emissions from fossil fuels have been about 35 billion tons [3] and it is increasing rapidly as shown in Fig. 1-1. The transportation industry can also increase CO<sub>2</sub> emissions if conventional vehicles are supplied with fossil fuels. These reasons and the limited resources of fossil fuels and growing oil prices have led the international community to use clean and renewable energies as the main energy resource [4]. Electric vehicles (EVs) are a new solution due to their contribution towards reducing greenhouse gas emissions.

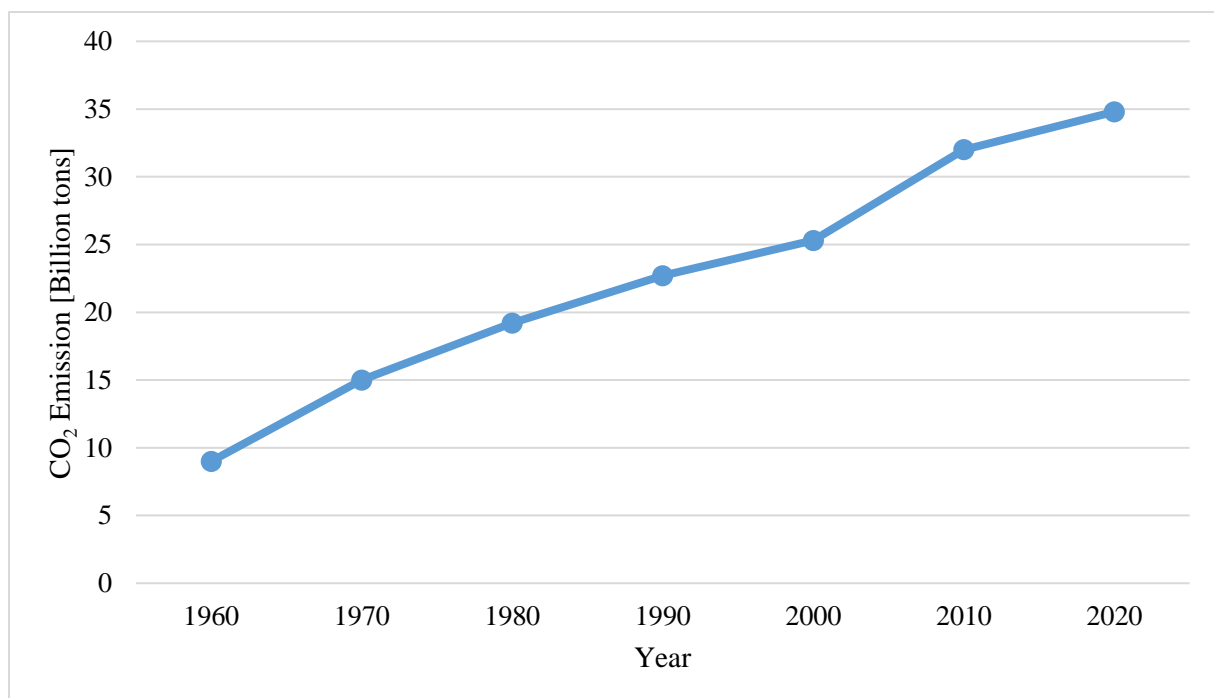


*Fig. 1-1: Annual CO<sub>2</sub> emission from fossil fuels and industry.*

*Source: Global Carbon Project [3]*

An electric vehicle, as an alternative to traditional fuel vehicles, has an electric motor that can be used in the propulsion part of a vehicle to promote transportation. As part of an ambitious plan for electrified transportation under the Paris climate accord, France will eradicate sales of conventional vehicles by 2040 [5]. Some governments have undertaken to abolish the internal combustion engine vehicle for the automotive industry of the future. Denmark planned to reduce 30% of CO<sub>2</sub> emissions by using EVs in transportation from 2020 to 2030 [6]. The impressive progress of EVs leads to a decrease of nearly 580 million tons in comparison with an equivalent use of ICE vehicles in the announced pledges scenario [7].

About 3.24 million EVs were sold in 2020 and it reached 6.75 million EVs in 2021, which means that the global demand for EVs has increased by 108% from 2020 to 2021 as shown in Fig. 1-2 [8].

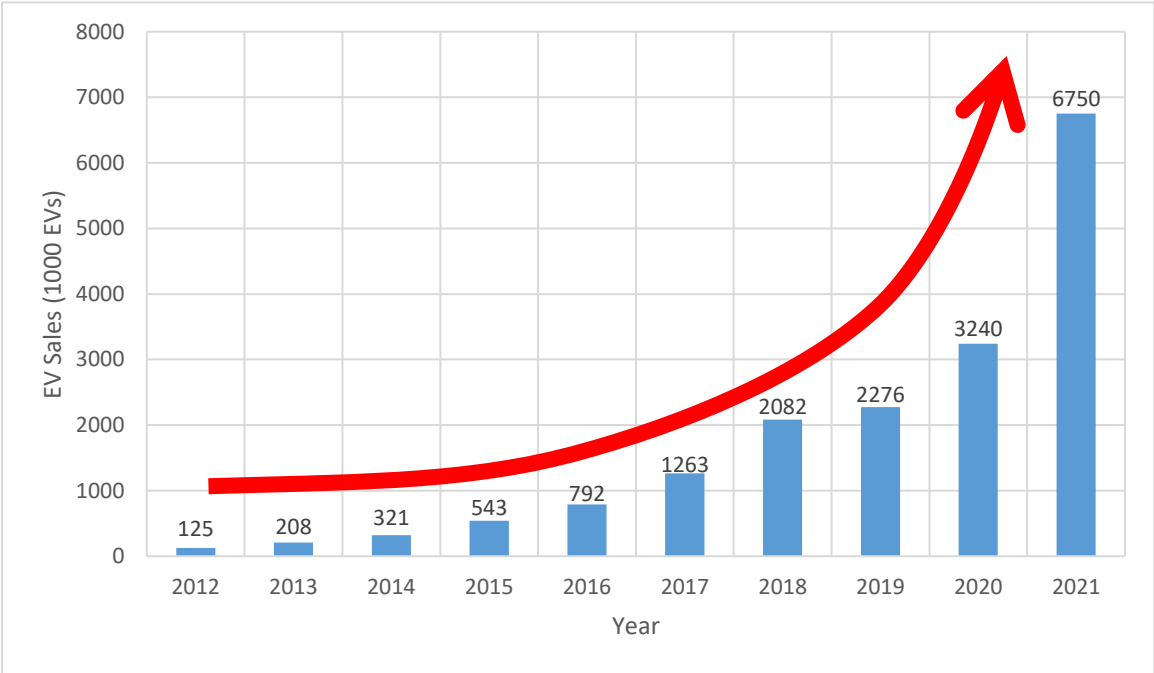


Fig. 1-2: EV sales in the world from 2012 to 2021 [8]

The above figure manifests that global EV sales have exponentially increased since 2012, and the US Energy Information Administration (EIA) expects to grow them to 2.21 billion vehicles by 2050 [9].

In general, the advantages of electric vehicles in comparison with internal combustion vehicles can be presented as follows [10]:

- Higher efficiency;
- Less environmental pollution;
- Less noise;



- Ability to use different types of energy such as solar and wind;
- Ability to use different storage systems to store electrical energy such as batteries, supercapacitors, and flywheels;
- Ability to use the energy of braking mode and return braking energy to the vehicle;
- Smoother and more controllable movement.

Despite the many advantages of electric vehicles, one of their most important drawbacks is their short driving distance, which can be solved by using a larger capacity battery, improving the technologies of the batteries, using hybrid configuration, etc. [11].

The second disadvantage of electric vehicles is the limited number of charging stations in the world. Until 2021, there are only 569,000 fast public chargers in the world [7]. However, it is expected to reach 1.3 million public charger stations by 2025, and also 2.9 million stations by 2030 [12].

The third disadvantage of electric vehicles is the diversification of the existing EV charging standards which makes the designers perplexing. As an example, Table 1-1 shows the current and voltage levels of IEC and SAE standards for DC and AC charging [13]:

*Table 1-1: Different standards voltage and current levels [13]*

Standards	Phase	Level/Mode	Voltage (V)	Current (A)
IEC 62196	AC Single	Mode 1	120	16
	AC Single	Mode 2	240	32
	AC Single	Mode 3	250	32-250
	DC	Mode 4	600	400
IEC 61851	AC Single	Mode 1	120	16
	AC Single	Mode 2	240	80
	DC	Mode 4	200-450	80
SAE J1772	AC Single	Level 1	120	16
	AC Single	Level 2	240	32-80
	DC	Level 1	200-450	80
	DC	Level 2	200-450	200

As shown in Table 1-1 for 240V sourced by AC voltage, the IEC62196 offers a current of 32A, whereas the current is 80A for IEC61851 and it will be 32A~80A for SAEJ1772. In this dissertation, a 400V fixed DC voltage source will be considered, which is obtained by 240V AC rectified and boosted. It means that the selected EV charger would be Mode 2 of IEC62196, Mode 2 of IEC61851, and AC Level 2 and DC Level 1 SAEJ1772. The specifications of the selected EV charger are similar to the typical Level 2 charger. In the United States and since 2021, over 80% of electric vehicle supply equipment ports were Level 2 [14]. There exists also

other standards corresponding to the charging applications, such as SAE J3068 for on-board chargers and GB/T 20234 for on-board and off-board chargers.

The sales of different electric vehicles have increased from less than 210 thousand in 2014 to more than 6.7 million in 2021 [8]. The electric vehicle consists of several parts, including the electric motor, battery pack, onboard charger, power electronics controller, battery management system (BMS), and thermal cooling system. Fig. 1-3 shows the network of an all-electric vehicle [15].

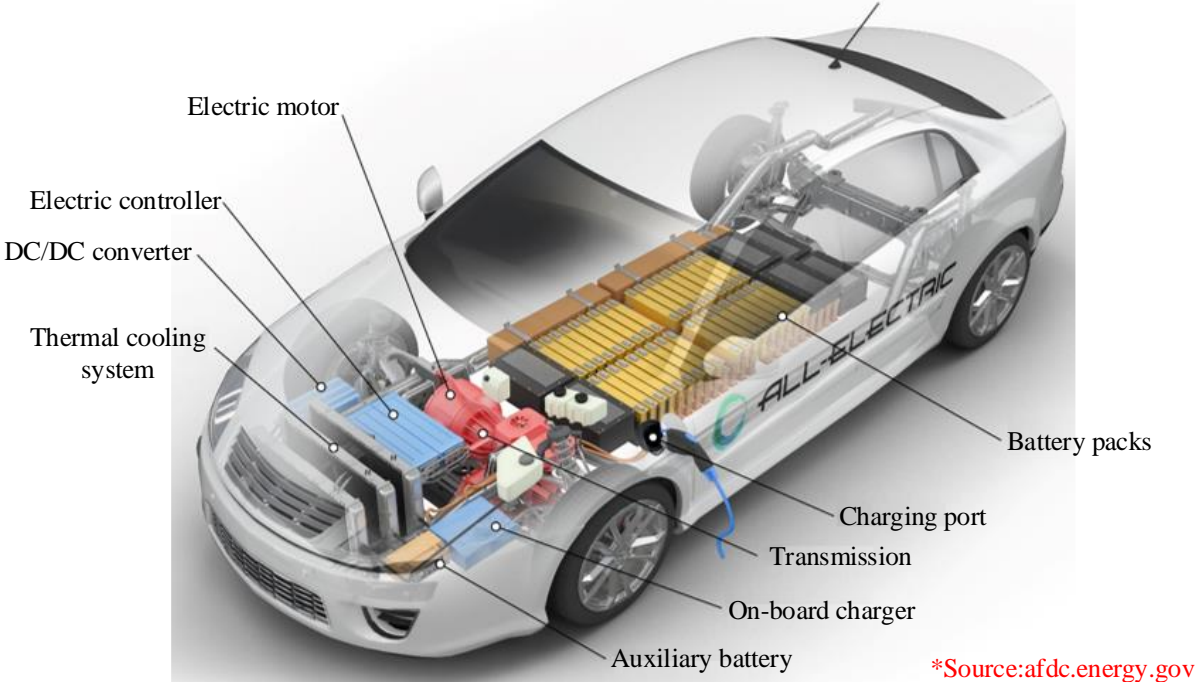


*Fig. 1-3: The main parts of an all-electric vehicle or battery electric vehicle.*

*\*Source: www.afdc.energy.gov*

Among them, battery chargers have played an important role in the development of the electric vehicle industry. The number of charging stations was 2,100 in 2011 and it reached 50,054 stations in 2021 [8]. In France, the number of charging stations has increased from 809 stations in 2012 to 37,128 stations in 2021 as shown in Fig. 1-4 [16]. For EV owners, the most reliable place to charge batteries is their home [17]. On-board chargers help EV owners to charge their vehicles wherever there is an appropriate electric outlet [18].

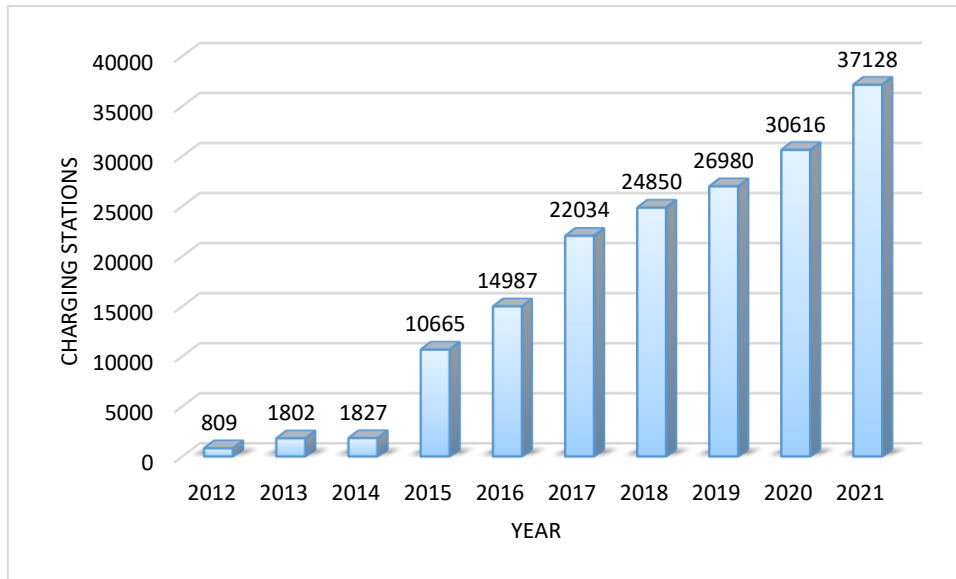


Fig. 1-4: Number of charging stations installed in France from 2012 to 2021 [18]

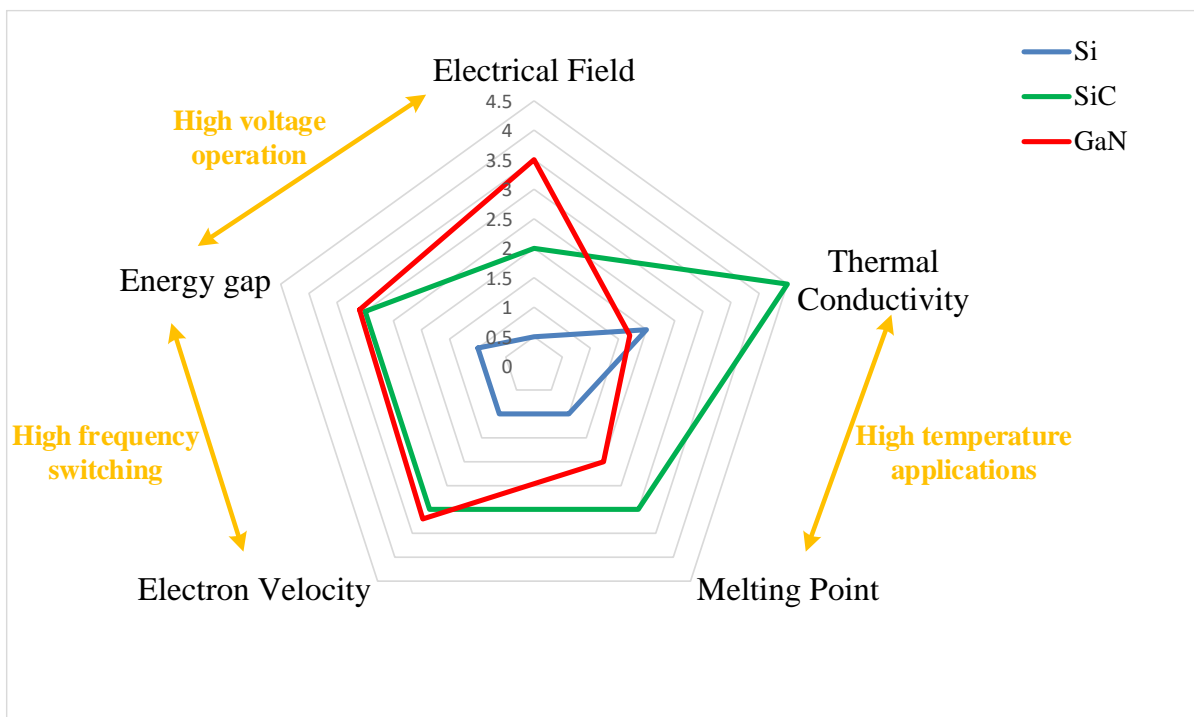
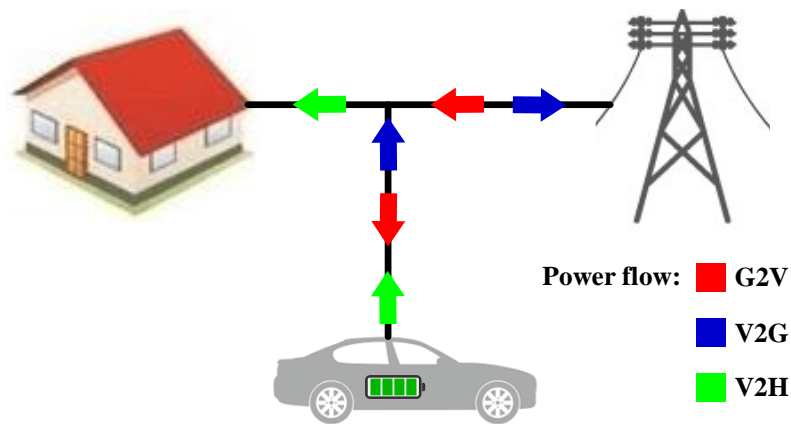


Fig. 1-5: General comparison between Si, SiC, and GaN semiconductors [19]

This advancement in the sale of electric vehicles has been made possible by the advent of wide band gap (WBG) semiconductors [20], which provide high-frequency and high-efficiency capabilities. GaN and SiC semiconductors are common WBG devices. The landscape for the use of SiC and GaN is estimated that the sales of these devices will increase from \$400 million sales to over \$3000 million sales from 2018 to 2025 [21]. As shown in Fig. 1-5, GaN devices are suitable for high frequency and high voltage applications [19], where research on GaN

semiconductors began in 2000 [22]. In this dissertation, GaN transistors are selected as the main switches.

The future of electric vehicle chargers is a bidirectional charger [23], which is an advanced EV charger and can charge or discharge the main battery if needed. To make it clear, in a unidirectional EV charger, energy flows from the grid into the battery packs but in a bidirectional EV charger, it can also be pushed back into the grid or other electricity-consuming equipment. Bidirectional power transferring for an EV charger can be used as vehicle-to-grid (V2G), vehicle-to-home (V2H), and vehicle-to-load (V2L) applications as shown in Fig. 1-6 [24] and [25].



*Fig. 1-6: The conceptual diagram of power flow direction for G2V, V2G, and V2H applications*

For V2G applications, the stored energy in the batteries can be sent into the grid. For this purpose, it is mandatory to invert the DC voltage of the batteries into AC voltage with grid synchronization (matching the frequency and voltage) [26]. It means the structure of a bidirectional charger is more sophisticated than a unidirectional charger. In the V2G applications, the battery can store energy during low profile and push it back to the grid in high demand. It tends to not only reduce the peak demand of power plants and avoid blackouts but also can earn money by charging the batteries at low-price hours and selling the stored electricity at high-price hours [27]. Furthermore, the surplus energy produced by renewable energies (such as solar and wind) can be stored in EVs and pushed back into the grid at required times. For example, CHAdeMO is an off-board charger designed by some major companies in Japan [28], which supports V2G applications.

In V2H applications, the EV plays the role of uninterruptable power supply (UPS) for domestic applications [29] and can directly supply the required power of a home without any

grid connection and synchronization, which makes its installation easy. The V2H application is useful for intelligent buildings with rooftop solar cells [30].

V2L applications can supply the appliances inside the vehicle such as laptops, lighting, telecommunication, etc. with the main battery packs of an EV [31]. In emergency conditions, the acid battery can be excited and the empty battery of other EVs can be charged shortly with an initial charge of the bidirectional V2L charger.

Generally, on-board chargers have high power density, high efficiency, and low weight. Also, they increase the flexibility of driving because they can be plugged in anywhere there is an electric outlet. However, due to the limited space in a vehicle, on-board chargers have a limited power level to achieve and their nominal power usually is lower than 3.5 kW [32]. Nowadays, the power rating of on-board chargers has been increased significantly with the progress of semiconductor devices (e.g. GaN transistors) and introducing the new high power-density power electronics converters (e.g. CLLC resonant converter). Considering these features, on-board charging can be the main type of EV charging by offering fast charging, high efficiency, high power density, bidirectional power transferring, reliability, and low manufacturing cost capabilities to the EV market. As a result, an optimization algorithm can design a bidirectional EV charger optimally while all requirements are also met.

## **1.2. Problem Statement and Challenges**

Owing to surpassing the EV market, the designed EV charger should offer competitive efficiency, power density, bidirectionally, and charging time. Although on-board chargers have been studied in recent publications, there are several challenges moving toward high efficiency and high power density bidirectional EV chargers. These challenges are related to various parts associated with the on-board chargers such as the selected converter, analysis method, optimization algorithm, implementation of magnetic components, control, and appropriate components selection.

According to the policies of some European Unions and the U.S., the production of petroleum vehicles will stop in the next few years and the world will turn to electric vehicles [33]. It means the widespread use of EVs will emerge in the world, and obviously, it leads to EV chargers being used every day and on a large scale. Therefore, a charger should be designed correctly to meet the following objectives.

- *Operating in a higher efficiency:* by increasing the total efficiency or reducing the losses associated with the charger, even by lower than a percent, global energy consumption will be decreased and more fossil fuel resources will be saved, due to the widespread use of the EV chargers. Therefore, designing a charger with higher efficiency is preferable.
- *Preparing required voltage ranges and current ranges:* the voltage and current of the battery packs vary according to the state-of-the-charge (SOC) of the batteries. Therefore, the charger should be designed correctly to prepare the required voltages and currents.
- *Having lower volume and mass of product:* a crucial step towards achieving a bestselling product is to reduce the volume and/or mass of that product. A designer can perform an analysis to design an impacted charger. Therefore, geometrical considerations are also mandatory in the designing process.
- *Ensuring ZVS and ZCS in the feasible operating regions:* there is a need for zero voltage switching and zero current switching capability for the designed charger to reduce switching losses. They can provide a higher efficiency charger with a lower operating temperature, which can also increase the lifespan of the charger.
- *Lower conducted and radiated emissions:* conducted emission is unintended energy propagated through the cables or harness to the components. Radiated emission is also unintended energy, which propagates through the electric and/or electromagnetic fields without any harness. These emissions are generated by a component and affect other components. Some standard levels are defined to clarify the allowable noise levels. A designer can decrease these emissions by adding LC filters, common mode chokes, ground-plane in the printed circuit board (PCB), shielding, etc.
- *Establishing power factor correction:* for the grid-connected converters, the power factor close to unity can reduce losses in the distribution system. In this dissertation, a bidirectional battery charger will be designed, which supplies from the grid. So, this part should be considered in the design process.
- *Reducing costs:* the cost of a product has a direct effect on the rapid market progress and success of that product to sell like hotcakes. Design considerations can play a crucial role in reducing costs.
- *Increasing reliability and accessibility:* precise peak and RMS values analysis related to the voltage across and current passed through a component, real conditions (such as ambient temperature, nonlinear behavior of a component, magnetic cores saturation), applied fields (such as magnetic field and solar irradiance), physical stresses on the components, humidity, etc. have to be considered for reliability and accessibility assessment [34]. A designer should adopt comprehensive analysis and proper component selection to meet the reliability criteria.
- etc.

The role of analysis in design and optimization has received increased attention across several pieces of research in recent years [18], [35], [36], [37], [38], [39], [40], [41], [42], [43], and [44]. Analysis methods using such an assumption reduce the accuracy of the designed and optimized converter. Furthermore, an analysis method without a closed form requires some iterations to find the parameters and increases run time and complexity. Therefore, the following considerations should be attended to for an analysis method:

- Precise
- Closed-form
- Fast
- Comprehensive

An optimized battery charger with the minimum volume/mass, which operates in multiple operating points and satisfies several constraints is a fundamental property of a world-class EV charger. High efficiency and high power density battery charger are necessary to achieve them. A set of inputs is found to find the minimum/maximum of an objective function while the constraints have been met. For the optimization process, the following characteristics are mandatory:

- *Accuracy and convergence*: it is obvious that the accuracy of an optimization method plays a vital role in the selection of that method. Stochastic and recursive algorithms suffer from a lack of well-accuracy convergence. Deterministic algorithms can improve the accuracy of the optimization. However, it lacks regarding for the absolute extremum value convergence and may converge into relative or local extremum values. Initialization with different starting points may resolve this issue as shown in Fig. 1-7.

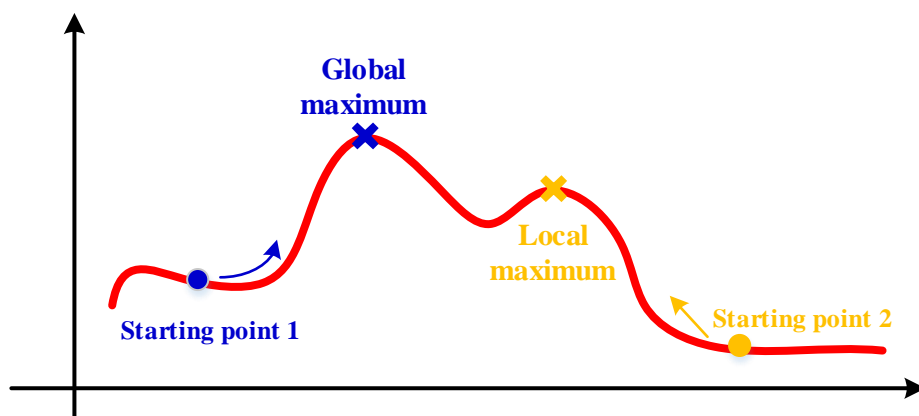


Fig. 1-7: Different operating points to reach the global or local maximum.

- *Multi operating points capability*: there are multiple operating points for an EV battery charger since it operates in different voltage levels and currents. Previous studies have mainly concentrated on a single operating point (e.g. [18] and [35]). Furthermore, some EV chargers are designed for battery charging applications regarding the wide output

voltage and different current levels (e.g. [36] and [39]). However, the designed converters suffer from the lack of optimum design for the chargers with multiple operating points. So, it makes adequate performance difficult to obtain.

Therefore, the main challenges of this dissertation are to obtain a new exact analyzing method, to present a design methodology for an EV battery charger design, and to attain an optimized battery charger with the maximum power density regarding multiple operating points.

It should be mentioned that the connection of battery chargers to the grid can produce detrimental harmonic effects on it and increase total harmonic distortion and noise emission. This drawback can be mitigated by using differential and common mode chokes as an input filter, reducing the rising time and falling time of sharp waveforms, and using an active front-end rectifier for the rectifying part. In this dissertation, only DC to DC converter will be analyzed, because designing an EMI filter, switching time control, etc. are beyond the scope of this dissertation.

The DAB, LLC, and CLLC converters are commonly used as the DC-to-DC stages of EV chargers. Therefore, the proper selection of the main DC-to-DC converter is the first challenge of an EV charger. Besides, the current on-board chargers, specially DAB-based, LLC-based, and CLLC-based chargers, have been analyzed based on the conventional analyzing method, i.e. the first harmonic approximation (FHA) method [43], [45], [46], [47], [48], [49], and [50]. Furthermore, the efficiency of the designed charger based on the conventional method deteriorates when the load is far away from the nominal point. This deviation also occurs for power density and other features of the EV charger. Moreover, there is no precise method for the analysis of high-order resonant converters in order to be used in this dissertation. In addition to approximate methods, the parameters sweeping method has been adopted in several publications (e.g. [18], [51], [52]) and its accuracy is challenging.

Generally, the resonant tank of a CLLC resonant converter has a transformer with specific magnetizing inductance, two resonant inductors, and two resonant capacitors [53]. This converter realizes soft switching in a wide operating region. Most previous works have designed CLLC resonant converters on a single operating point. However, owing to the battery charging process, the charger operates in constant current (CC) and constant voltage (CV) modes. Therefore, the on-board converter should be designed in corresponding with the whole of the operating region. It is needed to provide a global design methodology for the converter, and especially for magnetic design of the resonant tank.



The new semiconductor devices, like GaN transistors, introduce high power-density capability for power electronics converters [54]. Understanding the GaN power loss modeling, whether switching loss or conduction loss, is one of the most important parts of the optimum design of GaN-based EV chargers. Despite a considerable number of analytical loss measurements, there is no simple and accurate analytical model appropriate for design engineers. Most of the works carried out on the switching loss analysis use an integral form which leads to a complicated and time-consuming analyzing model. Furthermore, for one device, the switching losses are provided at one operating point associated with the datasheet's value, and for a specific gate-driver circuit [55]. Therefore, a model is needed to predict the losses for other operating points and different parameters.

Designing a high efficiency and high power density on-board charger is another challenge for an on-board charger in the EV market. Due to the limited space inside an EV, it is needed the power density to be considered in the optimization process. It means a mathematical-based formula of power density shall be obtained and put into the optimization process. Conventional algorithms have not considered power density as a function of electric parameters to optimize in it the whole of the system. The conventional methods have used parameter sweeping or iteration-based algorithms. Also, in several studies, the trial-and-error method has been considered to find the optimum result. Therefore, there is not any guarantee that the obtained results are the best possible result. Besides, a single operating point at a fixed switching frequency has been considered in literature but the charger should be optimized in the whole operating region of the charger.

### **1.3. Research Scopes and Objectives**

According to the previous discussions, the research objectives are:

#### **1.3.1. Analysis**

Firstly, among the commonly used converters, such as DAB, LLC, and CLLC converters, the LLC is not suitable for bidirectional power transfer. Between the DAB and CLLC converters, the CLLC converters are slightly better than the DAB converters in terms of efficiency, power density, soft switching region, current stresses, size, and cost, for bidirectional EV charger applications [43]. Therefore, the CLLC resonant converter is selected in this dissertation.

Despite the advantages mentioned for the CLLC converter, it is difficult to achieve its inherent features and characteristics due to the complex structure of the resonant tank and its different operating modes, which make the design and control of the CLLC converter difficult. Also, as stated in the literature (and shown by the simulation and experimental results in this dissertation), if the first harmonic approximation (FHA) method is used for obtaining the CLLC converter parameters [43] and [44]: such as the voltage gain ratio, switching stresses, maximum voltage of capacitors, and maximum current of inductors, there is a crucial difference between the FHA-based results and actual results, which encounters a great obstacle in design and optimization [53]. Therefore, the first objective of this dissertation is to provide a detailed and exact analysis of the CLLC resonant converter based on the state-plane analysis method, which can be used to achieve all circuit parameters in different operating modes, loads, and frequencies.

Another analyzing part that has not been done yet for the CLLC resonant converter is to check and provide a precise relationship for the ZVS condition of the main primary switches. In the previous papers and dissertations about CLLC resonant converter, Eq. (1.1) was obtained using the first harmonic approximation method to check the ZVS condition of this converter [43], [45], and [46]:

$$L_m \leq \frac{t_{dt}}{16C_{SS}f_{s,max}} \quad (1.1)$$

where  $t_{dt}$  is dead-time,  $C_{SS}$  is the parasitic capacitor of a GaN transistor,  $L_m$  is the magnetizing inductance, and  $f_{s,max}$  is the maximum switching frequency. According to Eq. (1.1), it is obvious that this equation is not dependent on the load current and other circuit parameters which leads to deteriorate in accuracy, and causes the converter operates in a non-soft-switching region. This inaccuracy will be shown in chapter 3 by simulation and in chapter 5 by experimental results. Also, the FHA method cannot be used in discontinuous conduction mode [56], and its accuracy deteriorates when the switching frequency deviates from the resonant frequency.

In [44], an attempt has been done to provide a detailed analysis of this converter. In this reference, the differential equations corresponding to the state variables were solved and the relationships between the current of inductors and the voltage of capacitors were obtained in the time domain. But for the ZVS condition checking, the same approximate method (i.e. FHA) was used. Whether the proposed methods in [44] and [57] are remarkably accurate or not, possessing an exact closed-form method, with the ability of transient and steady-state analysis,

and easy to obtain the output characteristics, gain voltage ratio, and switching stresses is mandatory. The state-plane analysis method can be the solution.

By reviewing the literature, the state-plane analysis of this converter has not been presented so far. Therefore, one of the objectives of this dissertation is to provide a precise analysis of the CLLC resonant converter in the field of state-space. The desired outcomes are:

- The voltage gain ratio;
- Maximum voltage and current of resonant tank elements;
- RMS values of voltages and currents;
- An accurate relationship for ZVS condition;
- CCM and DCM boundary;
- CCM and DCM operating analysis;
- Output characteristics;
- Control plane characteristics;
- Exact loss calculation;
- Using closed-form equations into the optimization algorithm.

It should be mentioned that for completing the discussion, the dynamic analysis for transient behavior and startup conditions of this converter can also be examined, but it is beyond the scope of this dissertation.

Furthermore, there is another important aspect of exact analysis. Increasing the operating frequency of a power electronics converter is a promising road map for the power electronics industry, which leads to obtaining a high power density converter. However, operating in high switching frequencies make the influence of parasitic components in the converter performance essential. In this case, the inductance of tracks of a printed circuit board (PCB), parasitic junction capacitors of transistors and diodes, and the leakage inductance of transformers participate actively in resonance. These parasitic elements convert a low-order resonant circuit to a high-order circuit, and its exact analysis will not be possible with the previous methods. For example, if a series resonant converter operates at a high frequency, this converter may convert to LLC, LLLC, or another high-order resonant converter, which requires a precise analysis method. Therefore, the analysis method performed in this dissertation can also be used not only for high-order resonant converters but also for low-order resonant converters while operating in high-frequency applications.

### 1.3.2. Optimization

Compared with unidirectional LLC resonant converters and DAB converters, the bidirectional CLLC resonant converter can prepare higher efficiency in two opposite power directions because it can ensure ZVS condition for primary side switches and ZCS for

secondary side rectifiers over a wide load range, which is useful for high variation voltage and current applications [53]. Furthermore, it has a low turn-off current for the primary switches and a low di/dt current for the secondary rectifiers. But these benefits are met when a proper resonant tank is designed based on an optimization strategy. For example, a high value of magnetizing inductance can decrease the circulating current by increasing the impedance of the parallel path, which reduces circulating loss and increases efficiency. However, according to Eq. (1.1) and by increasing  $L_m$ , the required dead-time for ZVS operating will be increased. High dead-time not only reduces the amount of power transmitted to the load and reduces efficiency, but also can impose a restriction on increasing the switching frequency, which leads to the reduction of switching losses and also reduction of power density by a massive selection of passive components. As a result, there is a tradeoff for magnetizing inductance selection and an optimization strategy can solve this requirement. Some tradeoffs may need to be used for other components to obtain a high efficiency and high power density bidirectional CLLC resonant converter.

There is another important aspect of optimization due to the application of the selected resonant converter. The battery charging process includes a wide range of input and output voltages, as well as a whole range of currents from full-load to near-no-load. Therefore, it is necessary to design an optimum charger for the entire voltage and current ranges of the battery, using accurate analysis. A lot of references in the literature considered only one operating point, as a rated point, to optimize the CLLC resonant converter. Also, bidirectional operating must be considered in the optimization process.

It is not possible to increase the volume and mass of an on-board charger whatever you want due to the limited space inside an electric vehicle. Consequently, power density is a crucial rule in the design of an on-board charger. Furthermore, electric vehicles will emerge in widespread use in the world, and obviously, operating at high efficiency is imperative. Therefore, efficiency can be selected as an objective function or constraint to fulfill the aforementioned requirement.

Besides, the first harmonic approximation method was performed in the previous works (e.g. [18]), which decreases precision. The proposed method based on state-plane analysis can improve the accuracy of the optimization result. In summary, the objectives of the optimization part are as follows:

- There are some tradeoffs in the component selection, which can be solved by optimization;
- A wide range of voltages and currents;

- Multiple operating points based on the charging process;
- A bidirectional capability that may change the objective functions;
- Limited space inside an EV;
- High efficiency operating constraint;
- Using an exact method in the optimization part for obtaining the objective functions and constraints.

#### 1.4. Thesis Outline

This dissertation contains 6 chapters, which focus on the analysis and optimization of a bidirectional full-bridge CLLC resonant converter.

**Chapter 1** gives an introduction to the research motivation, types of EV chargers, and the selected power electronics converter.

**Chapter 2** provides a literature review of types of electric vehicles, types of EV chargers, the importance of bidirectional transferring, and a general review of CLLC resonant converter in terms of analysis and optimization.

**Chapter 3** gives the first harmonic approximation method for the CLLC resonant converter. The obtained results are compared with PSIM simulation.

**Chapter 4** presents the fundamental concepts of the global design, and optimization for using bidirectional EV charging, an optimization algorithm is adopted and the objective function is expressed. Corresponding constraints in EV applications are also investigated. Then, the previous methods for the analysis of the CLLC resonant converter are evaluated and it is shown that there are some design challenges in using previous methods.

**Chapter 5** proposes a new approach for the exact analysis and design of a full-bridge resonant converter, as the state-plane analysis. Based on this method, the switching stresses of the components, output characteristic, control plane diagram, and soft switching condition are obtained in continuous conduction mode (CCM) and discontinuous conduction mode (DCM). Furthermore, the CCM and DCM boundaries are expressed. By simulation, the proposed state-plane analysis for CLLC resonant converter is verified.

**Chapter 6** provides an algorithm for the optimization of multi operating points problems in bidirectional EV charging applications. At the first of this chapter, the input parameters, output parameters, and constraints are expressed. Then state-plane analysis codes are implemented into *CADES* software based on C++ integrated design environment. The implemented codes are verified using Maxwell simulation. In *CADES* software, a single operating point

optimization is done and it is shown that the designed converter based on the single operating point cannot meet all the constraints for the other points. Therefore, the multi operating points optimization algorithm is proposed which can find an optimum converter through 9 steps, when all the constraints are met.

**Chapter 7** is dedicated to the conclusions and future work.

## 2. Literature Review

In this chapter, a review of previous works is presented, and transportation electrifications background, types of battery chargers of these vehicles, vehicle-to-grid (V2G) power transfer, and a detailed review of resonant converters, especially the CLLC resonant converter are described.

One of the aspects of a charger is that the charger is installed on the vehicle, i.e. the on-board charger, or a charger is installed outside the vehicle and at the charging station, i.e., the off-board (stand-alone) charger, as shown in Fig. 2-1.

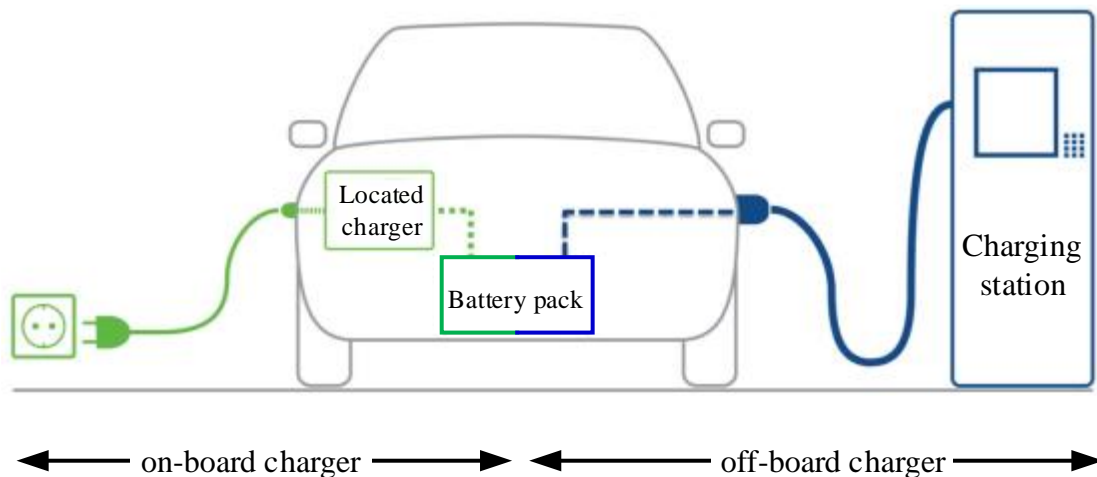


*Fig. 2-1: Basic concept of an Off-board charger (left side) and On-board charger (right side).*

On-board chargers have high power density, high efficiency, and low weight. Also, they increase the flexibility of driving because they can be plugged in anywhere there is an electric outlet. However, due to the limited space in a vehicle, on-board chargers have a limited power level to achieve and their nominal power usually is lower than 3.5 kW [32]. Off-board chargers can be used as a charging station with fast charging technology and high power transfer. But, due to the flexibility and household applications of on-board chargers, in this dissertation, the on-board charger will be discussed.

Also, depending on whether the power transfer to the charger is done directly through the wire or it is transferred wirelessly through a magnetic coupling, a charger can be classified as a wired or wireless charger, respectively, as shown in Fig. 2-2.

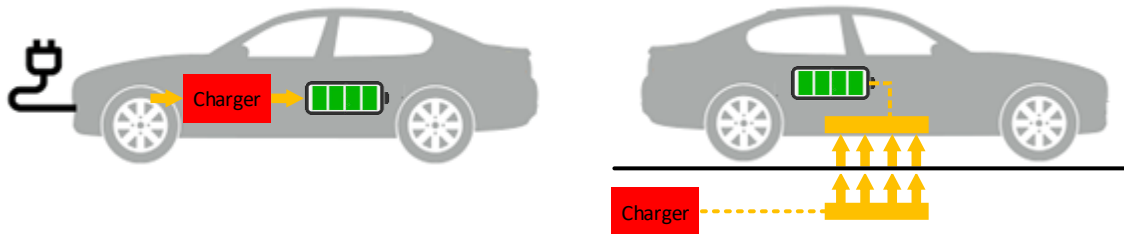


*Fig. 2-2: Basic concept of a wired charger (left side) and wireless charger (right side).*

Unidirectional and bidirectional capability is another feature of the EV charger. The unidirectional charger enables to transfer of power only from the grid to the battery. In this structure, diode bridges are usually used for rectification parts, which makes it easier to control and build, and will reduce costs and increase reliability. In comparison, the vehicle-to-grid (V2G) system requires the vehicle to have bidirectional power transferring technology as shown in Fig. 2-3, where power can transfer from the grid to the main battery (i.e. G2V) and also from the main battery to the grid or the auxiliary battery.

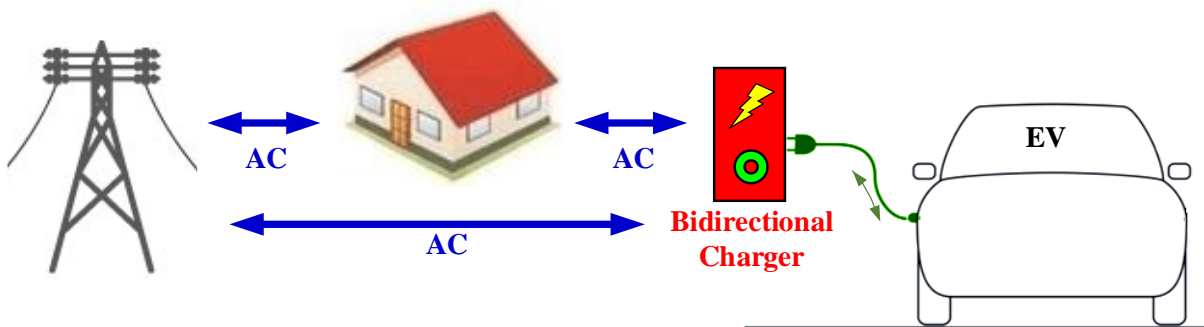


*Fig. 2-3: Conceptual diagram of a bidirectional charger for V2G applications*

Using a bidirectional charger, energy can be stored in the vehicle during low load hours and returned to the grid during peak hours, where the vehicle helps the power grid as a distributed generation (DG). Also, if solar energy is used to charge the battery, the amount of excess produced energy can be returned to the grid. Given the importance of this issue in the future of the power grid, this dissertation will use a bidirectional charger.

In terms of classification according to the standard voltage level, three levels are defined: Level 1 has an input voltage of 120V, a current of 20A, and a power of 1.9 kW and is installed



on the vehicle. Level 2 includes voltages from 208V to 450V, a current of 3.3A to 14.4A and is installed on the vehicle. Level 2 chargers have the advantage that they can be powered from both private homes and public places as they require AC 240V. Level 3 also requires high-voltage DC power, which is used for fast charging in less than 1 hour [10]. Since level 2 can be charged via household electricity, this standard level will be used in this dissertation.

In terms of a multi-stage converter, it can also be considered that first, a converter raises the input voltage to the desired level and second, another converter performs the task of controlling the battery voltage. For grid-connected applications, usually, there is a boost converter in the input part as the first stage to use as power factor correction, and the other stage controls the required power. So, the selected charger for this dissertation can be considered as a two-stage charger. The reason for using a boost converter in the first stage is the simple structure, continuous input current, and low total harmonic distortion (THD) [58].

By determining the characteristics of the required charger as a charger with voltage level 2, bidirectional, on-board, power transmission with wire, and two stages, the most important feature of the charger is its converter structure, which will be evaluated in the next section.

Different topologies and their controlling strategies are the most important aspect of structure selection. Fig. 2-4 shows the typical structure of a two-stage charger:

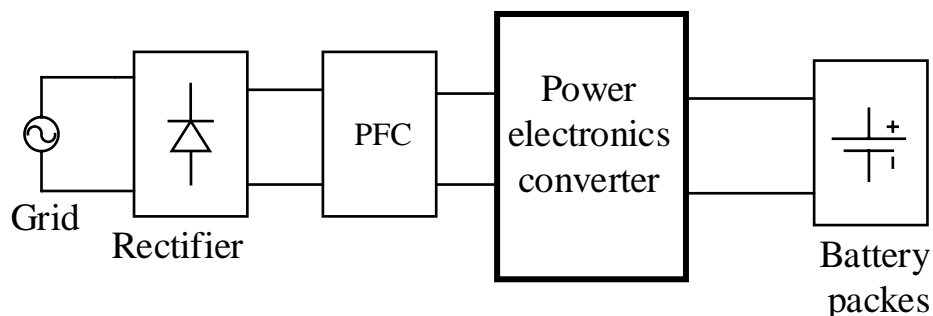


*Fig. 2-4: Typical structure of a two-stage charger.*

where the grid AC voltage rectifies via diode rectification for the unidirectional charger or via synchronous rectification for the bidirectional charger. Then the rectified voltage is applied to a boost converter for power factor correction and also increasing the voltage. It should be mentioned that there exist some structures which integrate the rectifier part with the PFC part [59]. Finally, a power electronics converter charges the battery packs to the required voltage and current. The main goal of this dissertation is to analyze and optimize the main DC-to-DC converter for battery charging, therefore the rectifier part and PFC part are ignored in our analysis.

According to the mission of this dissertation in designing an optimal bidirectional EV charger, it is necessary to provide conditions such as high efficiency, high power density, high switching frequency, bidirectional power transferring, and soft switching for a wide range of loads. For these reasons and especially for high-efficiency power transferring, the solution is to use resonant converters [60]. For high-power DC-DC applications, resonant converters have become a desirable and widely used selection [45] and [46], where the resonant converter can be designed as highly impacted and high-efficiency applications, without any snubber [45]. The well-designed resonant converters can operate in soft switching conditions for wide operating areas. Therefore, a resonant converter will be used in this dissertation.

The general structure of a battery charger based on a resonant converter can be shown in Fig. 2-5:

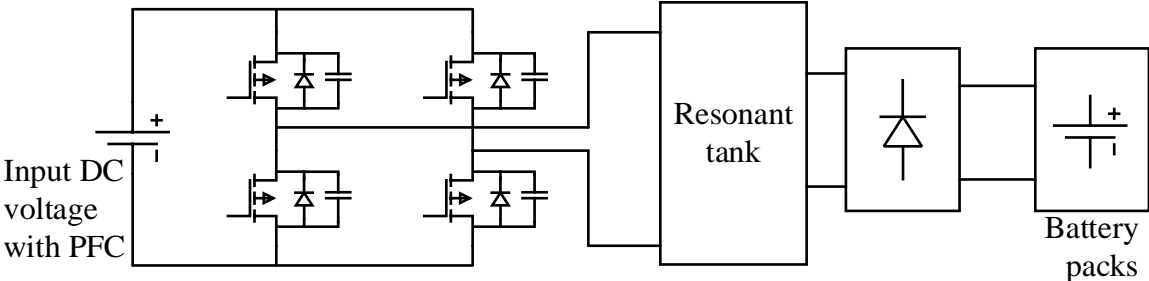


Fig. 2-5: Basic structure of a full-bridge resonant converter.

where the inverter part can be a full-bridge or half-bridge and the rectifier part can be a diode rectifier or synchronous rectification. In the next part, a review of resonant converters and their utilization in bidirectional power transfer will be presented.

Resonant converters are classified based on the number of inductors and capacitors and also their positions, usually such as the series resonant converter (SRC), parallel resonant converter (PRC), dual active bridge (DAB), LLC, LCC, CLLC, CLLLC, etc.

The schematic diagram of the series resonant converter (SRC) is shown in Fig. 2-6. SRC operates in ZVS for above the resonant frequency and ZCS for below the resonant frequency. The gain is unity at the resonant frequency. The circulating current and turn OFF current are low at frequencies near the resonant frequency. However, for light load and high input voltage conditions, the voltage regulation is hard to fulfill and also the circulating current is increased. Also, the series resonant converter is not a good candidate for grid-connected and front-end applications [61]. Furthermore, the efficiency of SRC is decreased when the switching frequency deviates from the resonant frequency.

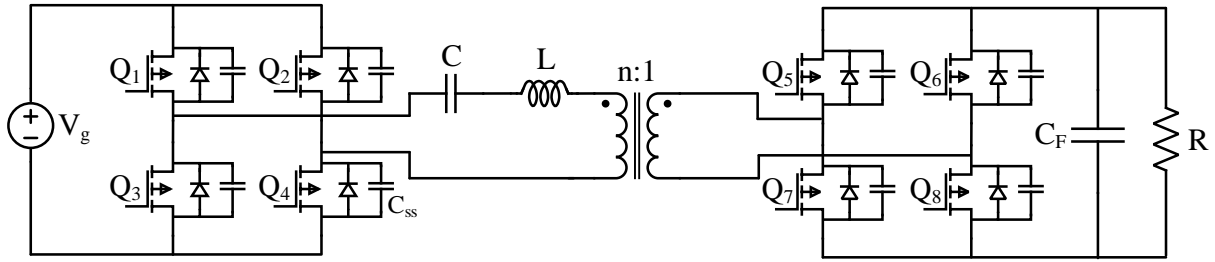


Fig. 2-6: Schematic diagram of a full bridge series resonant converter (SRC).

The parallel resonant converter (PRC), as shown in Fig. 2-7, plays a role of a step-up converter and can obtain ZVS and ZCS depending on the required current and voltage. But this converter suffers from a high circulating current and high turn OFF current. Also, this converter is not suitable for grid-connected and front-end applications [61].

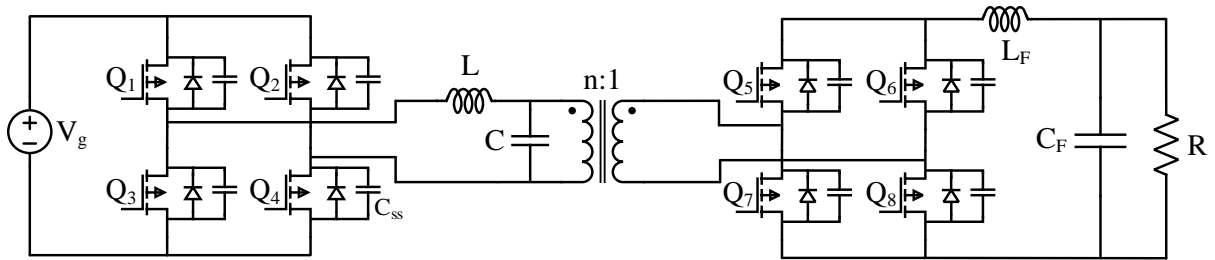


Fig. 2-7: Schematic diagram of a full bridge parallel resonant converter (PRC).

The LLC resonant converter is composed of SRC and PRC converters. Fig. 2-8 shows the schematic diagram of the LLC resonant converter. This converter has a lower circulating current in comparison with PRC, and lower load sensitivity in comparison with SRC. But conduction loss and switching loss are raised in high input voltage and it is not suitable for EV charging.

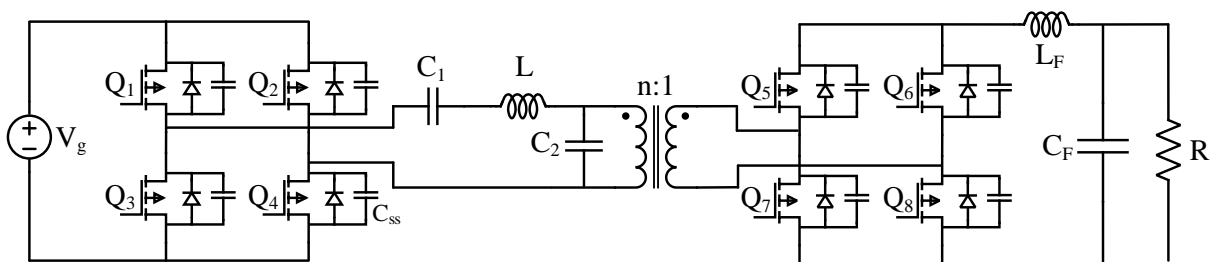


Fig. 2-8: Schematic diagram of a full bridge LLC resonant converter.

Fig. 2-9 shows the schematic diagram of the dual active bridge (DAB) converter, which is popular for various applications, such as EV battery chargers, DC distribution systems, etc. It has a wide soft switching region and works in ZVS for both the primary and secondary sides [43]. Galvanic isolation, high switching frequency, high power density, and bidirectional power transferring make the DAB converter a proper candidate for wired and wireless EV chargers

[43]. By now, the DAB converter can be selected as the main DC-to-DC converter of this dissertation, but it is not the final selection.

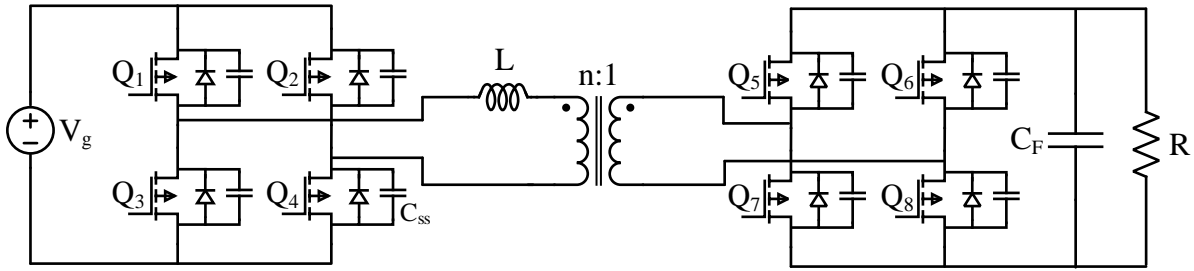


Fig. 2-9: Schematic diagram of a dual-active bridge converter (DAB).

The full-bridge (see Fig. 2-10) and half-bridge LLC resonant converters are broadly used in many applications, such as EV chargers, LED drivers, renewable energy systems, etc. [], due to the advantage of wide voltage gain, wide soft switching region, galvanic isolation, high efficiency, high switching frequency. Furthermore, the main primary switches operate with ZVS and the output rectifier part operates in ZCS [61], which is caused lower switching loss and circulating current in comparison with SRC, PRC, and LCC, over wide load ranges. Also, the LLC resonant converter can be designed with high power density by integrating  $L_m$  into the transformer as its magnetizing inductance and  $L_l$  as its leakage inductance. Therefore, the overall volume of magnetic components will be reduced. According to the aforementioned advantages, the LLC resonant converter can be also selected as the main DC-to-DC converter of this dissertation.

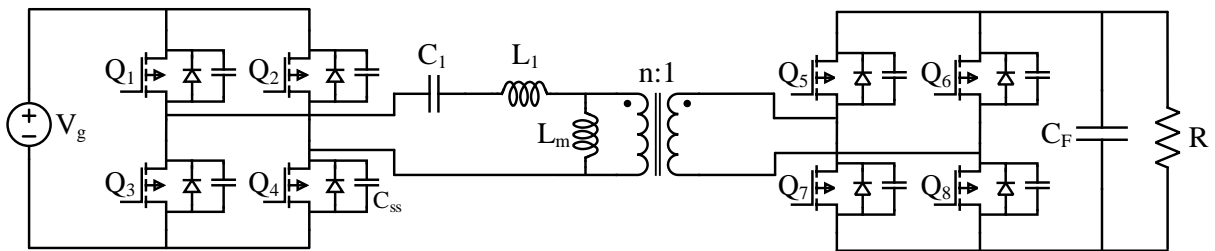


Fig. 2-10: Schematic diagram of a full bridge LLC resonant converter.

By increasing the number of resonant elements, some benefits such as short circuit protection and bidirectional operating can be obtained [62]. It means a better topology selection is always challenging [61].

According to the previous discussion about different topologies, the dual-active bridge converter and LLC resonant converter are good candidates for the main DC to DC converter selection of bidirectional EV charger. If we use LLC resonant converter, in vehicle-to-grid condition, the magnetizing inductance ( $L_m$ ) is clamped by the battery voltage because it is in

parallel with a DC voltage source as shown in Fig. 2-11. Therefore, the LLC resonant converter operates similar to a series resonant converter (SRC) [63] and the advantage of the LLC resonant converter is dissipated, e.g. efficiency will be decreased when the switching frequency deviates from the main resonant frequency [64]. As a result, the traditional LLC resonant converter is unidirectional and cannot be used effectively in V2G applications. For bidirectional LLC resonant converter [65], the functional behavior of the converter, e.g. voltage gain ratio and switching stresses, are different in the forward mode and reverse mode. So, it causes different optimum components for each direction. Also, the voltage gain of bidirectional LLC resonant converters in reverse mode is similar to series resonant converters [65] and loses its benefit. Therefore, the LLC resonant converter cannot be selected for the main DC-to-DC converter of this dissertation.

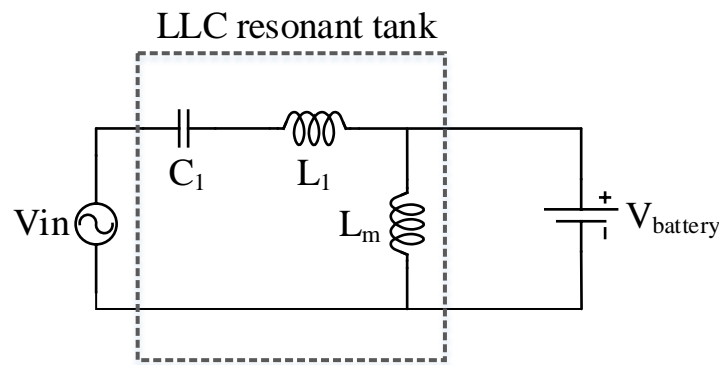


Fig. 2-11: The applied voltages to the resonant tank of an LLC resonant converter.

Another candidate is the DAB converter. In [43], it is shown that the efficiency and power density of the DAB converter is lower than the capacitor-inductor-inductor-capacitor (CLLC) resonant converter. Therefore, the CLLC resonant converter is superior to the conventional dual active bridge converter in terms of efficiency and power density [66], [47], and [67] and to the LLC resonant converter in terms of bidirectional capability [68].

The circuit diagram of the bidirectional full-bridge CLLC resonant converter is shown in Fig. 2-12. The primary active full bridge is composed of four GaN transistors. The switching network of the secondary side is also formed in a similar manner as the synchronous rectifier [53]. The CLLC resonant converter has a high-order resonant tank, which is comprised of capacitors  $C_1$  and  $C_2$ , the transformer magnetizing inductance  $L_m$ , and the primary and secondary leakage inductances  $L_1$  and  $L_2$ . Depending on the desired power flow direction, the bridge of one side acts as an inverter and that of the other side acts as a synchronous rectifier.

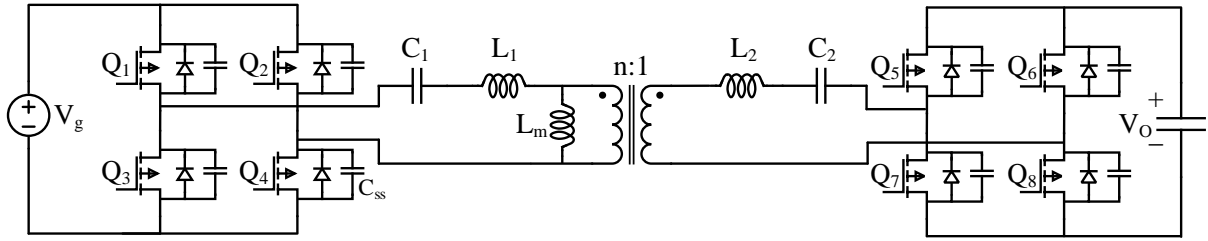


Fig. 2-12: Schematic diagram of a bidirectional full-bridge CLLC resonant converter.

The CLLC resonant converter is the bidirectional version of the LLC resonant converter [69]. The structure of a CLLC resonant converter has three inductors, therefore this converter can be named a CLLLC resonant converter. But in this dissertation, it is stated as CLLC resonant converter [70]. The reason is that there is an inductive cutset in the resonant tank, and by having the current of two inductors, the current of the other inductor can be calculated independently. It means only two inductors have an effect on state space equations and therefore CLLC notation is selected.

For grid-to-vehicle (G2V) applications, the primary side active bridge acts as an inverter to apply the inverted voltage to the resonant tank, and the secondary side active bridge acts as a rectifier using synchronous rectification or antiparallel diodes of the transistors when these transistors are OFF [53]. Finally, this voltage is refined by a filter which is formed by only one capacitor. For vehicle-to-grid (V2G) applications, the secondary side active bridge inverts the voltage of batteries and applies it to the resonant tank, and the primary side active bridge rectifies the derived AC voltage of the resonant tank.

According to the schematic diagram of the CLLC resonant converter, this converter comprises two LLC resonant converters on each side [46], which ensure ZVS for the main primary switches and ZCS for the secondary rectifying switches. The advantage of the CLLC resonant converter can be expressed as:

- Bidirectional power transferring capability;
- Wide voltage gain ratio;
- Wide soft switching region under wide load ranges (from no load to full load);
- Ensuring ZVS in G2V mode and ZCS in V2G mode for the primary switches;
- Ensuring ZCS in G2V mode and ZVS in V2G mode for the secondary switches;
- Higher efficiency in comparison to DAB and LLC;
- Lower turn OFF current in comparison to other resonant converters;
- Frequency modulation control method;
- Galvanic isolation;
- Short circuit protection capability.

A common way to charge lithium batteries is to first charge the battery with a constant current equal to the maximum tolerable current of the battery. This area is called the constant current (CC) area. The battery voltage then increases to reach its nominal value. After that, the battery voltage will remain constant and the battery will be charged at a constant voltage; until the battery current is close to zero. This area is called the constant voltage (CV) area [71]. This method of charging for a battery cell is shown in Fig. 2-13.

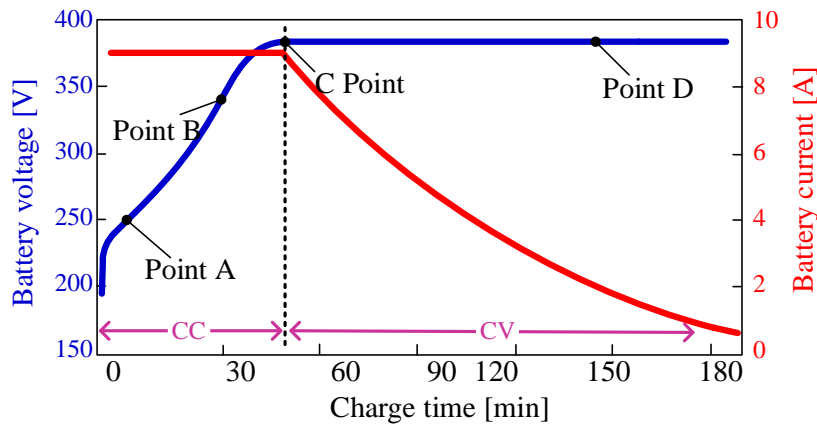


*Fig. 2-13: Charging process of a lithium-ion cell in constant current (CC) and constant voltage (CV) processes.*

According to the above figure, it is clear that the process of charging the battery, firstly, includes a wide range of voltages, and secondly, this process will continue from full load to near no load. Therefore, one of the most important criteria for choosing a charger is that the charger operates at the optimum point and maintains efficiency of the charger throughout the battery charging process in a wide range of current and voltage variations. The selected CLLC resonant converter must be designed in different operating points correctly, which is one of the goals of this dissertation.

Half-bridge and full-bridge configurations are the most conventional topologies used in bidirectional converters [72]. A full-bridge and half-bridge single-phase DC-to-DC converters were presented in [73] to provide G2V, V2G, and traction-to-auxiliary (T2A) capabilities. A bidirectional AC-to-DC converter was discussed in [74] for operating in V2G applications. In [75], a V2G multilevel converter was proposed for battery energy management, where each battery cell can be controlled to be connected to the circuit or to be bypassed by a half-bridge converter. About the CLLC resonant converter, this converter can be implemented as a half-bridge or full-bridge. In [43], four 1kW bidirectional converters, i.e. half-bridge and full-bridge DAB converters and half-bridge and full-bridge CLLC converters were compared, and it was shown that for bidirectional EV charging applications, the CLLC converters are slightly better

than the DAB converters, in terms of the efficiency, power density, size, and cost. Future chargers will move towards being bidirectional and the CLLC resonant converter is a proper candidate.

In summary, the advantage of a bidirectional charger is:

- Begin the consistent trends of the future;
- Can earn money by selling electricity;
- More using renewable energies capabilities;
- Reduce the peak demand for power plants;
- Use as an uninterruptable power supply and avoid blackouts;
- Associate with intelligent building systems;
- Supply appliances inside the vehicle;
- EVs play a role of distributed generation systems;
- Useful for emergency modes.

However, it has the following disadvantage:

- High cost;
- Complicated production and control;
- Use synchronization with the grid for V2G applications.

Based on the aforementioned discussion, a two-stage bidirectional on-board charger is selected, when the full-bridge CLLC resonant converter is selected as the main DC-to-DC converter.

The bidirectional capability of the CLLC resonant converter was first proposed in [45]. The CLLC resonant converter is a promising converter for bidirectional power conversion in applications such as bidirectional EV chargers and hybrid vehicle DC-DC converters [18], [66], [76], [77], [78], [68], [79], [80], and [81]. This converter is bidirectional in nature [66], where the power can be transferred as the forward mode (i.e. G2V) and the reverse mode (e.g. V2G) at high efficiency, independently. However, a symmetrical structure of a CLLC resonant converter allows the same operation in two different power flow directions [66], and makes its design easy. The symmetrical structure of the CLLC resonant converter was first proposed in [46], which was analyzed the voltage gain ratio in terms of switching frequency variation. The symmetrical structure of CLLC resonant converter makes its analysis, design, optimization, and control easy [47], [48], [82], [83], [84], and [85]. A detailed design procedure of the bidirectional CLLC resonant converter for a battery charging application is introduced in [47] to simply the CLLC converter to CLLC converter. In [78], a design methodology for an asymmetric parameter design is proposed, but the corresponding relationship between the circuit parameters of charging and discharging modes has not been analyzed fairly. The voltage



gain ratio of a symmetrical half-bridge CLLC resonant converter in terms of charging mode and discharging mode is expressed in [80]. A design methodology for maximum efficiency tracking is proposed in [68], and the circulating current and efficiency are compared for LLC and CLLC resonant converters, where was shown the conditions are better for CLLC in comparison with LLC, but without any experimental results.



















The first harmonic approximation (FHA) is a simple analysis method, which is widely used in the analysis and design of CLLC resonant converters [46], [68], [80], and [86]. However, the accuracy of this method deteriorates when the voltage and current of load (i.e. the battery) are widely changed or the converter operates in discontinuous conduction mode (DCM) [56].

Time domain analysis (TDA) or state space analysis (SSA) is a general steady-state approach for the exact analysis of resonant converters, which was performed in [47] for state analysis of CLLC resonant converter. In this method, the state space equations of each subinterval are solved and the time domain expressions of state variables are obtained over one switching period. TDA is particularly useful for simulation purposes but it is too complicated to be used for the design of a resonant converter with several energy storage elements [87]. In [88], it was shown that the CLLC resonant converter has multiple resonant frequencies based on  $C_1$ , and  $L_1$ , as well as  $C_2$  and  $L_2$ , to which  $L_m$  can also be added. It is also mentioned that for frequencies above the resonant frequency of  $C_1$  and  $L_1$ , the converter operates in ZVS, which is lost for those below this resonant frequency. However, this statement is generally incorrect, and the adequate proof is mandatory. In [89], a CLLC resonant converter with a power of 3.3 kW was built for a bidirectional EV charger. In [90], a CLLC resonant converter operates as an inverter to transfer power from the batteries to the grid, while the first harmonic approximation method was considered for analysis. A relationship for leakage inductance calculation of the main transformer according to its dimensions was presented in [91] for a bidirectional on-board charger. An effective test bed was proposed in [66] for a bidirectional DC distribution system based on a 5 kW CLLC converter, 3 kW DAB converter, and 3 kW LLC converter, for the main DC-bus voltage control, battery voltage interface, and the renewable energy simulator, respectively.

A graphical and geometrical method for exact analyzing of the resonant converter is the state-plane analysis where the current or voltage of the resonant tank elements is calculated as a function of the other variables and plotted in a 2D or 3D diagram [92] and [93]. The exact circuit behavior and design criteria in CCM and DCM operation can be obtained using this method [94] and [95]. The analytical equations extracted by state-plane analysis can be used

directly in the optimization process to increase accuracy. State-plane analysis has been applied to the converters with two or three resonant elements [94], [96], [97], and [98], but the CLLC resonant converter has five resonance elements (two series capacitor-inductor and one transformer) and state-plane analysis is hard to accomplish. Therefore, most of the research has been focused on FHA and TDA methods [18], [43], [44], [45], [46], [47], [48], [80], [88], [49], and [50]. Table 2-1 demonstrates a comparison between the analyzing methods.

Table 2-1: Basic comparisons between analyzing methods

Method	Accuracy	Implementation	Steady-state	Transient	Visual inspection	Control capability
<b>FHA</b>						
<b>Time-domain</b>						
<b>State-plane</b>						

Owing to the electrical constraints, it is mandatory to find a closed-form of them to utilize in the design and optimization process. The first harmonic approximation (FHA) is a simple analysis method, which only considers the fundamental components of applied voltage and current to the resonant tank [99]. The accuracy of the FHA method for the CLLC resonant converter is deteriorative [53] and it is needed to present a new exact method.

In [100], another type of CLLC resonant converter was proposed, where mutual inductors were used instead of typical inductors and a transformer. Triple phase shift modulation was implemented to reduce circulating current and increase power factor. A dual three-level neutral point clamped half-bridge was used in place of the inverter part of the CLLC resonant converter for applying in high voltage applications [101]. But in this reference, the magnetizing inductance was considered as infinity, or in other words, the transformer was imagined as an ideal transformer, which makes the behavior of the proposed CLLC converter different from conventional CLLC resonant converters.

Laplace analysis was employed in [68] to find maximum efficiency tracking, where switching near the main resonant frequency can fulfill this goal by decreasing the circulating current, turn-OFF current of the main switches, and  $di/dt$  of the secondary side diodes. The variable DC link voltage control method was considered in [68] to operate at the resonant frequency and obtain maximum efficiency using the sinusoidal approximation method. However, it may cause a low-frequency oscillation in the output voltage. A two-stage AC to

DC converter based on a boost converter and CLLC resonant converter was presented in [102], where the boost converter can control the DC link voltage while preparing power factor correction, and the CLLC resonant converter can transfer the required power in a high switching frequency and galvanic insulation. In [86], a two-stage DC-to-DC converter was proposed, where the first stage is a buck/boost converter for decreasing/increasing the output voltage, and the second stage is the CLLC resonant converter for controlling the voltage gain ratio and preparing soft switching conditions. However, the first harmonic approximation was used in this reference, which reduces accuracy.

The influence of the junction capacitance of the secondary side diodes on output power and switching stresses was evaluated in [103]. A 6-kW on-board charger with a variable turn ratio was implemented in [81] based on 600 V GaN transistors due to their low output capacitance and reverse current operating capability.

In [43], full-bridge and half-bridge CLLC resonant converters as well as full-bridge and half-bridge DAB converters were compared for EV charger applications. Among them, the half-bridge CLLC resonant converter has the highest power density, the highest efficiency, and the lowest cost. Also, the full-bridge CLLC resonant converter has the lowest peak current. As a result, CLLC resonant converters are better than DAB converters for bidirectional EV charger applications.

The low accuracy of the first harmonic approximation method for obtaining the voltage gain ratio and operating modes of the CLLC resonant converter was investigated in [44], which causes an obstacle in the design and control of the CLLC resonant converter. So, an accurate operating mode analysis in the time domain was proposed. However, the ZVS condition is based on the first harmonic approximation method and suffers from low accuracy [53].

Some research has been done to optimize the CLLC resonant converter. In [52], with the first harmonic approximation method, the important parameters of the resonant tank were obtained, where the objective functions are maximizing efficiency, minimizing the coupling capacitance of magnetic parts, and adequate insulating for the coil. The optimization was done by parameter sweeping. It should be mentioned that in this reference, the inductance of the coil was obtained numerically with MATLAB, which is hard to implement. In [104], with time-domain analysis, the efficiency was maximized with the constraints of ZVS boundary, maximum gain voltage, minimum gain voltage, and operating mode boundary, to find the value of the resonant tank's elements. A design methodology of high-frequency transformer design based on the Pareto optimization was established in [105] for one operating point to maximize

efficiency and power density. In [51], a high-frequency transformer was optimized by sweeping the parameters to find minimum losses at low volume. A planar transformer was optimized in [106] by selecting the combinations of some discrete parameters and comparing all the local optimal designs at one operating point. A modular high-frequency transformer was designed in [76] for a 400 V CLLC resonant converter, while the maximum efficiency reaches 98%. A symmetrical PCB transformer structure was presented in [107], where it is shown that operating in high switching frequencies can actualize PCB-winding transformers. But it causes a higher level of common mode noise, which was solved by splitting the cores. The optimization strategy for an LLC resonant converter was proposed in [108] in terms of the relative permeability and air gap to minimize losses.

A symmetrical CLLC resonant converter was optimized for a constant power load and the fixed output voltage, with the particle swarm optimization (PSO) method [109] and iteration. The same method was used in [110] to maximize power efficiency. By sweeping some variables, a CLLC resonant converter was optimized in [18] to minimize losses and minimum volume in one operating point. In [111], a parameter design methodology based on the ratio of magnetizing inductance to leakage inductance was proposed to increase efficiency. A two-stage optimization method was presented in [112] to minimize the power losses of a symmetrical CLLC resonant converter, where the first stage found the optimum value of the resonant tank by minimizing total power losses, and in the second stage, the thickness of the air gap and distance between the primary winding and the secondary winding. In [112], the total losses were optimized using the genetic algorithm (GA) and particle swarm optimization (PSO) with the constraints of minimum window area and maximum allowable flux density.

*Table 2-2: Previous methods and parameters done for CLLC resonant converter*

<b>Parameters→ Methods↓</b>	<b>Voltage gain ratio</b>	<b>Switching stresses</b>	<b>ZVS condition</b>	<b>Optimization</b>
<b>First Harmonic Approximation</b>	[43], [45], [46], [47], [48], [50], [112]	[46], [48], [112]	[18], [43], [45], [46], [47], [50], [112]	[18], [47], [48], [49], [112]
<b>Time-domain Analysis</b>	[44], [88]	[38], [44]	[38]	[38], [44]
<b>State-plane Analysis</b>	Not done	Not done	Not done	Not done

Nevertheless, none of the aforementioned studies provides any general optimization method in terms of bidirectional power transferring, using an exact method for optimization, a wide range of voltages and currents, power density criteria, effects of core sizes on the power losses, ZVS conditions, constraints of an on-board charger, etc, as shown in Table 2-2. These requirements will be considered in this dissertation.

# 3. First Harmonic Approximation Model of CLLC Resonant Converter

## 3.1. Introduction

One of the most widely used methods in modeling resonant converters is the first harmonic approximation (FHA) method or the sinusoidal approximation method, which only considers the fundamental components of applied voltage and current to the resonant tank [99]. Due to its simplicity, the FHA method is widely used in the analysis and design of CLLC resonant converters [46], [68], [80], and [86]. In this part, the FHA method is utilized for obtaining electrical constraints, where the presented method in [113] is extracted to apply to the FHA model of the CLLC resonant converter.

## 3.2. FHA Method

According to this method, the primary and secondary sides of the resonant tank are considered as a square voltage source as shown in Fig. 3-1.

For this square voltage source (see Fig. 3-2), only its fundamental harmonic (switching frequency) is comprised. For the primary voltage, the following condition is considered:

$$v_1(t) \approx \frac{4}{\pi} V_{in} \sin \omega_s t \quad (3.1)$$

Based on the applied sinusoidal voltage, the primary current is also sinusoidal because it is applied to a linear LC circuit. This current is determined as (3.2).

$$i_1(t) \approx I_1 \sin(\omega_s t - \varphi_1) \quad (3.2)$$

where  $I_1$  is the maximum value of the primary current, and  $\varphi_1$  is the phase shift between the voltage and current.

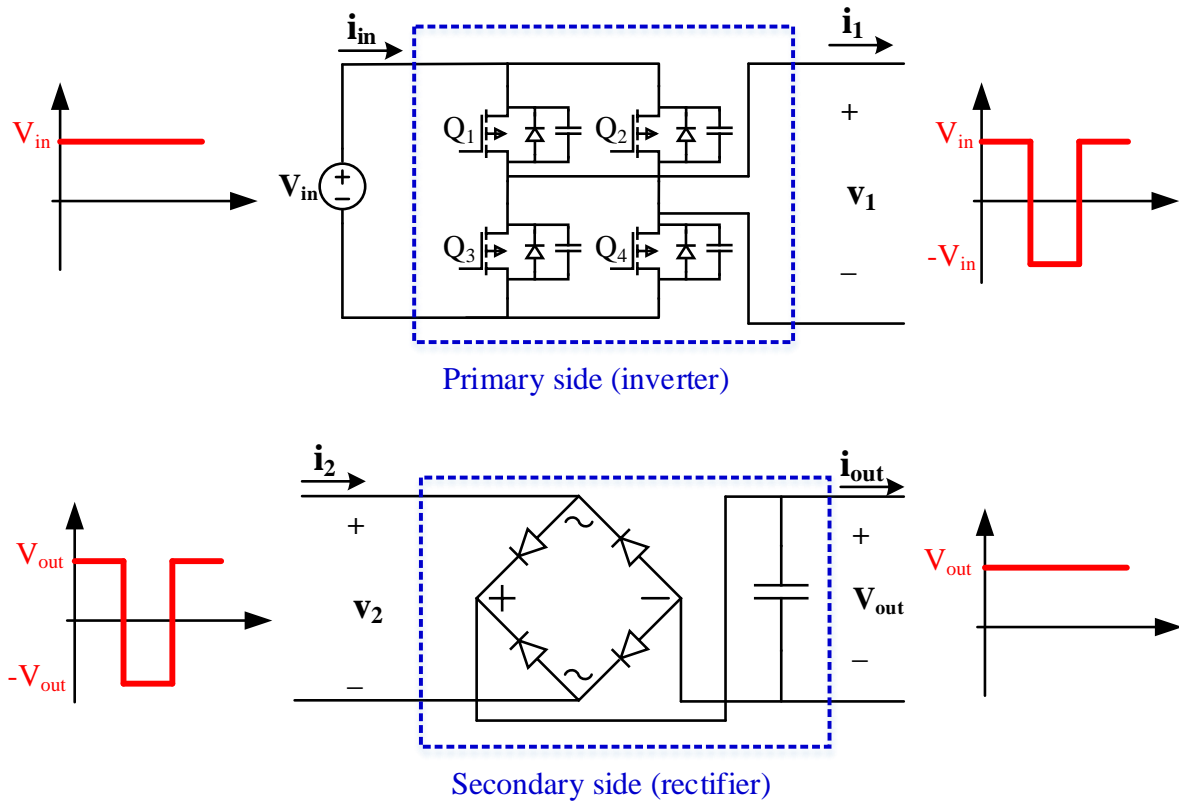


Fig. 3-1: The before and after voltages of the primary side (top) and secondary side (bottom)

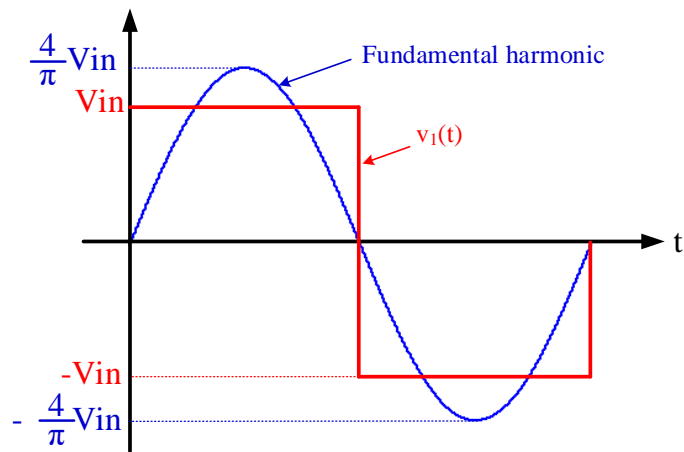


Fig. 3-2: the fundamental harmonic of a square voltage

The input current is the average of the absolute value of  $I_1$ , so we have:

$$\langle |i_{in}(t)| \rangle_{T_s} = \frac{2}{T_s} \int_0^{T_s/2} i_{in}(t) dt \quad (3.3)$$

$$\begin{aligned} &\approx \frac{2}{T_s} \int_0^{T_s/2} I_1 \sin(\omega_s t - \varphi_1) dt \\ &= \frac{2}{\pi} I_1 \cos \varphi_1 \end{aligned}$$

So, the approximated model of the inverter part can be modeled as a dependent voltage source, as shown in Fig. 3-3.

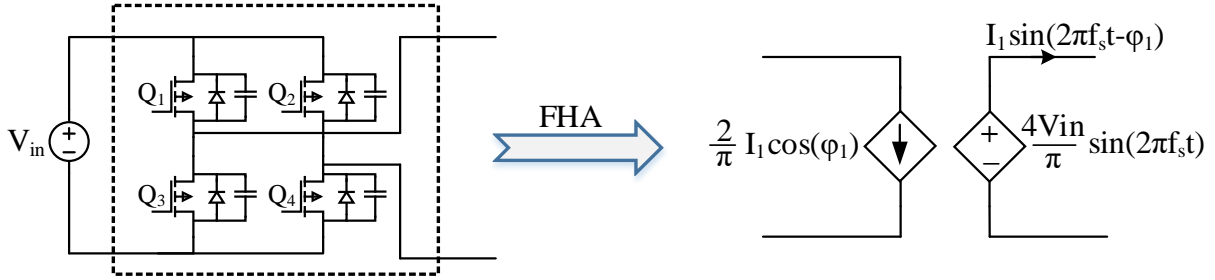


Fig. 3-3: FHA model of the full-bridge inverter

Now, let's consider the secondary side. The first harmonic of the secondary side rectifier is similar to the primary. So we have:

$$v_2(t) \approx \frac{4}{\pi} V_{out} \sin(\omega_s t - \varphi_2) \quad (3.4)$$

where  $\varphi_2$  is the phase shift between the primary voltage and secondary voltage.

Owing to the linear resonant tank, the secondary current is also sinusoidal with the same phase shift:

$$i_2(t) \approx I_2 \sin(\omega_s t - \varphi_2) \quad (3.5)$$

where  $I_2$  is the maximum value of the secondary side current.

It should be mentioned that  $i_2$  and  $v_2$  have the same phase ( $\varphi_2$ ) because of the zero crossing of the rectifier part.

The load current is equal to the average of the absolute value of  $i_2$ , i.e.:

$$I = \langle |i_2(t)| \rangle_{T_s} = \frac{2}{T_s} \int_0^{T_s/2} i_2(t) dt \quad (3.6)$$

Hence we have:



$$\begin{aligned}
 I &\approx \frac{2}{T_s} \int_0^{T_s/2} I_2 \sin(\omega_s t - \varphi_2) dt \\
 &= \frac{2}{\pi} I_2
 \end{aligned} \tag{3.7}$$

The effective resistance of the rectifier input port is determined as follows:

$$R_e = \frac{v_2(t)}{i_2(t)} = \frac{8}{\pi^2} \frac{V_{out}}{I} = \frac{8}{\pi^2} R_{Load} \tag{3.8}$$

Therefore, the equivalent circuit model of the rectifier part is shown in Fig. 3-4.

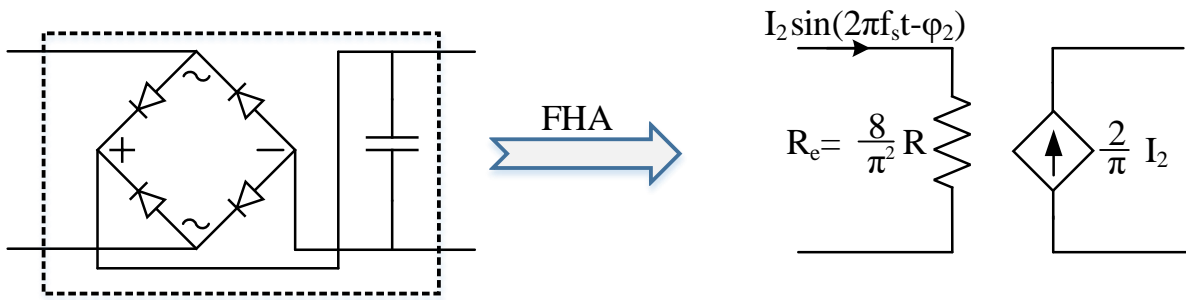


Fig. 3-4: FHA model of the full-bridge rectifier

Now it is time to get the FHA model for the CLLC resonant converter. This modeling is depicted in the next part.

### 3.3. FHA Model for the CLLC Resonant Converter

Let's consider the schematic diagram of the full-bridge CLLC resonant converter, which was shown in Fig. 2-12. By substituting the inverter and rectifier part, the first harmonic approximation model of the CLLC resonant converter can be drawn as Fig. 3-5.

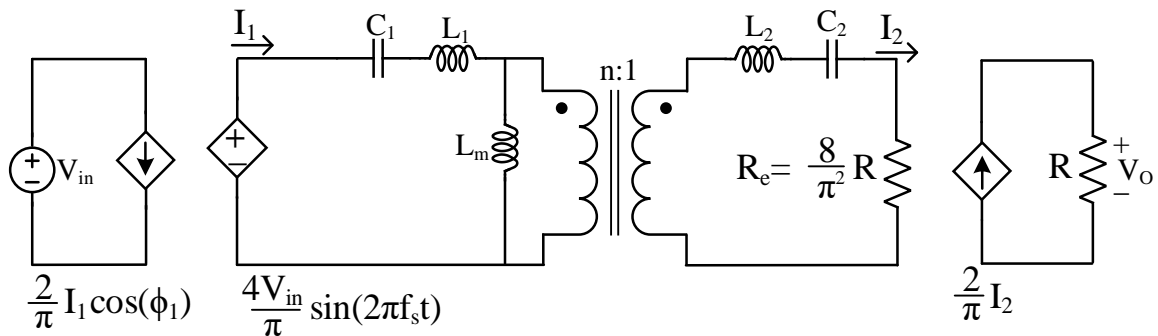


Fig. 3-5: FHA model of the full-bridge CLLC resonant converter

By solving the above figure, the electrical parameters can be obtained as:

$$I_1 = \frac{4}{\pi} V_{in} \times \frac{n^2}{\sqrt{a^2 + b^2}} \times \sqrt{R_e^2 \times (2\pi f_s)^4 + \left( L_2 \times (2\pi f_s)^3 + L_m \times n^2 \times (2\pi f_s)^3 - \frac{2\pi f_s}{C_2} \right)^2} \quad (3.9)$$

$$I_2 = \frac{4}{\pi} V_{in} \times L_m \times n^3 \times \frac{(2\pi f_s)^3}{\sqrt{a^2 + b^2}} \quad (3.10)$$

$$V_{C1} = \frac{I_1}{2 \times C_1 \times \pi \times f_s} \quad (3.11)$$

$$V_{C2} = \frac{I_2}{2 \times C_2 \times \pi \times f_s} \quad (3.12)$$

$$V_O = \frac{2}{\pi} I_2 \quad (3.13)$$

where

$$a = -(L_1 L_2 n^2 + L_1 L_m n^4 + L_2 L_m n^2) \times (2\pi f_s)^4 + \left( \frac{L_1 n^2}{C_2} + \frac{L_2 n^2}{C_2} + \frac{L_m n^2}{C_2} + \frac{L_m n^4}{C_1} \right) \times (2\pi f_s)^2 - \frac{n^2}{C_1 C_2} \quad (3.14)$$

$$b = R_e \times \left( L_1 n^2 (2\pi f_s)^3 + L_m n^2 (2\pi f_s)^3 - \frac{2\pi n^2 f_s}{C_1} \right) \quad (3.15)$$

and

$$R_e = \frac{8 \times R}{\pi^2} \quad (3.16)$$

Now, it is needed to evaluate the FHA model for the CLLC resonant converter.

### 3.4. Evaluation of Electrical Constraints

So far, the bidirectional CLLC resonant converter was selected for the main power converter of an onboard charger, and a model was presented to find an optimum result subject to the constraints. Therefore, it is needed to examine the accuracy of the models. In the beginning, the FHA is used as a modeling framework for the evaluation of electrical constraints. Table 3-1 contains the specifications of a CLLC resonant converter:

Table 3-1: Electrical specifications of the prototype converter

Symbol	Quantity	Value
$L_m$	Transformer magnetizing inductance	58.9 $\mu$ H
$L_1$	The primary resonant inductance	11.8 $\mu$ H
$L_2$	The secondary resonant inductance	11.8 $\mu$ H
$C_1$	The primary resonant capacitor	149.2nF
$C_2$	The secondary resonant capacitor	149.2nF
$n$	Transformer turn ratio	1:1

Now, the electrical parameters of the CLLC resonant converter are examined.

### 3.4.1. Current Evaluation based on FHA

The primary and secondary inductor currents are illustrated in Fig. 3-6:

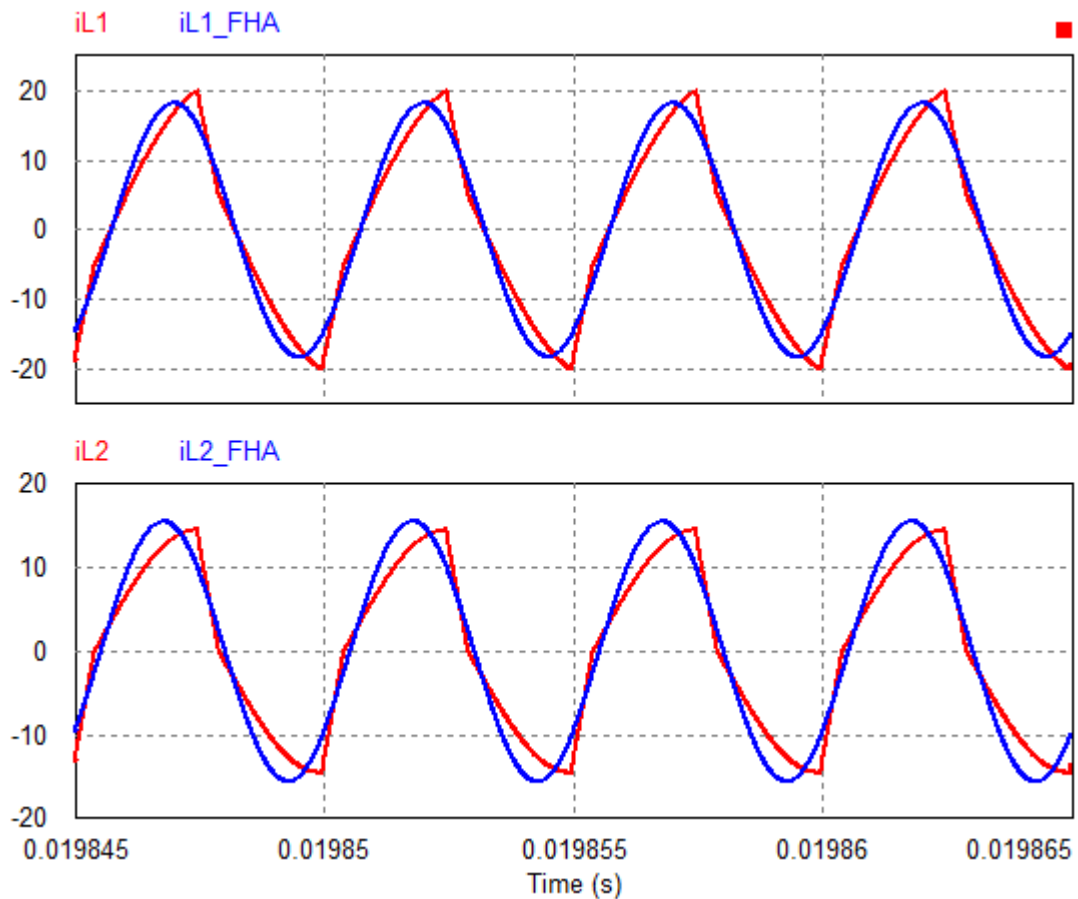


Fig. 3-6: The current of  $L_1$ (top) and  $L_2$  (bottom) (red curves) and their FHA model (blue curves)

According to the above figure, it is manifest that the FHA-based waveforms are not exactly matched to the simulation-based results. Also, the maximum  $i_{L1}$  of time-domain simulation is higher than the FHA model, however, this condition is opposed to  $i_{L2}$ . For a favorable comparison, the maximum values and RMS values are also compared in Table 3-2.

*Table 3-2: The maximum and RMS values of  $i_{L1}$  and  $i_{L2}$  obtained by the PSIM simulation and FHA model*

Parameter	Maximum values			RMS values		
	Sim.	FHA	Error	Sim.	FHA	Error
$i_{L1}$ [A]	20.039	18.198	9.19%	12.351	12.865	-4.16%
$i_{L2}$ [A]	14.511	15.561	-7.24%	9.953	10.995	-10.47

The above table describes that the error for the maximum value reaches 9.19% and it is 10.47% for the RMS value. Therefore, the designed or optimized converter may deviate from the desired converter. It should be mentioned that these errors were obtained in one specific operating point, and there is a possibility for the error to be increased in different operating points.

### 3.4.2. Voltage Evaluation based on FHA

Fig. 3-7 demonstrates the voltage of primary and secondary capacitors,  $v_{C1}$  and  $v_{C2}$  in the time domain:

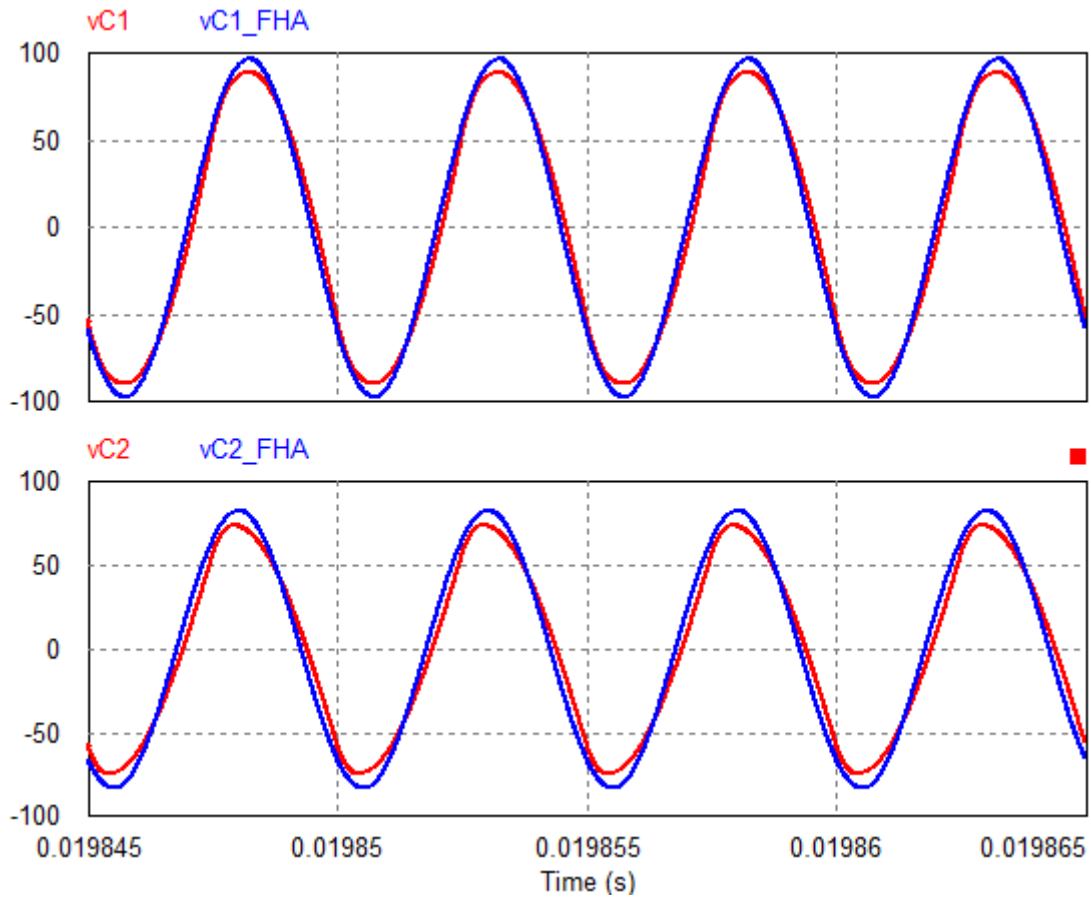


Fig. 3-7: The voltage of  $C_1$ (top) and  $C_2$  (bottom) (red curves) and their FHA model (blue curves)

According to the above figure, the FHA-based waveforms are not also exactly matched to the simulation-based results. It means the accuracy is challenging. The maximum values and RMS values also are in comparison in Table 3-3 for a better evaluation of electrical constraints.

Table 3-3: The maximum and RMS values of  $i_{L1}$  and  $i_{L2}$  obtained by the PSIM simulation and FHA model

Parameter	Maximum values			RMS values		
	Sim.	FHA	Error	Sim.	FHA	Error
vC1 [V]	89.47	97.04	-8.46%	65.04	68.62	-5.50%
vC2 [V]	74.31	82.99	-11.68%	52.21	58.68	12.39%

The above table describes that the error for the maximum value reaches 11.68% and it is 12.39% for the RMS value. Therefore, the designed or optimized converter may deviate from

the desired converter. It should be mentioned that these errors were obtained in one specific operating point, and there is a possibility for the error to be increased in different operating points.

### 3.4.3. ZVS Evaluation based on FHA

In literature, a ZVS condition formula for CLLC resonant converters is based on the FHA method and is derived from the LLC resonant converter, which was presented in (1.1).

Using the listed values of Table 3-1,  $t_{dt}=100ns$ , and  $C_{OSS}=30pF$  (parasitic junction capacitance of the transistor), the maximum allowable magnetizing inductance for ZVS operating is as determined in (3.17).

$$L_m|_{max} = \frac{t_{dt}}{16 \times C_{OSS} \times f_{sw}} = \frac{100n}{16 \times 30p \times 200k} = 1.04 \text{ mH} \tag{3.17}$$

It means that choosing  $L_m$  lower than 1.04mH leads to definitely operate in ZVS. Therefore,  $L_m$  is selected as 58.9μH (based on Table 3-1) for ZVS checking. Fig. 3-8 illustrates the switching instance:

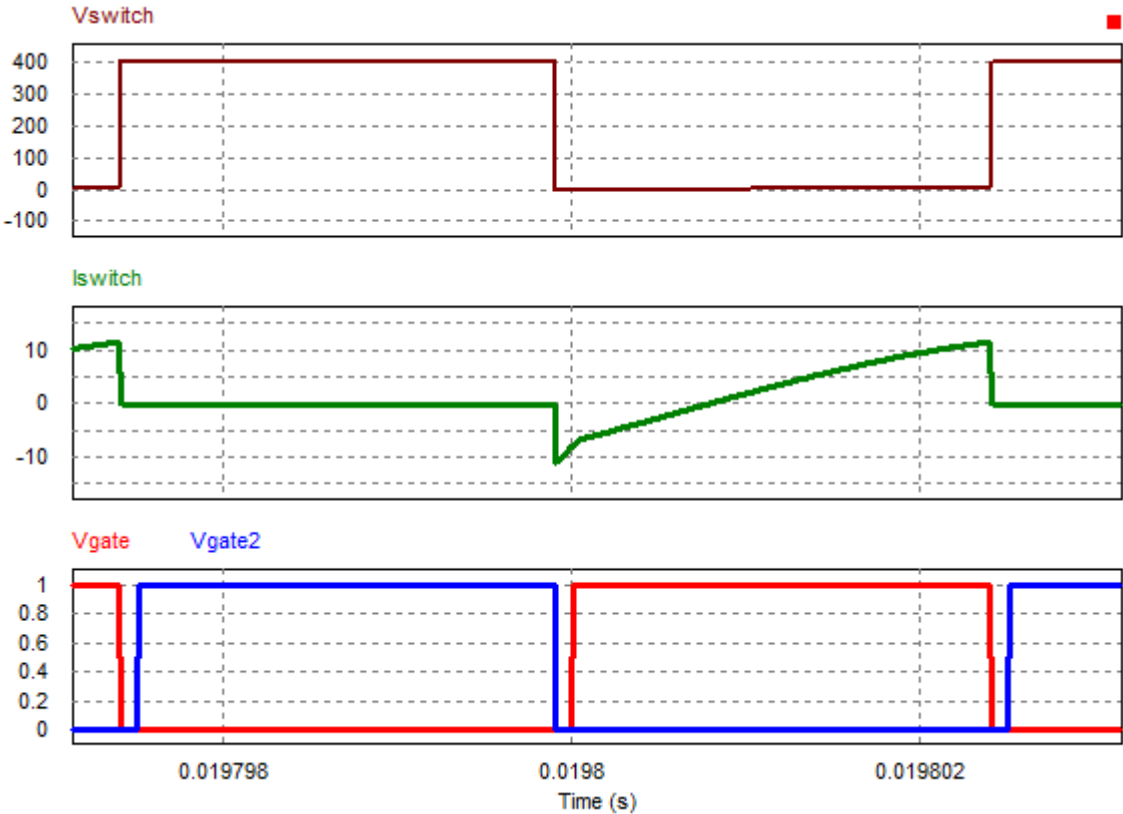


Fig. 3-8: The switching instance for  $L_m=58.9\mu H$ : switch voltage (brown), switch current (green), and gate-to-source voltages (red and blue)

Fig. 3-8 shows that the ZVS condition is satisfied for the inductor lower than (3.17). Now, we select a higher value for the magnetizing inductance as  $L_m=1.5\text{mH}$ . Fig. 3-9 depicts this condition:

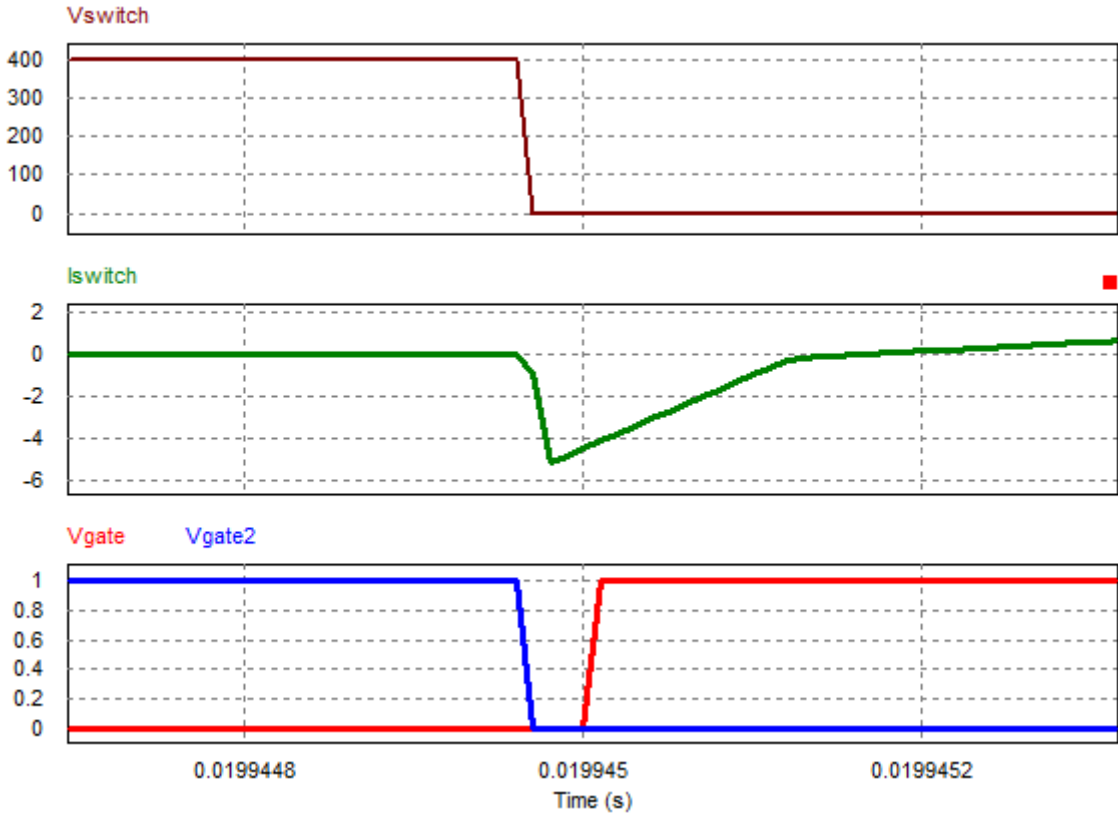


Fig. 3-9: The switching instance for  $L_m=1.5\text{mH}$ : switch voltage (brown), switch current (green), and gate-to-source voltages (red and blue)

The above figure shows that the ZVS is also satisfied for the value above than the value shown in (3.17). This simulation proves that (3.17) is not the boundary condition for ZVS. Another examination is that (3.17) is independent of the load and other parameters. Therefore, the FHA method is not a good method for ensuring ZVS operation.

### 3.5. Summary

Table 3-4 shows the results obtained from the FHA model and time-domain simulation. Two scenarios have been considered to evaluate the precision of the FHA-based results.

Table 3-4: FHA method and PSIM simulation comparisons for two different output powers

PARAMETER	P <sub>OUT</sub> =1281W			P <sub>OUT</sub> =527W		
	SIM.	FHA	ERROR	SIM.	FHA	ERROR
$V_{out}$ [V]	347.3	347.3	0.00	216.8	216.8	0.00
$I_{out}$ [A]	3.69	3.69	0.00	2.43	2.43	0.00
$f_{sw}$ [kHz]	129.3	146	12.14	272	330	10.74
$i_{L1max}$ [A]	9.07	7.47	15.59	6.35	4.63	23.47
$i_{L2max}$ [A]	5.46	5.80	12.62	4.55	3.82	13.18
$v_{C1max}$ [V]	102.91	82.29	14.73	28.85	22.58	16.37
$v_{C2max}$ [V]	72.58	63.85	18.66	22.76	18.61	19.09

As shown in Table 3-4, the error reaches as high as 23.47% for  $i_{L1max}$ , 13.18% for  $i_{L2max}$ , 16.37% for  $v_{C1max}$ , and 19.09% for  $v_{C2max}$ . Furthermore, when the power decreases and the converter operates near the DCM condition, the error increases dramatically. Hence, the first harmonic analysis is not very precise in comparison with the time-domain analysis. It should be mentioned that the high errors can affect the constraints, and the optimum results may not be achieved. Furthermore, it can also affect the designing process and causes miscalculation (such as inductor operating in saturation mode, etc.). Consequently, presenting a new method for analysis of CLLC resonant converters is essential, which will be presented in **Chapter 5**.



## 4. Global design methodology

### 4.1. Introduction

The half-bridge and full-bridge CLLC resonant converters (and other resonant converters) have been designed as a conventional method by parameter sweeping to select a proper value for resonant tank elements. Furthermore, in this method, it is supposed that the converter operates in one operating point. Therefore, using conventional methods for the optimization of bidirectional CLLC resonant converters has the following drawbacks:

1. The CLLC resonant converter is a high-order resonant converter and selecting appropriate parameters for parameter sweeping is difficult. Therefore, it needs comprehensive knowledge of circuit behaviors as well as multiple tries and errors to meet desired requirements.
2. Conventional methods have employed approximated methods for optimization, which leads to inaccuracy in the solution.
3. The operating region of an on-board charger contains a wide range of voltages and currents. So, the designed converter should be optimized in corresponding with the whole operating region. But, a single operating point at a fixed switching frequency has been considered in conventional optimization methods.
4. Due to the limited space inside an EV, it is needed the power density to be considered in the optimization process. It means a mathematical-based formula of power density shall be obtained and put into the optimization process. Conventional algorithms have not considered power density as a function of electric parameters to optimize the whole of the system in one step.
5. The conventional methods have used parameter sweeping or iteration-based algorithms. Therefore, there is not any guarantee that the obtained results are the best possible result.

This dissertation contains an optimization method based on an exact, deterministic, single-stage, and multi-operating point methodology to optimize power density.

## 4.2. Optimization Problem Definition

In an optimization problem, the goal is to find the minimum or maximum value of an objective function by changing the inputs. The operating region can be either constrained or not. In the scope of this dissertation, there are some constraints based on the voltages, currents, temperatures, space, power density, etc. Therefore, the optimization problem of this dissertation is a constrained optimization problem, which is presented as (4.1) [114]:

$$\begin{aligned}
 & \text{Maximize } y(x) \\
 & \text{Subject to } g_i(x) \leq 0 \quad i = 1, 2, \dots, p \\
 & \quad \quad \quad h_i(x) = 0 \quad i = 1, 2, \dots, m \\
 & \quad \quad \quad x = [x_1, x_2, \dots, x_n]^T \\
 & \quad \quad \quad x_i^{\min} < x_i < x_i^{\max} \quad i = 1, 2, \dots, n
 \end{aligned} \tag{4.1}$$

where  $y$  is the objective function,  $x$  is the vector of input variables,  $g$  is the inequality constraints function with the number of  $p$  functions,  $h$  is the equality constraints function with the number of  $m$  functions, and  $n$  is the number of input variables. Fig. 4-1 shows the corresponding functions and the operating region (yellow region) for a one-variable optimization function ( $n=1$ ).

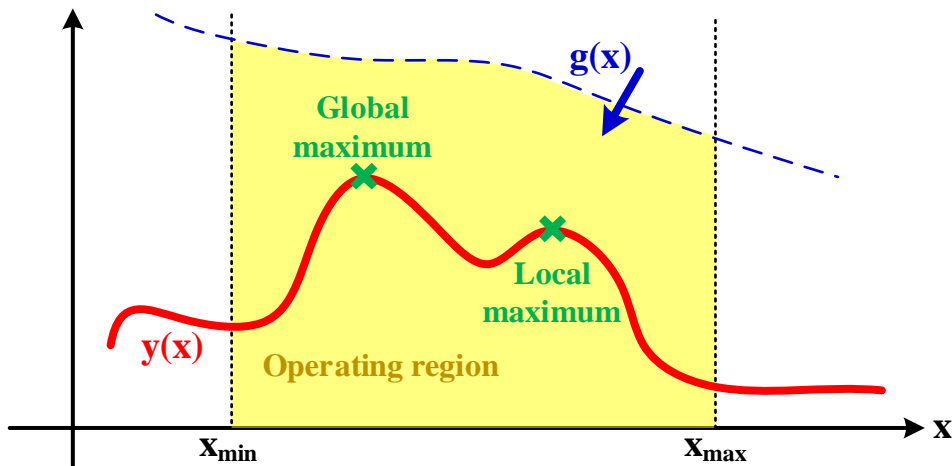


Fig. 4-1: The operating region and constraint of a single-variable objective function

In this dissertation, it is assumed that at least the first derivative of the objective function and constraint functions is available.

Some optimization algorithms have been presented to solve (4.1) and find the global optimum point. In the following part, a review of the different optimization algorithms is expressed.

### **4.3. Optimization Algorithms**

An optimization algorithm is a method that seeks the inputs to find the minimum or maximum of an objective function while constraints have been met.

#### **4.3.1. Stochastic Algorithms**

In stochastic algorithms, random algorithms are used as heuristic searching, where may or may not find the optimum result. These algorithms are inspired by stochastic, environmental, biological, or physical processes. In the genetic algorithm as an example, a population of solutions is evolved toward a better solution with a population generation. The fitness of each generation is evaluated and the more fit generations are selected and the others are recombined or mutated into a new generation. Finally, the genetic algorithm is finished when either the number of generations reaches its maximum value or a fitness level is lower than the required level.

Stochastic algorithms such as Simulated Annealing (SA) [115], Bee Colony (BC) [116], Stochastic Hill Climbing (SHC) [117], Genetic Algorithm (GA) [118], Particle Swarm Optimization (PSO) [119], etc. have been used in some applications. For example, the GA and PSO algorithms were used for two-stage optimization for a hybrid AC-DC micro-grid application [112], however, it may cause to get stuck in a local optimum point instead of the absolute optimum point.


























For the stochastic algorithms, it is obvious that any single run of the algorithm will be different due to different starting points, the randomness of the algorithm, the selection of the number of iterations, and the selected fitness level. As a result, the stochastic algorithm may have a high convergence speed and be highly sensitive to the initial parameters. Also, it may not converge into a result, and there is no guarantee that the obtained result is the best possible result.

### 4.3.2. Deterministic Algorithms

A deterministic algorithm can provide the absolute (global) extremum or at least a local extremum can be guaranteed using the deterministic algorithm [120], where there exists a theoretical guarantee within a predefined tolerance for obtaining the results.

Linear programming (LP), which contains linear equations, is able to efficiently solve an optimization problem involving even millions of variables to find the local or global extremum point [121]. Non-linear programming (NLP) is a deterministic optimization method for solving non-linear equations for global optimization [122]. The branch-and-bound [123], DIRECT [124], outer-approximation [125], and extended cutting plane [126] algorithms are other types of deterministic algorithms. In the branch-and-bound algorithm as an example, the search space of optimization is the whole range of all variables, and each range is bounded to find an optimum value. However, it can find the optimum solution when each range can be solved. Also, it may cause the optimization process to get stuck in a local extremum. The Sequential Quadratic Programming (SQP) algorithm is a gradient-based optimization technique, which is an appropriate method for non-linear programming optimization in a constrained space. The SQP has been applied for different optimization applications. In Table 4-1, a comparison of different optimization algorithms is shown:

*Table 4-1: The main properties of some optimization algorithms [114]*

Type	Example	Number of objectives	Speed	Capability of complex problems	Accuracy	Supporting discrete parameters	Stuck in local extremum
Deterministic	DIRECT	1					
	SQP	1					
	Newton's method	1					
Stochastic	Random Search	1					
	Genetic Algorithm	1~5					

In this dissertation, the SQP method will be utilized as the optimization algorithm, which is discussed in the next part.

#### 4.4. Sequential Quadratic Programming (SQP)

An SQP problem can be iteratively solved by linearization of Eq. (4.1) using Taylor's approximation to find the searching direction at each iteration. The Jacobian matrix is calculated to find the right direction of the new system variable as (4.2).

$$\mathcal{L}(x, \lambda, \sigma) = y(x) - \lambda g(x) - \sigma h(x) \quad (4.2)$$

where  $\lambda$  and  $\sigma$  are Lagrange multipliers.

The new variable  $x$  i.e.  $x_k$  is obtained by solving (4.3).

$$\begin{aligned} \max \quad & y(x_k) + \nabla y(x_k)^T(x - x_k) + \frac{1}{2}(x - x_k)^T \nabla^2 y(x_k)(x - x_k) \\ \text{Subject to} \quad & g(x_k) + \nabla g(x_k)^T(x - x_k) \geq 0 \\ & h(x_k) + \nabla h(x_k)^T(x - x_k) = 0 \end{aligned} \quad (4.3)$$

According to the above equation, the first and second derivatives of the objective function must be available. However, there exist some discrete parameters in the power electronics circuits, which must be derivable. This modeling is presented in the next part.

#### 4.5. Continuous Modeling of Discrete Parameters

The discrete parameters of the CLLC-based EV charger can be classified into two parameters, i.e. standard core sizes and the number of turns.

##### 4.5.1. Standard core sizes

Let's consider the following dimension as Fig. 4-2 for the conventional and planar EE cores.

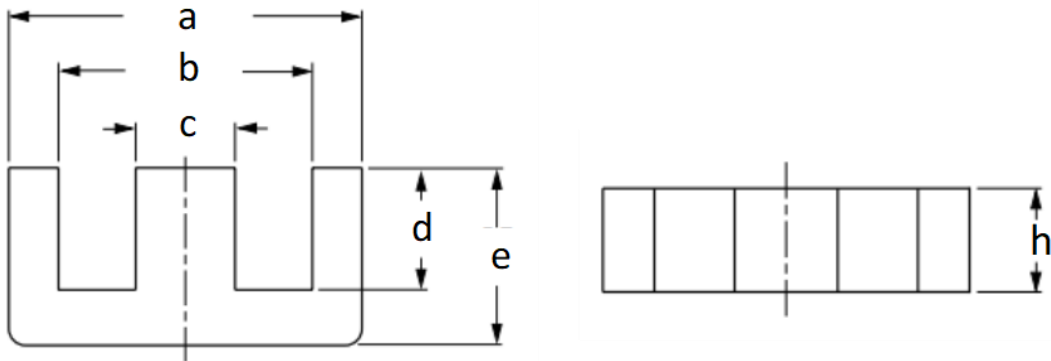


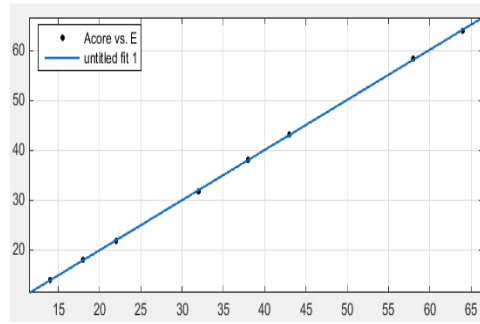
Fig. 4-2: Geometrical diagram of E-shape core

Table 4-2 contains information about the size of some E-type cores.

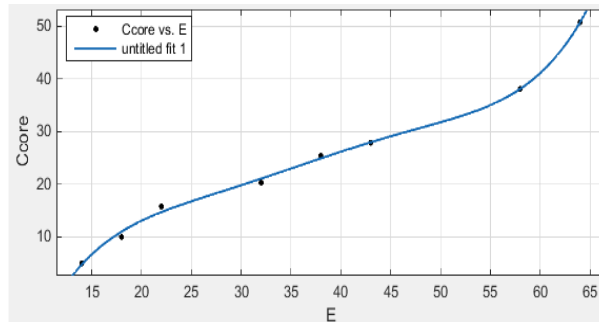
*Table 4-2: Important dimensional of the conventional E cores and planar E cores*

	Parameter $X$	Effective Length (mm)	Effective Area (mm <sup>2</sup> )	a (mm)	b (mm)	c (mm)	d (mm)	e (mm)	h (mm)
Conventional E Core	16	37.6	20.1	16	8.2	4.7	5.7	11.3	4.7
	20	42.8	31.2	20.7	10	5.3	6.3	12.8	5.2
	25	49	39.5	25.4	9.65	6.35	6.4	18.8	6.35
	30	67	60	30.8	15	7.3	9.7	19.5	7.2
	35	80.7	100	35	17.5	10	12.5	24.5	10
	42	97	178	43	21	15.2	14.8	29.5	12.2
	47	88.9	234	46.9	19.6	15.6	12.1	32.4	15.6
	55	124	353	56.2	27.5	21	18.5	37.5	17.2
	65	147	540	65	32.8	27.4	22.2	44.2	20
	71	149	683	70.5	33.2	32	21.9	48	22
Planar E Core	14	20.7	14.5	14	3.5	5	2	11	3
	18	24.3	39.5	18	4	10	2	14	4
	22	32.5	78.5	21.8	5.7	15.8	3.2	16.8	5
	32	41.4	129	31.75	6.35	20.32	3.18	24.9	6.35
	38	52.4	194	38.1	8.26	25.4	4.45	30.23	7.6
	43	61.1	225	43.2	9.5	27.9	5.4	35.4	8.1
	58	80.6	305	58.4	10.5	38.1	6.5	50	8.1
	64	79.9	511	64	10.2	50.8	5.1	53.8	10.2

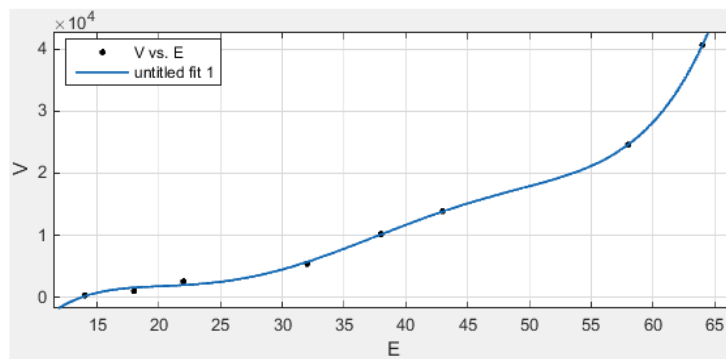
The parameter  $X$  is defined as a continuous variable to make the core sizes continuous using interpolation with Matlab. The interpolation of some variables is shown in Fig. 4-3. The continuous model of each variable is listed in Table 4-3.



(a)



(b)



(c)

*Fig. 4-3: Continuous models for some variables using interpolation for parameter X (a); parameter C (b); and the volume of the core (c).*

Using parameter X, all the variables corresponding to the core sizes will be continuous, if the parameter X is selected as a free positive number.

#### 4.1.1. The number of turns

Another discrete parameter is the number of turns and also the number of turns in each layer. No interpolation is needed and these values can be directly considered as continuous parameters.

Table 4-3: Continuous equations for the core sizes of conventional and planar E cores

Conventional E Core	$A = 0.9917 \times X + 0.6851$
	$B = -8.708 \times 10^{-7} \times X^4 + 6.652 \times 10^{-5} \times X^3 + 0.000437 \times X^2 + 0.3899 \times X + 1.634$
	$C = 4.9110 \times 10^{-6} \times X^4 - 0.0009099 \times X^3 + 0.06433 \times X^2 - 1.512 \times X + 15.99$
	$D = 4.832 \times 10^{-6} \times X^4 - 0.0009239 \times X^3 + 0.06026 \times X^2 - 1.232 \times X + 13.45$
	$E = 0.674 \times X + 0.4873$
	$F = A - E$
	$\text{Mass} = 0.001018 \times X^3 - 0.01525 \times X^2 - 0.4638 \times X + 10.31$
	$\text{Volume} = -0.0008576 \times X^5 + 0.1719 \times X^4 - 12.57 \times X^3 + 451.2 \times X^2 - 7640 \times X + 4.887 \times 10^4$
Planar E Core	$A = X$
	$B = F$
	$C = 1.464 \times 10^{-6} \times X^5 - 0.0002725 \times X^4 + 0.0198 \times X^3 - 0.7021 \times X^2 + 12.79 \times X - 81.36$
	$D = F/2$
	$E = -0.0001884 \times X^3 + 0.02389 \times X^2 - 0.03055 \times X + 7.61$
	$F = A - E$
	$\text{Mass} = 0.08002 \times X^4 - 1.03 \times X^3 + 5.869 \times X^2 - 10.19 \times X + 5.938$
	$\text{Volume} = 0.002014 \times X^5 - 0.3591 \times X^4 + 24.2 \times X^3 - 754.4 \times X^2 + 1.11 \times 10^4 \times X - 6.115 \times 10^4$

## 4.2. Design Methodology and Models

Whether stochastic or deterministic algorithms are selected, it is mandatory to obtain the objective function precisely due to the fact that the objective function is calculated repeatedly and a small error in the models can cause a high error in the final result. In this part, the total losses and design methodology will be presented.

### 4.2.1. Semiconductor Losses

The calculation of semiconductor losses depends on the selected technology of switching and circuit behavior. Gallium Nitride (GaN) transistors and Schottky diodes are used in this dissertation as the semiconductor parts.

#### *Proposed Switching Losses Calculation for GaN transistors*

Understanding the GaN power loss modeling, whether switching loss or conduction loss, is one of the most important parts of the optimum design of GaN-based EV chargers. The



switching losses, involving turn-on and turn-off situations, are commonly calculated by multiplying the switching frequency by the energy losses which are provided in the datasheet of a GaN transistor. It should be mentioned that the losses are usually given at a specific operating point [127]. Even these data are not always given within the datasheet of some GaN transistors. So, it is necessary to propose a method for switching loss modeling.

In [128], authors presented an analytical loss model in the integral form for a high-voltage GaN transistor in cascode configuration considering parasitic inductance and nonlinearity of capacitors. In [129], the loss analysis of a low-voltage GaN transistor was calculated according to the switching processes modeling for a synchronous buck converter and the qualitative analysis for charging the gate resistances, the drain-source capacitances, etc. was presented. In [130], an analytical switching loss model was presented for a GaN-based buck converter; the proposed equations of power losses are based on buck converter parameters and cannot be applied to other topologies. In [131], a switching loss model by the interpolation of the input capacitance and transconductance was presented for a 650V GaN transistor. A datasheet-based analytical switching loss model was presented in [132] for totem-pole PFC converters. In [133], the LTSPICE simulation was carried out on the preliminary calculation of the EON and EOFF. In [134], the impact of GaN transistor packaging on switching loss was illustrated. In [135] with an analytical method, all the parasitic inductors and capacitors were considered for a cascode configuration and only the turn-ON transition was analyzed. In [136] authors used the analysis of the switching waveforms to obtain loss prediction of SiC and GaN devices.

However, despite a considerable number of analytical loss measurements, there is no simple and accurate analytical model appropriate for design engineers. Most of the works carried out on the switching loss analysis use an integral form which leads to a complicated and time-consuming analyzing model. Furthermore, for one device, the switching losses are provided at one operating point associated with the datasheet's value. Therefore, a model is needed to predict the losses for other operating points.

Fig. 4-4 illustrates the switching loss test circuit of the GS66508B GaN transistor [137]. It is noted that this circuit can be utilized for other GaN transistors with different parameters.

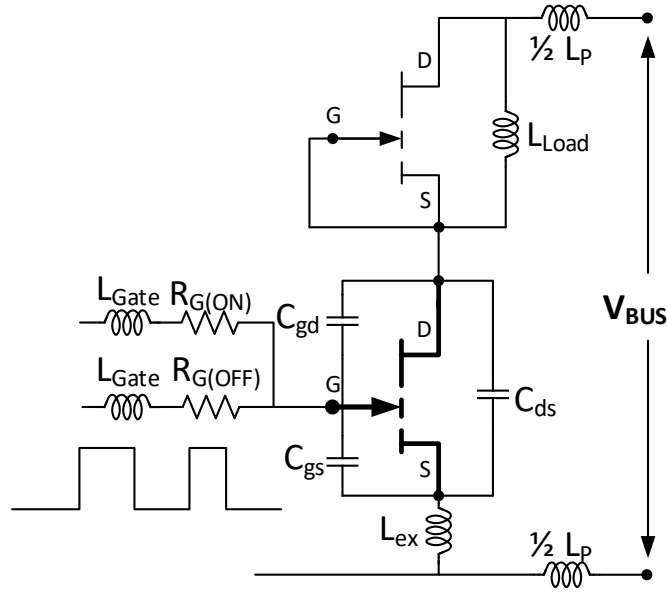


Fig. 4-4: The circuit test for switching loss calculation of a GaN transistor based on the datasheet information

The value of  $L_{Load}$  is considered to prepare the required current for the double pulse tester of the selected GaN device [138]. For this circuit, one specific condition is considered as the base value of GaN parameters. Table 4-4 shows the base values of GaN parameters where partially extracted from the GS66508B GaN transistor and the values of non-linear capacitance  $C_{iss}$ ,  $C_{oss}$ , and  $C_{rss}$  are the ones obtained for the high voltage. The switching loss test circuit (see Fig. 4-4) with the base parameters (shown in Table 4-4) is simulated on LTSPICE and the base value of energy loss is obtained as (4.4) by performing the double pulse tester.

Table 4-4: Based values of the proposed model for switching loss calculation

Parameter	Symbol	Value	Unit
Bus Voltage	$V_{BUS}$	400	V
Drain-Source Voltage	$V_{DS}$	$\approx 400$	V
Drain Current	$I_D$	15	A
Junction Temperature	$T_j$	25	$^{\circ}\text{C}$
Gate Resistor for OFF state	$R_{gOff}$	1	$\Omega$
Gate Resistor for ON state	$R_{gOn}$	10	$\Omega$
Gate Series Inductor	$L_{gate}$	1	nH
Positive Gate-Source Voltage	$V_{gPos}$	6	V
Negative Gate-Source Voltage	$V_{gNeg}$	-3	V
GaN Series Inductor	$L_{ex}$	10	pH
PCB Track Series Inductor	$L_P$	2	nH
GaN Input Capacitor	$C_{iss}$	242	pF
GaN Output Capacitor	$C_{oss}$	65	pF
GaN Reverse Capacitor	$C_{rss}$	1.5	pF

$$E_{base} = 53.3 \mu J \quad (4.4)$$

The proposed method must possess high accuracy for any type of circuit parameters, e.g. different voltage, current, gate resistor, GaN transistor, etc. The criteria for general loss modeling analysis are obtained by comparing them with the base values. For this purpose, the LTSPICE simulation is performed and then, an algebraic equation is presented by the interpolation.

There are four kinds of parameters for a circuit based on its operating point and components:

- Electrical operating point:  $V_{DS}, I_D$ ,
- Thermal operating point:  $T_j$
- Circuit operating point:  $R_{gate}, V_{gate}, L_p$ , etc.
- Device characteristics:  $C_{iss}, C_{oss}, C_{rss}$ .

Owing to the GaN circuit parameters dependencies, the proposed method is divided into two types of energy loss equations. The first type is a function with two variables and the second type is a function with one variable.

- a) *Type I (Two Variables Function)*:** It is obvious that in the switching power devices, there is a close relationship between the drain current,  $I_D$ , and junction temperature,  $T_j$ . Another alternative explanation is the clear association between the temperature and current, which are not independent. Current generates losses and increases the temperature indeed. Therefore, a combined formulation is used. Fig. 4-5 shows the switching energy as a function of  $I_D$  and  $T_j$ , where the switching loss dramatically increases by the temperature and current increments.

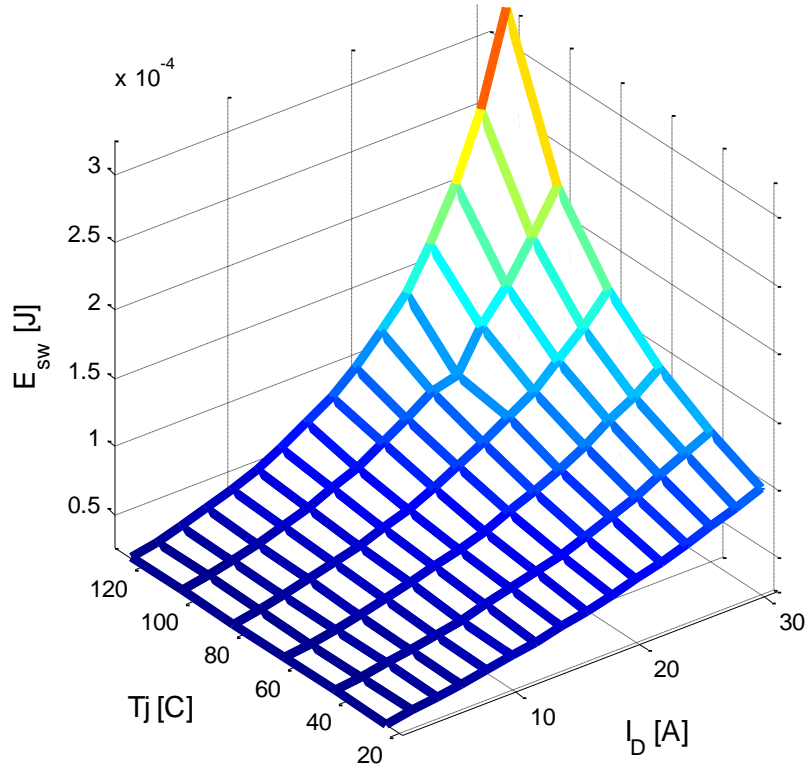


Fig. 4-5: Switching losses based on the variation of junction temperature and drain-to-source current for a GaN transistor operating at the base values

With some interpolations into MATLAB, it was found that the 5<sup>th</sup> order polynomial equation is a good candidate for the modeling of switching losses based on the variation of  $I_D$  and  $Tj$ . So, the normalized switching energy losses,  $Eb$ , can be calculated as a function of two variables  $I_D$  and  $Tj$  as (4.5).

$$Eb(I_D, Tj) = \frac{E(I_D, Tj)}{E_{base}} = P_1 + P_2 I_D + P_3 Tj + P_4 (I_D + P_5 Tj)^3 + P_6 (I_D + P_7 Tj)^5 \quad (4.5)$$

where coefficients  $P_1, P_2, \dots, P_7$  are defined in Table 4-5. It should be mentioned that  $I_D$  is the drain current at the switching instant and it is neither RMS nor average current.

Table 4-5: List of coefficients for the proposed method for switching loss calculation, Type I (Eq. (4.5)) and Type II (Eq. (4.6)) Variables

Para.	Type	Coefficients	RMSE <sup>a</sup>	Range
<i>ID,Tj</i>	Type I	$P_1=2.4130 \times 10^{-1}$ , $P_2=4.6170 \times 10^{-2}$ , $P_3=3.9430 \times 10^{-3}$ , $P_4=-2.0480 \times 10^{-6}$ $P_5=4.7550 \times 10^{-1}$ , $P_6=7.7370 \times 10^{-9}$ , $P_7=2.1210 \times 10^{-1}$	0.0444	<31A, <150°C
<i>VDS</i>	Type II	$P_1=1.0267 \times 10^{-9}$ , $P_2=7.1253 \times 10^{-7}$ , $P_3=2.1950 \times 10^{-3}$ , $P_4=-5.4802 \times 10^{-2}$	0.0046	<650V
<i>RgOff</i>	Type II	$P_1=1.8403 \times 10^{-7}$ , $P_2=2.5648 \times 10^{-4}$ , $P_3=5.3940 \times 10^{-4}$ , $P_4=1.0012$	0.0019	<12Ω
<i>RgOn</i>	Type II	$P_1=8.1053 \times 10^{-6}$ , $P_2=-4.2601 \times 10^{-4}$ , $P_3=2.9752 \times 10^{-1}$ , $P_4=7.3991 \times 10^{-1}$	0.0052	<20Ω
<i>VgNeg</i>	Type II	$P_1=4.9380 \times 10^{-6}$ , $P_2=3.0799 \times 10^{-4}$ , $P_3=2.2815 \times 10^{-3}$ , $P_4=1.0048$	0.0018	-3V< <0V
<i>VgPos</i>	Type II	$P_1=-5.0753 \times 10^{-2}$ , $P_2=8.2630 \times 10^{-1}$ , $P_3=-4.6115$ , $P_4=9.8830$	0.0097	3.5V< <6.5V
<i>Lpara</i>	Type II	$P_1=1.0814 \times 10^{-5}$ , $P_2=-1.0120 \times 10^{-4}$ , $P_3=-1.3194 \times 10^{-2}$ , $P_4=1.0269$	0.0228	<34nH
<i>Lgate</i>	Type II	$P_1=3.6372 \times 10^{-5}$ , $P_2=-1.1871 \times 10^{-3}$ , $P_3=4.9717 \times 10^{-3}$ , $P_4=9.9182 \times 10^{-1}$	0.0067	<35nH
<i>Lex</i>	Type II	$P_1=1.0997 \times 10^{-9}$ , $P_2=-1.2736 \times 10^{-6}$ , $P_3=7.6525 \times 10^{-4}$ , $P_4=9.9240 \times 10^{-1}$	0.0010	<2nH
<i>Ciss</i>	Type II	$P_1=3.4789 \times 10^{-9}$ , $P_2=-2.2825 \times 10^{-6}$ , $P_3=6.1659 \times 10^{-4}$ , $P_4=9.3160 \times 10^{-1}$	0.0045	<422pF
<i>Coss</i>	Type II	$P_1=4.3957 \times 10^{-8}$ , $P_2=-8.0368 \times 10^{-6}$ , $P_3=2.1937 \times 10^{-3}$ , $P_4=8.8031 \times 10^{-1}$	0.0015	<110pF
<i>Crss</i>	Type II	$P_1=1.5521 \times 10^{-4}$ , $P_2=-4.6845 \times 10^{-4}$ , $P_3=3.3020 \times 10^{-2}$ , $P_4=9.4955 \times 10^{-1}$	0.0015	<7pF

a. Root mean square error

b) **Type II (One Variable Functions):** Some simulations are carried out on LTSPICE for the variation of other parameters shown in Table 4-5, noted by type II, and the switching energy losses are recorded for each case (see Fig. Fig. 4-6). MATLAB interpolations for the switching losses evince that, the lost energy can be modeled independently as a third-order polynomial function with an acceptable root-mean-square error (RMSE). It should be mentioned that the loss modeling of some parameters shown in Fig. 4-6 can be modeled as a first or different-order equation, for example, the variation of switching energy with the negative gate driver voltage, *VgNeg*, is almost constant and can be modeled as a constant value, but all the type II parameters have been considered as a third order equation for the sake of simplicity. So, the switching energy losses can be modeled as the same equation as (4.6) for each type II parameter.

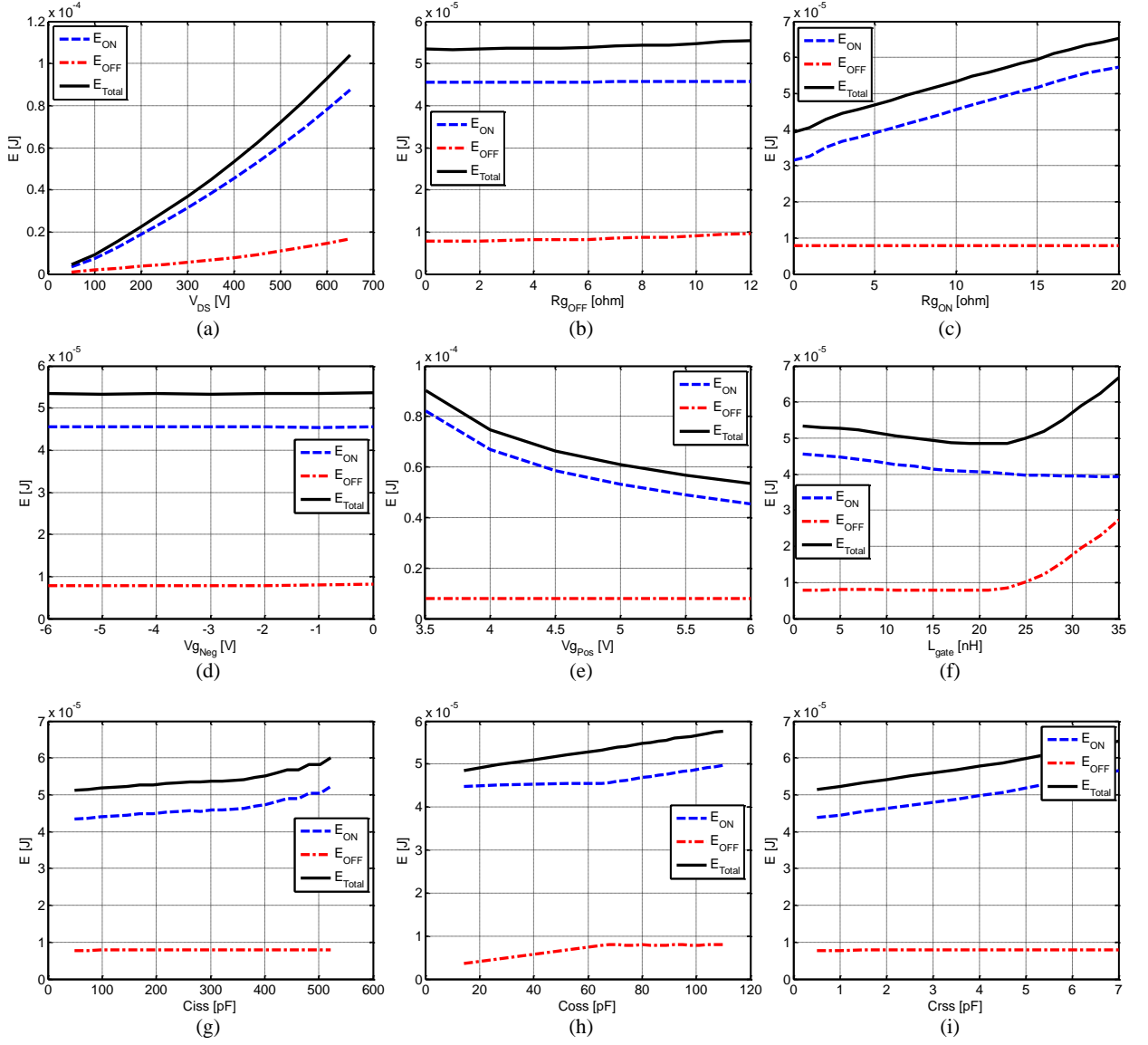


Fig. 4-6: Switching losses based on considering the type II parameters for a GaN transistor operating at the base value. Variation of drain-to-source voltage from 50V to 650V (a), the gate resistor for OFF state (b), the gate resistor for ON state (c), the gate-to-source voltage for OFF condition (d), the gate-to-source voltage for ON condition (e), the parasitic inductor for a gate pin with considering internal gate inductance (f), Ciss (g), Coss (h), and Crss (i) capacitors effects consideration for switching losses. The red line, blue line, and black line are OFF switching loss, ON switching loss, and total switching loss, respectively.

$$Eb(X) = \frac{E(X)}{E_{base}} = P_1 X^3 + P_2 X^2 + P_3 X + P_4 \quad (4.6)$$

where coefficients  $P_1$ ,  $P_2$ ,  $P_3$ , and  $P_4$  are also defined in Table 4-5 and  $X \in \{V_{DS}, Rg_{Off}, Rg_{On}, Vg_{Neg}, Vg_{Pos}, L_{para}, L_{gate}, L_{ex}, C_{iss}, C_{oss}, \text{ and } C_{r_{ss}}\}$ .

Finally, the switching loss energy of GaN transistors,  $E_{Loss}$ , can be calculated as (4.7).

$$E_{Loss} = \left( E_b(I_D, T_j) \times \prod_{X \in U} E_b(X) \right) \times E_{base} \quad (4.7)$$

where  $U = \{\text{Type II parameters: } V_{DS}, RgOff, RgOn, VgNeg, VgPos, Lpara, Lgate, Lex, Ciss, Coss, \text{ and } Crss\}$  as listed in Table 4-5, and  $E_{base} = 53.3 \mu\text{J}$  as shown in Eq. (4.4).

In summary, a specific device model in LTSPICE was considered and the impact of all parameters variation on the losses was studied. Therefore, for switching loss calculation, the GaN parameters are needed to calculate the  $E_b$  for each parameter as (4.6) with the coefficients shown in Table 4-5. Eq. (4.7) calculates switching losses for any types of electrical, thermal, and device parameters. The switching power loss of a GaN transistor,  $P_{sw}$ , can be calculated by multiplying equation (4.7) by the switching frequency,  $f_{sw}$ , as (4.8).

$$P_{sw} = E_{Loss} \times f_{sw} \quad (4.8)$$

Fig. 4-6 shows the ON switching loss, OFF switching loss, and total switching loss for a GaN transistor tested under the base values. According to Fig. 4-6, it is shown that ON-switching energy losses dominate the total energy losses [128] but for this analysis, OFF-switching energy losses have been also considered. Fig. 4-6 (a) depicts that the switching loss extremely depends on the drain-to-source voltage. As shown in Fig. 4-6 (b), by increasing the OFF gate resistor, the turn-off switching loss slightly increases. Fig. 4-6 (c) shows that the turn-on switching loss reduces by decreasing the gate resistance [139]. According to Fig. 4-6 (d), the negative gate-to-source voltage has a low effect on switching losses. By reducing the positive gate-to-source voltage, the switching losses will be increased which may be affected by increasing the ON state resistance (Fig. 4-6 e). Furthermore, the gate inductance has a non-linear relationship with switching losses (Fig. 4-6 f). The switching loss will be increased by increasing  $Ciss$ ,  $Coss$ , and  $Crss$  (Fig. 4-6 g, h, and i). Other parameters, such as drain and source parasitic inductors, and the DC line inductance, have not been shown in Fig. 4-6.

As a result, Eq. (4.8) is used to calculate the switching losses of GaN transistors, when  $I_D < 31\text{A}$ ,  $V_{DS} < 650\text{V}$ , and  $T_j < 150^\circ\text{C}$ .

It should be mentioned that the proposed method can be used for different GaN transistors because the switching loss relationship is also based on the GaN transistor's parameters (e.g.  $Ciss$ ,  $Coss$ ,  $Crss$ ,  $Lpara$ , and  $Lex$ ). In this work, the selected technology for switching is

predetermined and the GS66508B GaN transistor has been selected. So, the aforementioned parameters are fixed and the switching loss formula can be simplified as (4.9).

$$\begin{aligned}
P_{SW}|_{GS66508B} &= f_{sw} \times 53.3\mu \\
&\times \left( 0.2413 + 4.617 \times 10^{-2} \times I_D + 3.943 \times 10^{-3} \times T_j \right. \\
&- 2.048 \times 10^{-6} \times (I_D + 0.4755 \times T_j)^3 \\
&\left. + 7.7370 \times 10^{-9} \times (I_D + 0.2121 \times T_j)^5 \right)
\end{aligned} \tag{4.9}$$

where  $I_D$  is its current at the switching instance, and  $T_j$  is the junction temperature. For G2V applications,  $V_{DS}$  is 400V for the primary switches (inverter) and it is equal to  $V_{out}$  for the secondary switches (rectifier). For V2G applications, it depends on the discharging profile for the secondary switches (inverter), and it is equal to  $V_{out}$  for the primary switches (rectifier).  $I_D$  is related to the charging/discharging current (defined operating points).

#### *Proposed Conduction Losses Calculation for GaN transistors*

The conduction losses are usually calculated by multiplying the ON resistance by the RMS current to the square [140]. In [141], the authors presented the modeling of frequency-based ON resistance for GaN transistors, especially at frequencies above MHz and an electrical circuit was considered for the ON resistance calculation. Impacts of soft-switching and hard-switching on dynamic ON-resistance of GaN transistors were analyzed in [142]. However, experiments and simulations have indicated temperature-dependency in the ON state resistance of GaN transistors. This dependency demonstrates a need to model the relationship between the ON state resistance and temperature.

An easy and exact modeling method is presented for obtaining the conduction power loss which is directly relevant to the ON resistance of the GaN transistor. For this purpose, the values of the ON resistance at two different temperatures can be found on the GaN transistor's datasheet,  $T_1$  and  $T_2$ , typically 25°C and 150°C. Table 4-6 shows these values for the selected GaN transistors.

Two values of ON resistances,  $R_1$  and  $R_2$ , have been assigned to these temperatures as (4.10) and (4.11):

$$R_1 = R_{ON} \Big|_{T_j=T_1} \tag{4.10}$$



$$R_2 = R_{ON} \Big|_{T_j=T_2} \quad (4.11)$$

Table 4-6: Two values of temperatures and resistance mentioned in the GaN transistors datasheet

GaN device	$T_1$ (°C)	$R_1$ (mΩ)	$T_2$ (°C)	$R_2$ (mΩ)
GS66502B	25	200	150	516
GS66506T	25	67	150	175
GS66508B	25	50	150	129
GS66516T	25	25	150	65
IGOT60R070	25	55	150	100
IGT60R19	25	140	150	260
TP65H150LS	25	150	150	307
TP65H035G4	25	35	170	72
TP65H300G	25	240	150	492
GPI8HINOIC	25	175	150	Unknown
PGA26E07B	25	56	150	110
EPC2105C	25	3.2	125	5.1

Some simulations for the measurement of ON resistance in different temperatures have been carried out which consistently show that there is a direct relationship between the temperature and ON resistance. Therefore, an algebraic equation can be fitted as (4.12).

$$R_{ON}(T_j) = \frac{R_2 - R_1}{T_2 - T_1} T_j + \frac{T_2 R_1 - T_1 R_2}{T_2 - T_1} \quad (4.12)$$

where the values of ON resistance and related temperatures for some GaN transistors have been presented in Table 4-6.

Finally, the conduction power loss can be calculated as (4.13).

$$P_{cond.} = R_{ON} I_{RMS}^2 \quad (4.13)$$

where  $I_{RMS}$  is the root mean square current of the GaN transistor and depends on the type of the converter and the load current.

In summary for obtaining conduction losses, only the ON state resistance is needed, which is temperature-dependent. So, using the model presented in (4.12), the conduction losses are computed as (4.13).

### Diode Losses

Transistors can be applied as synchronous rectification to increase the total efficiency. However, a controller and external components are needed to detect the exact transition time. In this dissertation, an extra diode is parallel to each GaN transistor for having an alternative solution. In this case, the gate driver of GaN transistors is OFF and the current will pass through the corresponding diodes. Therefore, it is needed to obtain the diode losses, which are usually calculated using multiplying the diode voltage drop by the DC current as (4.14).

$$P_{diode} = V_{drop} \times I_{DC} \quad (4.14)$$

Although the voltage drop is a function of the current and junction temperature, in this dissertation, only the typical value in its datasheet is considered. For more accuracy, considering V-I characteristics of the diode is preferred.

#### 4.2.2. Core Losses in Magnetic Components

The core losses are the sum of eddy-current loss and hysteresis loss, and anomalous loss, which play an important role in the design and optimization of power electronics converters. There are some methods to evaluate the core losses. The simplest method is the Steinmetz equation captured using an empirical approach and is precise for pure sinusoidal waveforms. The Steinmetz equation is expressed as (4.15).

$$P_{core} = K \times V_{core} \times f^{\alpha} \times B^{\beta} \quad (4.15)$$

where  $P_{core}$  is the core losses,  $V_{core}$  is the core's volume,  $B$  is the maximum flux density of the core, and  $K$ ,  $\alpha$ , and  $\beta$  are the coefficients related to the core's material and geometry, and usually mentioned in the core's datasheet. However, the waveforms are not pure sinusoidal in the power electronics converter, and the accuracy of the Steinmetz equation may deteriorate for non-sinusoidal flux waveforms. It should be mentioned that due to the non-linear behavior of the core loss equation, the superposition cannot be applied.

In [143], a temperature-dependent form of the Steinmetz equation was considered as (4.16).

$$P_{core} = K \times V_{core} \times f^{\alpha} \times B^{\beta} (C_0 - C_1 T + C_2 T^2) \quad (4.16)$$

But there is not any information about the value of  $C_0$ ,  $C_1$ , and  $C_2$ . In [142], the Steinmetz equation was modified and an equivalent frequency was introduced for non-sinusoidal waveforms:

$$f_{eq} = \frac{2}{\Delta B^2 \pi^2} \int_0^T \left( \frac{dB(t)}{dt} \right)^2 dt \quad (4.17)$$

and the core loss is calculated as (4.18).

$$P_{core} = K \times V_{core} \times f_{eq}^{\alpha-1} \times f_r \times B^\beta \quad (4.18)$$

Another modification was the generalized Steinmetz equation as [144]:

$$P_{core} = \frac{1}{T} \int_0^T K_i \left| \frac{dB(t)}{dt} \right|^\alpha |B(t)|^{\beta-\alpha} dt \quad (4.19)$$

The Steinmetz equation was extended for rectangular and trapezoidal waveforms in [145], and the simpler version of this method was discussed in [146] as (4.20).

$$P_{core} = \left( \frac{8}{\pi^2} \right)^{\alpha-1} K \times V_{core} \times f^{\alpha-1} \times B^\beta \quad (4.20)$$

An experimental-based methodology for core loss calculation was presented in [147], but it is hard to implement into the optimization process.

In this dissertation, the more simple version of the Steinmetz equation i.e. Eq. (4.15) is selected because the CLLC resonant tank plays a role of a filter for the applied DC voltage, and the magnetic component waveforms in each subinterval are a part of a sinusoid. Also, it is difficult to implement integral forms in the optimization process.

### 4.2.3. Copper Losses in wires

In high-power applications, the copper loss is a considerable part of the total power losses, which is created by a current path through a conductor. For a conductor, the DC resistance is calculated as (4.21).

$$R_{DC} = \frac{\rho \times l_{eff}}{A_{eff}} \quad (4.21)$$

where  $\rho$  is the specific resistance and it is  $1.68 \times 10^{-8} \Omega/\text{m}$  for copper,  $A_{eff}$  is the effective cross-section area of the conductor, and  $l_{eff}$  is the total effective length of the conductor.

However, owing to the frequency of the current path through a wire, adjacent magnetic fields of other wires, and the placements of each turn in a winding, additional losses are caused, which are called the skin effect and proximity effect.

The skin effect is the tendency of AC current to follow near the surface of a conductor and it leads to a decrease in the skin depth by increasing the frequency. As shown in Fig. 4-7, the skin depth  $\delta$  at the specific frequency can be obtained as (4.22).

$$\delta = \sqrt{\frac{100 \text{kHz}}{f}} \times 0.21 \text{mm} \quad (4.22)$$

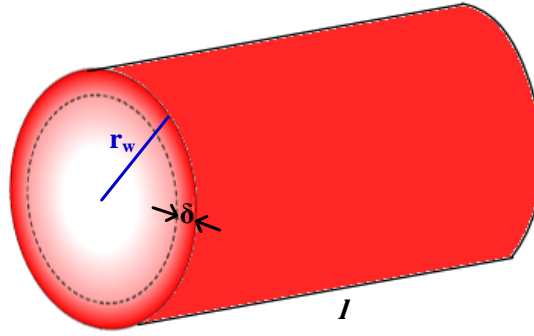


Fig. 4-7: Cross-section area of a circular wire and its skin depth

It leads to a reduction in the effective cross-section area of a wire as (4.23).

$$A_{eff} = \pi r_w^2 - \pi (r_w - \delta)^2 \quad (4.23)$$

where  $r_w$  is the radius of a wire.

Although this method can be used for skin effect consideration, this behavior is complicated. Furthermore, the proximity effect has another effect on copper loss. The Dowel equation [148] can model these effects via obtaining AC resistance  $R_{AC}$  instead of DC resistance  $R_{DC}$  as [140]:

$$R_{AC} = R_{DC} \times A \times \left[ \frac{\sinh 2A + \sin 2A}{\cosh 2A - \cos 2A} + \frac{2(N_l^2 - 1)}{3} \frac{\sinh A - \sin A}{\cosh A + \cos A} \right] \quad (4.24)$$

Where  $N_l$  is the number of layers and

$$A = \frac{\pi^{(3/4)} d}{4 \delta} \quad (4.25)$$

and  $d$  is the wire diameter.

Finally, the copper loss is calculated by multiplying the resistance by the RMS current to the square:

$$P_{copper} = R_{AC} \times I_{RMS}^2 \quad (4.26)$$

It should be mentioned that the skin effect can be dramatically reduced using Litz wires for conventional magnetic components or using planar transformers and inductors. The proximity effect can be also decreased via the sandwich formation of layers.

#### 4.2.4. Capacitor Losses

The equivalent series resistor (ESR) of a capacitor represents the power loss as:

$$P_{capacitor} = ESR \times I_{C, RMS}^2 \quad (4.27)$$

The ESR is typically mentioned in the capacitor datasheet at different frequencies. Furthermore, the following equation can be used for ESR estimation:

$$ESR = \frac{\tan \delta}{C \times \omega} \quad (4.28)$$

where  $\delta$  is the loss angle, which depends on the dielectric material and usually is mentioned in the datasheet.

It should be mentioned that multilayer ceramic capacitors (MLCCs) have high efficiency and low ESR, which offer low losses for resonant converters. In this dissertation, the MLCCs are used as the capacitors of the resonant tank.

#### 4.2.5. Inductor Design

Fig. 4-8 shows a typical EE-shape magnetic circuit with  $N$  turns, and air gap length  $g$ :

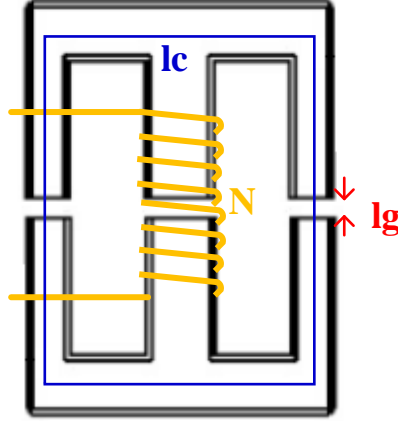


Fig. 4-8: Typical structure of a conventional EE core

The reluctance  $\mathfrak{R}$  (magnetic resistance) of a portion of the core is defined as:

$$\mathfrak{R}_c = \frac{l_c}{\mu_0 \times \mu_r \times A_c} \quad (4.29)$$

where  $l_c$  is the length of the core,  $A_c$  is the area of the core,  $\mu_0=4\pi \times 10^{-7}$  H/m is the permeability of free space, and  $\mu_r$  is the magnetic permeability of the magnetic material. The reluctance of an air gap can be obtained as:

$$\mathfrak{R}_g = \frac{g}{\mu_0 \times A_g} \quad (4.30)$$

where  $g$  is the length of the air gap, and  $A_g$  is the area of the air gap.

Basically, the reluctance of magnetic materials is much lower than the air gap reluctance and can be neglected. However, a general solution is considered in this dissertation.

The value of inductance can be calculated as:

$$L = \frac{N^2}{\mathfrak{R}_{total}} \quad (4.31)$$

where  $N$  is the number of turns, and  $\mathfrak{R}_{total}$  is the equivalent reluctance. The above equation establishes a relationship between the electrical parameter  $L$  and physical parameters  $N$  and  $\mathfrak{R}$ , which will be used in the optimization process.

However, the physical parameters are important to build the converter. To select the right core for the inductor, it is necessary to fit the number of turns in the selected core, and also to check the effect of the core saturation.

To do this, one core is selected from the existing database of cores. Then, according to the required inductance (obtained in optimization or based on the designer’s opinion), the required number of turns is calculated using (4.32).

$$N = \sqrt{L \times \mathfrak{R}_{total, L}} \tag{4.32}$$

where  $\mathfrak{R}_{total, L}$  is the equivalent reluctance of  $L$ .

Then, it needs to be checked if the core is saturated with this number of turns or not. To do this, the maximum number of turns to avoid saturation is calculated as (4.33).

$$N_{max, L} = \frac{l_e \times B_{max}}{\mu \times i_{L, max}} \tag{4.33}$$

where  $l_e$  is the effective length of the core,  $B_{max}$  is the maximum flux density, and  $i_{L, max}$  is the maximum current of the inductor.

Now, if the selected number of turns as (4.32) is less than the maximum number of turns as (4.33), the selected core will be suitable, otherwise, a larger core should be selected. Finally, the feasibility of the turns to fit in the core window must be checked. Fig. 4-9 shows the core selection steps for an inductor:

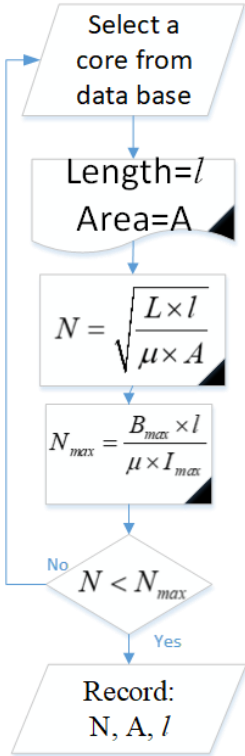


Fig. 4-9: The flowchart for core selection

Consequently, the required number of turns, cross-section, and effective length of the core will be calculated. Also, according to the selected core, the volume of the core can be calculated, which will be required for the optimization process with the power density objective function.

#### 4.2.6. Transformer Design

A transformer is usually designed at the minimum switching frequency to have the minimum losses. On the other hand, the size of a transformer is decreased by increasing the switching frequency. Hence, there is a trade-off for switching frequency selection. In EV charger applications, the switching frequency usually changes to regulate the output voltage. Therefore, it is suitable that the range of switching frequencies should not be wide. The transformer turn ratio can help to reduce this range. For the CLLC resonant converter as an example, operating near the resonant frequency leads to the maximum output voltage. Therefore, the transformer turn ratio can be calculated as (4.34) to meet all the voltage ranges:

$$n = \frac{V_{out,max}}{V_{in} \times M_{max}} \quad (4.34)$$

In our design,  $V_{out,max} = 400V$ ,  $V_{in} = 400V$ , and  $M_{max} = 1$ , which leads  $n = 1$ . A unity turn ratio also leads to a symmetrical transformer.

Now, other aspects of the transformer design are examined. According to Eq. (1.1) for the ZVS condition, the minimum required dead-time is based on the initial current of the primary side inductor, input DC voltage, and the capacitor parallel to the GaN transistors. It should be noted that during the dead time, no power will be applied to the resonant tank (and also load). But in general, the magnetizing inductor has also a great effect on the minimum dead-time [44]. To examine this effect, it can be said that the minimum dead-time is directly (but not linearly) related to the amount of the magnetizing inductor. In other words, by increasing the value of  $L_m$ , the minimum dead time value increases, as shown in Fig. 4-10. But this will lead to an increase in the circulating current and conduction losses because  $L_m$  is located in parallel. As shown in Fig. 4-11,  $L_m$  varies from  $100\mu H$  to  $180\mu H$ .



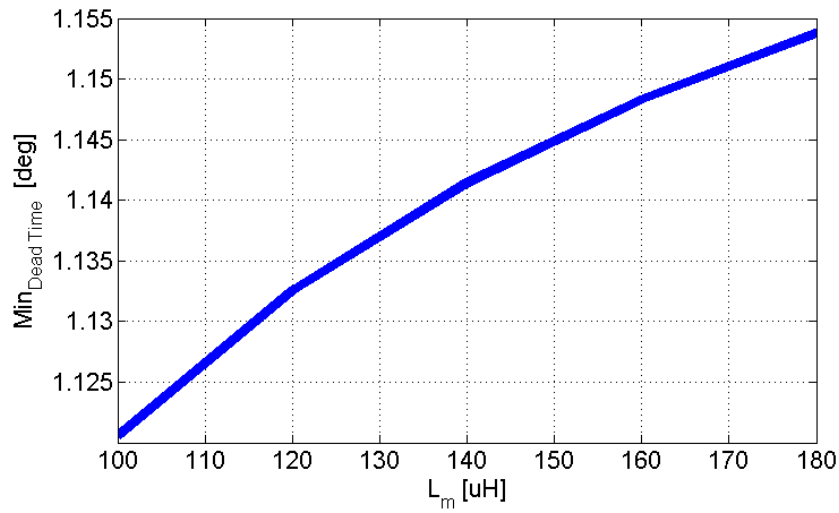


Fig. 4-10: Minimum dead-time versus the magnetizing inductance

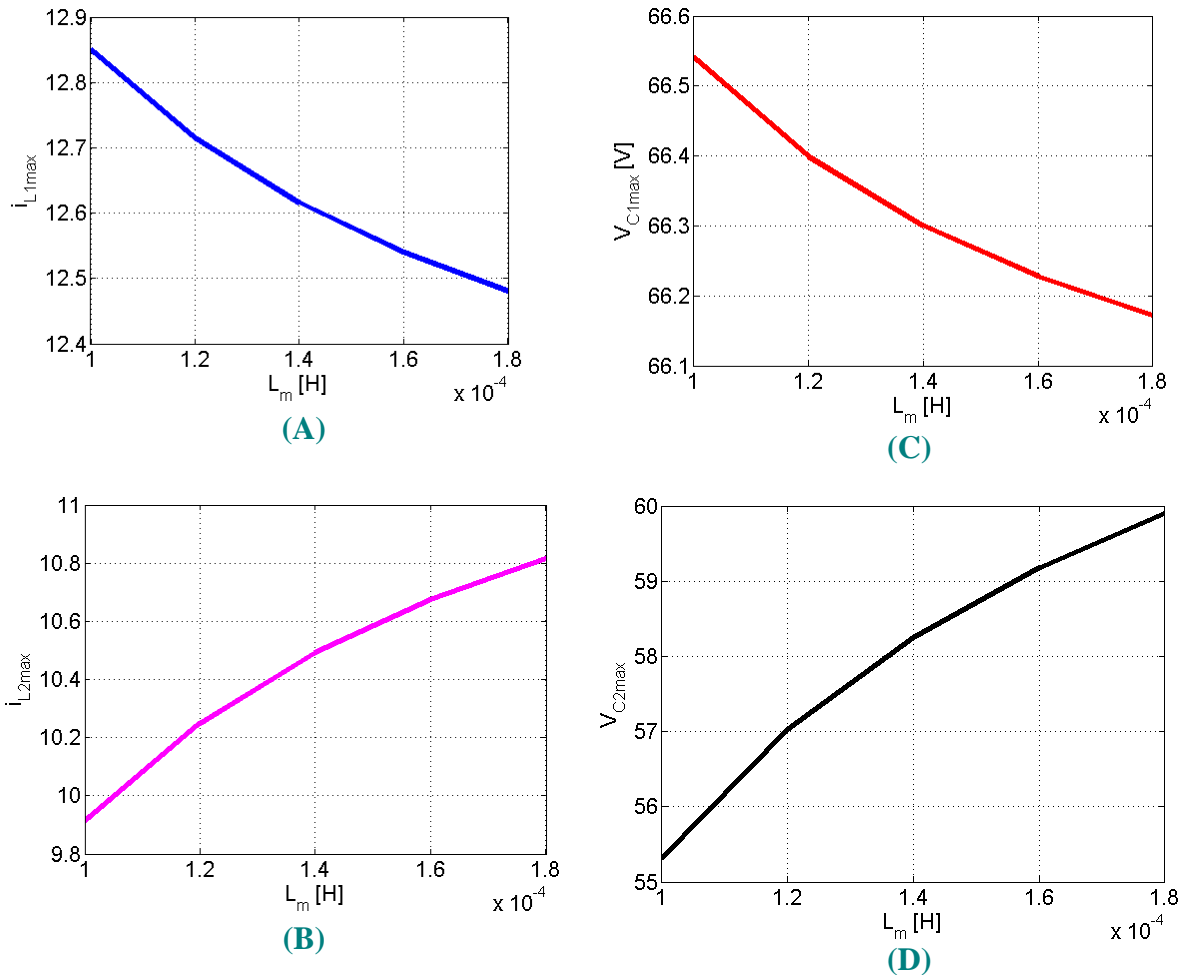


Fig. 4-11: Effect of magnetizing inductance on (A) maximum current of the primary side; (B) maximum current of the secondary side; (C) maximum voltage of C1; (D) maximum voltage of C2.

As shown in the above figure, by increasing  $L_m$ , the maximum current of the primary side ( $i_{L1, max}$ ) decreases and the maximum current of the secondary side ( $i_{L2, max}$ ) increases. Similarly, the maximum voltage of the primary side capacitor ( $v_{C1, max}$ ) decreases and the maximum voltage of the secondary side capacitor ( $v_{C2, max}$ ) increases.

Also, to investigate the effect  $L_m$  on the output characteristic (i.e. the normalized output current,  $J$ , versus normalized output voltage,  $M$ ), Fig. 4-12 can be analyzed:

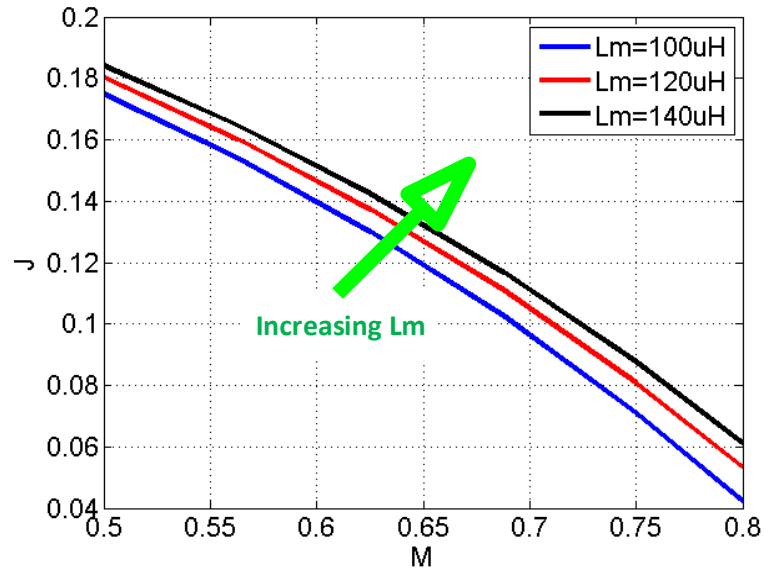


Fig. 4-12: Effect of magnetizing inductance on the  $J$ - $M$  curve

whereby increasing  $L_m$ , the output characteristic curves step up, and more current can be obtained at the same voltage. However, this increasing leads to the CLLC resonant converter operates as like as a series resonant converter, and losing its advantages. Therefore, a trade-off exists for  $L_m$  calculation.

These investigations show that the transformer has a direct effect on the converter behaviors. Therefore, the following criteria are considered in the optimization process and discussed as follows.

#### Core Selection

To choose the right core for the transformer, the following criteria should be met:

- The number of turns for the primary side and secondary side must be fitted in the core window;
- The required transformer turn ratio must be prepared;
- The transformer must not work in saturation region for each operating point;

- The core material should be selected based on the maximum frequency.

To do this, a database is created from existing cores and one of them is selected. In this dissertation, ferrite cores with 3C90 or 3F3 will be used based on the maximum frequency.

### *Number of Turns*

According to the above 4 criteria, the number of turns of the windings is calculated. E-type cores are selected with the dimensions shown in Fig. 4-2. For obtaining the number of turns, one of the above cores is selected. Based on the selected core and required magnetizing inductance, the number of turns for the primary winding is calculated as (4.35).

$$N_1 = \sqrt{L_m \times \mathfrak{R}_T} \quad (4.35)$$

where  $N_1$  is the number of turns for the primary side and  $\mathfrak{R}_T$  is the reluctance (magnetic resistance) of the transformer core. It is assumed that  $L_m$  is located on the primary side and therefore,  $N_1$  was obtained.

Then, core saturation should be checked. The maximum allowable turns for operating in the linear region are:

$$N_{\max} = \frac{l_e \times B_{\max}}{\mu \times i_{1,\max}} \quad (4.36)$$

where  $l_e$  is the effective length of the core,  $B_{\max}$  is the maximum flux density, and  $i_{1,\max}$  is the maximum current of the primary side.

Therefore, the number of turns calculated in (4.35) should be less than the number of turns in (4.36). After passing this step, the number of secondary side turns is calculated using the transformer conversion ratio as (4.37).

$$N_2 = \frac{N_1}{n} \quad (4.37)$$

If necessary, the saturation condition for secondary winding can be also checked.

Finally, it must be calculated whether the number of turns is fitted to the desired core window or not. If this is not possible, a larger core should be selected, and this process continues to meet all the constraints.

#### 4.2.7. Selection of Resonant Capacitor

Power electronics circuit designers can select the resonant frequency,  $f_{res}$ , based on their knowledge, the design requirements, or independently through the optimization algorithm. The value of the resonant capacitor,  $C$ , is obtained as (4.38).

$$C = \frac{1}{4\pi^2 \times f_{res}^2 \times L} \quad (4.38)$$

It should be mentioned that for CLLC resonant converter, the aforementioned resonant frequency ( $f_{res}$ ) is the resonant frequency of series  $L$  and  $C$  without the magnetizing inductance  $L_m$ .

#### 4.2.8. Objective Functions Evaluation

Conventional EV chargers have been facing the challenge of efficiency increment. Using special magnetic cores like planar cores, and high technology switching components like GaN transistors, the existing EV onboard chargers are transferring into a high-efficiency and high power density converter, the so-called optimum onboard charger. The objective function of the optimization process can be examined in different aspects:

- **Size:** the optimal size of an onboard charger is to decrease the volume and/or weight of the charger to determine a suitable battery capacity in the limited space. Therefore, a small-in-size charger is preferable.
- **Efficiency:** the efficiency of the charger should remain high at different operating points. Therefore, a high-in-efficiency charger is preferred.
- **Losses:** power loss in magnetic components and switching components can increase the temperature of the components which reduces the lifespan of the converter and leads to failure. Therefore, a small-in-losses charger is preferable. On the other hand, increasing losses will decrease efficiency. However, low losses have the same meaning as high efficiency and therefore will not be considered in this dissertation as the objective function.
- **Power Density:** for a power electronics converter, possessing high output power in a low volume is increased the power density. The high power density was obtained by reducing the size of the passive components in [149], and minimizing losses and volume in [18], whereas it was achieved by minimizing the output power divided by

volume in [150], and minimizing the output power divided by mass in [151]. It means the power density is not fairly independent of the size, efficiency, and losses.

- **Cost:** a low-cost product can make it a leader in the competitive market. So, a small-in-cost charger is preferred. However, it is beyond the scope of this dissertation.
- **Reliability:** EV's driver dissatisfaction is expressed with charger failure. Proper component selection and derating, good printed circuit board (PCB) designing with minimum inter-connections, decreasing operating temperature, etc. can increase the reliability of an onboard charger. However, reliability is also beyond the scope of this dissertation.

So, in this thesis, the size and efficiency of the charger are simultaneously selected as the objective function, which should be minimized and maximized, respectively. Therefore, the objective function can be computed as:

$$\text{Objective function} = \max\left\{\frac{\text{Efficiency}}{\text{Size}}\right\} \text{ or } \min\left\{\frac{\text{Size}}{\text{Efficiency}}\right\} \quad (4.39)$$

where *Size* can be either weight or volume, and efficiency is the efficiency of the selected point or the average efficiency of all operating points. We select a weight for the objective function, and volume will be considered as a constraint. Therefore, the objective function is to maximize the new version of power density as (4.40).

$$\text{Objective function} = \max\left\{\frac{\text{Efficiency}}{\text{Size}}\right\} \quad (4.40)$$

#### 4.2.9. Constraints Discussion

The solution and input variables must satisfy some conditions called constraints:

$$\begin{aligned} & \text{Maximize } f(x) \quad , x = [x_1, x_2, \dots, x_n]^T \\ & \text{Subject to } g(x) = A \\ & \quad \quad \quad h(x) \leq B \end{aligned} \quad (4.41)$$

where  $g(x)$  is the equality constraints,  $h(x)$  is the inequality constraints,  $n$  is the number of input variables, and  $A$  and  $B$  are circuit-based vectors. For onboard charger applications, the following constraints must be considered in the optimization process:

### Operating Region

Owing to the battery charging process, the voltage of the battery varies between  $V_{MIN}$  at the start of CC mode to  $V_{MAX}$  at the end of CV mode. Therefore, there exists the following constraint for the output voltage:

$$V_{MIN} \leq V_{OUT} \leq V_{MAX} \quad (4.42)$$

where we select  $V_{MIN}=250V$  and  $V_{MAX}=400V$ . This voltage constraint is shown in Fig. 4-13(a).

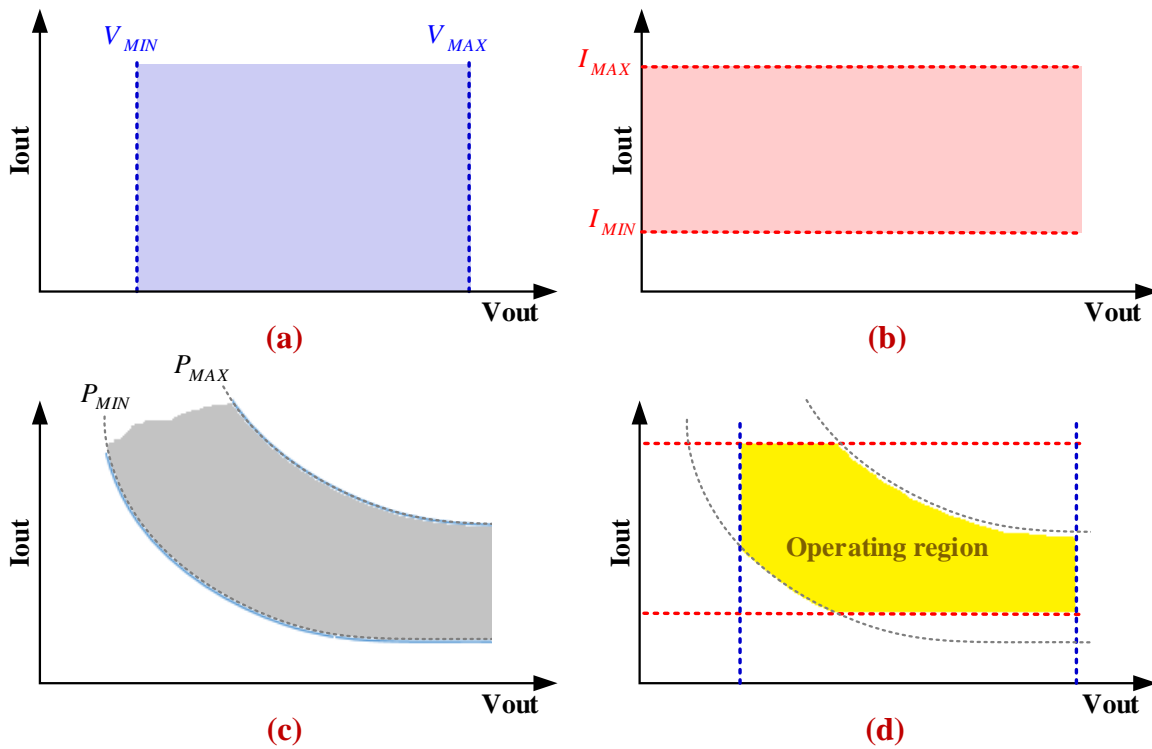


Fig. 4-13: Effect of different constraints on J-M curve: (a) voltage; (b) current; (c) power; (d) the complete operating region

Another constraint exists for the current, while it changes from  $I_{MAX}$  at the start of CC mode to  $I_{MIN}$  at the end of CV mode:

$$I_{MIN} \leq I_{OUT} \leq I_{MAX} \quad (4.43)$$

where we select  $I_{MIN}=1A$  and  $I_{MAX}=12A$ . This current constraint is shown in Fig. 4-13 (b).

The operating region of an onboard charger is also limited by the charger power rating. It is assumed that the charger is designed to prepare a power between  $P_{MIN}$  to  $P_{MAX}$  as shown in Fig. 4-13 (c).

$$P_{MIN} \leq P_{OUT} \leq P_{MAX} \quad (4.44)$$

Consequently, the complete operating region of an onboard charger can be shown in Fig. 4-13 (d) by superimposing all the constraints.

### Maximum Temperature

Ambient temperature affects the operating temperature of components. Based on their datasheet, hardware requirements, and reliability reasons, the maximum temperature must not be exceeded. In the following, the temperature constraints of the components are examined.

#### 1- Semiconductors:

The junction temperature ( $T_j$ ) of semiconductors must be limited to a specific value entitled maximum junction temperature,  $T_{jMAX}$ , which is typically 150°C. It should be mentioned that this value is the upper margin of the junction temperature and approaching this value will exponentially decrease the lifespan.

As shown in Fig. 4-14, for a semiconductor device, the junction temperature ( $T_j$ ) can be obtained as (4.45).

$$T_j = T_A + R_{JA} \times P_{Loss} \quad (4.45)$$

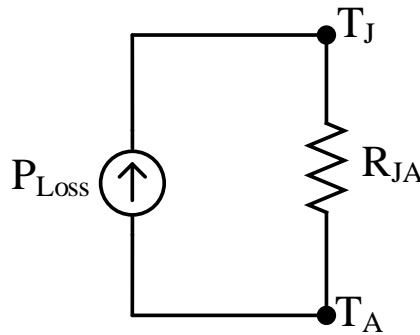


Fig. 4-14: Thermal modeling of a semiconductor

where  $T_A$  is the ambient temperature,  $R_{JA}$  is the junction-to-ambient thermal resistance, and  $P_{Loss}$  is the total power dissipation of the semiconductor, which is obtained for GaN transistors and diodes in (4.9) and (4.14), respectively. The typical thermal resistance of some semiconductor devices is listed in Table 4-7.

Table 4-7: Thermal resistance of some semiconductors

Component	Type	$R_{th}$ [ $^{\circ}C/W$ ]
GS66508B	GaN transistor	0.5 to 24
TP65H035G4WS	GaN transistor	0.8 to 40
C3M0015065K	SiC transistor	0.35 to 40
APT60N60BCSG	COOLMOS	0.29 to 62
IRF840	N-channel Mosfet	1 to 62.5
C4D10120E	SiC diode	0.9
1N5819	Schottky diode	88

where the thermal resistance changes based on the selected PCB trace width, heatsinks, and cooling systems.

According to (4.45), it is concluded that the junction temperature can be decreased by decreasing  $P_{Loss}$  and/or  $R_{JA}$ .  $P_{Loss}$  reduces by decreasing the switching frequency, changing the circuit parameters, and operating at different points. Also,  $R_{JA}$  can be decreased by adding a heatsink or fan. In this dissertation, it is assumed that  $R_{JA}$  is fixed and only  $P_{Loss}$  is optimized in the optimization process. The temperature constraint for semiconductors is defined as (4.46).

$$T_j < 85^{\circ}C \quad (4.46)$$

where  $T_j$  is the junction temperature.

## 2- Magnetic components:

The core loss and copper loss generate heat, which leads to either changing the magnetic behavior of the core or damage to the wire insulation and causes a short circuit. Therefore, it is necessary to impose a constraint on the temperature of magnetic components. Eq. (4.45) can be also used for the calculation of the hotspot in a magnetic core. However, it is hard to model the thermal resistance of a magnetic core. Also, using approximate methods lead to low accuracy. Hence, finite element methods (FEMs) have been developed to determine temperature, which is beyond the scope of this thesis.

On the other hand, the Curie temperature of common magnetic materials such as 3C90 and 3F4 is higher than  $200^{\circ}C$  [152](see Fig. 4-15), which is too high. It should be mentioned that the full thermal modeling of the transformer is difficult to implement and also it is beyond the scope of this dissertation. Therefore, we replace it with a rule of thumb constraints, i.e. checking the saturation condition for a transformer to avoid approaching the Curie temperature.



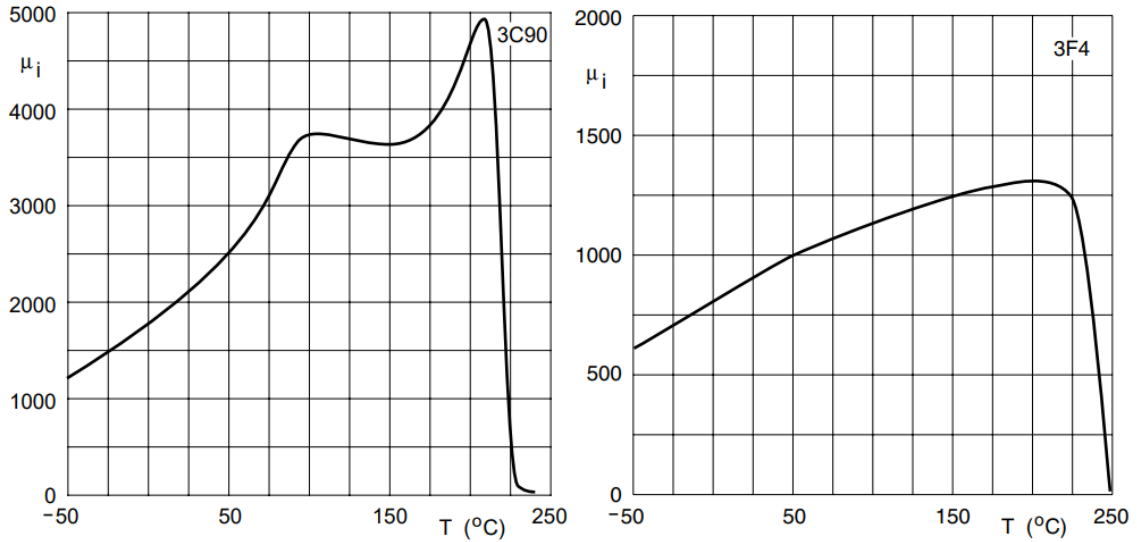


Fig. 4-15: Effect of temperature on different materials 3C90 (left circuit) [152], and 3F4 (right circuit) [153].

### 3- Wires:

Copper loss sources are the windings of magnetic components, and PCB tracks. In [154], there exists an empirical curve for PCB tracks to obtain the trace width based on the desired temperature rise. However, for a pre-selected trace, temperature calculation can be done like a conductor resistance. For the windings, this condition is the same. Therefore, the power loss and temperature of a conductor are calculated.

A conductor with the cross-sectional area  $A$  and the length  $l$  is presumed (see Fig. 4-7). The DC resistance of this conductor was calculated in (4.24). However, due to the frequency of the current passing through the copper and also the position of the transformer layers relative to each other, two effects can change the amount of DC resistance, skin effect and proximity effect, which were examined in part 4.5.4.

Eq. (4.23) showed that the effective area is decreased, which leads to an increase in the resistance. The core temperature of a resistor can be obtained according to the following conventional equation as (4.47).

$$T_J = T_A + R_{th,JA} \times P_{Loss} \quad (4.47)$$

Where  $P_{Loss}$  is the power loss obtained in (4.26), and  $R_{th,JA}$  is the core-to-ambient thermal resistance, which is affected by the width of wires, choice of material, soldering pattern, insulation, terminations, and cooling system [155].

Therefore, this power loss increases the temperature of the resistor. It is a well-known fact that the conductor resistance varies linearly with the temperature as shown in (4.48).

$$R(T) = R_0 \left( 1 + \alpha (T - T_{ref}) \right) \quad (4.48)$$

where  $R(T)$  is the conductor resistance at the required temperature  $T$ ,  $R_0$  is the conductor resistance at the reference temperature ( $T_{ref}$ ), usually 20°C, and  $\alpha$  is the temperature coefficient for the conductor material, which is equal 0.004041 °C<sup>-1</sup> for copper.

In this dissertation, the following constraint is considered for wires:

$$J \leq 5 \frac{A}{mm^2} \quad (4.49)$$

where  $J$  is the current density of a wire.

#### *Maximum RMS Current for resonant capacitors and inductors*

The absolute maximum rating current of capacitors must not exceed the specified value in their datasheet. With rising the current, the capacitor temperature may exceed the allowable hot spot temperature. It causes damage to the dielectric material and reduces the capacitor lifespan. Therefore, it is necessary to ensure the following constraint [156]:

$$I_{C,RMS} \leq I_{C,RMS,MAX} \quad (4.50)$$

The multilayer ceramic capacitors (MLCCs) are selected in this dissertation owing to their low equivalent series resistance (ESR), low cost, high frequency, low size, and high reliability. TDK capacitors are chosen for the resonant capacitors that the following constraint can be considered for the maximum RMS current based on their datasheets:

$$I_{C,RMS} \leq 20 \text{ A} \quad (4.51)$$

For inductors, the maximum allowable current density for a wire can be considered equal to  $J=5 \text{ A/mm}^2$ . Therefore, based on the RMS current of an inductor, the minimum diameter of the wire should be:

$$J = 5 \frac{A}{mm^2} \geq \frac{I_{L,RMS}}{\pi d^2/4} \longrightarrow d \geq \sqrt{\frac{4I_{L,RMS}}{5\pi}} \text{ mm} \quad (4.52)$$

where  $d$  is the wire diameter.

### Maximum Voltage

Applying a voltage beyond the breakdown voltage causes failure and usually, the capacitor becomes a short circuit. TDK MLCCs have a rated voltage from 4V up to 3kV. Owing to the voltage rating of the onboard chargers, a capacitor with a 1000V voltage rating is acceptable. Therefore, the following constraint is considered for the capacitor voltage rating.

$$V_{C,MAX} \leq 1000V \quad (4.53)$$

As an example, CGA6 capacitors from TDK® have a breakdown voltage of 1kV and also AEC-Q 200 standard feature. Fig. 4-16 shows the DC bias characteristic of 8.2nF  $\pm 5\%$  CGA6N1C0G3A822J230AE capacitor:

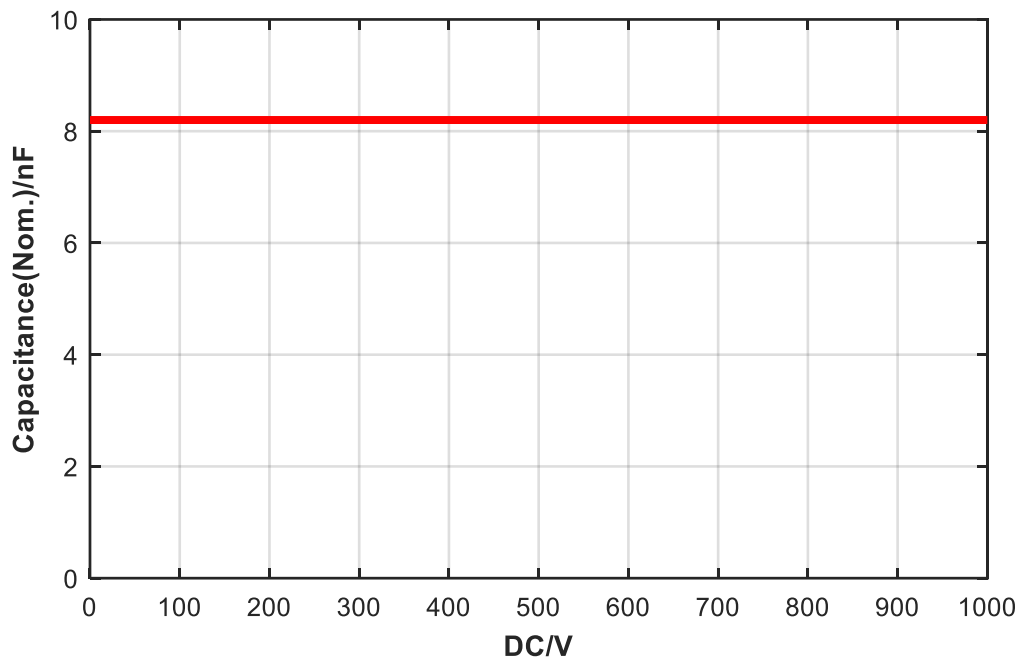


Fig. 4-16: The DC bias characteristic of the CGA6N1C0G3A822J230AE capacitor

\* Source: [product.tdk.com](http://product.tdk.com)

### ZVS Condition

Zero voltage switching (ZVS) condition enables the power electronics converters to operate in low loss, fast switching, high efficiency, and high power density EV applications [157]. For accomplishing ZVS operation for the main power switches e.g.  $S_2$  and  $S_3$ , the energy stored in the transformer leakage inductance  $L_l$  must discharge the parallel capacitors  $C_{s2}$  and  $C_{s3}$  until the switch  $S_2$  turns OFF. Therefore, the following inequality must be satisfied for achieving the ZVS condition [43]:

$$Lm \leq \frac{t_{dead\ time}}{16 \times C_{OSS} \times f_{SW,MAX}} \quad (4.54)$$

The above constraint can be used as the ZVS operating condition based on the FHA method. However, the exact relationship of the ZVS condition for the CLLC resonant converter was presented in [53] and we use the equations as mentioned in **Chapter 5**.

### *CCM Condition*

Although there are some disadvantages to CCM operating such as turn-off switching loss, proper design of this converter can improve this loss. However, DCM has more disadvantages. For example, a bulky capacitor is needed for the DC link capacitors, DCM has a higher peak current for switches and other components in comparison with CCM, higher conduction losses, etc. Operating in CCM condition is superior in high current applications. Therefore, in this dissertation, the continuous conduction mode (CCM) is considered as a constraint. This constraint can be met if the voltage of the section before the rectifying part (i.e.  $v'_2$ ) is higher than the section after the rectifying part (i.e.  $V_{out}$ ) when the diode current has a zero crossing. Therefore, (4.55) is considered as the CCM operating:

$$CCM\ condition: \quad V'_2 > V_{OUT} \quad (4.55)$$

## **4.3. Requirements of EV chargers**

There are some requirements for EV battery chargers, which are mandatory to meet. These requirements can be classified into 4 considerations: electrical requirements, placement requirements, environmental requirements, and safety requirements. In this dissertation, electrical requirements will be discussed in detail, and a review of the other requirements will be presented briefly.

### *4.3.1. Electrical Requirements*

The electrical requirements of a household EV charger can be selected as follows [10]:

- Input AC voltage range: 85-265 V
- Output DC voltage range: 170-440 V
- Maximum input RMS current: 16 A
- Maximum output DC current: 12 A
- Maximum output power: 3.3kW
- Power factor:  $\geq 0.98$
- Efficiency:  $>94\%$  (for DC to DC converter)

In this dissertation, only the DC to DC part of the charger is analyzed. It means commonly there exists a power factor correction (PFC) converter on the grid side which rectifies the AC voltage of the grid to a DC voltage level while correcting the power factor. Also, as shown in Fig. 4-17, there is also a DC link capacitor to stabilize the DC link voltage. However, these parts are neglected in our analysis.

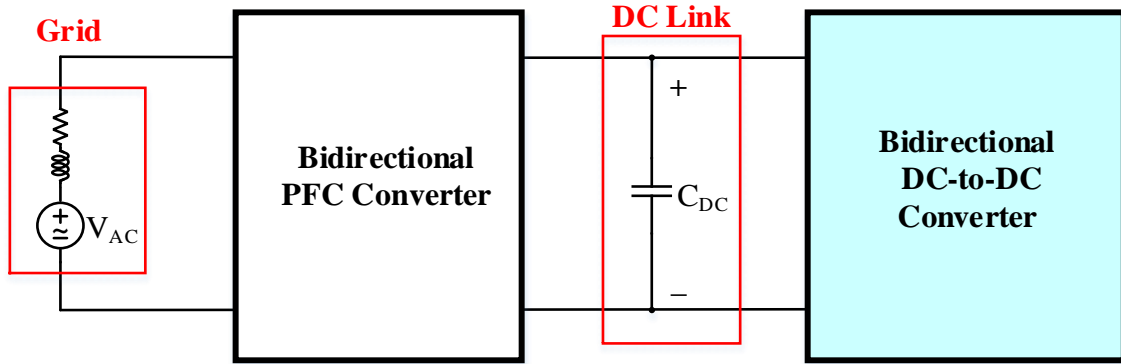


Fig. 4-17: Complete structure of an on-board charger.

Furthermore, there is a boost converter to increase the DC voltage to a fixed value of 400V and also play the role of power factor correction (PFC). Therefore, we have a constant voltage of 400V in the input part of the DC-to-DC converter and any variation of AC input voltage does not affect on our analysis. So, the electrical requirements can be rearranged as:

- Input DC voltage: 400V
- Output DC voltage range: 170-440 V
- Maximum input current: 16 A
- Maximum output current: 12 A
- Maximum output power: 3.3kW
- Efficiency: >94% (for DC to DC converter)

It should be mentioned that the aforementioned requirements are related to the basic electrical characteristics of a charger.

#### 4.3.2. Placement Requirements

Due to the fact that the on-board charger is located inside the EV, the size and weight of the charger shall be selected based on the defined place in the EV. Furthermore, the selected socket outlet and the associated plug shall comply with IEC 60309. GEN2.5 is a 3.3kW battery charger provided by Valeo and Siemens Companies that has a weight of 3.5 kg and a size of 31cm × 19.4cm × 6.9cm. For this on-board charger, the power density is 0.98kW/kg or 1.1 kW/dm<sup>3</sup> [158] . Furthermore, CAD332DF-400A is a 3.3kW EV on-board charger from OVARTECH

Company that its weight is 8.4kg and its dimension is 30.5cm × 12.5cm × 17cm [159]. However, the placement checking of an on-board charger is beyond the scope of this dissertation.

#### 4.3.3. Environmental Requirements

Temperature, humidity, dust, and vibration are the most important parts of the environmental requirements for the components and the charger. However, in this dissertation, only temperature-based requirement is considered:

- -40°C to 105°C ambient temperature;
- The junction temperature of transistors: based on their datasheets (usually 110°C);
- Magnetic cores temperature: based on the core material (usually 110°C);
- PCB track temperature: based on the allowable over-temperature related to the ambient temperature (usually 10~20°C);
- Temperature criteria of other components: based on their datasheet, and standards e.g.: AEC-Q100 for integrated circuits (ICs), AEC-Q101 for discrete semiconductor components, and AEC-Q200 for passive components.

In this dissertation, only the DC-to-DC converter is analyzed. Therefore, the temperature of all components is considered and the effect of ambient temperature on the components is neglected.

#### 4.3.4. Safety Requirements

High voltage transition rate ( $dv/dt$ ), high power transfer, and high switching frequency can increase the electromagnetic interference (EMI) of a power electronics converter, where the converter can emit noise to the environment or absorb noise from it. For this reason, some standards are authorized for electromagnetic compatibility (EMC) such as CISPR 25 [160]. In this dissertation, it is supposed to there exists an EMI filter and well-designing for PCB tracks to reduce common mode and differential mode noises. Therefore, noise considerations are neglected. Other safety standards can be considered as:

- IEC 61851-21: Conductive charging system of an EV charger;
- ISO 6469: Safety specifications of electric road vehicles;
- UL 2202: EV charging system equipment;
- ECE R100: Electric shock;
- etc.

It should be mentioned that the aforementioned standards are for safety. However, in this dissertation, only the DC-to-DC converter is analyzed. Therefore, safety considerations are also ignored.

#### 4.4. Simulation Verification of Switching and Conduction Losses model

In order to verify the proposed model, some GaN transistors are selected as case studies. The characteristics of these transistors are listed in Table 4-8.

Table 4-8: Specifications of the GaN transistors

GaN Device	Ciss [pF]	Coss [pF]	Crss [pF]	Rg [Ω]	Lg [nH]	LD [nH]	LS [nH]
GS66502	65	17	0.5	2.3	0.7	170	215
GS66506	195	49	1.5	1.1	2.27	124	73
GS66508	242	65	1.5	1.13	1	200	1200
GS66516	520	130	4	0.34	3.1	370	150
IGOT60R070	380	72	0.3	0.78	5	1500	1300
IGT60R19	157	28	0.15	0.27	4.3	1300	800
TP65H150LS	576	36	2	U	U	U	U
TP65H300G	1500	147	5	U	U	U	U
GPI8HINOIC	760	16	2	U	U	U	U
PGA26E07B	405	71	0.4	0.6	U	U	U
EPC2105C	980	710	18	0.3	U	U	U

For all parameters undefined in Table 4-8 (“U”), the used values in Table 4-4 for the reference case have been considered.

##### 4.4.1. Verifying the Switching Power Loss Model

Table 4-9 shows the results obtained from the proposed model and LTSPICE simulations, where some scenarios have been considered to verify its precision for a variety of GaN transistors:

Table 4-9: Scenarios for the Accuracy Verification of Proposed Method for the Switching Losses Calculation

Other para. are according to the selected GaN and base values	Scenario 1: $V_{DS}=50V, I_{DS}=7A, T_j=60^\circ C$			Scenario 2 $V_{DS}=300V, I_{DS}=13A, T_j=90^\circ C,$			Scenario 3 $V_{DS}=400V, I_{DS}=25A, T_j=70^\circ C,$ $R_{gON}=12, R_{gOFF}=5$			Scenario 4 $V_{DS}=400V, I_{DS}=10A, T_j=110^\circ C, L_g=3n, L_p=4n$		
	Mod.	Sim.	Err.	Mod.	Sim.	Err.	Mod.	Sim.	Err.	Mod.	Sim.	Err.
GS66502	1.87	1.69	-10.49	X	X	X	X	X	X	X	X	X
GS66506	2.11	2.01	-5.08	40.20	37.50	-7.19	X	X	X	50.46	44.27	-13.98
GS66508	2.21	2.33	5.29	40.70	41.88	2.81	114.42	118.98	3.84	51.45	51.02	0.83
GS66516	3.22	3.45	6.79	60.32	65.64	8.09	157.68	145.70	-8.22	75.73	82.36	8.06
IGOT60R070	2.26	2.70	16.34	68.89	78.05	11.73	117.11	126.52	7.44	55.08	56.09	1.81
IGT60R19	2.61	2.73	4.45	36.06	38.15	5.48	103.34	106.59	3.05	48.60	47.16	-3.06
TP65H150LS	1.99	2.53	21.27	52.30	44.35	-17.93	135.21	138.81	2.59	63.59	56.69	-12.17
GPI8HINOIC	3.38	2.77	-21.92	62.34	49.26	-26.56	175.00	151.73	-15.34	82.31	59.68	-37.91
PGA26E07B	2.29	2.71	15.63	42.23	43.89	3.77	118.55	125.54	5.57	55.75	56.38	1.11
EPC2015C	1.88	1.78	-5.72	X	X	X	X	X	X	X	X	X

X: Device cannot be used at this operating point

For these scenarios, the electrical operating points ( $V_{DS}$ ,  $I_D$ ), thermal operating point ( $T_j$ ), circuit operating points ( $R_{gate}$ ,  $L_{gate}$ ,  $L_p$ ), and device characteristics (different GaN transistors) are changed to evaluate the accuracy of the proposed model. Errors can be calculated as:

$$Error = \frac{Simulation\ Result - Modeling\ Result}{Simulation\ Result} \times 100 \quad (4.56)$$

As shown in Table 4-9, there is a significant positive correlation between the results obtained from the proposed model and LTSPICE simulations for some scenarios. The error reaches as high as 37% for the GPI8HINOIC transistor and it is lower than 10% for most of the cases, which means this error can be considered as an acceptable value for the switching losses owing to its non-linear behavior. It should be mentioned that some parameters for GaN devices are unknown (see Table 4-8), which leads to inaccuracies in the model. Also, the impact of the transconductance on the switching losses and interpolation has not been considered in this work. Adding this parameter should help in improving the model's accuracy.

A closer inspection of Table 4-9 shows that the GS66508B transistor has lower switching losses error than the others, due to the base values, the proposed model has been selected based on this transistor. Consequently, we can achieve higher accuracy by using different transistors as the base value parameters, if needed.

#### 4.4.2. Verifying the Conduction Power Loss Model

In this part, the conduction losses evaluation and temperature dependency of ON state resistors are presented. GaN transistors listed in Table 4-6 are considered and the simulations are carried out at the junction temperature equal to 70°C. The results for each transistor are shown in Table 4-10.

*Table 4-10: ON Resistance Comparison with the Proposed Model and LTSPICE Simulation*

<b>GaN Devices</b>	<b>Model (mΩ)</b>	<b>Simulation (mΩ)</b>	<b>Error (%)</b>
GS66502	313.76	292.08	-7.42
GS66506	105.88	99.04	-6.91
GS66508	78.44	79.45	1.27
GS66516	39.40	37.48	-5.12
IGOT60R070	71.20	76.14	6.49
IGT60R19	183.20	192.03	4.60
TP65H150LS	206.52	195.96	-5.39
TP65H035G4	48.32	46.31	-4.34
TP65H300G	330.72	310.86	-6.39
PGA26E07B	75.44	71.13	-6.06
EPC2015C	4.05	4.03	-0.62



It can be observed that the proposed method has sufficient accuracy and errors are lower than 8%. So, the most obvious finding to emerge from this analysis is that the conduction losses can be modeled by interpolated algebraic equations with high precision.

### 4.5. Maxwell Verifications of the Magnetic Design

Suppose that there exists an E64 transformer core with 8 turns for the primary and 8 turns for the secondary sides. For the simle implementation in Maxwell, a planar technology is adopted with an 8-layer PCB with FR4 and 2 turns in each layer as shown in Fig. 4-18:

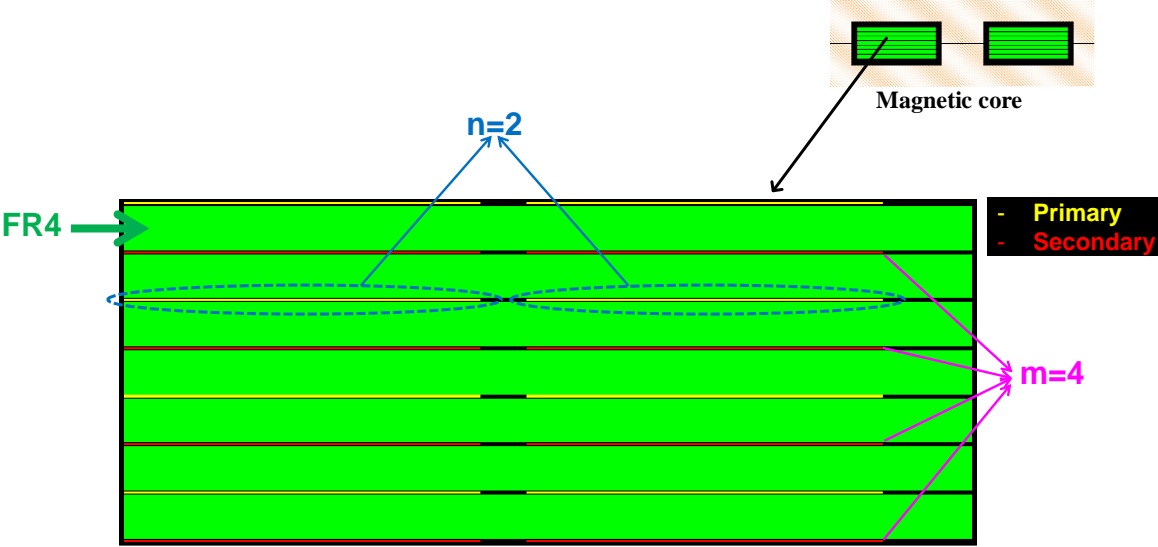


Fig. 4-18: 2-D Maxwell implementation of a transformer with 8 turns

With electrical analysis in Maxwell, the leakage inductance is obtained at about 160nH, and therefore an extra inductor for each side as the leakage inductance is needed. Fig. 4-19 illustrates the leakage inductance by changing the frequency.

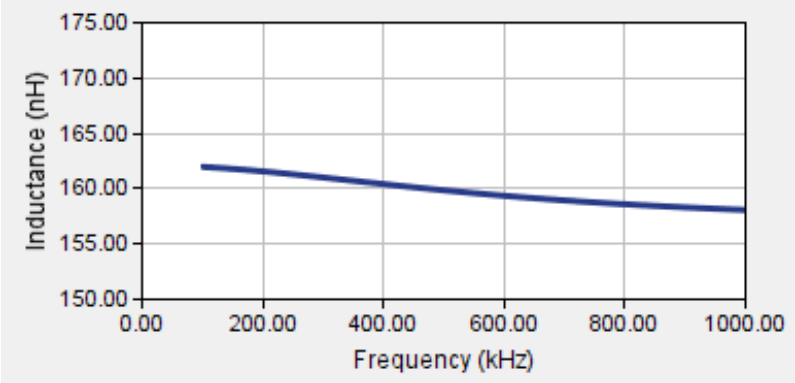


Fig. 4-19: Maxwell simulation result for leakage inductance measuring

Furthermore, the magnetizing inductance based on the *CADES* analysis is calculated as  $86.76\mu\text{H}$ . This value is obtained as  $84.3827\mu\text{H}$  using the Maxwell, which is shown in Fig. 4-20. As a result, the calculated magnetizing inductance using *CADES* and simulated result using Maxwell are approximately equal to each other and it verifies the accuracy of the implemented code.

<i>Winding</i>	<i>DC Resistance (mOhm)</i>	<i>Magnetizing Inductance (uH)</i>
<i>Winding A</i>	70.2325	84.3827
<i>Winding B</i>	70.2325	84.369

*Fig. 4-20: Maxwell simulation results of magnetizing inductance*

The above result also shows that the magnetizing inductance from the primary side (i.e.  $84.3827\mu\text{H}$ ) is equal to the magnetizing inductance from the secondary side (i.e.  $84.369\mu\text{H}$ ) and it proves the symmetrical structure of the implemented transformer. Also, the DC resistance is about  $70\text{m}\Omega$ , which leads to low voltage dropout for each side. The 3-D diagram of the device-under-test is illustrated in Fig. 4-21:

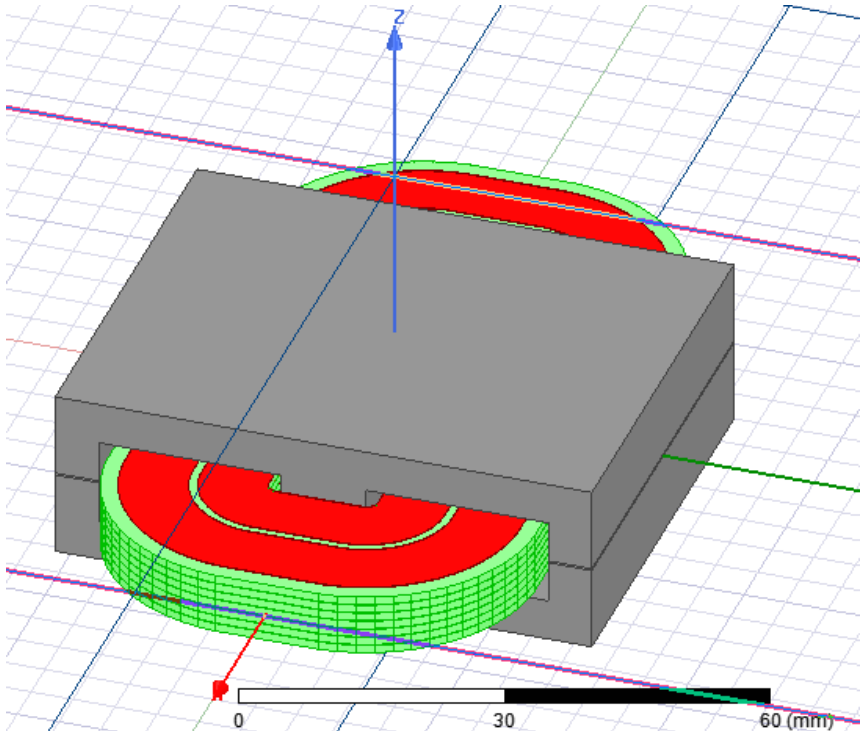


*Fig. 4-21: 3-D Maxwell implementation of the planar transformer with 8 turns*

The flux density of this magnetic core can be obtained using a simulation on Maxwell as shown in Fig. 4-22:

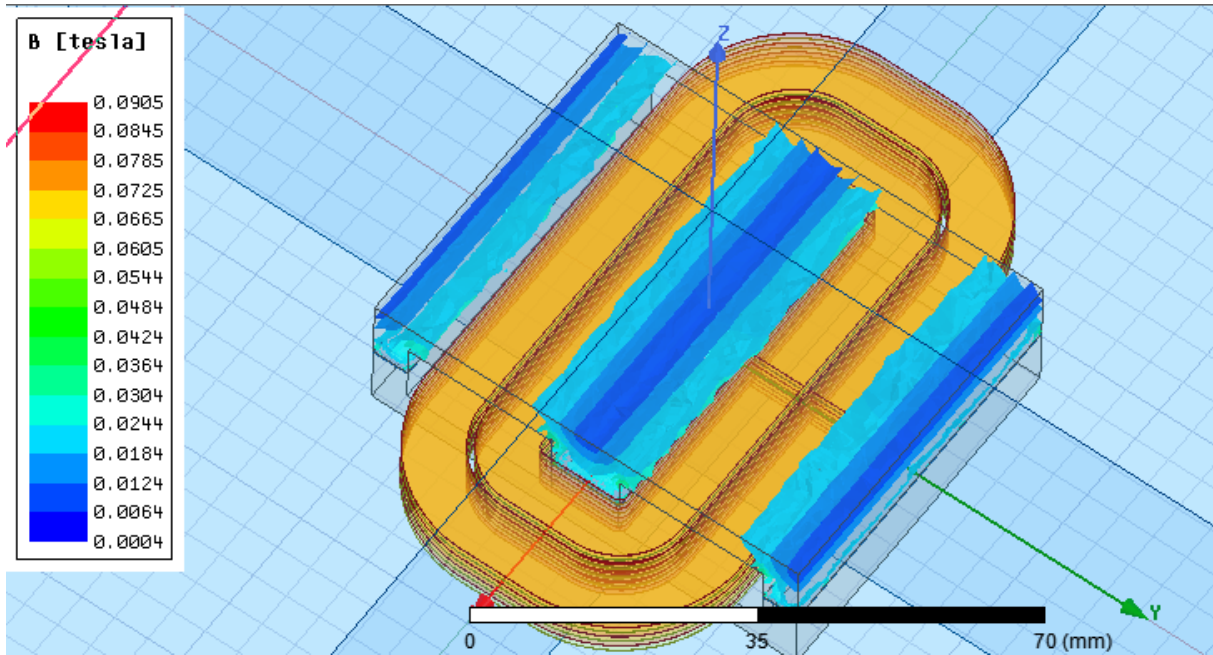


Fig. 4-22: 3-D flux density distribution obtained by Maxwell simulation

The above figure manifests that the maximum flux density of the core is always lower than 0.25T and it reaches 40mT. In CADES calculation, the maximum flux density is obtained as 32mT which has acceptable accuracy

#### 4.6. Summary

The fundamental concepts of global design and optimization for use in bidirectional EV charging were presented in this chapter. The complete loss calculation, magnetics design, and optimization constraints were discussed. A switching losses model for the GaN transistors was also presented in this chapter. A specific condition for the GaN transistor considered as the base value,  $I_D=15A$ ,  $V_{DS}=400V$ ,  $T_j=25^\circ C$ ,  $R_{gON}=10\Omega$ ,  $R_{gOFF}=1\Omega$ ,  $L_{gate}=1nH$ ,  $L_{ex}=10pH$ ,  $L_p=2nH$ ,  $C_{iss}=242pF$ ,  $C_{oss}=65pF$ , and  $C_{rssi}=1.5pF$ , and the base value of switching losses calculated as  $E_{sw}=53.3\mu J$ . Then, these parameters were changed for understanding their effects on the switching losses. With MATLAB interpolation, it was investigated that both  $I_D$  and  $T_j$  have a 5th polynomial relationship and other parameters are independent of each other and have a 3rd polynomial equation for the switching losses calculation. With the proposed method, any type of parameters such as electrical, thermal, and device parameters can be considered to obtain switching losses without any time domain simulation. Multiple scenarios were considered to verify the accuracy of the proposed method and it was investigated that in most cases, the errors were lower than 10%. Then, the effect of temperature upon ON-state resistance was investigated. Two datasheet-based values of ON-state resistance in different temperatures,

typically 25°C and 150°C, were considered to model the temperature-dependency of ON-state resistance and the conduction loss calculated using multiplying the ON resistance by the RMS current square. The error of the predicted conduction loss was lower than 8%. This proposed model enables simple, rapid, and remarkably accurate estimation of switching losses and conduction losses and can be used in the optimization process without any time domain simulation for switching and conduction losses. Now, it is needed to present a new approach for the analysis of the CLLC resonant converter.

# 5. Proposed State Plane Analysis

## 5.1. Introduction

The CLLC resonant converter has to be carefully designed, to provide soft switching and proper control over a wide operating range. In this chapter, a detailed exact analysis approach based on state-plane analysis is proposed for the bidirectional full-bridge CLLC resonant converter. For this purpose, a new formulation of state-space equations is presented and the high-order system of the CLLC resonant converter is decoupled into two lower-order systems. Based on the proposed method, the exact analysis of the converter in CCM, the voltage and current stresses of the resonant elements and switching components, the gain ratio, soft switching criteria, and the boundary between CCM/DCM are obtained. The accuracy and feasibility of the proposed method are verified by simulation and the results are compared with the FHA method.

This chapter is a slightly modified version of [53] published in *IEEE Transactions on Power Electronics* and has been reproduced here with the permission of the copyright holder.

## 5.2. Operating Modes of the CLLC Resonant Converter

The circuit diagram of the bidirectional full-bridge CLLC resonant converter is shown in Fig. 5-1, where the voltage polarities and current directions for the forward power conversion are denoted in red and for the reverse power conversion are denoted in blue. Also, the switches can be either a GaN transistor or a MOSFET. The GaN transistors can operate in both directions and the MOSFETs can operate in the forward direction and utilize in the reverse mode using their anti-parallel diode.

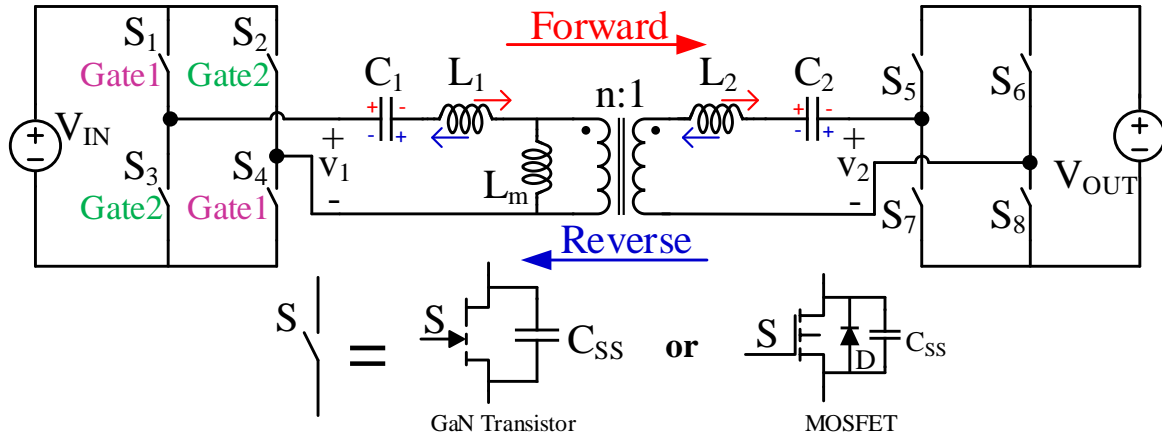


Fig. 5-1: Schematic diagram of the full-bridge bidirectional CLLC resonant converter. The red and blue signs are corresponding to the forward and the reverse power conversion, respectively.

Thanks to the symmetric structure of the CLLC resonant the circuit analysis of the converter is the same for both cases. In this chapter, only the forward power transfer mode will be discussed in detail. The analysis of the converter in the reverse power transfer mode can be performed in the same manner just by exchanging the notations as shown in Table 5-1.

Table 5-1: Parameters exchanging for forward and reverse modes for using a symmetrical method for both

Forward mode		Reverse mode
$V_{IN}$	$\leftrightarrow$	$V_{OUT}$
$C_1$	$\leftrightarrow$	$C_2$
$L_1$	$\leftrightarrow$	$L_2$
$L_m$	$\leftrightarrow$	$L_m'' (=L_m/n^2)$
$L_2' (=n^2L_2)$	$\leftrightarrow$	$L_1'' (=L_1/n^2)$
$C_2' (=C_2/n^2)$	$\leftrightarrow$	$C_1'' (=n^2C_1)$
$V_{OUT}' (=nV_{OUT})$	$\leftrightarrow$	$V_{IN}'' (=V_{IN}/n)$

The primary active full bridge is composed of four GaN transistors. The switching network of the secondary side is also formed in a similar manner as the synchronous rectifier. The resonant tank is comprised of capacitors  $C_1$  and  $C_2$ , the transformer magnetizing inductance  $L_m$ , and the primary and secondary leakage inductances  $L_1$  and  $L_2$ . Depending on the desired power

flow direction, the bridge of one side acts as an inverter and that of the other side acts as a synchronous rectifier.

Typical waveforms are shown in Fig. 5-2, assuming that the converter operates in the CCM and that the secondary side H-bridge acts as a diode rectifier, where the gate signals of transistors  $S_5 \sim S_8$  are applied at the  $i'_{L2}$  zero crossing, i.e.  $t_2$  and  $t_4$ .

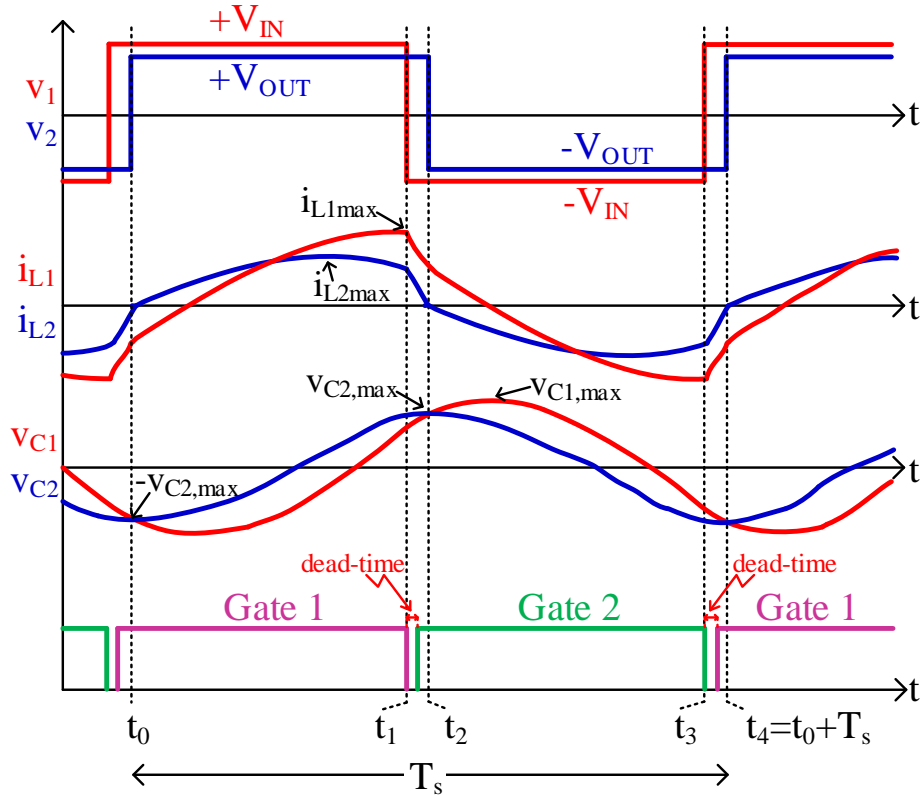


Fig. 5-2: Typical CLLC resonant converter waveforms for the above resonant frequency in the forward power transfer mode

Depending on the switching state and the secondary side current, the CLLC resonant converter operates in four possible operation modes in a complete switching period. The equivalent circuits of each operation mode are shown in Fig. 5-3.

To have a single voltage level, the equivalent circuits are referred to their primary sides by defining:

$$L_2' = n^2 L_2, C_2' = C_2 / n^2, V'_{OUT} = n V_{OUT}, v_2' = n v_2 \quad (5.1)$$

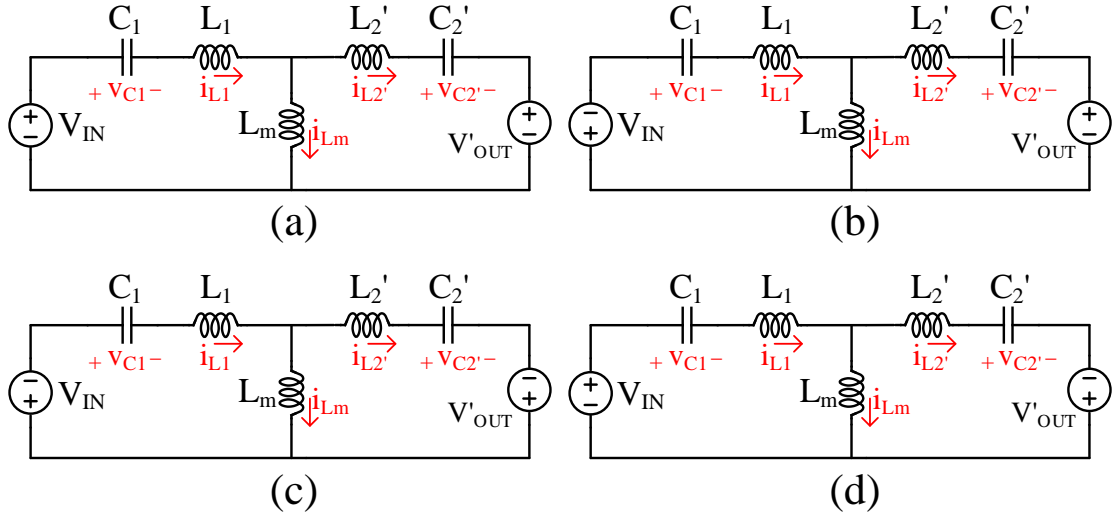


Fig. 5-3: Equivalent circuit of CLLC resonant converter in subinterval 1 (a), subinterval 2 (b), subinterval 3 (c), and subinterval 4 (d).

There are four subintervals in a cycle during each one the converter operates in a particular mode:

**Subinterval 1** ( $t_0 \leq t < t_1$ ): This interval begins with a positive-going zero crossing of the secondary current  $i'_{L2}$ . The primary current,  $i_{L1}$ , is negative and passes through  $S_1$  and  $S_4$  in the reverse mode operating of the GaNs which leads to  $v_1 = V_{IN}$ . Also,  $i'_{L2}$  is positive and the synchronous rectifying GaN transistors  $S_5$  and  $S_8$  are conducting causing  $v'_2 = V'_{OUT}$ . From the equivalent circuit shown in Fig. 5-3 (a), the state space equations of the CLLC resonant converter during subinterval 1 can be expressed as follow:

$$\begin{aligned}
 \frac{dv_{C1}(t)}{dt} &= \frac{1}{C_1} i_{L1}(t) \\
 \frac{dv'_{C2}(t)}{dt} &= \frac{1}{C'_2} i'_{L2}(t) \\
 \frac{di_{L1}(t)}{dt} &= -\frac{L'_2 + L_m}{\Gamma} v_{C1} - \frac{L_m}{\Gamma} v'_{C2} - \frac{L'_2 + L_m}{\Gamma} v_1 - \frac{L_m}{\Gamma} v'_2 \\
 \frac{di'_{L2}(t)}{dt} &= -\frac{L_m}{\Gamma} v_{C1} - \frac{L_1 + L_m}{\Gamma} v'_{C2} - \frac{L_m}{\Gamma} v_1 - \frac{L_1 + L_m}{\Gamma} v'_2
 \end{aligned} \tag{5.2}$$

where  $\Gamma$  is defined as:

$$\Gamma = L_1 L'_2 + L_1 L_m + L'_2 L_m \tag{5.3}$$

This interval ends when the gate signal ‘‘Gate 1’’ to the transistors  $S_1$  and  $S_4$  is turned OFF.

**Subinterval 2** ( $t_1 \leq t < t_2$ ): Fig. 5-3 (b) shows the circuit in this subinterval. At the beginning, the gate signals force all the inverter side transistors to be OFF. The transistors  $S_2$  and  $S_3$  are



turned ON during this subinterval with zero voltage switching (ZVS), and conduct in the reverse mode, hence  $v_I = -V_{IN}$ . This subinterval ends when  $i'_{L2}$  reaches zero. Consequently, the zero current switching (ZCS) is obtained for rectifying GaN transistors  $S_6$  and  $S_7$ . The state space equations of this subinterval are similar to (5.2) knowing that  $v_I$  has the opposite polarity from subinterval 1.

**Subinterval 3** ( $t_2 \leq t < t_3$ ): As shown in Fig. 5-3 (c), in this subinterval, the switches  $S_2$  and  $S_3$  are ON and the input voltage with reverse polarity is applied to the circuit, so  $v_I = -V_{IN}$ . The secondary side current is negative and GaN rectifiers  $S_6$  and  $S_7$  are ON, hence  $v'_2 = -V'_{OUT}$ . This interval is similar to subinterval 1 except that the polarity of the input and output voltages are reversed. Therefore, a similar analysis can be performed. This interval ends when the gate signal “Gate 2” to the transistors  $S_2$  and  $S_3$  is turned OFF.

**Subinterval 4** ( $t_3 \leq t < t_4$ ): The circuit diagram during this interval is illustrated in Fig. 5-3 (d). In this interval, the transistors  $S_1$  and  $S_4$  are turned ON under ZVS conditions due to the negative current of the tank at the beginning of this interval. This interval ends when  $i'_{L2}$  reaches zero which provides the ZCS condition for transistors  $S_5$  and  $S_8$ . The state space equations of this subinterval are similar to (2) with  $v_I = V_{IN}$  and  $v'_2 = -V'_{OUT}$ .

The four sets of state-space equations are coupled and the state-plane trajectory cannot be represented in two- or three-dimensional coordinates. Therefore, a new method is given here for the state-plane analysis of the CLLC resonant converter.

### 5.3. Proposed New State-Plane Analysis of the CLLC Resonant Converter

This section provides new decoupled sets of state-space equations for analysis of the CLLC resonant converter. Let us define the new state space variables  $i_{LP}$ ,  $i_{LN}$ ,  $v_{CP}$ , and  $v_{CN}$  as (5.4).

$$\begin{aligned} i_{LP} &= a_P i_{L1} + i'_{L2} \\ i_{LN} &= a_N i_{L1} - i'_{L2} \\ v_{CP} &= e_P v_{C1} + v'_{C2} \\ v_{CN} &= e_N v_{C1} - v'_{C2} \end{aligned} \quad (5.4)$$

where  $a_P$ ,  $a_N$ ,  $e_P$ , and  $e_N$  are constants that depend on circuit parameters as described in **Appendix I**:

$$\begin{aligned}
a_P &= K e_P \\
a_N &= K e_N \\
e_P &= \frac{K L'_2 - L_1 + (K-1)L_m + \sqrt{(L_1 - K L'_2 + L_m - K L m)^2 + 4 K L m^2}}{2 K L m} \\
e_N &= \frac{-K L'_2 + L_1 + (1-K)L_m + \sqrt{(L_1 - K L'_2 + L_m - K L m)^2 + 4 K L m^2}}{2 K L m}
\end{aligned} \tag{5.5}$$

In which  $K = C_2/C_1$  represents the ratio of resonant capacitors. By substituting (5.4) into (5.2), the new decoupled state space equations denoted by P and N are obtained.

$$\begin{cases} \frac{dv_{CP}}{dt} = \frac{1}{C_P} i_{LP} \\ \frac{di_{LP}}{dt} = -\frac{1}{L_P} v_{CP} - \frac{a_P L'_2 + (1+a_P)Lm}{\Gamma} v_1 - \frac{L_1 + (1+a_P)Lm}{\Gamma} v'_2 \end{cases} \tag{5.6}$$

$$\begin{cases} \frac{dv_{CN}}{dt} = \frac{1}{C_N} i_{LN} \\ \frac{di_{LN}}{dt} = -\frac{1}{L_N} v_{CN} - \frac{a_N L'_2 + (1-a_N)Lm}{\Gamma} v_1 + \frac{L_1 + (1-a_N)Lm}{\Gamma} v'_2 \end{cases} \tag{5.7}$$

where  $C_P = C_N = C'_2$ , and  $L_P$  and  $L_N$  are the equivalent inductances for P and N states:

$$L_P = \frac{(e_P + e_N)(L_1 L'_2 + L_1 L_m + L'_2 L_m)}{K(L'_2 + L_m)e_P + (L_1 + 2L_m)e_N + L_m} \tag{5.8}$$

$$L_N = \frac{(e_P + e_N)(L_1 L'_2 + L_1 L_m + L'_2 L_m)}{(L_1 + L_m)e_P + K(L'_2 + L_m)e_N - L_m(Ke_N e_P + 1)e_N} \tag{5.9}$$

To generalize the analysis, the quantities are presented in normalized form using the base quantities defined in Table 5-2.

The normalized state space equations of the CLLC resonant converter can be expressed as (5.10) and (5.11).

$$\begin{cases} \frac{dm_{CP}}{dt} = \frac{1}{\sqrt{L_P C_P}} j_{LP} \\ \frac{dj_{LP}}{dt} = -\frac{R_{0,P}}{L_P} m_{CP} - \frac{a_P L'_2 + (1+a_P)Lm}{\Gamma} R_{0,P} - \frac{L_1 + (1+a_P)Lm}{\Gamma} R_{0,P} M \end{cases} \tag{5.10}$$

$$\begin{cases} \frac{dm_{CN}}{dt} = \frac{1}{\sqrt{L_N C_N}} j_{LN} \\ \frac{dj_{LN}}{dt} = -\frac{R_{0,N}}{L_N} m_{CN} - \frac{a_N L'_2 + (1-a_N) Lm}{\Gamma} R_{0,N} + \frac{L_1 + (1-a_N) Lm}{\Gamma} R_{0,N} M \end{cases} \quad (5.11)$$

where  $m$  and  $j$  denote the normalized voltage and current, respectively.

Table 5-2: Base values for the parameters of SRC-P and SRC-N

Definition [unit]	Parameter	Value
Base voltage for P-type [V]	$V_{base,P}$	$V_{IN}$
Base Voltage for N-type [V]	$V_{base,N}$	$V_{IN}$
Base impedance for P-type [ $\Omega$ ]	$R_{0,P}$	$\sqrt{L_P/C_P}$
Base impedance for N-type [ $\Omega$ ]	$R_{0,N}$	$\sqrt{L_N/C_N}$
Base current for P-type [A]	$I_{base,P}$	$V_{IN}/R_{0,P}$
Base current for N-type [A]	$I_{base,N}$	$V_{IN}/R_{0,N}$
Base frequency [Hz]	$f_0$	$\frac{1}{2\pi\sqrt{L_1 C_1}}$

Fig. 5-4 (a) and (b) represent the equivalent circuits described by (5.10) and (5.11) [161], which are denoted by the P-type series resonant converter (SRC-P) and the N-type series resonant converter (SRC-N), respectively.

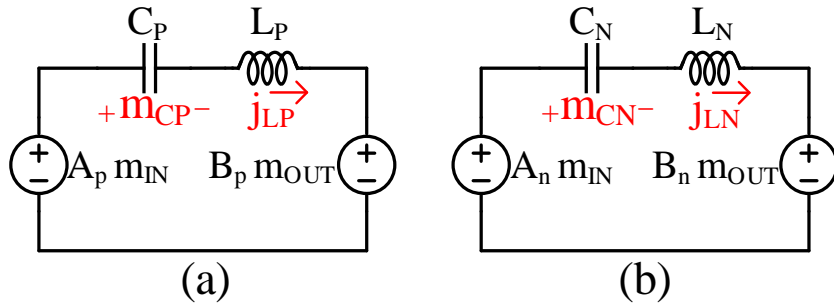


Fig. 5-4: Equivalent circuit for SRC-P (a) and SRC-N (b).

One can see that the behavior of the CLLC resonant converter can be modeled by two series resonant converters which are shown in Fig. 5-4. The parameters  $A_P$ ,  $B_P$ ,  $A_N$ , and  $B_N$  are defined as follows:

$$\begin{aligned}
A_P &= (a_P (L'_2 + L_m) + L_m) \times L_P / \Gamma \\
B_P &= (L_m (a_P + 1) + L_1) \times L_P / \Gamma \\
A_N &= (a_N (L'_2 + L_m) - L_m) \times L_N / \Gamma \\
B_N &= (L_m (a_N - 1) - L_1) \times L_N / \Gamma
\end{aligned} \tag{5.12}$$

In Fig. 5-4, the polarity of  $m_{IN}$  and  $m_{OUT}$  depends on the particular subinterval. In subinterval 1, the applied voltages to the resonant tank are  $+V_{in}$  and  $-V_{out}$ . Therefore, the state plane diagrams of this subinterval are two circles for SRC-P and SRC-N as shown in Fig. 5-5.

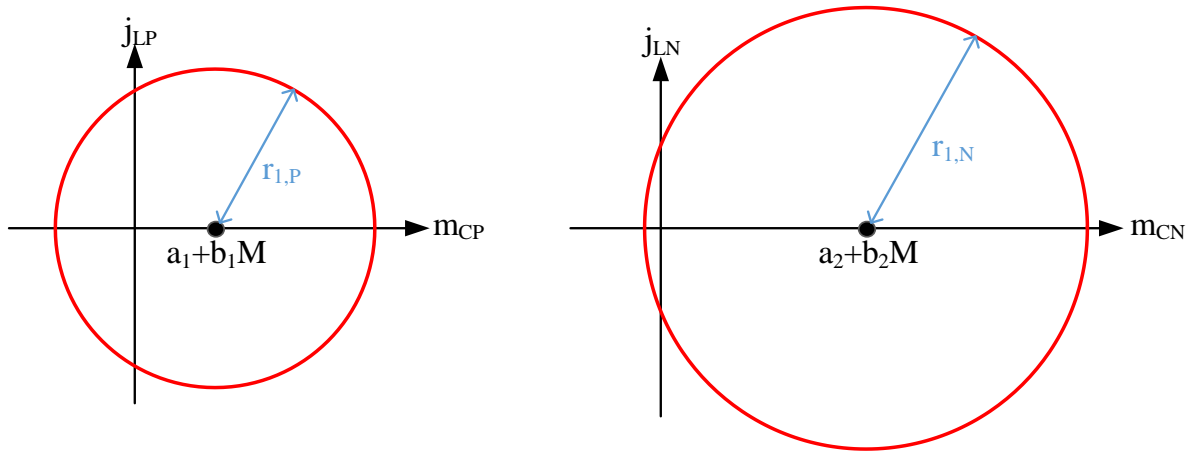


Fig. 5-5: State plane diagram of Subinterval 1 for SRC-P (left) and SRC-N (right)

In subinterval 2, the polarity of the applied voltage changes to  $+V_{out}$  by changing the polarity of the secondary side current. Therefore, the state plane diagrams of this subinterval are two circles for SRC-P and SRC-N as shown in Fig. 5-6.

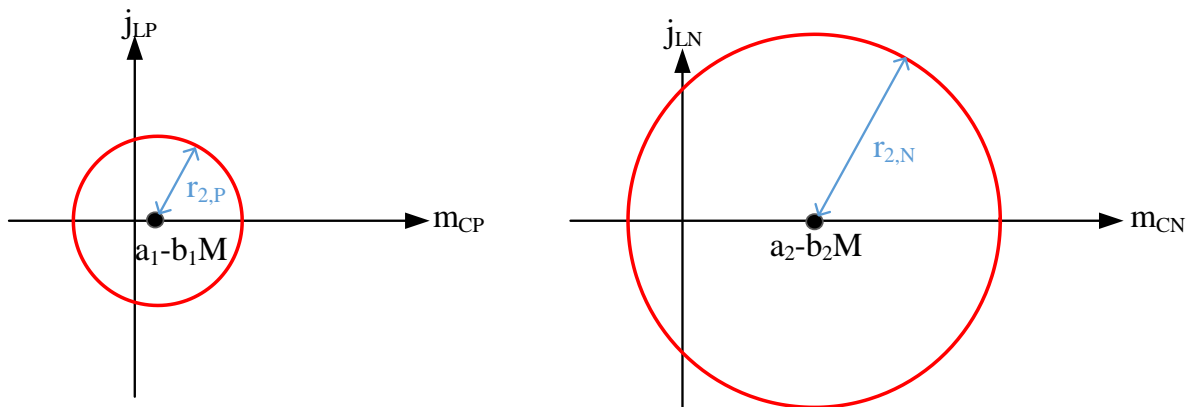


Fig. 5-6: State plane diagram of Subinterval 2 for SRC-P (left) and SRC-N (right)

In subinterval 3, the polarity of the inverter part changes and  $-V_{in}$  is applied to the tank. Therefore, the state plane diagrams of this subinterval have also two circles for SRC-P and SRC-N as shown in Fig. 5-7.

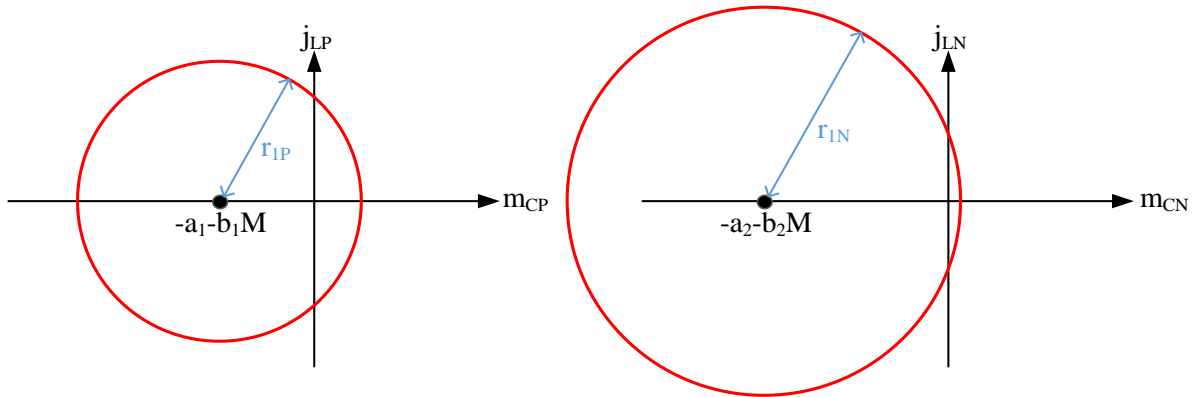


Fig. 5-7: State plane diagram of Subinterval 3 for SRC-P (left) and SRC-N (right)

In subinterval 4, the polarity of the applied voltage changes to  $-V_{out}$  by changing the polarity of the secondary side current. Therefore, the state plane diagrams of this subinterval are two circles for SRC-P and SRC-N as shown in Fig. 5-8:

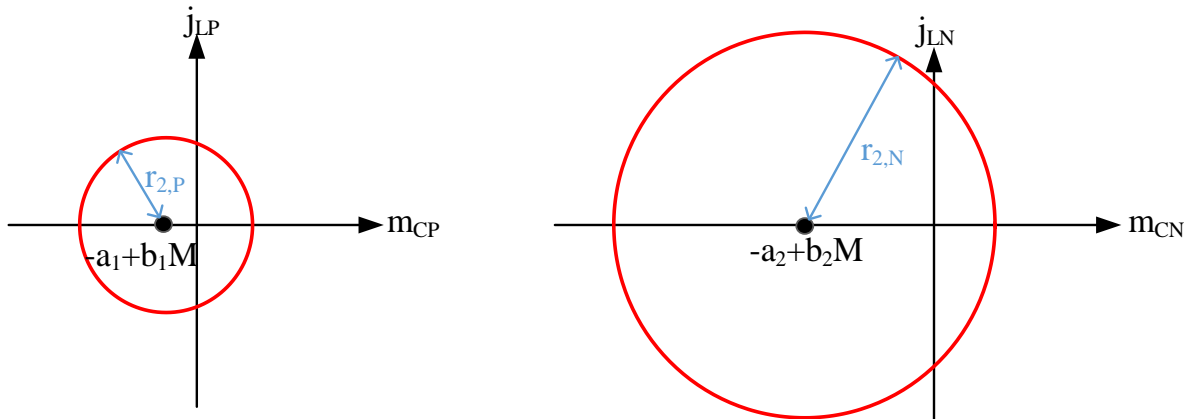


Fig. 5-8: State plane diagram of Subinterval 4 for SRC-P (left) and SRC-N (right)

As shown in the above diagrams, the state-plane diagram of each series resonant converter consists of four circular arcs [92]. Consequently, Fig. 5-9 shows the state-plane diagram of the SRC-P and SRC-N, where the center and radius of arcs are given in Table 5-3. The included angles of the arcs can be found by solving the geometry of the state-plane as shown in Table 5-4.

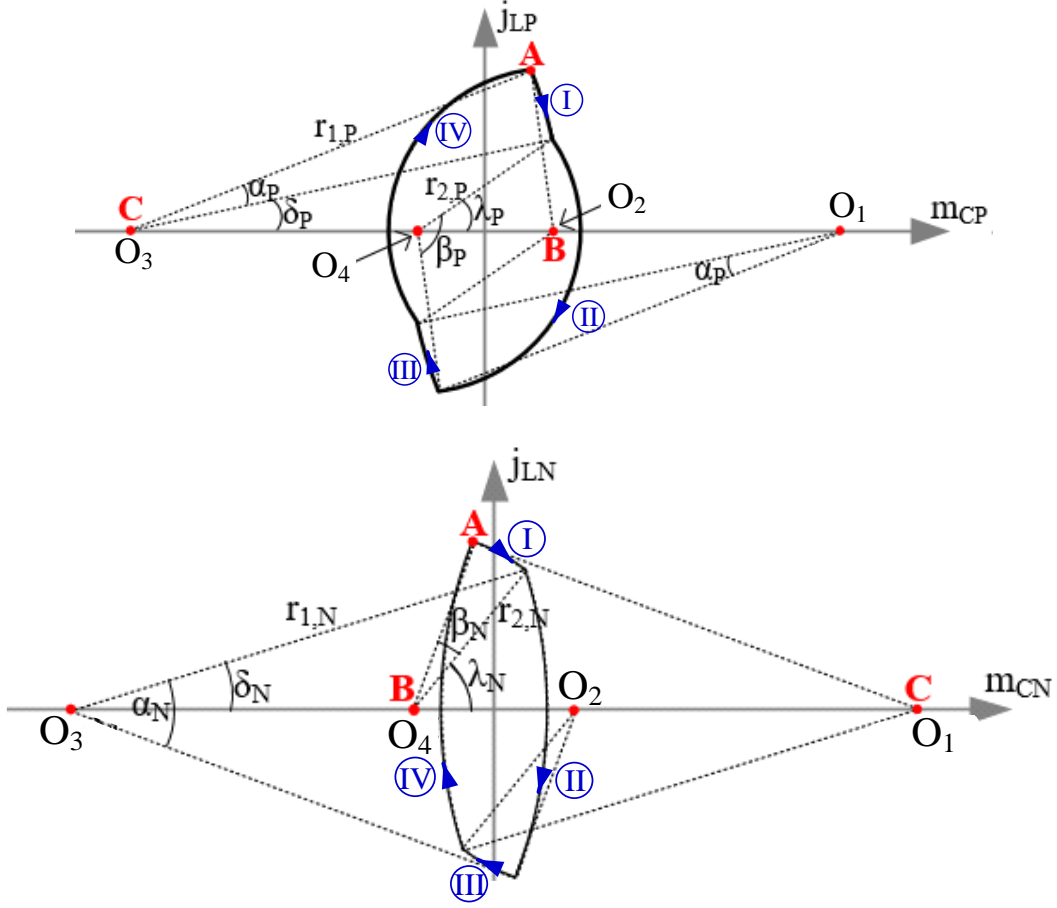


Fig. 5-9: State-plane diagram of the CLLC resonant converter operating on CCM, for SRC-P (top) and SRC-N (bottom).

Table 5-3: Radius ( $r$ ) and center ( $O$ ) of the SRC-P and SRC-N arcs

	SRC-P	SRC-N
$r_1$	$\sqrt{(-M_{CP0} + A_p + B_p M)^2 + J_{LP0}^2}$	$\sqrt{(M_{CN0} + A_N - B_N M)^2 + J_{LN0}^2}$
$r_2$	$\sqrt{(M_{CP0} + A_p - B_p M)^2 + J_{LP0}^2}$	$\sqrt{(-M_{CN0} + A_N + B_N M)^2 + J_{LN0}^2}$
$O_1$	$A_p + B_p \times M$	$A_N + B_N \times M$
$O_2$	$A_p - B_p \times M$	$A_N - B_N \times M$
$O_3$	$-A_p - B_p \times M$	$-A_N - B_N \times M$
$O_4$	$-A_p + B_p \times M$	$-A_N + B_N \times M$

From Fig. 5-9, It can be observed that for the half switching period, the sum of the arc angles of subintervals 1 and 2, i.e.,  $\alpha_x + \beta_x$ , satisfies the following condition for  $x \in \{P, N\}$ .

$$\alpha_x + \beta_x = \frac{\omega_{0,x}}{2f_{sw}} = \frac{\pi}{F_x} \quad , \quad F_x = \frac{f_{sw}}{f_0} \quad (5.13)$$

where  $\omega_{0,x}$  is the base value of angular frequency and  $F_x$  is the normalized switching frequency with  $x \in \{P, N\}$ .

Table 5-4: Some angles for the state-plane diagrams of SRC-P and SRC-N in CCM

Angle	Value	Condition
$\alpha_P$ $\alpha_N$	$\cos^{-1} \left( \frac{r_2^2 - r_1^2 + 4a^2}{4a \times r_2} \right) \mp \delta$	$- \rightarrow P$ $+ \rightarrow N$
$\beta_P$ $\beta_N$	$\cos^{-1} \left( \frac{r_1^2 - r_2^2 + 4a^2}{4a \times r_1} \right) \pm \lambda$	$+ \rightarrow P$ $- \rightarrow N$
$\delta_P$ $\delta_N$	$\sin^{-1} \left( \frac{r_2}{r_1} \sqrt{1 - \left( \frac{r_1^2 - r_2^2 - 4b^2 M^2}{4b \times M \times r_2} \right)^2} \right)$	same
$\lambda_P$ $\lambda_N$	$\cos^{-1} \left( \frac{r_1^2 - r_2^2 - 4b^2 M^2}{\pm 4b \times M \times r_2} \right)$	$+ \rightarrow P$ $- \rightarrow N$

In the following section, component stresses are analyzed using the state-plane diagram.

### 5.3.1. Stresses of Components

Calculations of voltage and current stresses of the resonant elements and switches are an important step in designing resonant converters. The selection of switches and other components is commonly considered based on their maximum voltage and current.

#### Current Stresses

Fig. 5-10 shows three possible trajectories depending on the value of  $\beta_P$  which is the arc angle of subinterval 1.  $\theta_0$  is the angle corresponding to the time difference between the zero crossing of  $i_{L1}$  and  $i_{L2}$ .

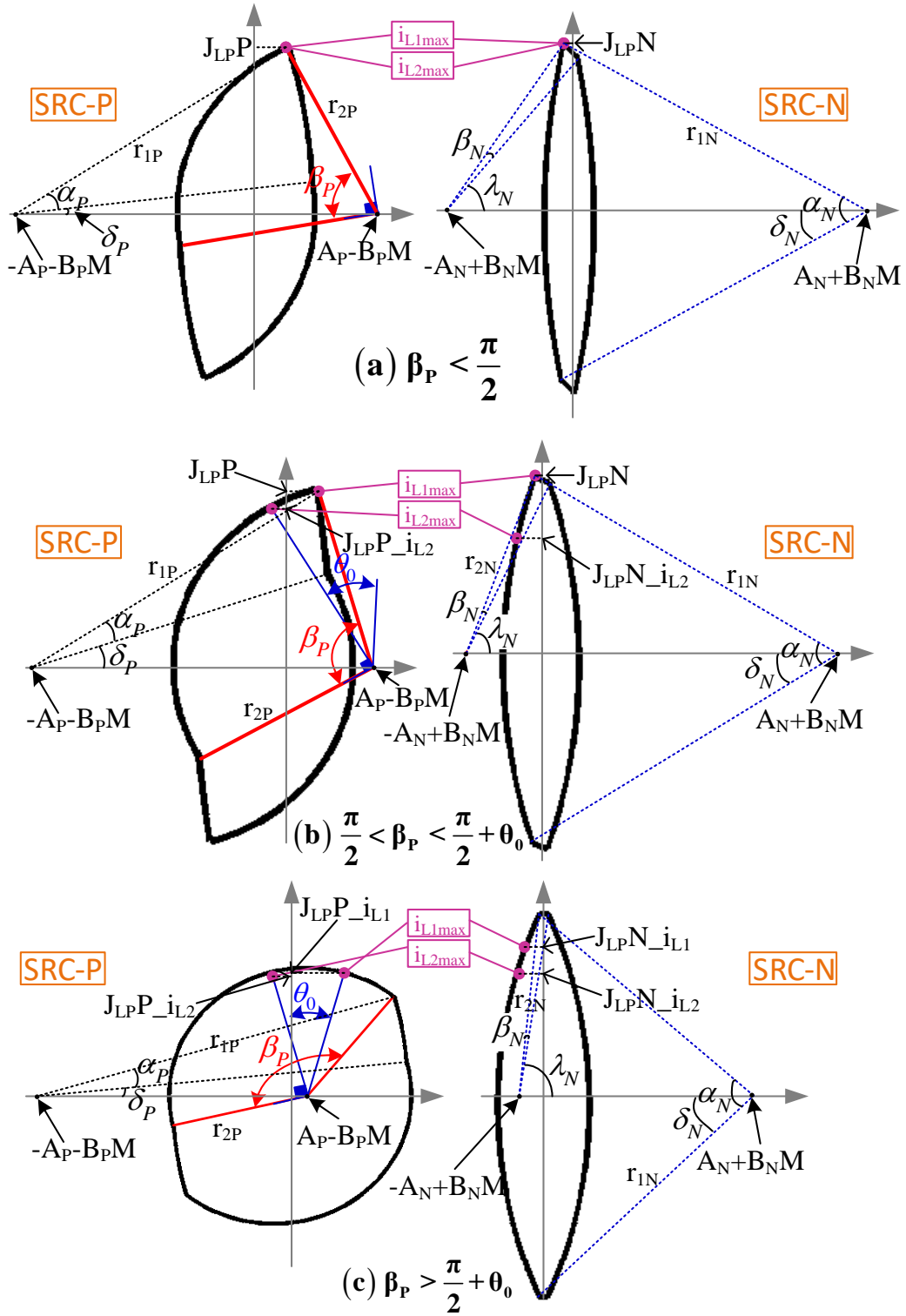


Fig. 5-10: Maximum currents of the primary and the secondary sides in SRC-P and SRC-N state-plane diagrams for;  $\beta_P < \pi/2$  (a),  $\pi/2 < \beta_P < \pi/2 + \theta_0$  (b), and  $\beta_P > \pi/2 + \theta_0$  (c).

For  $\beta_P < \pi/2$ , the peak current values,  $J_{LP}P$  and  $J_{LP}N$ , can be calculated from Fig. 5-10 (a) as:



$$J_{LP}P = r_{1P} \sin(\alpha_P + \delta_P) \quad (5.14)$$

$$J_{LP}N = r_{1N} \sin(\alpha_N - \delta_N) \quad (5.15)$$

The radii  $r_{2,P}$  and  $r_{2,N}$  of the state-plane trajectory in Fig. 5-10 (a), can be found as follow:

$$r_{2,P}^2 = r_{1,P}^2 + (2A_P)^2 - 2r_{1,P} (2A_P) \cos(\alpha_P + \delta_P) \quad (5.16)$$

$$r_{2,N}^2 = r_{1,N}^2 + (2A_N)^2 - 2r_{1,N} (2A_N) \cos(\alpha_N - \delta_N) \quad (5.17)$$

From (5.16) and (5.17), and using the trigonometric equation of  $\sin x = \sqrt{1 - \cos^2 x}$ , the following equations are obtained:

$$\sin(\alpha_P + \delta_P) = \sqrt{1 - \left( \frac{r_{2,P}^2 - r_{1,P}^2 - 4A_P^2}{4A_P r_{1,P}} \right)^2} \quad (5.18)$$

$$\sin(\alpha_N - \delta_N) = \sqrt{1 - \left( \frac{r_{1,N}^2 - r_{2,N}^2 + 4A_N^2}{4A_N r_{1,N}} \right)^2} \quad (5.19)$$

By substituting (5.18) and (5.19) into (5.14) and (5.15), the peak current values can be found as:

$$J_{LP}P = r_{1P} \sqrt{1 - \left( \frac{r_{2,P}^2 - r_{1,P}^2 + 4A_P^2}{4A_P r_{1,P}} \right)^2} \quad (5.20)$$

$$J_{LP}N = r_{1N} \sqrt{1 - \left( \frac{r_{1,N}^2 - r_{2,N}^2 + 4A_N^2}{4A_N r_{1,N}} \right)^2} \quad (5.21)$$

Using (5.20) and (5.21), the peak current of the primary and secondary inductors,  $I_{L1,max}$  and  $I_{L2,max}$ , can be expressed as:

$$I_{L1,max} = \frac{1}{a_P + a_N} (J_{LP}P \times I_{base,P} + J_{LP}N \times I_{base,N}) \quad (5.22)$$

$$I_{L2,max} = \frac{n}{a_P + a_N} (a_P J_{LP}P \times I_{base,P} - a_N J_{LP}N \times I_{base,N}) \quad (5.23)$$

For  $\beta_P > \pi/2 + \theta_0$ , as shown in Fig. 5-10 (c) the peak values  $J_{LP}P$  and  $J_{LP}N$  can be obtained as:

$$J_{LP}P - i_{L1} = r_{1P} \cos(\lambda_P - \theta_0) \quad (5.24)$$

$$J_{LP}N - i_{L1} = r_{1N} \sin\left(\left(\theta_0 + \frac{\pi}{2}\right) \frac{I_{base,N}}{I_{base,P}} - \delta_N\right) \quad (5.25)$$

$$J_{LP}P - i_{L2} = r_{1P} \cos(\lambda_P) \quad (5.26)$$

$$J_{LP}N - i_{L2} = r_{1N} \sin\left(\frac{\pi}{2} \frac{I_{base,N}}{I_{base,P}} - \delta_N\right) \quad (5.27)$$

On the other hand for  $\pi/2 < \beta_P < \pi/2 + \theta_0$ , the maximum value of the primary side current happens at the switching instant. So,  $J_{LP}P$  and  $J_{LP}N$  should be calculated from (5.20) and (5.21) in order to find  $i_{L1,max}$ . The peak value of the secondary current happens at  $\omega_{0t} = \pi/2$ . Therefore,  $J_{LP}P$  and  $J_{LP}N$  should be calculated from (5.26) and (5.27) in order to find  $i_{L2,max}$ .

### Voltage Stresses

In a steady state, the peak tank capacitor voltages occur when the inductor currents reach zero since the resonant capacitor and inductor are in series on both sides, hence the capacitor voltage is maximum when the inductor current is zero. In this condition, one can find from (5.4) that:

$$\begin{aligned} i_{LP} &= a_P i_{L1} + i'_{L2} = i'_{L2} \\ i_{LN} &= a_N i_{L1} - i'_{L2} = -i'_{L2} \end{aligned} \quad (5.28)$$

which means  $i_{LP} = -i_{LN}$  or in the normalized form:

$$j_{LP} = -\frac{I_{base,N}}{I_{base,P}} j_{LN} \quad (5.29)$$

which is a line in the  $j_{LP}$ - $j_{LN}$  coordinate system. Therefore, we need to plot a new state-plane trajectory, i.e.  $j_{LP}$ - $j_{LN}$ . Fig. 5-11 shows the state-plane trajectory of  $j_{LP}$ - $j_{LN}$  which is obtained by superimposing loci of  $j_{LP}$ - $m_{CP}$  and  $j_{LN}$ - $m_{CN}$ . The related triangles for the calculation of normalized voltage at  $i_{L1}=0$ ,  $m_{XP}$  and  $m_{XN}$ , are redrawn in Fig. 5-11.

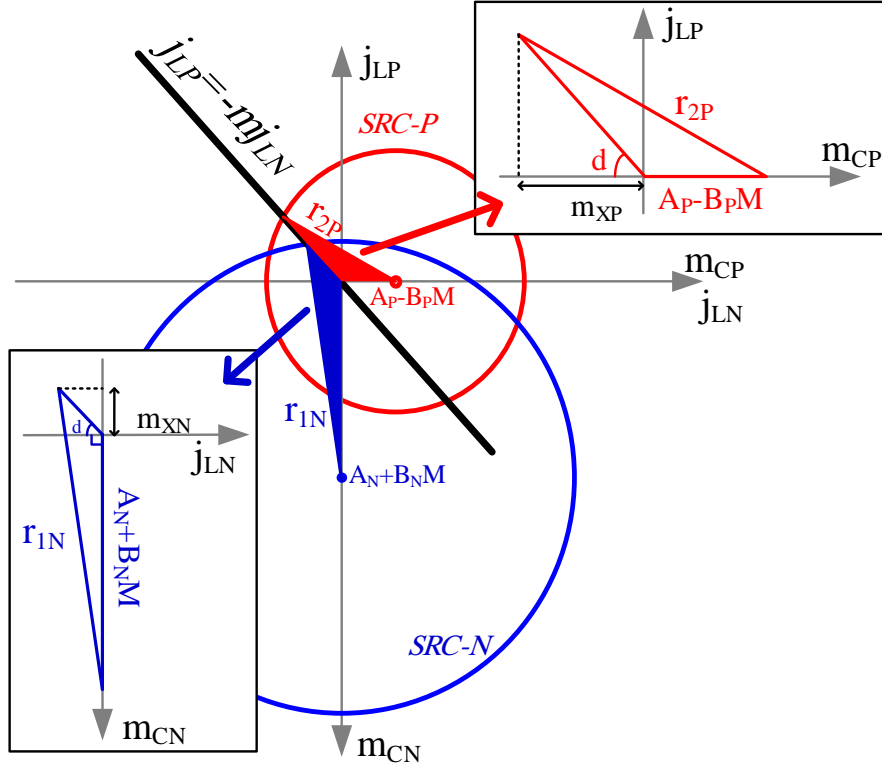


Fig. 5-11: The  $j_{LP}$ - $j_{LN}$  state-plane trajectory for calculating  $v_{C1max}$ .

Using the law of cosines in Fig. 5-11, one can write:

$$r_{2P}^2 = (A_P - B_P M)^2 + \frac{m_{XP}^2}{\cos^2 d} - 2(A_P - B_P M) \frac{m_{XP}}{\cos d} \cos(\pi - d) \quad (5.30)$$

$$r_{1N}^2 = (A_N + B_N M)^2 + \frac{m_{XN}^2}{\sin^2 d} - 2(A_N + B_N M) \frac{m_{XN}}{\sin d} \sin\left(\frac{\pi}{2} + d\right) \quad (5.31)$$

where  $d = \tan^{-1}(I_{base,N}/I_{base,P})$ . Therefore,  $m_{XP}$  and  $m_{XN}$  are calculated as:

$$m_{XP} = -(A_P - B_P M) \cos^2 d + \cos d \sqrt{r_{2P}^2 - \sin^2 d (A_P - B_P M)^2} \quad (5.32)$$

$$m_{XN} = -(A_N + B_N M) \sin^2 d + \sin d \sqrt{r_{1N}^2 - \cos^2 d (A_N + B_N M)^2} \quad (5.33)$$

Consequently, the maximum voltage across  $C_1$ ,  $v_{C1max}$ , can be calculated by transforming normalized variables from  $P$  and  $N$  states to the real value.

$$V_{C1,max} = \frac{1}{e_P + e_N} (m_{XP} \times V_{base,P} + m_{XN} \times V_{base,N}) \quad (5.34)$$

On the other hand, the maximum voltage across  $C_2$ ,  $v_{C2max}$ , occurs when  $i_{L2}$  reaches zero. So, the normalized voltage can be expressed as:

$$m_{CP}P = r_{2P} \cos(\lambda_P) - A_P + B_P M \quad (5.35)$$

$$m_{CP}N = r_{2N} \cos(\lambda_N) - A_N - B_N M \quad (5.36)$$

where  $m_{CP}P$  and  $m_{CP}N$  are the normalized voltages when  $i_{L2}=0$ , in the SRC-P and SRC-N, respectively.

Knowing  $m_{CP}P$  and  $m_{CP}N$ ,  $V_{C2,max}$  can be obtained as:

$$V_{C2,max} = \frac{1/n}{e_P + e_N} (e_P M_{CP}P \times V_{base,P} - e_N M_{CP}N \times V_{base,N}) \quad (5.37)$$

### 5.3.2. Soft Switching Conditions

One of the most important features of resonant converters is the zero voltage switching capability of the devices. For CLLC resonant converter, in most literature first harmonic approximation is used to find the soft switching conditions. In this paper, the accurate state-plane analysis is used to examine exact soft switching conditions.

As shown in Fig. 5-2 at the end of subinterval 1,  $S_1$  and  $S_4$  conduct,  $i_{L1}$  is positive and the voltage across drain-source capacitors  $C_{SS1}$  and  $C_{SS3}$  are 0 and  $+V_{IN}$ , respectively. During the dead time as shown in Fig. 5-12, all inverter switches are OFF and the primary side inductor current flows through the transistor parasitic output capacitances:

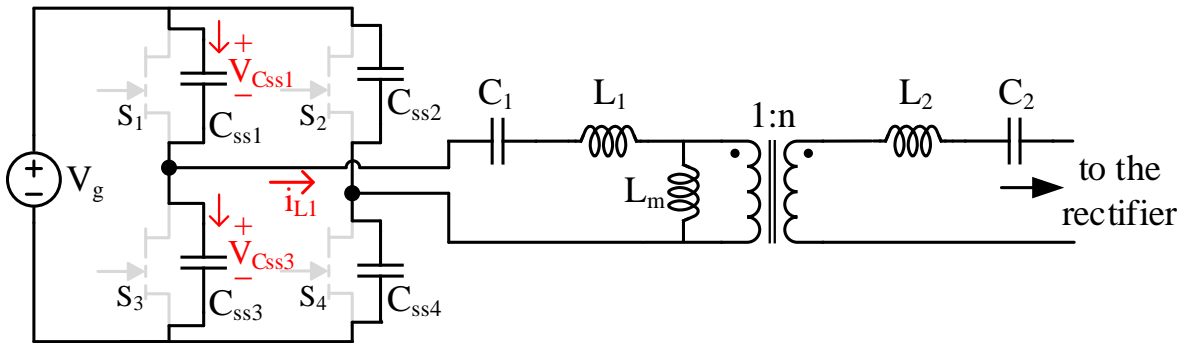


Fig. 5-12: Circuit condition between subintervals 1 and 2 for the ZVS analysis.

Therefore:

$$V_{C_{SS1}} + V_{C_{SS3}} = V_{IN} \quad (5.38)$$

As the switches are similar to the capacitor current formula  $i = C(dv/dt)$  one can find that:

$$I_{CSS1} + I_{CSS3} = 0 \rightarrow i_{L1} = \frac{I_{CSS1}}{2} = -\frac{I_{CSS3}}{2} \quad (5.39)$$

Eq. (5.39) implies that the total energy of the two parasitic capacitors remains unchanged during this subinterval, as a result, no power is transferred to the resonant network.

This mode will continue until the voltage across  $C_{SS3}$  is discharged to zero. After that, the GaN transistors  $S_2$  and  $S_3$  conduct in the reverse direction, therefore ZVS can be achieved. By assuming linear discharging, the minimum dead time to ensure ZVS is given by:

$$\frac{I_{t=t_{dt}}}{2} = C_{SS} \frac{dV_{CSS}}{dt} \cong C_{SS} \frac{V_{IN} - 0}{t_{dt}} \Rightarrow t_{dt} = \frac{2C_{SS}V_{IN}}{I_{t=t_{dt}}} \quad (5.40)$$

In steady state, the state-plane trajectory is symmetrical. Hence [44];

$$I_{L1}(0) = -I_{L1}(\pi/\omega_s) \quad (5.41)$$

By substituting (5.41) into (5.40), the minimum dead-time which ensures ZVS can be calculated as:

$$t_{dt} \geq \frac{2C_{SS}V_{IN}}{I_{t=0}} \quad (5.42)$$

Obviously, the dead-time depends on the input voltage, the drain-source capacitance of inverter switches, and the initial value of primary current which is a function of circuit parameters and the load. The procedure to drive the initial value of resonant elements has been discussed in [44].

On the other hand, the maximum allowable dead time for remaining in ZVS is  $\alpha + \theta_0$  when the  $i_{L1}$  reaches zero. Therefore, the dead-time must be selected as (5.43) to meet operating at the ZVS condition.

$$\frac{2C_{SS}V_{IN}}{I_{t=0}} \leq t_{dt} \leq \alpha + \theta_0 \quad (5.43)$$

It should be mentioned that this ZVS condition is a general formula and is also valid when other parasitic capacitances such as transformer inter-winding and PCB interlayer capacitances exist. In this case, the value of  $I_{t=0}$  with consideration of parasitic capacitances should be

calculated and used. Fig. 5-13 represents the ZVS operating region as a function of voltage gain and dead-time equivalent angle.

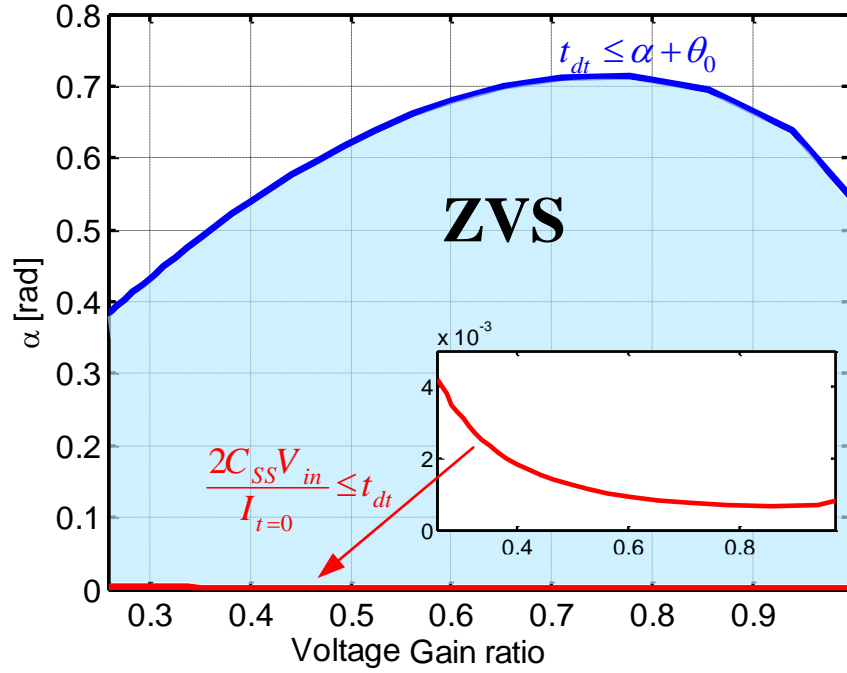


Fig. 5-13: The ZVS operating region as a function of voltage gain and dead-time equivalent angle.

### 5.3.3. Output Characteristic

The output characteristics describe how the converter output voltage depends on the load current. As can be seen in Fig. 5-2 during the half switching period where the secondary side current  $i_{L2}$  is positive, the secondary resonant capacitor voltage increases from its negative peak  $-V_{C2,max}$  to its positive peak  $+V_{C2,max}$ . This voltage change corresponds to the net charge transferred to the load, hence:

$$I_{Load} = \langle i_{L2} \rangle = \frac{2}{T_s} \int_0^{\frac{T_s}{2}} i_{C2} dt = \frac{2}{T_s} (C_2 \Delta V_{C2}) = \frac{4C_2 V_{C2,max}}{T_s} \quad (5.44)$$

By substituting (5.37) into (5.44) and normalizing the equation, we can find the relationship between normalized current  $J$ , and the voltage stresses of SRC-P and SRC-N:

$$J = \frac{4C_2 F_s}{e_P + e_N} (e_P m_{CP,P} - e_N m_{CP,N}) \quad (5.45)$$

Now, substituting (5.35) and (5.36) into (5.45), the relationship between normalized output voltage  $M$ , normalized load current  $J$ , and normalized switching frequency which features the output characteristics can be expressed as:

$$J = \frac{4C_2F_S}{e_P + e_N} \{e_P (r_{2P} \cos(\lambda_P) + A_P - B_P M) - e_N (r_{2N} \cos(\lambda_N) - A_N - B_N M)\} \quad (5.46)$$

Fig. 5-14 shows the output characteristics of the CLLC resonant converter for different normalized switching frequencies.

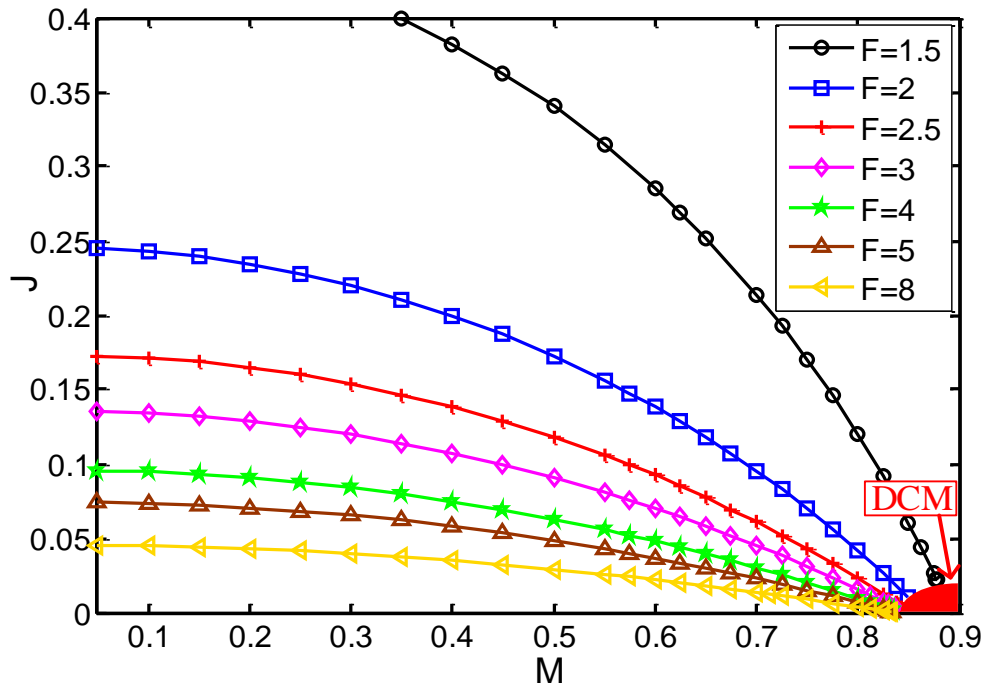


Fig. 5-14: Output characteristics of the CLLC resonant converter for different normalized switching frequencies.

The output short circuit current,  $J_{SC}$ , can be calculated using the output characteristics by substituting  $M=0$  into (5.46).

$$J_{SC} = \frac{4C_2F_S}{e_P + e_N} \left( e_P (r_{2P} \cos(\lambda_P) + A_P) - e_N (r_{2N} \cos(\lambda_N) - A_N) \right) \quad (5.47)$$

It can be seen that the converter's short-circuit current is inherently limited.

#### 5.3.4. Control Plane Characteristics

One of the most informative curves for the analysis and design of resonant converters is the steady control plane characteristics i.e. voltage conversion ratio,  $M$ , vs. normalized switching frequency,  $F$ . The load characteristics can be superimposed on the converter output

characteristics to determine the output voltage vs. switching frequency. For a resistive load satisfying  $I=V/R$  or in the normalized form:

$$J = MQ \tag{5.48}$$

with  $Q = \sqrt{L_1/C_1}/R$ ,  $J$  can be eliminated from (5.46) by substituting (5.48) into it.

$$M = \frac{4C_2f_0F}{(e_P + e_N)Q} (e_P M_{CP,P} - e_N M_{CP,N}) \tag{5.49}$$

Eq. (5.49) reveals the relationship between  $M$  and  $F$  which can be used in the control of the CLLC resonant converter.

### 5.3.5. Constant stresses of the resonant components

Another important advantage of the state plane analysis is to find a graphical diagram of constant stresses in the  $J$ - $M$  curves. Fig. 5-15 shows the output characteristics when the stress of resonant components is fixed.

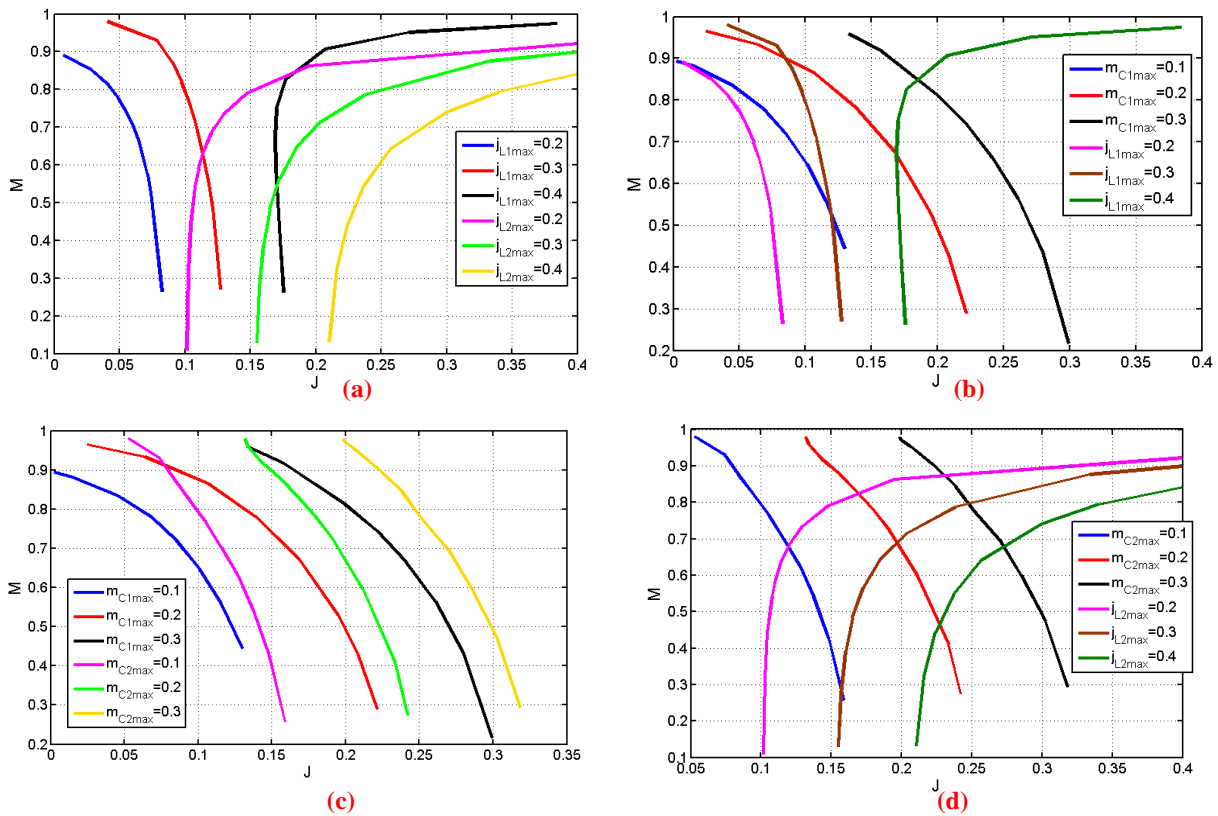


Fig. 5-15: Constant stresses diagram based on the different resonant elements. (a)  $j_{L1}$  and  $j_{L2}$  are fixed; (b)  $j_{L1}$  and  $m_{C1}$  are fixed; (c)  $m_{C1}$  and  $m_{C2}$  are fixed; (d)  $j_{L2}$  and  $m_{C2}$  are fixed.



where in Fig. 5-15(a), the  $M$ - $J$  diagram is shown for  $j_{L1}=0.2\sim 0.4$  and  $j_{L2}=0.2\sim 0.4$ . Also, this diagram is shown in Fig. 5-15(b) for  $j_{L1}=0.2\sim 0.4$  and  $m_{C1}=0.1\sim 0.3$ . Fig. 5-15(c) displays the  $M$ - $J$  diagram for  $m_{C1}=0.1\sim 0.3$  and  $m_{C2}=0.1\sim 0.3$ , and Fig. 5-15(d) shows it for  $j_{L2}=0.2\sim 0.4$  and  $m_{C1}=0.1\sim 0.3$ . These diagrams can be applied as another method for designing the CLLC resonant converter.

## 5.4. Proposed DCM Analysis for CLLC Resonant Converter

### 5.4.1. DCM state-plane diagram

The steady-state waveforms of the CLLC resonant converter operating in the discontinuous conduction mode (DCM) during a half switching period are shown in Fig. 5-16. The intervals I~II are similar to the CCM.

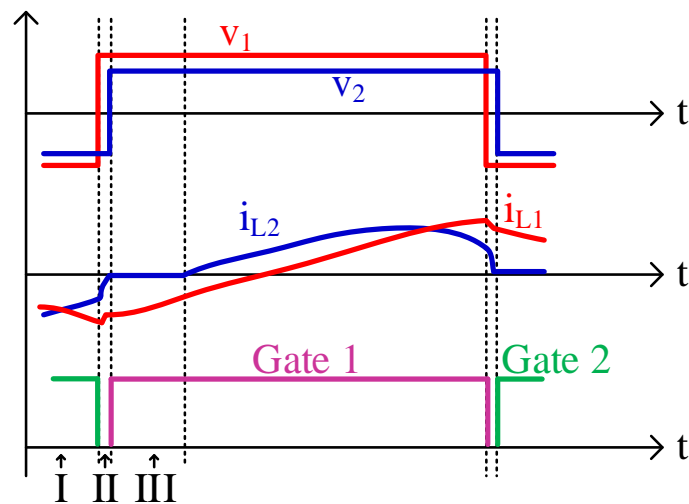


Fig. 5-16: Typical CLLC resonant converter operation in the discontinuous conduction mode during a half switching period

In subinterval III, the secondary side current  $i_{L2}$  remains at zero for a while and therefore, the resonant components of the secondary side are decoupled from the resonance. This mode is denoted by D and it is shown in Fig. 5-17.

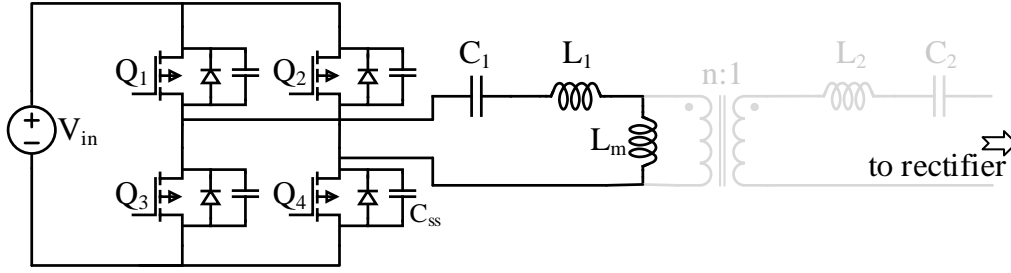


Fig. 5-17: The subinterval of III for DCM operating

According to Fig. 5-18, the DCM operation of the CLLC resonant converter can be considered as a series resonant converter denoted by SRC-D with a tank circuit comprises of capacitance  $C_1$  and inductance  $L_1+L_m$ .

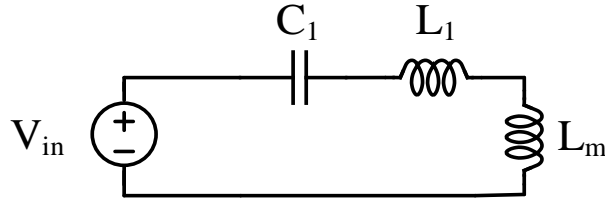


Fig. 5-18: The resonant tank model in subinterval III of DCM operating

Therefore, the state-space equation of SRC-D during interval III can be expressed as:

$$\begin{cases} \frac{dv_{C_1}}{dt} = \frac{1}{C_1} i_{L_1} \\ \frac{di_{L_1}}{dt} = \frac{V_{in} - v_{C_1}}{L_1 + L_m} \end{cases} \quad (5.50)$$

The solution of this second-order system of differential equations describes a circle as:

$$\left( \frac{v_{C_1}}{V_g} - 1 \right)^2 + \left( \sqrt{\frac{L_1 + L_m}{C_1}} \frac{i_{L_1}}{V_g} \right)^2 = A_D^2 \quad (5.51)$$

with radius  $A_D$  that depends on the initial conditions as shown in **Appendix II**.

In the DCM,  $i_{L_2}$  is zero and  $v_{C_2}$  remains constant at  $v_{C_2,max}$ . Hence:

$$\begin{aligned} i_{L_2} = 0 &\Rightarrow i_{L_1} = \frac{i_{LP}}{a_p} \\ \text{for } P : & \\ v_{C_2} = v_{C_2,max} &\Rightarrow v_{C_1} = \frac{v_{CP} - v_{C_2,max}}{e_p} \end{aligned} \quad (5.52)$$

$$\begin{aligned}
i_{L2} = 0 &\Rightarrow i_{L1} = \frac{i_{LN}}{a_E} \\
\text{for } N : & \\
v_{C2} = v_{C2max} &\Rightarrow v_{C1} = \frac{v_{CN} + v_{C2max}}{e_N}
\end{aligned} \tag{5.53}$$

By substituting either (5.52) or (5.53) into (5.51), and using the normalizing base quantities listed in Table 5-2, the state plane trajectory for P-type and N-type forms are obtained as below:

$$(m_{CP} - m_{C2max} - e_P)^2 + \left( \sqrt{\frac{C_1}{C_2} \frac{L_1 + Lm}{L_P}} j_{LP} \right)^2 = A_D^2 e_P^2 \tag{5.54}$$

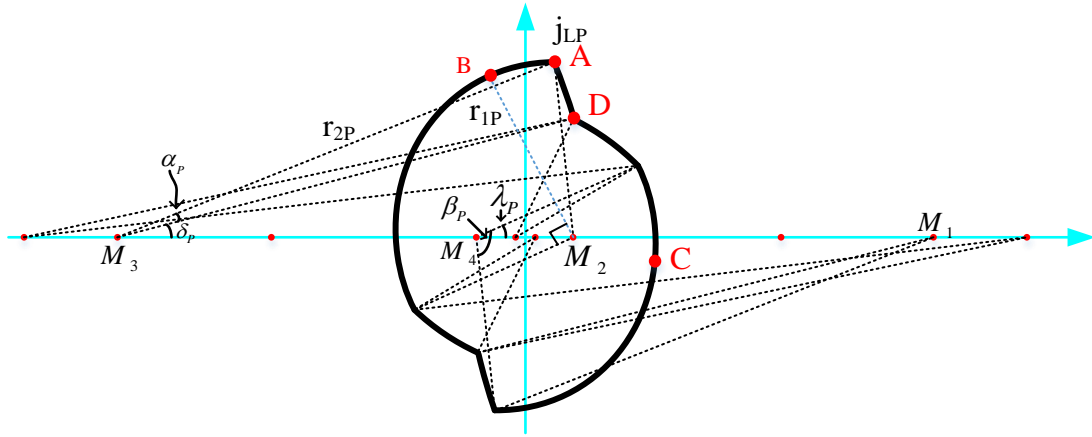
$$(m_{CN} + m_{C2max} - e_N)^2 + \left( \sqrt{\frac{C_1}{C_2} \frac{L_1 + Lm}{L_N}} j_{LN} \right)^2 = A_D^2 e_N^2 \tag{5.55}$$

where

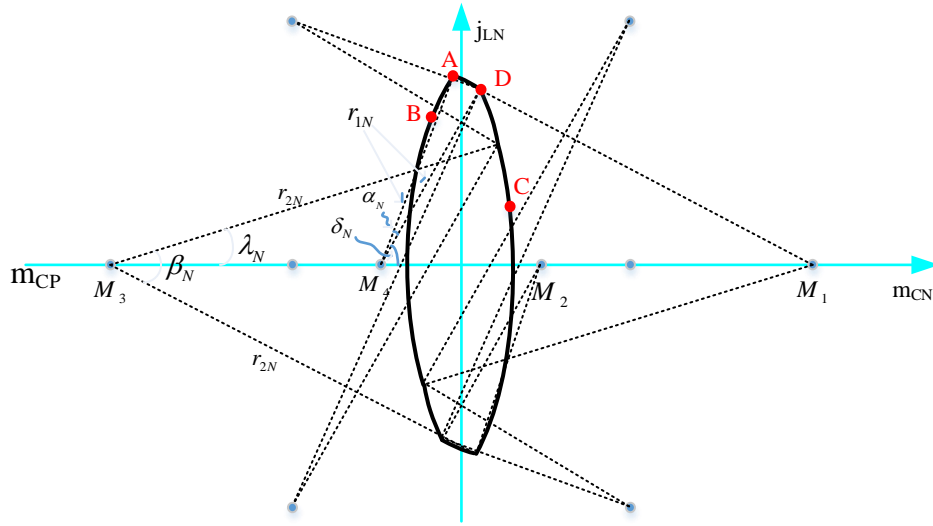
$$A_D = \sqrt{\left( \frac{m_{Cx0} + m_{Cx2} - e_x}{e_x} \right)^2 + \frac{j_{Lx0}^2 \times C_1 (L_1 + Lm)}{e_x^2 \times C_2 \times L_x}} \tag{5.56}$$

where  $m_{Cx0}$ ,  $m_{Cx2}$ , and  $j_{Lx0}$  are the initial values for  $x \in \{P, N\}$ .

The state plane trajectory for steady-state operation in DCM is shown in Fig. 5-19.



(a) SRC-P in DCM



(b) SRC-N in DCM

Fig. 5-19: The complete state-plane analysis of the CLLC resonant converter in DCM operating. (a) SRC-P and (b) SRC-N

The angles in Fig. 5-19 can be calculated as the equations shown in Table 5-5.

#### 5.4.2. Current stress in DCM

The maximum value of the primary side current occurs at point A in Fig. 13 where,  $j_{LP,max}$ ,  $j_{LN,max}$  are maximum. So, the peak value of the primary side current is:

$$i_{L_1,max} = \frac{j_{LP,max} I_{base,P} + j_{LN,max} I_{base,N}}{a_P + a_N} \quad (5.57)$$

where  $j_{LP,max}$  and  $j_{LN,max}$  are at point  $B$  in Fig. 13, the secondary side current reaches its maximum value when the current passes  $\pi/2$  after its zero crossing.

Table 5-5: Some angles for the state-plane diagrams of SRC-P and SRC-N in DCM

SRC-P	SRC-N
$\alpha_p = \sin^{-1}\left(\frac{j_{LP,1}}{r_{2P}}\right) - \delta_p$	$\alpha_N = \sin^{-1}\left(\frac{j_{LN,1}}{r_{1N}}\right) - \delta_N$
$\beta_p = \sin^{-1}\left(\frac{j_{LP,1}}{r_{1P}}\right) + \lambda_p$	$\beta_N = \sin^{-1}\left(\frac{j_{LN,1}}{r_{2N}}\right) + \lambda_N$
$\delta_p = \cos^{-1}\left(\frac{A_p + B_p M + m_{CP,0}}{r_{2P}}\right)$	$\delta_N = \sin^{-1}\left(\frac{j_{LN,0}}{r_{1N}}\right)$
$\lambda_p = \cos^{-1}\left(\frac{r_{1P}^2 + (A_p - B_p M - F_1)^2 - S_2^2}{2r_{1P}(A_p - B_p M - F_1)}\right)$	$\lambda_N = \sin^{-1}\left(\frac{j_{LN,X}}{r_{2N}}\right)$

Therefore, the peak value of the secondary current is obtained as:

$$i_{L_2 max} = \frac{r_{1P} \cos(\lambda_p) I_{base,P} + r_{1N} \sin\left(\beta_N - \frac{\pi}{2}d\right) I_{base,N}}{a_p + a_N} \quad (5.58)$$

#### 5.4.3. Voltage stress in DCM

It can be shown that the peak voltage of the resonant capacitors  $C_1$  and  $C_2$  in DCM occurs at points C and D respectively. At these points, the voltage across the  $C_1$  and  $C_2$  can be calculated:

$$v_{C1max} = V_{DC} \frac{m_{CP,0} + m_{CN,0}}{e_p + e_N} \quad (5.59)$$

$$v_{C2max} = \frac{V_{DC}}{n} \times \frac{e_N m_{CP,0} - e_P m_{CN,0}}{e_p + e_N} \quad (5.60)$$

### 5.5. Boundary Condition between CCM and DCM

Right before subinterval 1, when  $i_{L2}$  reaches zero if the voltage  $V_2$  in Fig. 1 is lower than  $V_{OUT}$ , the four bridge rectifier transistors cannot conduct and  $i_{L2}$  remains at zero. Therefore,

$$i_{L2} = 0 \rightarrow i_{L1} = i_{Lm} \rightarrow \frac{di_{L1}}{dt} = \frac{di_{Lm}}{dt} \rightarrow v_{L1} = \frac{L_1}{L_m} v_{Lm} \quad (5.61)$$

Writing Kirchhoff's Voltage Law in Fig. 5-20:

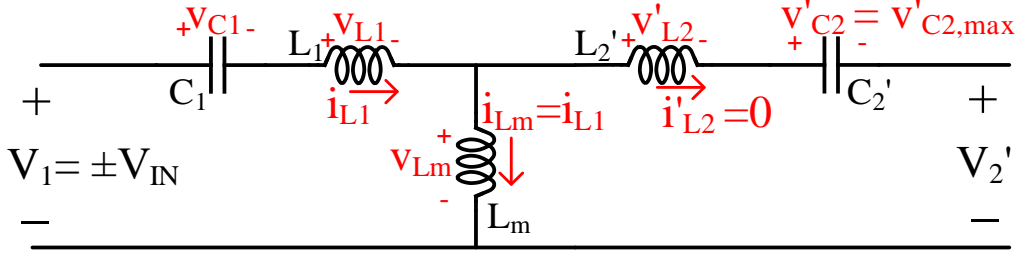


Fig. 5-20: The circuit diagram of the resonant tank for the DCM condition.

$$-V_1 + v_{C1} + v_{L1} + v_{Lm} = 0 \quad (5.62)$$

$$-v_{Lm} + v'_{L2} + v'_{C2} + V_2' = 0 \quad (5.63)$$

By solving (5.62) and (5.63), and knowing that  $v_{L2}$  is equal to zero,  $v_{C2}$  is maximum and  $V_1 = V_{IN}$ , then  $V_2'$  becomes:

$$V_2' = \frac{L_m}{L_1 + L_m} V_{IN} + \frac{L_m}{L_1 + L_m} v_{C1} + v'_{C2,max} \quad (5.64)$$

where  $v_{C1}$  at this instant can be obtained from (5.4) and (5.35):

$$v_{C1} = \frac{v_{CP} - v_{C2}}{e_P} = \frac{(r_{2P} + A_P - B_P M) V_{IN} - v'_{C2,max}}{e_P} \quad (5.65)$$

By substituting (5.65) into (5.64),  $V_2'$  would then become:

$$V_2' = \frac{L_m}{L_1 + L_m} \frac{e_P + r_{2P} + A_P - B_P M}{e_P} V_{IN} + \frac{e_P - 1}{e_P} v_{C2,max} \quad (5.66)$$

where  $v_{C2,max}$  was defined in (5.37).

The constraint for CCM operation ( $V_{rectifier} > V_{OUT}$ ) in normalized form is defined as:

$$M < \frac{(e_P + r_{2P} + A_P) L_m + (e_P - 1)(L_1 + L_m) \times v_{C2,max} / V_{IN}}{e_P (L_1 + L_m) + B_P L_m} \quad (5.67)$$

Fig. 5-21 shows the control plane characteristics of the CLLC resonant converter and the DCM boundary. This map is useful for design purposes as the designer can overlay the

operating region on it and see how the gain is changed with frequency and load and can find out if the converter operates in DCM.

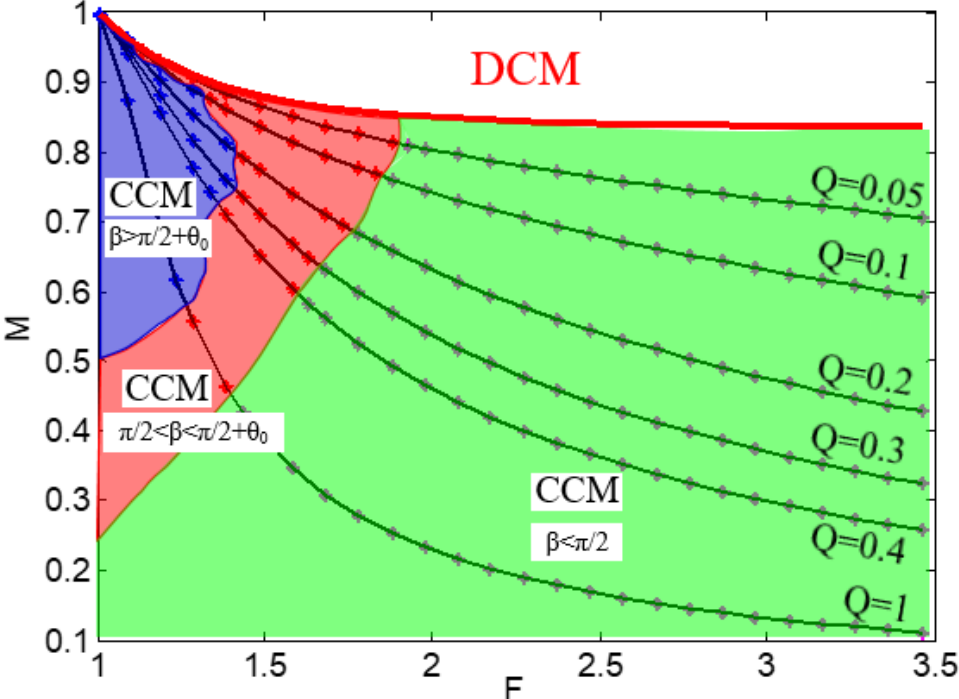


Fig. 5-21: Control plane diagram (M-F) with CCM/DCM boundaries for different values of  $Q$ .

When the switching frequency equals the resonant frequency ( $F=1$ ) then  $\beta_P=\pi$ . It means the switching-period consists of subintervals 1 and 3 and the duration of subintervals 2 and 4 is zero ( $\alpha_P=0$ ). The state-plane diagrams of SRC-P and SRC-N are given by two semicircles, as shown in Fig. 5-22.

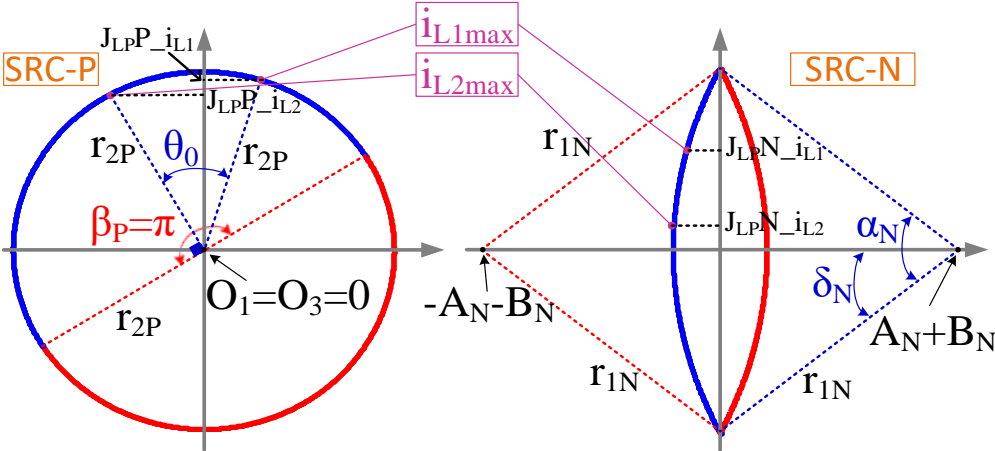
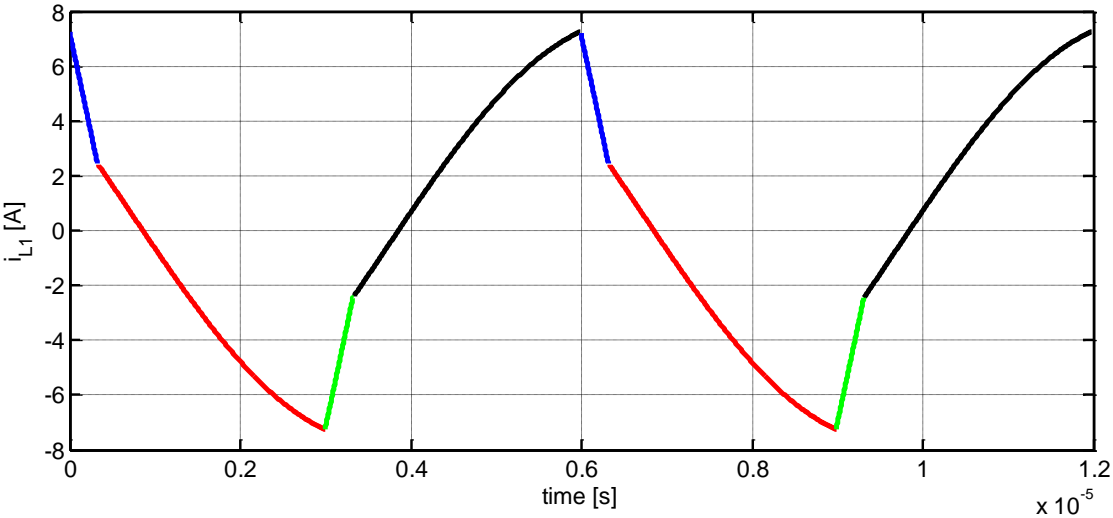


Fig. 5-22: State-plane analysis of SRC-P and SRC-N in the boundary condition.

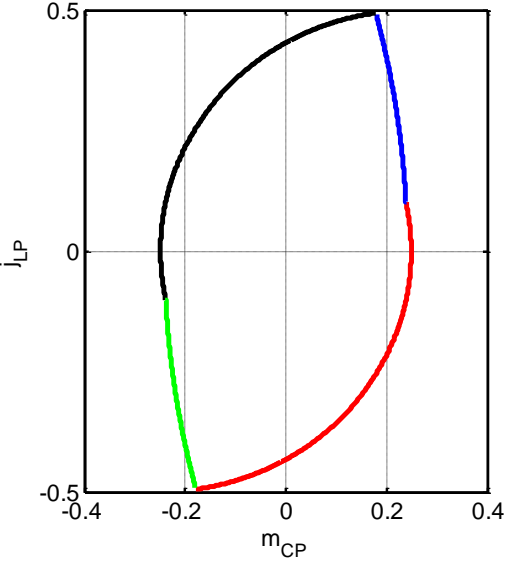
In this condition equations (22) through (27) will be used to obtain  $i_{L1,max}$ , and  $i_{L2,max}$ . The peak capacitor voltages  $v_{C1,max}$  and  $v_{C2,max}$ , can be calculated from (34) and (37).

### 5.6. Simulation Verification

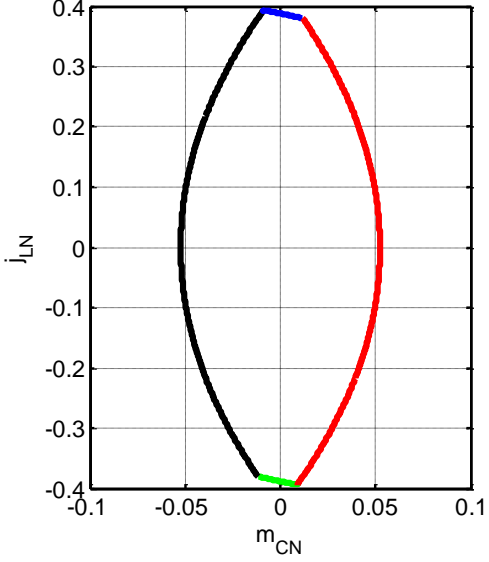
Fig. 5-23-(a) illustrates the time domain modeling based on the state plane analysis for the primary current of the CLLC resonant converter. The corresponding state plane analysis, i.e. SRC-P and SRC-N, are also shown in Fig. 5-23-(b) and Fig. 5-23-(c), respectively.



(a)



(b)



(c)

Fig. 5-23: The time domain waveform obtained by the state plane analysis of  $i_{L1}$  (a), and the state plane analysis of SRC-P (b), and SRC-N (c).



The maximum current of  $L_1$  can be determined by the state plane analysis (see Fig. 5-24-a) and time domain simulation with PSIM (see Fig. 5-24-b).

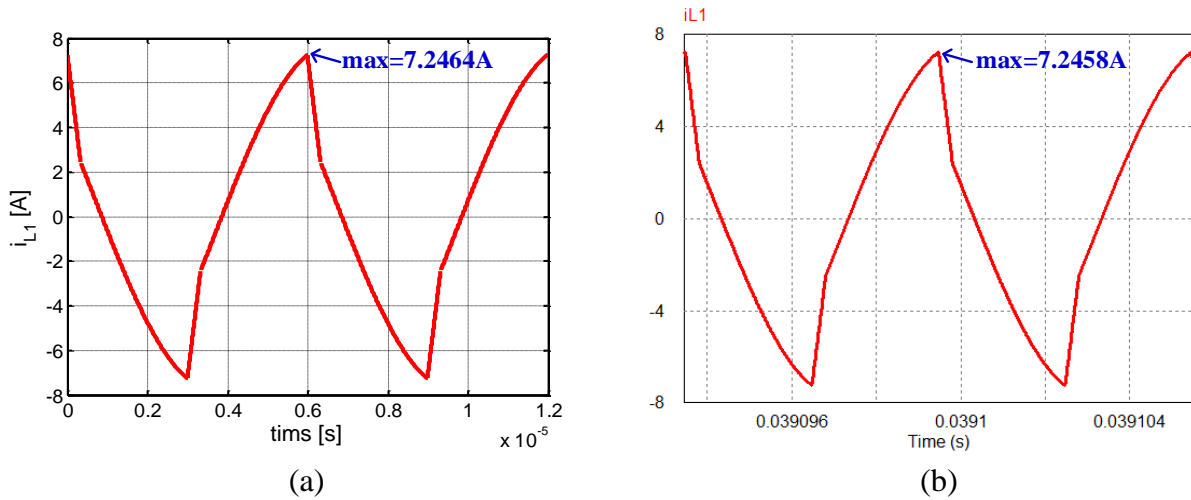


Fig. 5-24: A comparison for  $i_{L1max}$  based on the state plane analysis (a) and simulation with PSIM (b).

A detailed simulation verification will be done in the next part.

## 5.7. Experimental Verification

The state-plane analysis obtained in the previous part must be checked to physically verify the results obtained from the proposed state-plane analysis. Also, the results must be checked with simulation.

### 5.7.1. Specification of the experimental set up

An experimental prototype is considered to verify the proposed state plane analysis of the CLLC resonant converter. Table 5-6 shows the main specifications of the prototype.

Table 5-6: Components of the Experimental CLLC Resonant Converter

Parameter	Value	Parameter	Value
$S_1 \sim S_8$	GS66508B GaN	$L_1$	25 $\mu$ H
$D_1 \sim D_8$	C4D10120 SiC	$L_2$	25 $\mu$ H
$C_1$	99 nF	$L_m$	125 $\mu$ H
$C_2$	99 nF	$V_{out}$	250~400 V
$C_o$	220 $\mu$ F	$V_{in}$	400 V
$n$	1:1	$f_{sw}$	90~350 kHz

A 3.3-kW bidirectional CLLC resonant converter with the specifications, as listed in Table 5-6, has been developed to validate the proposed analysis. The prototype is built using

GS66508B GaN transistors on both sides. As the synchronous rectification is not a primary concern of the proposed method of analysis and for the sake of simplicity, during testing the circuit in each direction (forward or reverse power transfer) the transistors of the secondary side are bypassed by adding anti-parallel diodes. Fig. 5-25 depicts the experimental set up. It should be mentioned that the resistive load is used to provide the required voltage and output power.

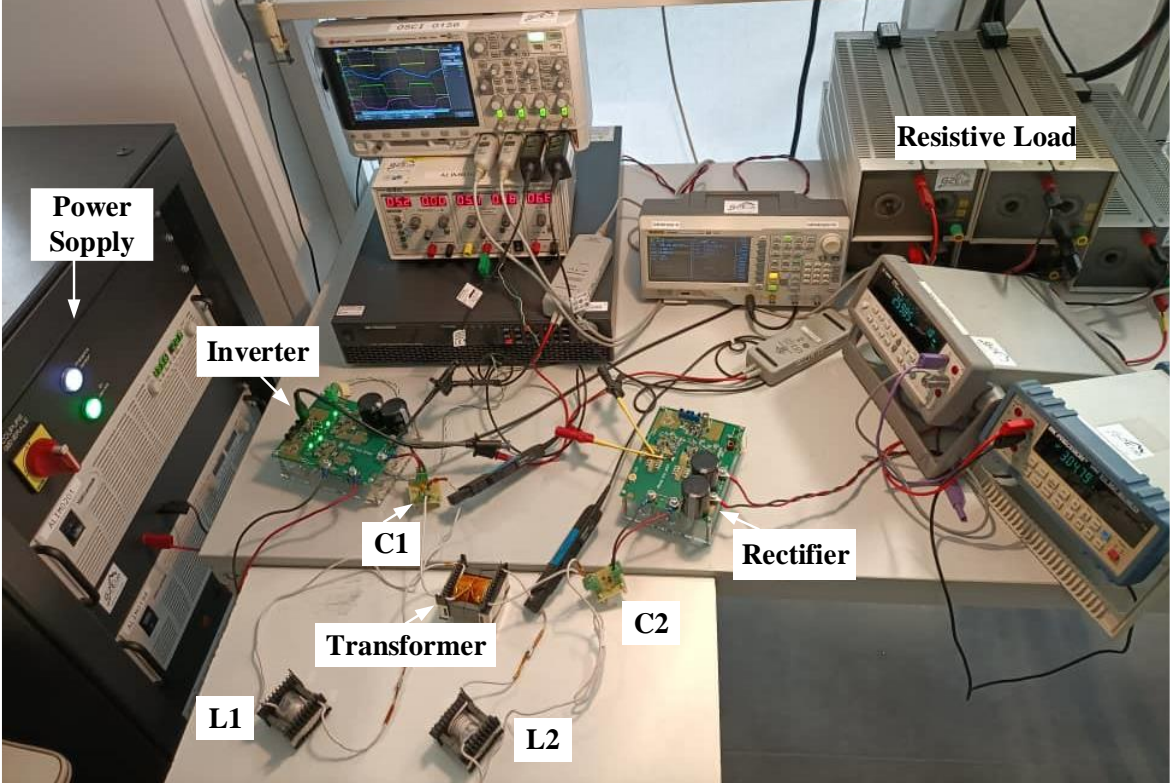



Fig. 5-25: The 3.3kW bidirectional EV charger experimental set up

The prototypes have been designed for the G2V application with the input voltage of 400V (which can be prepared by a power supply or by the rectified grid voltage (220V AC) and a boost converter) to prepare the output voltages between 250V to 400V and ensure the maximum power of 3.3kW.

5.7.2. Semiconductors

The GS66508B GaN transistor is employed for the inverting parts as the main switches. Low ON resistance and high frequency operating are the main advantages of this transistor. The absolute maximum voltage rating of this transistor is 650V, which is suitable for 250V~450V applications. A cooling system is ensured for the GaN transistors thanks to an external fan for each GaN transistor for reducing their junction temperature and fixing the thermal resistance. The electrical characteristics of this transistor are listed in Table 5-7.

Table 5-7: Electrical characteristics of GS66508B transistor

Parameter	Symbol	Value	Unit	Diagram
Drain-to-source voltage	$V_{DS}$	650	V	
Gate-to-source voltage	$V_{GS}$	-10 to +7	V	
Junction temperature	$T_J$	-55 to 150	°C	
Drain current (at 25°C)	$I_D$	30	A	
Drain current (at 100°C)	$I_D$	25	A	

The C4D10120E diode is also utilized for the rectifying parts in parallel with the GaN transistors while the corresponding transistors have been switched OFF.

### 5.7.3. Gate driver circuit

An eligible gate driver should meet the following requirements:

- for ON state: apply a correct positive voltage to the gate-to-source for possessing low ON resistance;
- for OFF state: keep the switch in OFF state regardless of any undesirable transient pulse;
- for transition state: make the transition correctly to not only bring about immediate transition for minimizing switching losses but also provide a leisurely slope to reduce electromagnetic interference (EMI).

In this dissertation, the IC SI8271GB-IS is applied as the gate driver to turn the corresponding transistors to ON and OFF conditions, where the Gate-to-Source voltage ( $V_{GS}$ ) of +6V makes the transistor ON, and  $V_{GS}=-3V$  makes it OFF (to prevent unexpected turn-on). Therefore, a 9V power supply is needed, where we employed the isolated DC/DC converter PES1-S5-S9-M-TR for changing 5V to 9V. The BZX84C6V2 diode Zener is utilized as a voltage divider for extending 9V to +6V and -3V. The gate driver power supply is shown in Fig. 5-26, where GNDH1 is the isolated GND, VDDH1 is the +6V voltage for turning-ON, and VEEH1 is the -3V voltage for turning-OFF the GaN transistor.

The generated voltages are applied to the SI8271GB-IS driver. Furthermore, this IC driver has separate pins for applying to the gate to have different ON and OFF resistors. The gate resistor for ON state is selected as 15Ω to limit the gate's current, and it is 2Ω for OFF state for

fast turn-OFF capability. A ferrite bead is also added in series to the gate circuit for high-frequency noise reduction. Fig. 5-27 demonstrates the complete diagram of the gate driver.

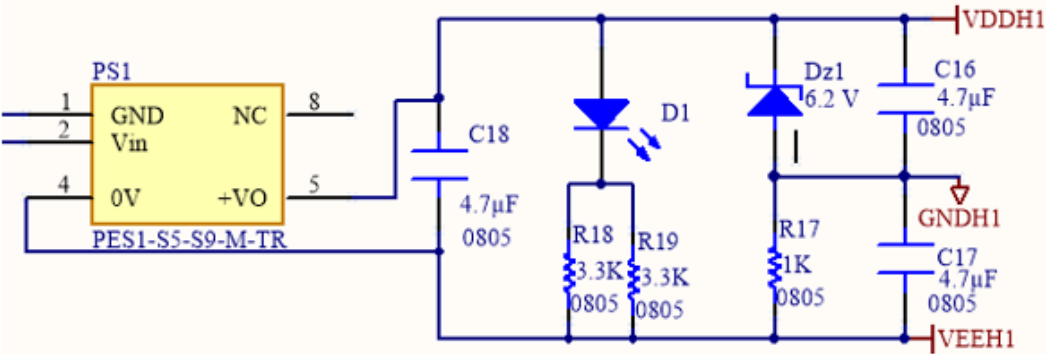


Fig. 5-26: The -3V and +6V circuit diagram using PES1-S5-S9-M-TR to supply gate driver

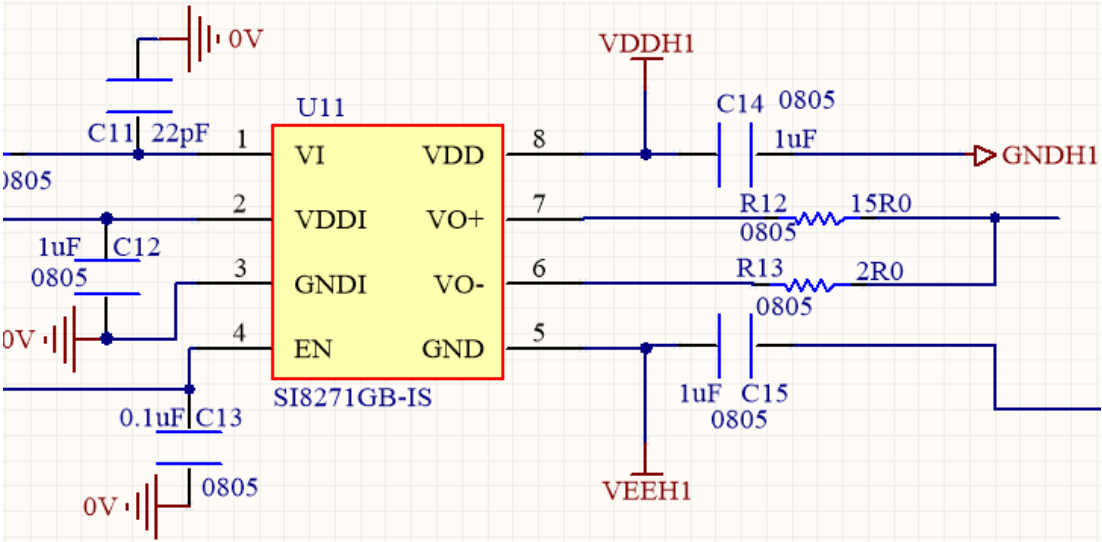


Fig. 5-27: The SI8271GB-IS gate driver circuit diagram

5.7.4. Input signals and dead-time circuit

In corresponding to the input signals of switching, the designed circuit has two independent capabilities:

1. In each leg, the high-side and low-side transistors are turned ON and OFF thanks to the independent signals generated by an external microcontroller. It should be mentioned that a specific dead-time between the signals must be implemented in the microcontroller.
2. A signal with typically 50% duty cycle is applied to a specific circuit (dead-time circuit) to provide the high-side and low-side signals with configurable dead-time.

A single pole double through (SPDT) switch is applied to prepare the capability of working with one of the aforementioned capabilities. In this dissertation, the second capability is employed. A configurable circuit is provided to control the dead-time from  $\approx 0\text{ns}$  to  $1000\text{ns}$  based on the designer's decision. It is done using a NAND integrated circuit 74VHC132MTCX, and an RC circuit to provide the expected dead-time using two potentiometers. This circuit is entitled the dead-time circuit and is shown in Fig. 5-28:

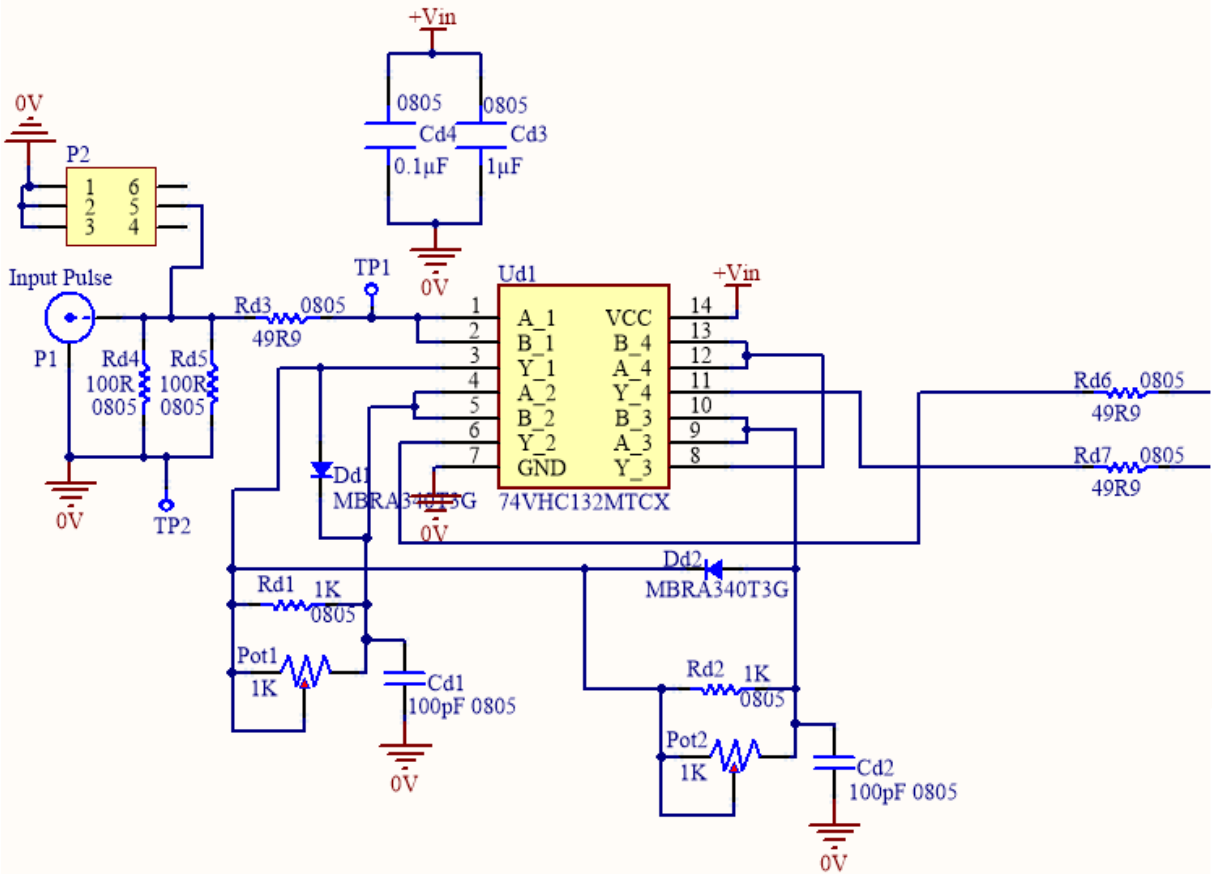


Fig. 5-28: The dead-time circuit using 74VHC132MTCX NAND IC and RC circuits

where the dead-time is controlled by the TR1 and TR2 potentiometers. The default value is set to 100ns.

5.7.5. Resonant tank

The resonant tank contains two parts: a magnetic part and resonant capacitors. The magnetic parts are made by EE-shape cores with 3C90 material. The value of leakage inductance and magnetizing inductance is measured by the impedance analyzer KEYSIGHT E4990A 20 Hz-120MHz with Keystone 16047E terminal for  $F \leq 100\text{MHz}$  (see Fig. 5-29).

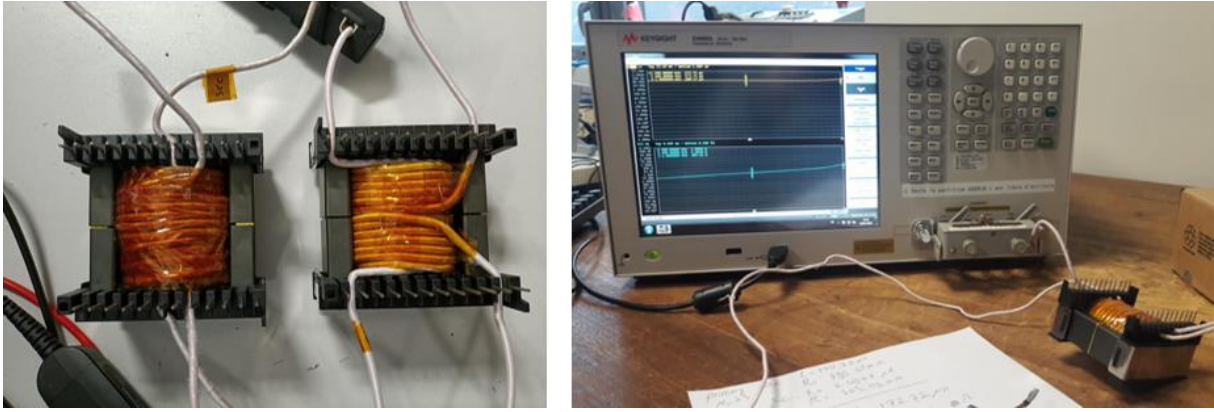


Fig. 5-29: The magnetic transformers (left figure) and impedance analyzer to measure leakage inductance and magnetizing inductance

The short circuit and open circuit tests are carried out to find the value of leakage and magnetizing inductance. For a short circuit test, the secondary side is shorted and the value of inductance ( $L_{SC}$ ) is measured in the related frequencies. The inductance value in the open circuit condition ( $L_{OC}$ ) is also measured when the secondary side is left as open circuit. These conditions are shown in Fig. 5-30.

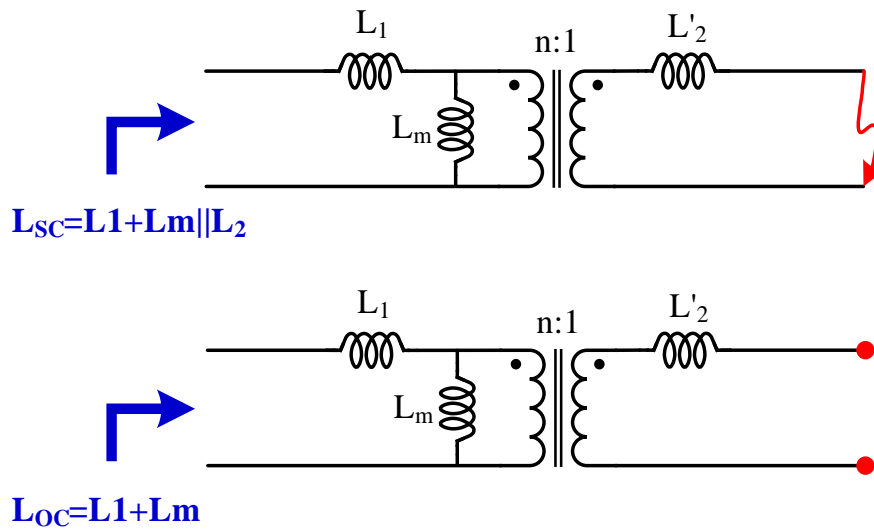


Fig. 5-30: Short circuit test (top) and open circuit test (bottom) to measure the leakage inductance and magnetizing inductance

Therefore, the leakage and magnetizing inductance can be determined for  $L_1 = L_2 = L_{Leakage}$  as (5.68) and (5.69), respectively.

$$L_{Leakage} = L_1 = L_2 = L_{OC} - \sqrt{L_{OC}^2 - L_{OC} \times L_{SC}} \quad (5.68)$$

$$L_{Magnetizing} = L_M = \sqrt{L_{OC}^2 - L_{OC} \times L_{SC}} \quad (5.69)$$

Also, the Litz wire 35819-D160 is also used for winding with 280 strands and a diameter of 0.15mm for each strand to reduce the skin effect. It should be mentioned that this selection is based on the maximum required current. The final magnetic part is shown in Fig. 6-10:

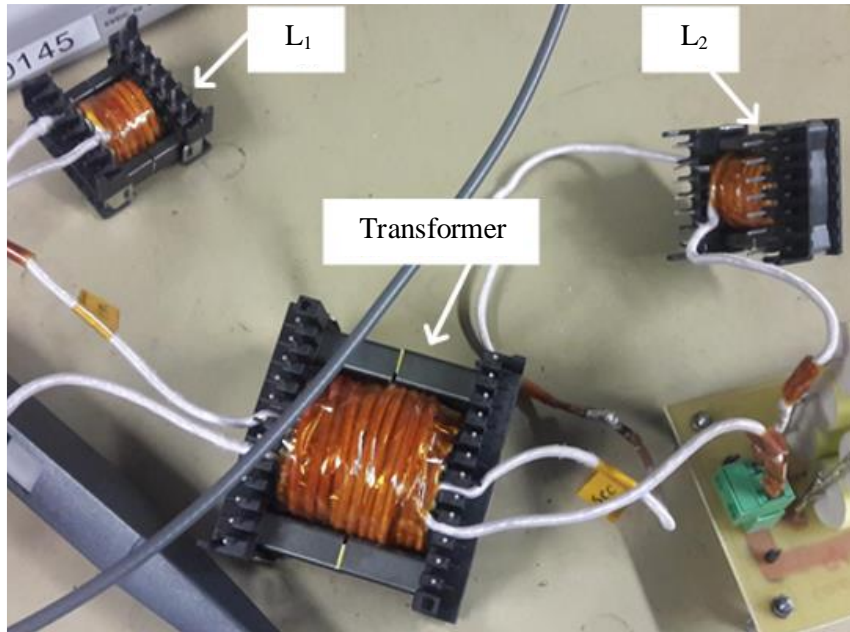


*Fig. 5-31: Physical implementation of the transformer, primary inductor (L1), and secondary inductor (L2) obtained by the initial design.*

The resonant capacitor with modularity capability is shown in Fig. 5-32:

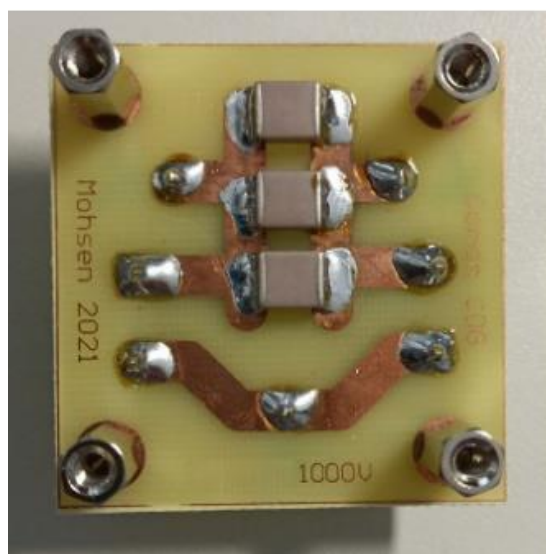
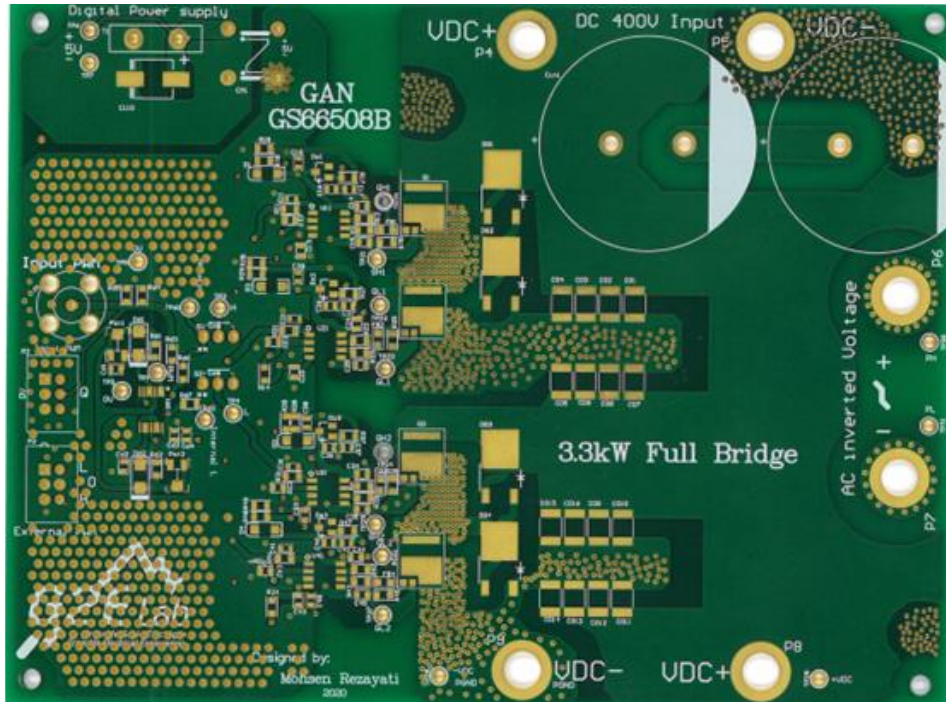


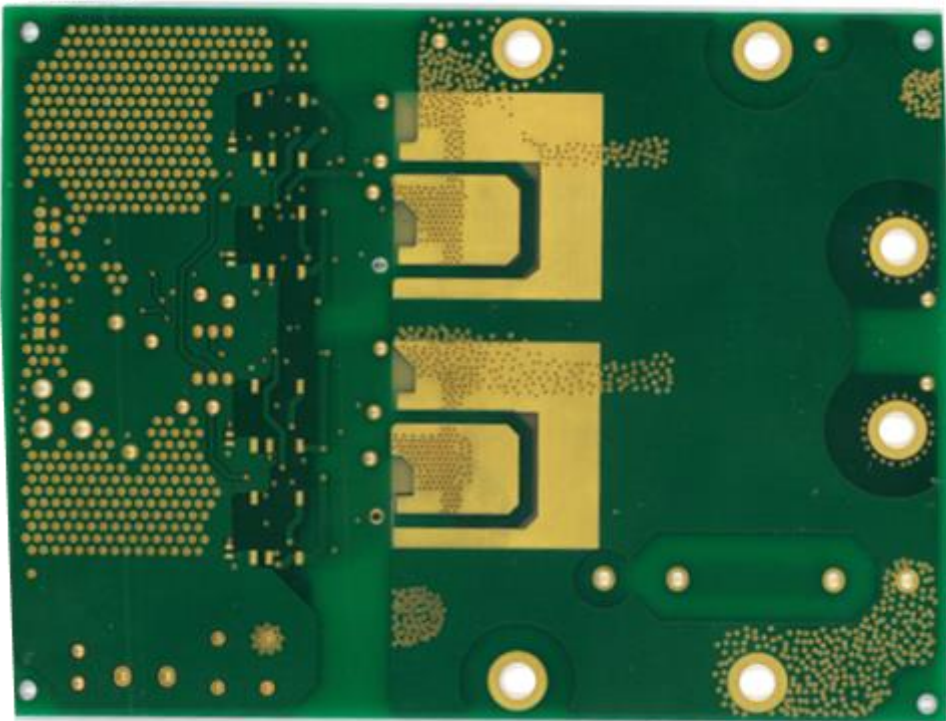
*Fig. 5-32 : The resonant capacitor for the resonant capacitors*

### 5.7.6. PCB

The printed circuit board (PCB) is designed in Altium Designer®, where a 4 layers PCB is considered to occupy a lower size and reduce EMI.



(a) Top layer



(b) Bottom layer

*Fig. 5-33: The top layer (a) and bottom layer (b) of the final PCB of the dual active full-bridge for using as the inverting and rectifying parts*



The PCB contains two exactly similar active bridges which will be used as the primary and secondary active bridges to provide bidirectional power transfer. The top and bottom layers of the PCB are shown in Fig. 5-33-(a) and Fig. 5-33-(b), respectively.

According to the bottom layer shown in Fig. 5-33-(b), it is manifest that the GaN transistor can dissipate the generated heat to the air around it by the uncoated metal plate. Furthermore, it is possible to add a heatsink to the plate for further temperature reduction. In this dissertation, we added a fan at the bottom of each active bridge in order to fix the thermal resistance and reduce the junction temperature of GaN transistors.

#### 5.7.7. Main Waveforms and Comparisons

Using two active bridge converters, one in the role of an inverter and the other in the role of a rectifier, it is possible to build a CLLC resonant converter by connecting them to the designed resonance tank. Fig. 5-31 shows the parts related to the transformer and two resonant inductors. It should be noted that their values were obtained from the initial design and their values are not optimal. Also, by performing several tests, the accuracy of the implemented converter was evaluated.

The voltage of resonant capacitors, the current of resonant inductors, and the voltage of switching parts have been measured thanks to the THDPO200 differential voltage probe and TCP0030 current probe on KEYSIGHT DSOX3024T 200MHz 5GSa/s oscilloscope. The observed waveforms will be compared with the results obtained by the state-plane analysis.

The main waveforms of resonant elements, i.e. the inductors currents and capacitors voltages, for different operating points are depicted in Fig. 5-34.

To verify the accuracy of the proposed model, the results coming from the proposed analysis are compared with those of the FHA method, time domain exact simulation by PSIM®, and experiments.

#### 5.7.8. State-plane Analysis Experimental Verifications

In this part, the proposed state-plane analysis, which was presented in chapter 3, is examined by the experimental tests. These verifications are as follows.

##### *Output and Control Plane Characteristics*

Fig. 5-35 compares the control plane characteristics obtained from the state-plane analysis, FHA method, simulation, and experiment results when the switching frequency changes from

101 kHz ( $F = 1$ ) to 350 kHz ( $F = 3.45$ ), and the output power is varied between 430 W and 1500 W.

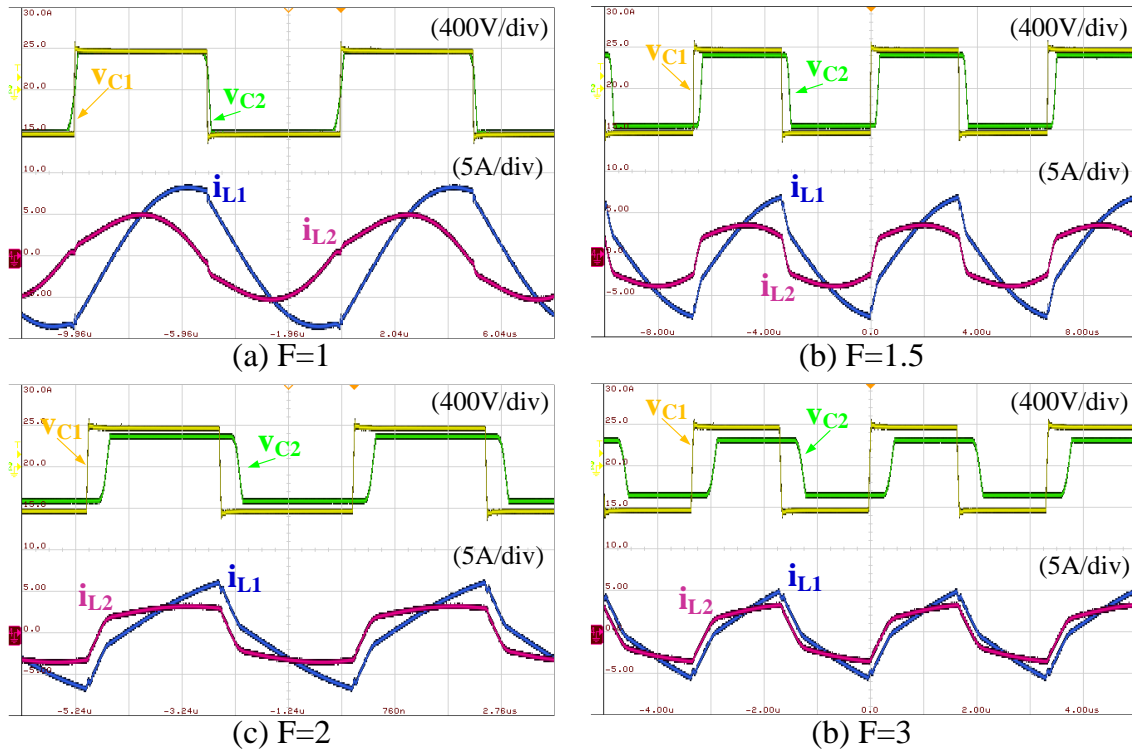


Fig. 5-34: Experimental waveforms of CLLC resonant converter in CCM for (a)  $F = 1$ ,  $P_{out} = 1.2$  kW, (b)  $F = 1.5$ ,  $P_{out} = 960$  W, (c)  $F = 2$ ,  $P_{out} = 790$  W, and (d)  $F = 3$ ,  $P_{out} = 570$  W.

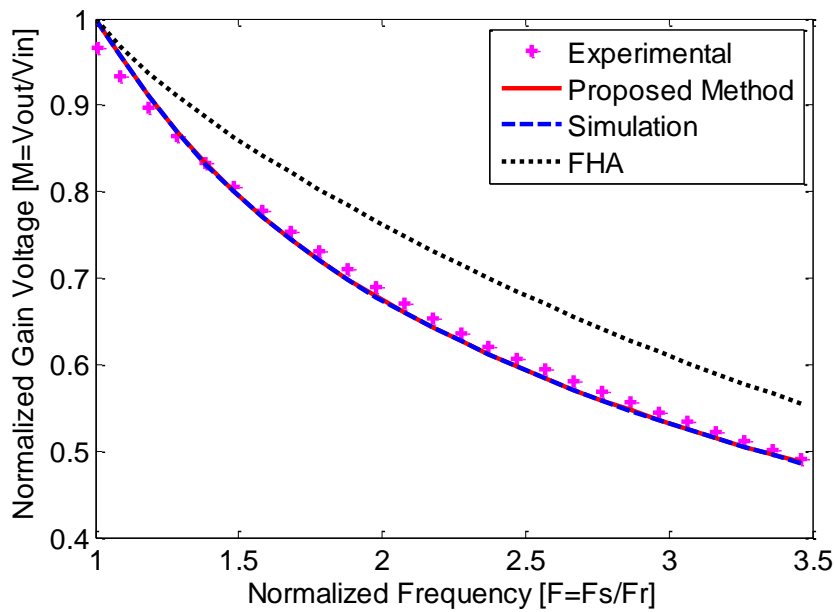


Fig. 5-35:  $M$ - $F$  diagram of the CLLC resonant converter.

As can be seen, the results from the proposed method are well matched with the simulation and experimental results. It can also be seen that the gain voltage predicted by FHA is substantially higher than the actual value, which means that care should be taken when the FHA method is used for the design and optimization of the CLLC converter. The proposed analysis gives exact values of the voltage and current of the components and can improve the power loss estimation and design optimization [55].

In Fig. 5-36, the output characteristic for  $f_{sw} = 150 \text{ kHz}$  and  $P_{out} = 0.9\sim 1.5 \text{ kW}$  is compared. The results based on the proposed state-plane analysis are consistent with experimental and simulation results in a wide range of load variation, in contrary to those of the FHA method.

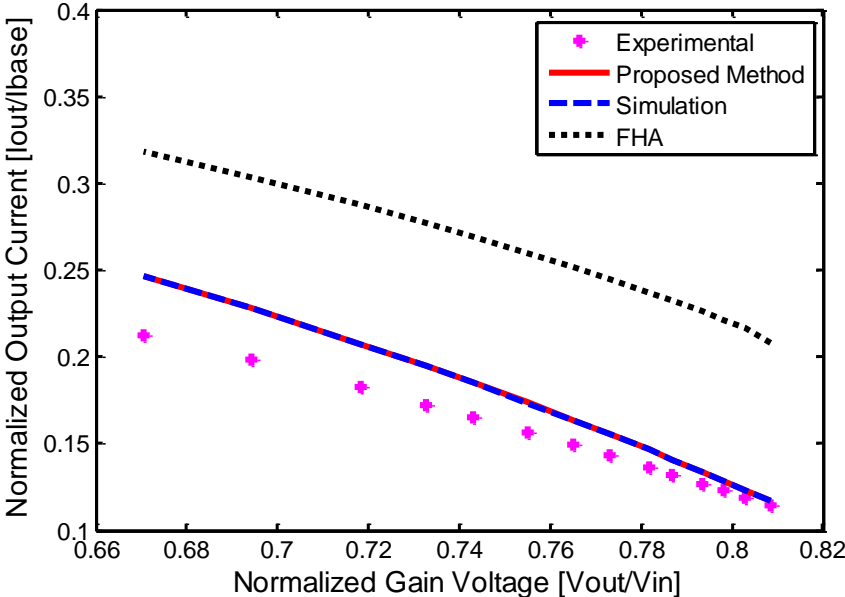
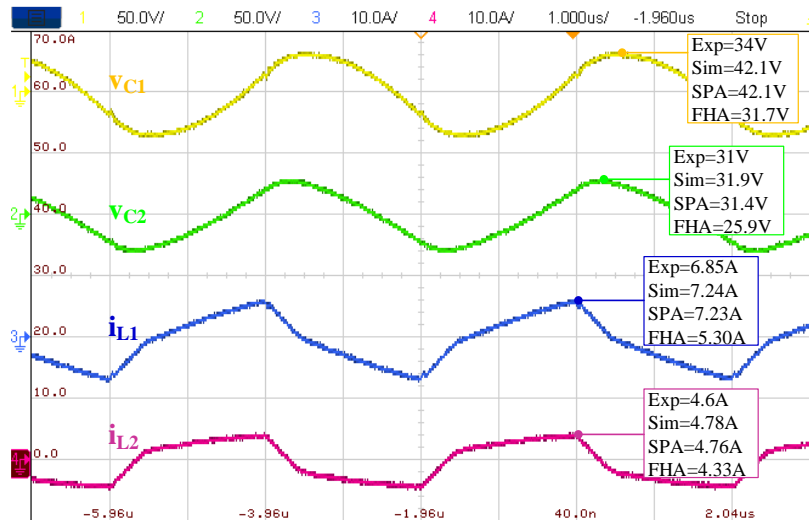


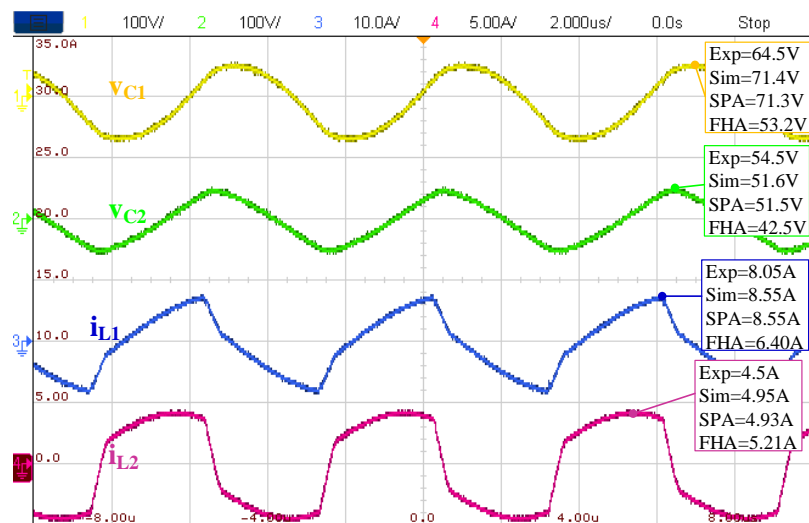
Fig. 5-36: M-J diagram of the CLLC resonant converter.

*Maximum Current and Voltage of Resonant Elements*

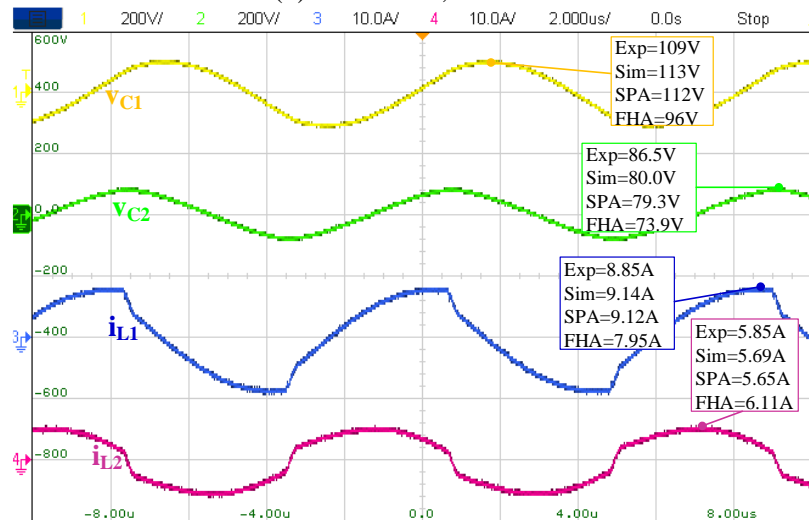
As previously explained, depending on  $\beta_P$  there are three possible trajectories that determine the peak inductors current accordingly. Fig. 5-37 shows waveforms for the forward power transfer operation at three operating points corresponding to each type of trajectory. Time domain representation is the experimental results. In this figure, the numbers on the box are the comparison between the peak values for experiments, simulations, state-plane analysis, and the FHA method. For the FHA method,  $f_{sw}$  is 268.5 kHz, 193 kHz, and 132.8 kHz respectively.



(a)  $P_{out}=700W$ ,  $V_{out}=254V$



(b)  $P_{out}=1kW$ ,  $V_{out}=307V$

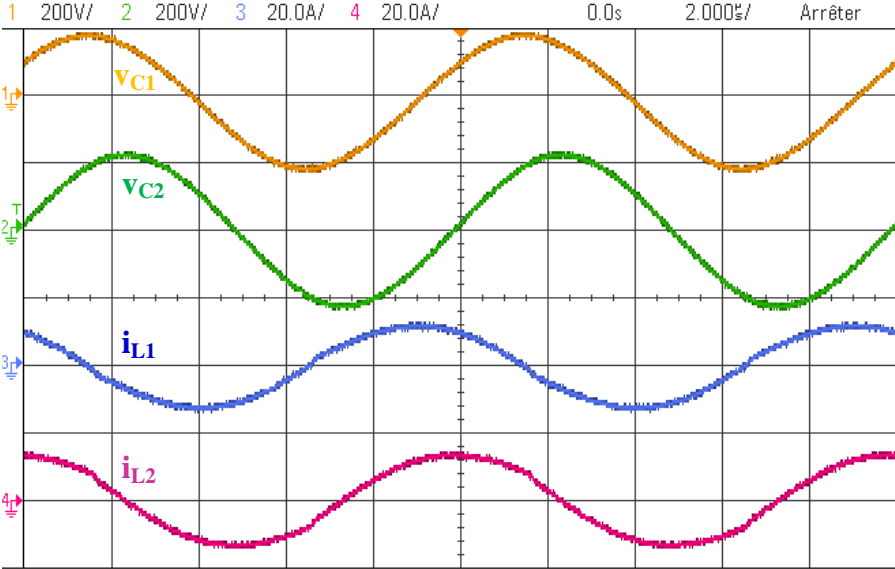


(c)  $P_{out}=1.4kW$ ,  $V_{out}=360V$

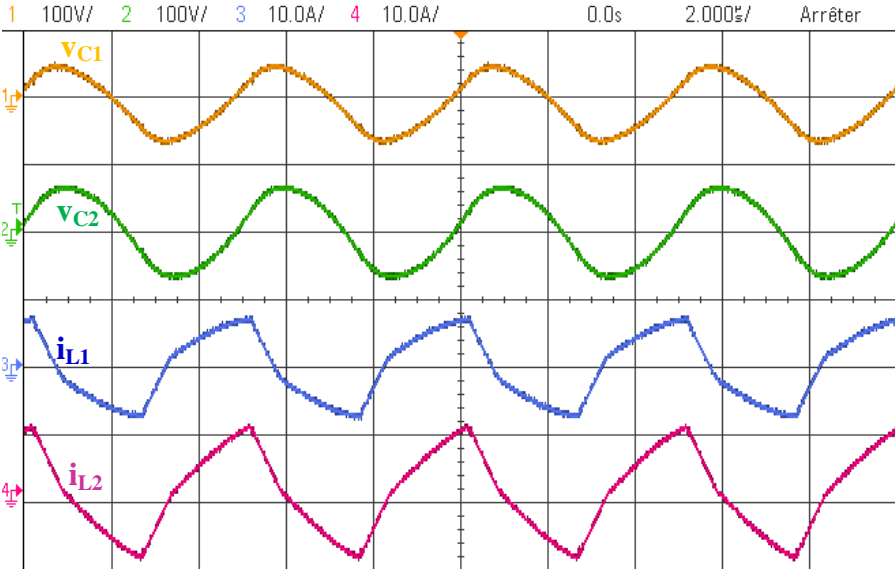
Fig. 5-37 : Current and voltage of the resonant elements for the forward power transferring at: (a)  $\pi/2 < \beta_P$  at  $P_{out} = 700 W$ ,  $V_{out} = 254 V$ ,  $f_{sw} = 250 kHz$ , (b)  $\pi/2 < \beta_P < \theta_0$  at  $P_{out} = 1 kW$ ,  $V_{out} = 307 V$ ,  $f_{sw} = 170 kHz$ , and (c)  $\beta_P > \pi/2 + \theta_0$  at  $P_{out} = 1.4 kW$ ,  $V_{out} = 360 V$ ,  $f_{sw} = 120 kHz$ .

Fig. 5-37 manifests that the peak values obtained by the proposed analysis are perfectly matched with the experimental results and the exact circuit simulation. The peak values predicted by the FHA analysis however are lower than the actual values which can lead to improper selection of the components.

Fig. 5-38 shows the reverse power transfer operation of the CLLC resonant converter at  $F = 1$  and  $F = 2$ . In this case, the input voltage is applied to the load connection, and a resistive load is connected to the input connector.



(a)  $P_{out}=3025W$ ,  $V_{out}=385V$



(b)  $P_{out}=918W$ ,  $V_{out}=212.5V$

Fig. 5-38: Current and voltage waveforms of the resonant elements for the reverse power transfer mode under different conditions: (a)  $P_{out} = 3025 W$ ,  $V_{out} = 385 V$ ,  $f_{sw} = 100 kHz$ , (b)  $P_{out} = 918 W$ ,  $V_{out} = 212.5 V$ ,  $f_{sw} = 200 kHz$ .

### Soft Switching Condition

Fig. 5-39 illustrates the voltage across a primary side transistor and the corresponding gate signal for minimum dead-time that ensures ZVS, i.e. (5.43).

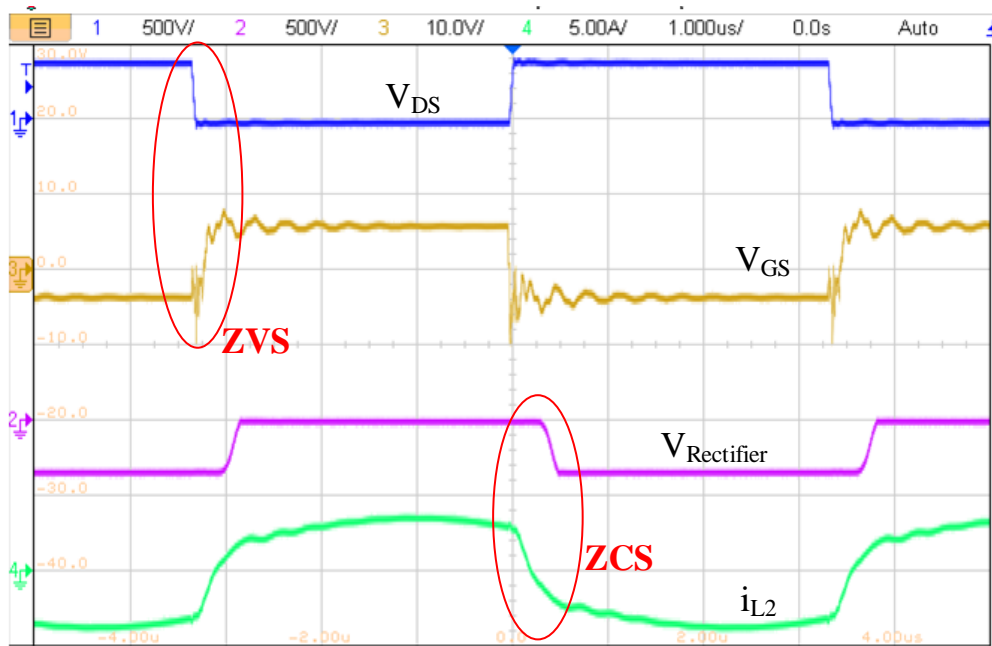


Fig. 5-39: Waveforms corresponding to minimum dead-time that ensures ZVS and ZCS on the rectifier.

In the above figure, the voltage and current waveforms of secondary side rectifier diodes are also shown, where the secondary side diodes are turned OFF in ZCS condition. Fig. 5-40 shows the simulation waveform of the switch voltage when the dead-time is set at the minimum value as in (5.43).

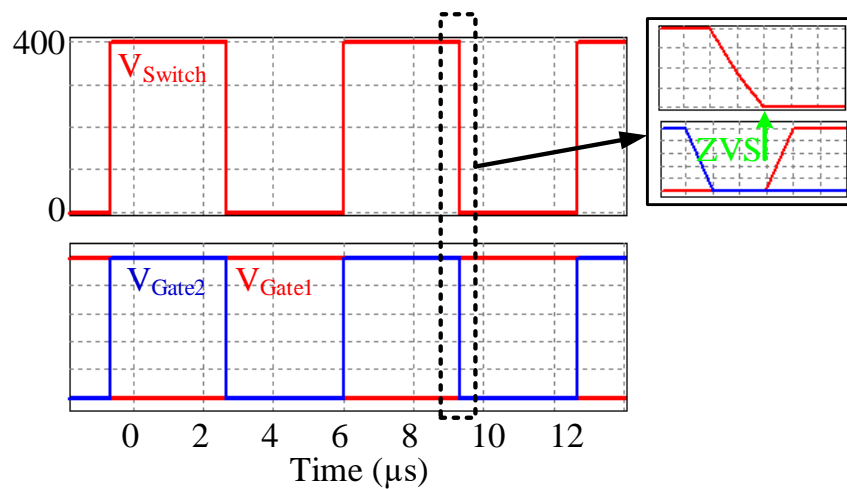


Fig. 5-40: Simulation of minimum dead-time (boundary condition) for gate pulses and the switch voltage to ensure ZVS.

As can be seen in the above figure, the dead-time is minimum and the switch operates in the boundary condition at ZVS. If a smaller value is applied to  $t_{dt}$ , the ZVS will be lost.

*Boundary and DCM Operating*

Investigating the constraint of (5.67) shows that a CCM to DCM transition happens at  $F = 1.3$  and  $Q = 0.0356$ . Also, Fig. 5-41 compares the secondary side current,  $i_{L2}$ , obtained by circuit simulation and the proposed state space equations.

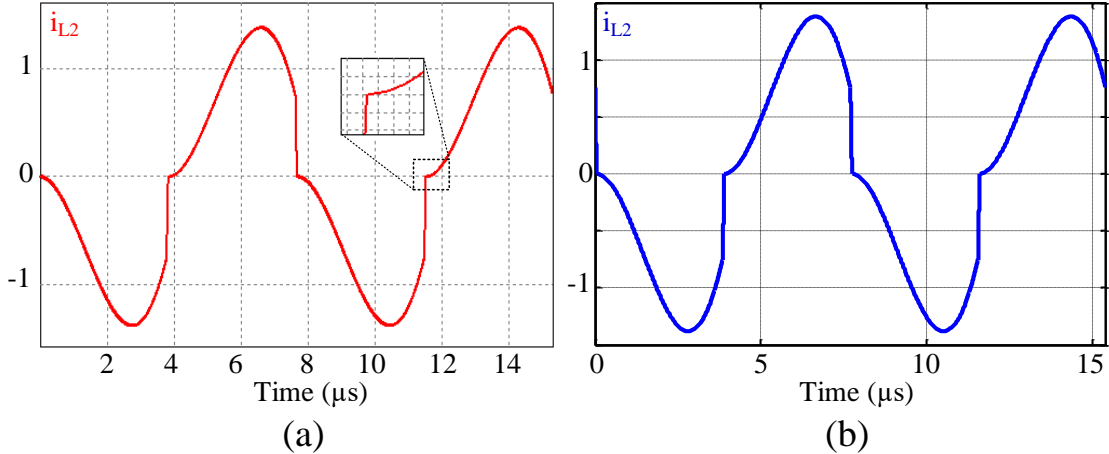


Fig. 5-41: The secondary side current in the boundary condition by; (a) simulation, and (b) state-plane analysis.

Obviously, the circuit simulation confirms the operation of the circuit in the boundary condition which is expected by the proposed state-plane analysis. Further decreasing the load current causes the converter to operate in DCM. Fig. 5-42 depicts experimental results showing DCM operation at 0.6A (corresponding to  $Q = 0.0239$ ) with  $M = 0.9953$ .

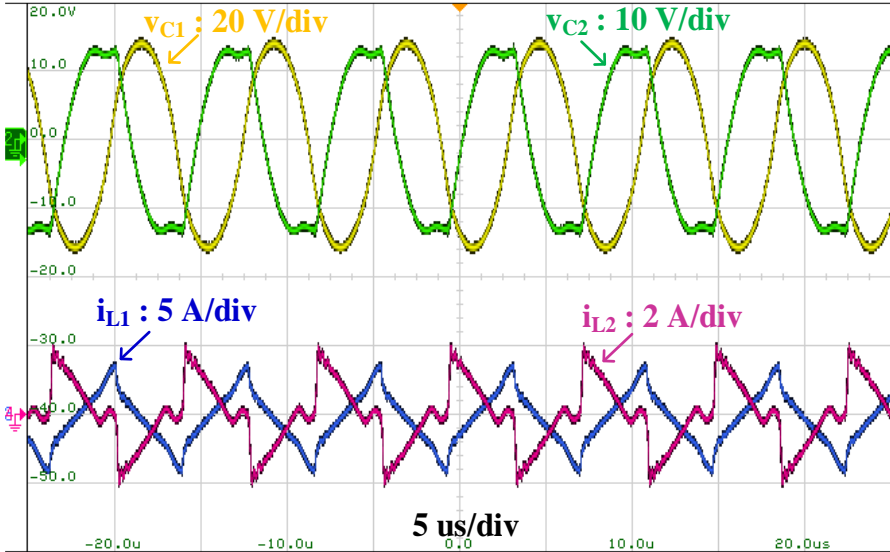


Fig. 5-42: Experimental test in the DCM operating.

### 5.7.9. General Comparisons

Table 5-8 compares the results obtained from the proposed state-plane analysis, exact circuit simulation, and the FHA method for two operating points when the converter operates in the forward power transfer mode. In this table, the error of a parameter  $X$  is defined by:

$$Error = \frac{|X_{MEASUREMENT} - X|}{X_{MEASUREMENT}} \times 100\% \quad (5.70)$$

*Table 5-8: Comparison of the Measurement (Meas.), PSIM Simulation (Sim.), State-Plane Analysis (SPA), and First Harmonic Approximation (FHA) Results for Forward Power Transfer and two output powers.*

Parameter	Power = 1281W								Power = 527W							
	Meas.		Sim.		SPA		FHA		Meas.		Sim.		SPA		FHA	
	Value	Value	Error	Value	Error	Value	Error	Value	Error	Value	Value	Error	Value	Error	Value	Error
V <sub>OUT</sub> [V]	347.3	347.3	0.00	347.3	0.00	347.3	0.00	216.8	216.8	0.00	216.8	0.00	216.8	0.00	216.8	0.00
I <sub>OUT</sub> [A]	3.69	3.69	0.00	3.69	0.00	3.69	0.00	2.43	2.43	0.00	2.43	0.00	2.43	0.00	2.43	0.00
f <sub>sw</sub> [kHz]	130.2	129.3	0.69	129.3	0.69	146	12.14	298	272	8.72	272	8.72	330	10.74		
i <sub>L1max</sub> [A]	8.85	9.07	2.49	9.03	2.03	7.47	15.59	6.05	6.35	4.96	6.35	4.96	4.63	23.47		
i <sub>L2max</sub> [A]	5.15	5.46	6.02	5.43	5.44	5.80	12.62	4.4	4.55	3.41	4.55	3.41	3.82	13.18		
V <sub>C1max</sub> [V]	96.5	102.91	6.64	101.48	5.16	82.29	14.73	27	28.85	6.85	29.30	8.51	22.58	16.37		
V <sub>C2max</sub> [V]	78.5	72.58	7.54	72.09	8.16	63.85	18.66	23	22.76	1.04	22.57	1.87	18.61	19.09		

*Table 5-9: Comparison of the Measurement (Meas.), PSIM Simulation (Sim.), State-Plane Analysis (SPA), and First Harmonic Approximation (FHA) Results for Reverse Power Transfer and two output powers.*

Parameter	Power = 3025W								Power = 918W							
	Meas.		Sim.		SPA		FHA		Meas.		Sim.		SPA		FHA	
	Value	Value	Error	Value	Error	Value	Error	Value	Error	Value	Value	Error	Value	Error	Value	Error
V <sub>OUT</sub> [V]	385	385	0.00	385	0.00	385	0.00	212.5	212.5	0.00	212.5	0.00	212.5	0.00	212.5	0.00
I <sub>OUT</sub> [A]	7.85	7.85	0.00	7.85	0.00	7.85	0.00	4.32	4.32	0.00	4.32	0.00	4.32	0.00	4.32	0.00
f <sub>sw</sub> [kHz]	105	107.4	2.28	107.5	2.28	110	4.76	199.5	196.9	1.30	196.9	1.30	220.5	10.53		
i <sub>L1max</sub> [A]	14.17	13.99	1.27	13.93	1.69	13.92	1.76	9.76	10.13	3.79	10.11	3.59	8.02	17.83		
i <sub>L2max</sub> [A]	11.76	11.93	1.44	11.89	1.10	12.33	4.85	7.09	7.67	8.18	7.65	7.90	6.79	4.23		
V <sub>C1max</sub> [V]	226.50	216.5	4.41	217.13	4.13	203.43	10.18	65.04	66.82	2.74	67.25	3.40	58.51	10.04		
V <sub>C2max</sub> [V]	185.33	184.75	0.31	184.55	0.42	180.23	2.75	58.44	55.55	4.94	55.45	5.11	49.56	15.19		

According to Table 5-8, with the same power and voltage in the forward power transfer mode, all the values resulted from the proposed analysis are well matched with the experimentally measured values, and the errors are much lower than those obtained from the



FHA method. As an example for  $i_{L1max}$ , the error of the value obtained from SPA is 2.03% while the error of the value given by FHA is 15.59%. Also, for  $v_{C1max}$  the errors are 5.16% and 14.73% for SPA and FHA respectively. Fig. 5-43 compare the obtained error based on the simulation, SPA, and FHA method with the experimental results, where the FHA-based error is too high.

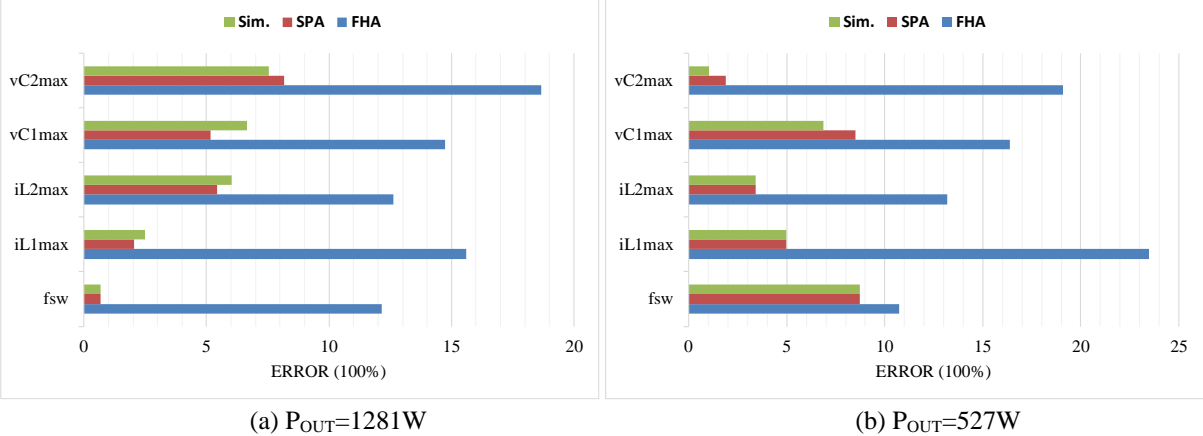


Fig. 5-43: Error comparison of the different parameters based on simulation, SPA, and FHA method in comparison with the experimental results for (a)  $P_{OUT}=1281W$  and  $P_{OUT}=527W$

The experimental results of the reverse power transfer mode, are also tabulated in Table 5-9. Comparing the results of the proposed analysis with the experimental and simulation results shows that the proposed analysis is also effective for the reverse power transfer operation. Furthermore, Fig. 5-44 shows that the maximum efficiency of the converter operating in forward power transfer is 95.72% while it is 95.62% for the reverse power transfer.

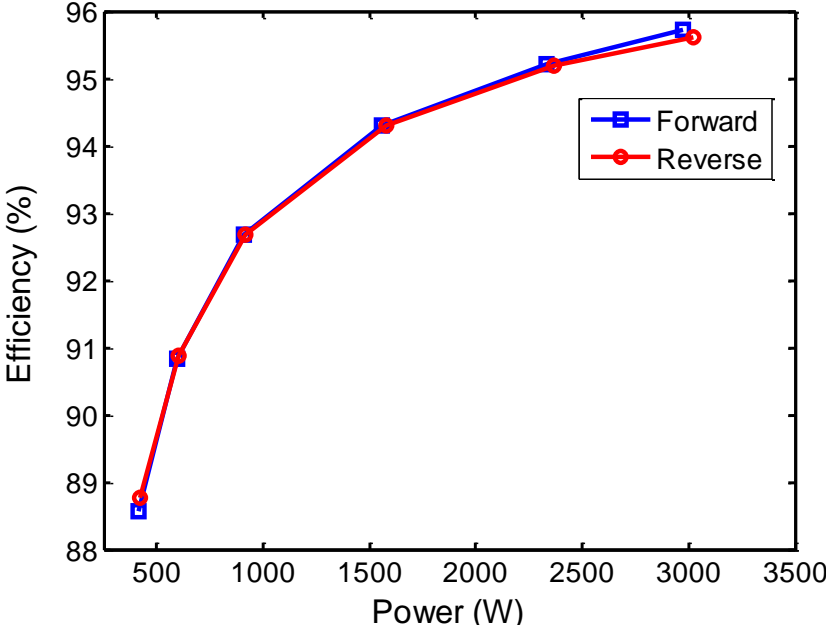


Fig. 5-44: Efficiency for the forward and reverse power transferring.

In conclusion, it can be deduced that the proposed method has much higher precision in comparison with the FHA method for both power transferring directions. This exact analysis can be used in the design, control, and optimization of the CLLC resonant converter as well as other high-order resonant converters. Owing to the mathematical expression of the converter behavior, this method is very helpful for practicing optimization algorithms to minimize voltage/current stresses, losses, and reliability assessment.

## **5.8. Summary**

This chapter proposed in detail the state-plane analysis of the bidirectional full-bridge CLLC resonant converter for the switching above the resonant frequency. A new formulation of state-space equations was presented and the fourth-order CLLC resonant converter was transformed into two second-order systems. Then using this mathematical method, the exact analysis of the converter in CCM, stresses of the components, voltage gain ratio, soft switching conditions, and the boundary between CCM/DCM were obtained. It should be mentioned that the proposed method is not completely exact but it is precise in comparison with FHA method. A 3-kW prototyping was built. Experimental results were used to verify the proposed method. Simulation and experimental results reveal the accuracy of the proposed analysis in the forward and reverse power transfer modes for different power and voltage levels. It is noted that the proposed state-plane analysis is exact in comparison with the simulation results and it has an acceptable precision in comparison with the experimental results. The proposed state-plane analysis is helpful in the design and optimization of the CLLC resonant converter in a wide operating range, which will be examined in the next chapter.

# 6. Proposed Multi Operating Points Two-Stage Optimization Method

## 6.1. Introduction

The state plane analysis was evaluated in the previous chapter, which proposed a new method for the exact analysis of the CLLC resonant converter. On the other hand, the sequential quadratic programming was examined to prepare the exact optimization of the CLLC resonant converter. In this chapter, both of these methods will be utilized in this chapter.

## 6.2. Software Environment

The closed-form state-plane analysis-based equations are implemented in a specific optimization platform, named the Component Architecture for Design of Engineering Systems (CADES) software, which was first developed in the *Grenoble Génie Electrique Laboratoire (G2ELab)*. The CADES software was further expanded by the Vesta System Company, and now has provided the capability of problem formulation, fast and exact optimization, and results in the analysis [162], [163], and [164], especially in the power electronics applications. In this thesis, the CADES software version 4.1.0 is used as shown in Fig. 6-1:



Fig. 6-1: The diagram of CADES Software

Fig. 6-2 shows the environment of the CADES software, where section 1 is the project management part, section 2 is the code editor, and section 3 is the output message plane.

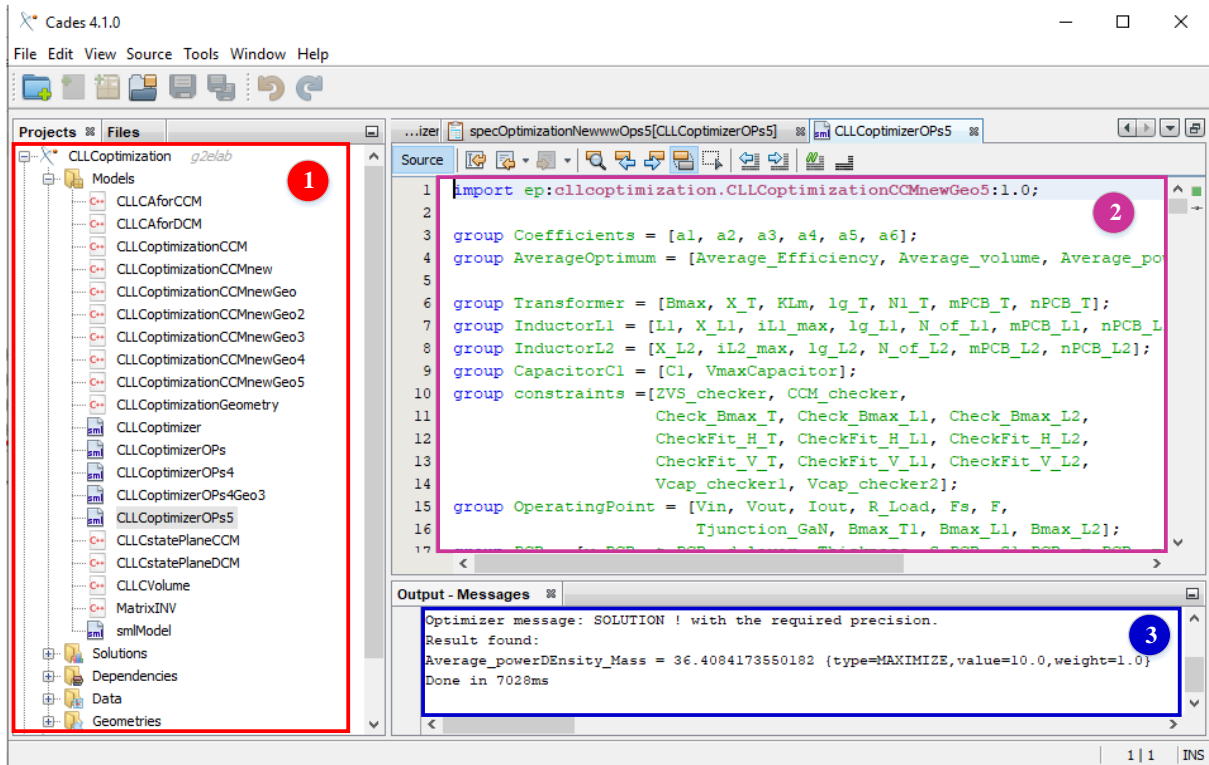


Fig. 6-2: The default environment of the CADES software

Among the different advantages of CADES, this software is able to use different programming languages such as SML (System Modeling Language), C++, Python, and Java. In this dissertation, the state-plane analysis equations have been written by C++ and the optimization algorithm has been implemented by SML. The exact Jacobian matrix of a gradient-based optimization problem is determined thanks to the automatic differentiation Adol-C integrated with CADES [165]. It leads to obtaining the derivatives more efficiently [114].

### 6.3. Optimization Parameters

In an optimization problem, the variables are input, output, or constraint, where the type of variables in CADES can be defined as free, fixed, interval, parametric, database, uncertain, or objective. Furthermore, there exists an objective function in the optimization process, which must be maximized/minimized, when all constraints are met. For the selected bidirectional EV charger, the following objective functions and variables are defined.

### 6.3.1. Objective function

The goal of bidirectional CLLC resonant converter optimization is to find a set of parameters such that the objective function is maximized/minimized subject to the constraints. The common objective functions are maximizing power density, maximizing efficiency, minimizing loss, minimizing mass, or minimizing volume. In this dissertation, minimizing the total mass and maximizing the efficiency are considered as the objective function:

$$\text{Objective function: (max Efficiency) \& (min Mass)}$$

$$\text{or } \max \frac{\text{Efficiency}}{\text{Mass}} \quad (6.1)$$

If we select only minimizing the total mass or maximizing the power density, undesirable results are obtained in this application. In this way, let's consider N operating points for G2V power transfer with the possibility of P and M operating points for V2G power transfer with the possibility of 1-P. Fig. 6-3 illustrates the probability of operating in G2V and V2G for an electric vehicle.

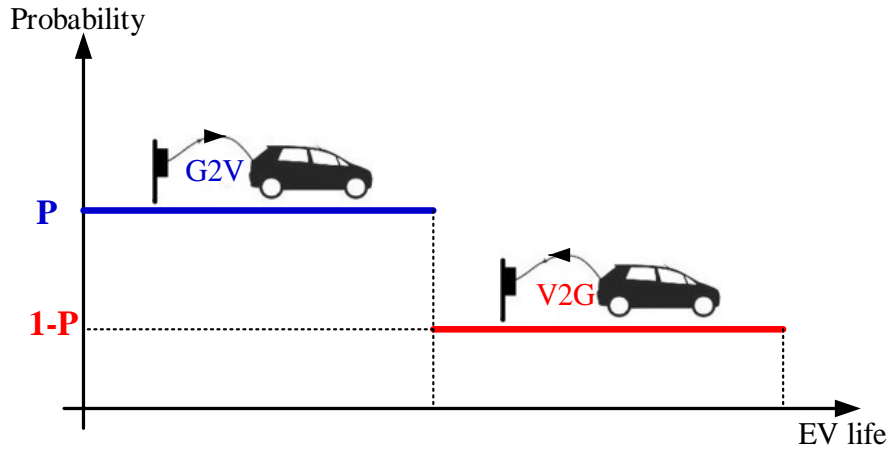


Fig. 6-3: The probability of operating in G2V and V2G in the EV's lifespan

Firstly, we consider minimizing mass as the objective function, the total objective function (*OF*) is calculated by the weighted sum of all operating points when they are considered simultaneously as:

$$OF = P \sum_{j=1}^N \lambda_{C,j} \times Mass_{C,j} + (1 - P) \sum_{j=1}^M \lambda_{D,j} \times Mass_{D,j} \quad (6.2)$$

where  $\lambda$  is the optimization coefficient, and the notation of *C* and *D* express charging and discharging conditions, respectively. Due to the fact that all operating points are considered

simultaneously, the mass of the converter does not depend on the operating points and remains constant. Therefore, Eq. (6.2) can be simplified as:

$$\begin{aligned}
OF &= \min P \sum_{j=1}^N \lambda_{C,j} \times Mass + (1 - P) \sum_{j=1}^M \lambda_{D,j} \times Mass \\
&= \min P \times Mass \sum_{j=1}^N \lambda_{C,j} + (1 - P) \times Mass \sum_{j=1}^M \lambda_{D,j} \\
&= \min \left( P \times \sum_{j=1}^N \lambda_{C,j} + (1 - P) \times \sum_{j=1}^M \lambda_{D,j} \right) Mass \\
&= \min K \times Mass \\
&= \min Mass
\end{aligned} \tag{6.3}$$

It means that if minimizing the total mass is selected as the objective function, the coefficients of each operating point as well as the probability of operating in G2V don't have any effect on the optimizing total mass for multi operating points optimization.

Secondly, if the power density is selected as the objective function, the coefficients of each operating point play an important role in maximizing the power density due to the fact that the output power depends on the operating point. However, the following condition is obtained:

$$\begin{aligned}
OF &= P \sum_{j=1}^N \lambda_{C,j} \times \frac{Pout_{C,j}}{Mass_{C,j}} + (1 - P) \sum_{j=1}^M \lambda_{D,j} \times \frac{Pout_{D,j}}{Mass_{D,j}} \\
&= \sum_{j=1}^N \frac{\lambda_A V_A I_A + \lambda_B V_B I_B + \lambda_C V_C I_C + \lambda_D V_D I_D}{Mass} \\
&\quad + (1 - P) \sum_{j=1}^M \frac{\lambda_A V_A I_A + \lambda_B V_B I_B + \lambda_C V_C I_C + \lambda_D V_D I_D}{Mass}
\end{aligned} \tag{6.4}$$

In the above fractions, the numerator is constant because it depends on the operating points which are selected as input parameters. So, (6.4) can be rewritten as (6.5):

$$= \max K \times \frac{1}{Mass} \tag{6.5}$$

$$= \max \frac{1}{Mass} \quad \text{or} \quad \min Mass$$

The above equation expresses that the coefficients of each operating point, as well as the probability of operating in G2V, don't have any effect on the optimization of the power density for multi operating points optimization when the output power is known. Nevertheless, the optimization results for minimizing the mass or maximizing the power density are shown in **Appendix III**. These results are shown that the optimization algorithm is converged to an unreal minimum mass (i.e. 9.23g for all magnetic parts) which is not true for a 3.3kW on-board charger.

Therefore, a new formulation of the objective function is considered for involving the efficiency and corresponding coefficients. Eq. (6.6) shows the objective function:

$$OF = \max \frac{Efficiency}{Total\ mass} \quad (6.6)$$

For the bidirectional multi operating points optimization, the objective function can be rewritten as:

$$OF = \max P \sum_{j=1}^N \lambda_{C,j} \times \frac{\eta_{C,j}}{Mass} + (1 - P) \sum_{j=1}^M \lambda_{D,j} \times \frac{\eta_{D,j}}{Mass} \quad (6.7)$$

where  $\eta_C$  and  $\eta_D$  are the efficiency of the selected operating point in charging (C) and discharging (D) modes.

In this dissertation, we consider 4 operating points (N=M=4 in which points A, B, C, and D) with a probability of 80% for G2V applications (i.e. P=0.8). Furthermore, due to the symmetrical structure of the selected bidirectional CLLC resonant converter, charging and discharging modes have the same functionality (i.e.  $\eta_{C,j} = \eta_{D,j}$  for  $j \in \{1,2,3,4\}$ ). Therefore, the objective function can be determined as:

$$\begin{aligned} OF &= \max \sum_{j=1}^4 \lambda_j \times \frac{\eta_j}{Mass} \\ &= \max \frac{\lambda_A \times \eta_A + \lambda_B \times \eta_B + \lambda_C \times \eta_C + \lambda_D \times \eta_D}{Mass} \end{aligned} \quad (6.8)$$

where  $\lambda_A = 0.033$ ,  $\lambda_B = 0.767$ ,  $\lambda_C = 0.126$ , and  $\lambda_D = 0.074$  are the coefficients of points A, B, C, and D, respectively, which are selected based on the values presented in [166] for an

EV charger based on the LLC resonant converter,  $\eta_A$ ,  $\eta_B$ ,  $\eta_C$ , and  $\eta_D$  are the efficiency of points A, B, C, and D, which are obtained based on the state-plane analysis present in the previous chapter, and  $Mass$  is the total mass of the charger, which is obtained based on the continuous modeling of the magnetic cores represented in 4.5.

Consequently, the objective function for single operating point optimization and multi operating points optimizations is defined in (6.9):

$$OF = \begin{cases} \max \frac{\lambda_A \times \eta_A + \lambda_B \times \eta_B + \lambda_C \times \eta_C + \lambda_D \times \eta_D}{Mass} & (4 \text{ operating points}) \\ \max \frac{\lambda \times \eta}{Mass} & (single \text{ operating point}) \end{cases} \quad (6.9)$$

where  $\lambda_A = 0.033$ ,  $\lambda_B = 0.767$ ,  $\lambda_C = 0.126$ , and  $\lambda_D = 0.074$  for 4 operating points optimization and  $\lambda = 1$  for single operating point optimization.

In this dissertation, Eq. (6.9) is named as a new version of the objective function. It should be mentioned that the common power density, i.e. the nominal output power divided by the mass/volume, is not considered as the objective function since the output power is limited to 3.3kW and the objective function will be independent of the operating points and their coefficients, as previously shown in (6.3).

### 6.3.2. Input Parameters

The input parameters are categorized into three categories, i.e. electrical parameters, geometrical parameters, and optimization parameters.

#### *Electrical input parameters*

Table 6-1 shows the list of the electrical input parameters. In this table, some inputs are fixed and others can be changed in an interval. For example, the input voltage is fixed and equal to 400V, and the output voltages are also fixed for 4 operating points. According to the selected GaN transistor, the value of its parasitic capacitor can be selected as a fixed value (its nominal value). For the interval inputs, it is assumed that the value can change in an interval with an initial guess, minimum, and maximum value. For example, the resonant circuit capacitor can be chosen from 20nF to 500nF with a 70nF initial guess, which is based on experience. It is noted that the resonant capacitors in the real world are also a discrete parameter, but it is possible to obtain the corresponding capacitance using series and parallel configuration. The switching frequency can be changed from 100kHz to 800kHz (based on the core material).



Table 6-1: Electrical input parameters for optimization

<b>Input variable</b>	<b>Description</b>	<b>Type</b>	<b>Initial guess</b>	<b>Min</b>	<b>Max</b>
<b>C1</b>	Primary resonant capacitor	Interval	70nF	20nF	500nF
<b>Vin</b>	Input voltage	Fixed	400V	-	-
<b>Vout_op1</b>	Output voltage of the first operating point	Fixed	250V	-	-
<b>Vout_op2</b>	Output voltage of the second operating point	Fixed	340V	-	-
<b>Vout_op3</b>	Output voltage of the third operating point	Fixed	370V	-	-
<b>Vout_op4</b>	Output voltage of the fourth operating point	Fixed	370V	-	-
<b>Iout_op1</b>	Output current of the first operating point	Fixed	9A	-	-
<b>Iout_op2</b>	Output current of the second operating point	Fixed	9A	-	-
<b>Iout_op3</b>	Output current of the third operating point	Fixed	9A	-	-
<b>Iout_op4</b>	Output current of the fourth operating point	Fixed	2A	-	-
<b>Fsw_op1</b>	Switching frequency of the first operating point	Interval	450kHz	100kHz	800kHz
<b>Fsw_op2</b>	Switching frequency of the second operating point	Interval	300kHz	100kHz	800kHz
<b>Fsw_op3</b>	Switching frequency of the third operating point	Interval	270kHz	100kHz	800kHz
<b>Fsw_op4</b>	Switching frequency of the fourth operating point	Interval	240kHz	100kHz	800kHz
<b>F_op1</b>	Normalized frequency of the first operating point	Interval	2	1.1	3
<b>F_op2</b>	Normalized frequency of the second operating point	Interval	1.4	1.1	3
<b>F_op3</b>	Normalized frequency of the third operating point	Interval	1.3	1.1	3
<b>F_op4</b>	Normalized frequency of the fourth operating point	Interval	1.3	1.1	1.5
<b>Css</b>	Parasitic capacitor of the selected GaN transistor	Fixed	30pF	-	-
<b>R_th_GaN</b>	Junction-to-ambient thermal resistance of GaN (with heatsink)	Fixed	3°C/W	-	-
<b>R_ON</b>	ON-state resistance of the GaN transistor	Fixed	32mΩ	-	-
<b>V_ON_d</b>	Forward voltage of the selected diode	Fixed	0.7V	-	-
<b>KLM</b>	The ratio of $L_m/L_1$	Interval	6	3	20
<b>V_Max_C</b>	Maximum voltage of resonant capacitors	Fixed	1000	-	-

Another input parameter is defined as:

$$K_{LM} = \frac{Lm}{L1} \quad (6.10)$$

$K_{LM}$  has been commonly selected among 4~20 in literature. In this dissertation, it is selected in the interval of 3~20.

### *Geometrical input parameters*

Table 6-2 demonstrates the list of the geometrical input parameters:

*Table 6-2: Geometrical input parameters for optimization*

<b>Input variable</b>	<b>Description</b>	<b>Type</b>	<b>Initial guess</b>	<b>Min</b>	<b>Max</b>
<b>X_L1</b>	Core number of $L_1$	Interval	38	10	64
<b>X_L2</b>	Core number of $L_2$	Interval	38	10	64
<b>X_T</b>	Core number of transformer	Interval	48	10	64
<b>lg_L1</b>	Airgap of $L_1$	Interval	800 $\mu$ m	100 $\mu$ m	5mm
<b>lg_L2</b>	Airgap of $L_2$	Interval	800 $\mu$ m	100 $\mu$ m	5mm
<b>lg_T</b>	Airgap of transformer	Interval	800 $\mu$ m	100 $\mu$ m	5mm
<b>m_L1</b>	Number of layers for $L_1$	Interval	2	1	8
<b>m_L2</b>	Number of layers for $L_2$	Interval	2	1	8
<b>m_T</b>	Number of layers for transformer	Interval	2	1	8
<b>w</b>	Diameter of each wire	Fixed	8mm	-	-
<b>t</b>	Vertical spacing between turns	Fixed	1mm	-	-
<b>Thickness</b>	Additional depth between turns	Fixed	70 $\mu$ m	-	-
<b>d</b>	Separator depth between layer	Fixed	1mm	-	-
<b>S</b>	Horizontal spacing between turns	Fixed	1mm	-	-
<b>S1</b>	Spacing between the ending turns and core	Fixed	1mm	-	-
<b>B_MAX</b>	Maximum flux density of the selected core	Fixed	0.25T	-	-

These geometrical parameters consist of the continuous form of the core, airgap, number of layers, the diameter of wires, etc. The size of the cores varies between 10~64 to an optimum charger to be found. The minimum airgap is selected as 100 $\mu$ m to make it implementable and its maximum value is considered as 5mm. The diameter of the wires is selected according to the current rating.

### *Coefficient of operating points and G2V probability*

The coefficients of each operating point and also the probability of operating in G2V applications are considered as the optimization process parameters, as listed in Table 6-3. It should be mentioned that the coefficients are adopted from [166], which were obtained based on the weighted average model of the energy of an EV charger based on the LLC resonant converter. Furthermore, the probability of the EV working in the G2V application is considered to be 80%.

*Table 6-3: Optimization parameters, which are the coefficients of operating points and G2V probability*

<b>Input variable</b>	<b>Description</b>	<b>Type</b>	<b>Value</b>
$\lambda_A$	Coefficient of the first operating point	Fixed	0.033
$\lambda_B$	Coefficient of the second operating point	Fixed	0.767
$\lambda_C$	Coefficient of the third operating point	Fixed	0.126
$\lambda_D$	Coefficient of the fourth operating point	Fixed	0.074
<b>P</b>	Probability of operating in G2V	Fixed	0.8

It can be possible to propose a new approach to find these coefficients for bidirectional CLLC-based on-board charger applications.

### 6.3.3. Constraints

Optimization constraints can affect the different parts i.e. the input part, the internal part of the optimization code, and the output part. For the input part as an example, the maximum voltage of resonant capacitors ( $V_{MAX\_C}$ ) can be selected as a constraint, nevertheless, we selected it as an input parameter. In this part, some important constraints are discussed. Among the optimization constraints, zero voltage switching (ZVS) and operating in continuous conduction mode (CCM) are critical.

#### *ZVS constraint*

For ZVS, the dead-time value must be met by the following inequality obtained in the previous chapter (see 5.3.2) for all the operating points:

$$\frac{2C_{SS}V_{in}}{i_{L10}} \leq t_{dt} \leq \alpha + \theta_0 \quad (6.11)$$

The above equation can be split into the following inequalities:

$$ZVS_{CHECKER} = \alpha + \theta_0 - \frac{2C_{SS}V_{in}}{i_{L10}} > 0 \quad (6.12)$$

$$\frac{2C_{SS}V_{in}}{i_{L10}} > 0 \quad \text{or} \quad i_{L10} > 0 \quad (6.13)$$

Eq. (6.12) is defined as a ZVS checker constraint, which should be always greater than zero. Eq. (6.13) is another ZVS constraint that ensures the primary current at the start of subinterval III to be positive.

If (6.12) and (6.13) are met for all the operating points, it can be said that the ZVS condition for primary inverters is definitely met. However, it is better to put a margin so that the dead time implementation is possible. For example, if the amount of dead time is calculated as 10ps, it will not be practically possible to implement. Therefore, we set a margin for it, which is assumed to be 20ns. Therefore, (6.13) is rewritten as follows:

$$\frac{2C_{SS}V_{in}}{i_{L10}} > 20\text{ns} \quad (6.14)$$

Consequently, (6.12) and (6.14) are utilized for ZVS condition checking.

#### CCM constraint

Another optimization constraint is that the CLLC resonant converter operates in CCM for all the operating points. The CCM operating has the benefit of higher efficiency and lower switching stresses in comparison with DCM operating. Let's consider the following circuit as shown in Fig. 6-4:

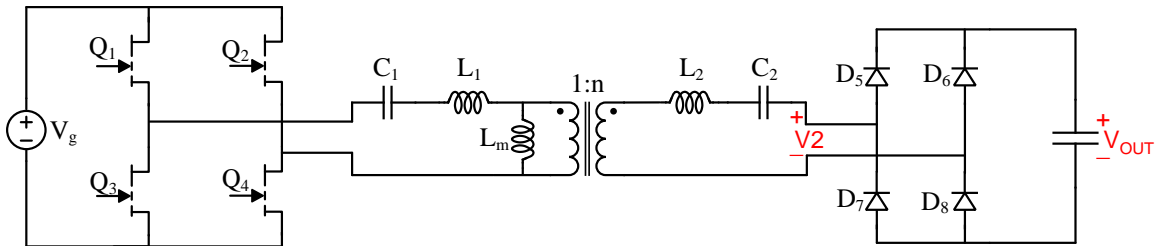


Fig. 6-4: Displaying the required voltages for CCM checking

The condition for operating in CCM is that when the current on the secondary side becomes zero and the diodes want to change state, the voltage  $V_2$  should be higher than the output voltage to turn ON the corresponding diodes, i.e.:

$$V_2|_{@i_D=0} > V_{OUT} \quad (6.15)$$

The following variable is defined to check the CCM operating and satisfy the above condition:

$$CCM_{CHECKER} = V_2|_{@i_D=0} - V_{OUT} > 0 \quad (6.16)$$

where the value of  $V_2|_{@i_D=0}$  was obtained in the previous chapter.

#### *Maximum junction temperature*

The junction temperature of GaN transistors must be lower than the maximum junction temperature mentioned in the datasheet. It is necessary to calculate the corresponding power dissipation of the GaN transistors. Then, the junction temperature ( $T_J$ ) is determined according to the thermal modeling:

$$T_J = T_A + P_{Loss} \times R_{th\_JA} \quad (6.17)$$

where  $T_A$  is the ambient temperature typically 25°C,  $P_{Loss}$  is the power dissipation of the GaN transistor, and  $R_{th\_JA}$  is the junction-to-ambient thermal resistance of the GaN transistor which is 3°C/W for GS66508B GaN transistor.

#### *Minimum efficiency*

Despite the efficiency that exists in the objective function for maximizing or not, the minimum allowable efficiency is also another constraint. In this thesis, we consider:

$$\eta_{MIN} = 94\% \quad (6.18)$$

#### *Transformer saturation checking*

The flux density of the cores should be lower than its maximum flux density mentioned in the datasheet for all the operating points. Therefore, the parameters  $CheckBmax\_L1$ ,  $CheckBmax\_L2$ , and  $CheckBmax\_T$  are defined to examine the saturation of  $L_1$ ,  $L_2$ , and the transformer, respectively:

$$CheckBmax\_L1 = Bmax - Bmax\_L1 \quad (6.19)$$

$$CheckBmax\_L2 = Bmax - Bmax\_L2 \quad (6.20)$$

$$CheckBmax\_T = Bmax - Bmax\_T \quad (6.21)$$

where  $B_{max}$  is the maximum allowable flux density of the selected core material,  $B_{max\_L1}$ ,  $B_{max\_L2}$ , and  $B_{max\_T}$  are the maximum flux density of the magnetic components in a specific operating point and they are determined as:

$$B_{max\_L1} = \frac{\mu_0 \times N_{L1} \times I_1}{lg\_L1} \quad (6.22)$$

$$B_{max\_L2} = \frac{\mu_0 \times N_{L2} \times I_2}{lg\_L2} \quad (6.23)$$

$$B_{max\_T} = \frac{V_{IN}}{4 \times N_1 \times F_{sw} \times Ae} \quad (6.24)$$

where  $I_1$  and  $I_2$  are the maximum current of the primary and secondary sides, respectively.

#### *Horizontally fit in the core*

Fig. 4-2 shows an EE core with the corresponding dimensions listed in Table 4-2. The number of wires in each layer is limited to:

$$Fit\_H = \frac{E - F}{2} - (n \times w + (n-1) \times t + 2 \times S) \geq 0 \quad (6.25)$$

where  $E$  and  $F$  are shown in Fig. 4-2,  $n$  is the number of turns per layer,  $w$  is the diameter of a wire,  $t$  is the space between turns,  $S$  is the spacing between the ending turns and the core, and  $Fit\_H$  is the variable for checking horizontal fitting of the layers in a core and must be checked for the magnetic core of the inductors and transformer. It should be noted that  $t$  and  $S$  are typically specified by the safety rules, required insulation, and fabrication tolerance.

#### *Vertically fit in the core*

The number of layers in the core window should be also limited to:

$$Fit\_V = 2D - (m \times w + 2S) \geq 0 \quad (6.26)$$

where  $D$  is shown in Fig. 4-2,  $m$  is the number of layers, and  $Fit\_V$  is the variable for checking the vertical fitting of the layers in a core and must be checked for the magnetic core of the inductors and transformer.

#### *Maximum voltage of the resonant capacitors*

The maximum voltage of each resonant capacitor must be lower than the absolute maximum rating mentioned in its datasheet. In this work, the selected resonant capacitors are MLLC capacitors with a 1kV voltage rating. Therefore, the following constraints must be also met:

$$V_{C1\_Checker} = V_{MAX\_C} - v_{C1,MAX} \quad (6.27)$$

$$V_{C2\_Checker} = V_{MAX\_C} - v_{C2,MAX} \quad (6.28)$$

where  $V_{MAX\_C}$  is equal to 1kV, and  $v_{C1,MAX}$  and  $v_{C2,MAX}$  are the maximum voltage of  $C_1$  and  $C_2$  which were obtained in the previous chapter based on the state plane analysis.

#### 6.3.4. Output parameters

The main output parameters are shown in Table 6-4, where the objective function is selected as a new version of power density.

Table 6-4: Some important output parameters

Output variable	Description	Type	Initial guess	Min	Max
$PD_{Mass}$	Efficiency divided by total mass [100%/g]	Maximize	0.1	-	-
$PD_{Vol}$	Efficiency divided by total volume [100%/cm <sup>3</sup> ]	Free	-	-	-
$PD_M$	Nominal output power divided by mass [W/g]	Free	-	-	-
$PD_V$	Nominal output power divided by volume [W/cm <sup>3</sup> ]	Free	-	-	-
$Efficiency$	Efficiency of the converter [100%]	Interval	-	94	100
$Junc\_GaN$	Junction temperature of GaN [°C]	Interval	-	-40	85
$Junc\_D$	Junction temperature of diode [°C]	Interval	-	-40	85
$N_T$	Total number of turns for the transformer	Free	-	-	-
$N_{L1}$	Total number of turns for $L_1$	Free	-	-	-
$N_{L2}$	Total number of turns for $L_2$	Free	-	-	-
$iL1\_max$	The maximum current of $L_1$ [A]	Interval	-	0	25
$iL2\_max$	The maximum current of $L_2$ [A]	Interval	-	0	25
$vC1\_max$	The maximum voltage of $C_1$ [V]	Interval	-	0	1000
$vC2\_max$	The maximum voltage of $C_2$ [V]	Interval	-	0	1000
$Bmax_T$	Maximum flux density of transformer [mT]	Interval	-	0	250
$Bmax_{L1}$	Maximum flux density of $L_1$ 's core [mT]	Interval	-	0	250
$Bmax_{L2}$	Maximum flux density of $L_2$ 's core [mT]	Interval	-	0	250

## 6.4. Single Operating Point Optimization

In this part, a single operating point is discussed. As shown in Fig. 6-5, the following operating points have been considered:

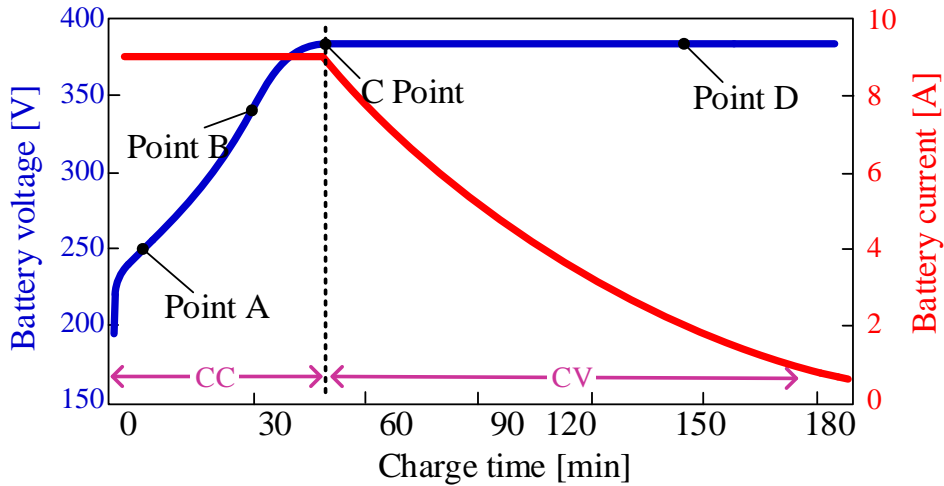


Fig. 6-5: Selection of 4 operating points based on the lithium battery charging process

- Point A: this point is selected as a starting point, where the current is maximum and the voltage is minimum ( $I_{MAX}, V_{MIN}$ ). The charger operates in CC mode.
- Point B: this point operates at the nominal power, where the voltage increases and reaches nominal voltage,  $V_{rated}$ , at the maximum current ( $I_{MAX}, V_{rated}$ ).
- Point C: this point occurs when the voltage reaches its maximum value ( $I_{MAX}, V_{MAX}$ ). At this point, the operating mode of the battery charger changes to CV mode.
- Point D: this point is just before the battery will be fully-charged while the current is decreasing ( $I_{MIN}, V_{MAX}$ ).

Generally, battery chargers are optimized at one operating point such as  $P_{rated}$  or  $P_{MAX}$ . For better comparison and in this section, each operating point is selected as the desired point and optimization will be done on it.

Table 6-5 compares the optimization results of different operating points for selecting each of them in the optimization process and obtaining its effect on the other operating points, where the red numbers mean that the constraint has not been met.



Table 6-5: Single operating point optimization results in the imaginary world, by considering a different operating point and checking the objective function and constraints on all points

Optimization results at	Parameter	Selected point for optimization			
		Point A	Point B	Point C	Point D
General parameters	C <sub>1</sub> (nF)	282.186	500	162.82	66.28
	L <sub>1</sub> (μH)	3.124	1	3.0729	7.549
	X [L <sub>1</sub> ,L <sub>2</sub> ,T]	30.18	24.22	23.27	21.68
		28.66	22.73	22.31	20.13
		38.38	38.43	24.66	24.88
	lg [L <sub>1</sub> ,L <sub>2</sub> ,T] (μm)	254.97	196.89	179.7	100
		197.6	147.43	135.9	100
		100	100	100.3	100
	N [L <sub>1</sub> ,L <sub>2</sub> ,T]	3.69	3.07	2.93	2.674
		3.47	2.839	2.70	2.232
		5.318	5.326	5.29	4.968
	m [L <sub>1</sub> ,L <sub>2</sub> ,T]	8	8	8	8
		8	8	8	8
8		8	8	8	
KLm	8.413	18.917	20	10.038	
Fit_H [L <sub>1</sub> ,L <sub>2</sub> ,T]	OK	OK	OK	OK	
Fit_V [L <sub>1</sub> ,L <sub>2</sub> ,T]	9.5mm	5mm	4.3mm	3.4mm	
	8.3mm	4mm	3.5mm	3.4mm	
	16.4mm	16.4mm	16.2mm	13.63mm	
Mass (g)	46.46	36.18	12.62	11.57	
Objective function (%/g)	2.106	2.720	7.813	8.357	
Optimization results at Point A	ZVS checker	0.226	0.354	0.348	0.383
	CCM checker	132.215	209.8	211.3	187.56
	Bmax checker	OK	NOK	NOK	NOK
	Efficiency	97.827	96.45	97.86	97.989
	Objective function %/g	2.106	2.666	7.754	8.469
	T <sub>j</sub> (°C)	85	247.63	89.92	65.66
Optimization results at Point B	ZVS checker	0.515	0.174	0.371	0.468
	CCM checker	133.8	56.17	193.05	150.1
	Bmax checker	NOK	OK	NOK	NOK
	Efficiency	98.19	98.418	98.53	98.75
	Objective function %/g	2.113	2.720	7.807	8.535
	T <sub>j</sub> (°C)	90.27	85	70.72	52.3
Optimization results at Point C	ZVS checker	0.698	0.362	0.33	0.564
	CCM checker	44.99	125.56	61.65	68.69
	Bmax checker	NOK	NOK	OK	NOK
	Efficiency	98.42	98.197	98.596	98.74
	Objective function %/g	2.118	2.714	7.813	8.534
	T <sub>j</sub> (°C)	64.43	104.98	85	45.7
Optimization results at Point D	ZVS checker	0.702	0.366	0.351	0.666
	CCM checker	44.99	125.56	129	14.12
	Bmax checker	NOK	NOK	NOK	OK
	Efficiency	98.51	98.316	98.889	96.69
	Objective function %/g	2.120	2.717	7.836	8.357
	T <sub>j</sub> (°C)	57.54	86.6	52.253	85

According to Table 6-5, by considering the minimum voltage (point A) as the operating point of the optimization, the magnetic core will be saturated at the maximum power (point C), point B, and point D, and also the converter temperature exceeds the margin and reaches 90.27°C at point B. Therefore, all the constraints cannot be met by considering the minimum voltage (point A) as the operating point of optimization. Also, Table 6-5 demonstrates that by considering points B, C, or D as the optimization operating point, the maximum junction temperature, and saturation will be exceeded at the other points and the constraint cannot be met. Furthermore, this table shows that the optimization at point D has the minimum mass and the maximum objective function.

It should be noted that the results shown in Table 6-5 are in the imaginary world and it is not possible to fully trust the accuracy of the obtained results. However, **Appendix IV** shows that all constraints of single operating point optimization cannot be met in the real world as well. Therefore, it can be concluded from the data in Table 6-5 and also **Appendix IV** that the limitation of single operating point optimization for EV charger applications is that all the constraints cannot be met completely, and it leads to cause a problem in the performance of the charger. Hence, it is needed to present a new method to address this problem and supplement the single operating points by considering multi operating points. This method will be discussed in the next part.

### **6.5. The Proposed Multi Operating Points Optimization (Algorithms and Transferring from the Imaginary World to the Real World)**

The objective function of this dissertation was expressed in (6.9) with the defined parameters in part 6.3. This optimization method is implemented in the imaginary world with continuous parameters. Indeed, the magnetic cores, number of turns, and number of turns in each layer are defined as any positive number, but they are only integer numbers in the real world. It means that there is not any guarantee that the obtained results are an implementable optimum result. Therefore, this optimization algorithm is a pre-optimization or a pre-design method until now, and it is mandatory to obtain the value of real components, i.e. in the real world. This section comprehensively assesses the concept of transferring from the imaginary world to the real world as well. The variables which must be discrete in the optimization algorithm are:

- Core sizes,
- Number of turns,

- The number of turns in each layer.

The proposed optimization algorithm can be considered as the flowchart diagram drawn in Fig. 6-6.

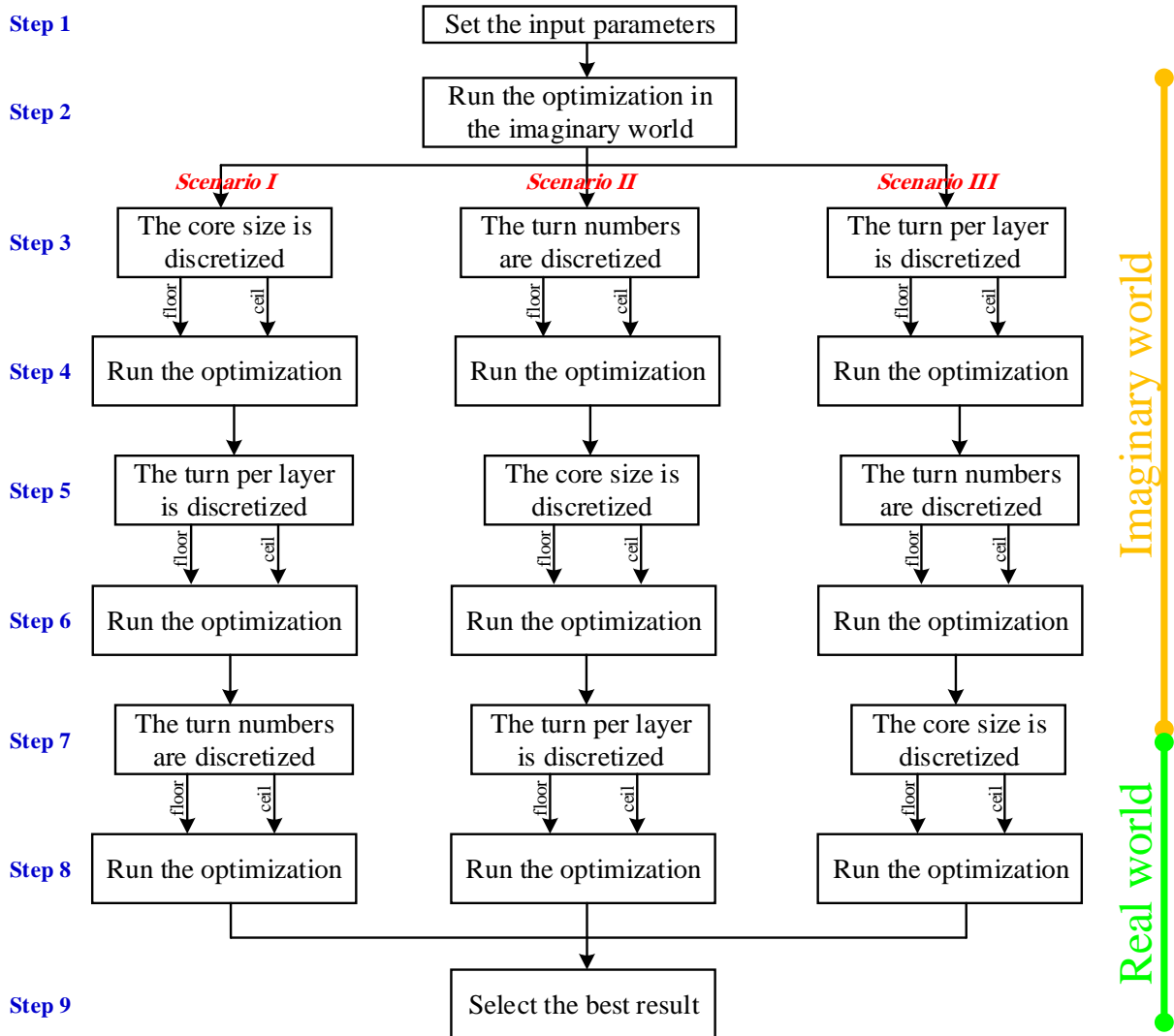


Fig. 6-6: The proposed optimization algorithm for multi operating point optimization in EV charging applications

The optimization procedure is described as follows:

- **Step 1:** the input parameters are defined, which are classified into three categories: electrical parameters, geometrical parameters, and optimization parameters (see section 4.2.1). In this case, 4 operating points have been considered.
- **Step 2:** the optimization will be performed to find the preliminary results as the pre-design process. In this step, the state-plane analysis is carried out to find the exact

value of the objective function and constraints in the imaginary world. Then, an optimum charger is obtained in this step. This step is a pre-optimization process, which provides a preliminary phase for power electronics designing to present a rapid and global glance for the pre-design results in a short time as the domain of the imaginary world. It helps the designer to find an approximate range of solutions. However, it is possible that not only these results do not accurately converge to the optimum point, but also the obtained result cannot be implemented experimentally due to the fact that some non-integer results are not possible (e.g. number of turns). Therefore, proposing a method for transferring from the imaginary world to the optimum and implementable real world is necessary, which will be done in the next steps.

- **Step 3:** this step initially attempts to leave the imaginary world by considering one of the discrete values as a fixed input value, where scenario I is the selection of the core size, scenario II is the selection of total turn numbers, and scenario III is the selection of the number of turns per layer. The obtained non-integer result is discretized by selecting the real integer values above (like ceil function) and below (like the floor function) of the obtained non-integer result. At the end of this step, one of the three discrete parameters is actualized in the real world and only two continuous parameters remain.
- **Step 4:** the optimization runs again and the corresponding constraints are checked to find an optimum result while one of the discrete values is a fixed input parameter. The optimization results will be obtained to make a decision for the next step.
- **Step 5:** this step more attempts to leave the imaginary world by considering the second discrete value as a fixed input. For scenario I (when the core size is fixed in step 3), we consider the number of turns per layer as the second discrete value, above and below the obtained non-integer result. This selection is due to the fact that the core size is known and it is optimum to completely fit the turns vertically as shown in Fig. 6-7.

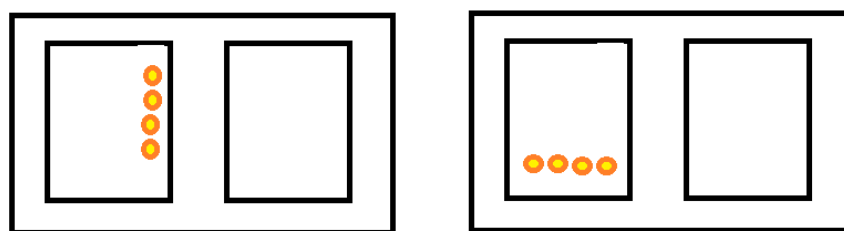


*Fig. 6-7: Horizontal and vertical arrangements of the turns*

- **Step 6:** the optimization runs once again and the corresponding constraints are checked to find an optimum result while two discrete values are a fixed input parameter. The optimization results will be obtained to make a decision for the next step.
- **Step 7:** the last integer variable is discretized based on the above and below the value of the obtained result. Therefore, at the end of this step, the core size, the total mass of the core, the total turn numbers, and the number of turns per layer are recognized because all the discrete variables are realized. However, there exist two candidates based on the selected values above and below the results. So, another optimization is also needed.
- **Step 8:** the last optimization is performed by selecting all the discrete parameters as a fixed input. Since the total mass of the converter is known, maximizing the efficiency and /or output power can be considered as the objective function to obtain the airgap of the magnetic cores. All the optimization results are available at the end of this step.
- **Step 9:** in this step, all scenarios and results are compared and the maximum  $\eta/mass$  is considered as the final solution. Therefore, the proposed optimization algorithm reaches the end.

The following part of this thesis moves on to describe in greater detail the proposed optimization process for a 3.3kW bidirectional CLLC resonant converter for EV charging applications.

## 6.6. Numerical Clarification of the Proposed Optimization Process

The optimization process shown in Fig. 6-6 is numerically examined in this part. Let's consider the input parameters described in part 4.2.1 and the constraints listed in part 4.2.2 in the optimization process (step 1). The optimization results will be obtained as shown in Table 6-6 (step 2).

A good comparison between the imaginary results of single operating point optimization (Table 6-5) and the imaginary results of multi operating points optimization (Table 6-6) shows that the total mass is 11.57g and 287.34g, respectively for single operating point and multi operating points optimization, which is obvious the obtained result for single operating point is not near to the real world.

Table 6-6: The optimization results in step 2, when all the discrete parameters are in the imaginary world

Parameter	Optimization results	Unit
XL1	54.319	-
XL2	49.312	-
XT	55.498	-
NL1	6.21	-
NL2	6.67	-
NT	7.44	-
nL1	0.999	-
nL2	0.598	-
nT	0.999	-
mL1	6.21	-
mL2	11.15	-
mT	7.44	-
lg_L1	1040.21	$\mu\text{m}$
lg_L2	447.28	$\mu\text{m}$
lg_Lm	113.3	$\mu\text{m}$
Objective function ( $\eta/\text{mass}$ )	0.3430	%/g
Efficiency	98.558	%
Mass	287.34	g
C <sub>1</sub>	120.24	nF
L <sub>1</sub>	8.1577	$\mu\text{H}$
KLM	14.159	-

According to the above table, XL1 is equal to 54.319. Therefore, it can be selected as XL1\_1=47 and XL1\_2=55 (above and below XL1=54.319) for step 3. For XL2, it was obtained as 49.312 therefore for the next step it can be selected as 47 and 55. XT was obtained as 55.498 therefore for the next step it will be 55 and 65. These considerations are noted as scenario I. Furthermore and in scenario II, the total turn numbers of  $L_1$ ,  $L_2$ , and transformer were 6.21, 6.67, and 7.44, respectively, which can be selected for the next step as 6 and 7 for  $L_1$ , 6 and 7 for  $L_2$ , and 7 and 8 for transformer. For the number of turns per layer, the optimum values were 0.999, 0.598, and 0.999. Due to these values being lower than 1, they should be considered as 1 and 2 (0 is prohibited), where are the corresponding discrete input parameters of scenario III. These considerations are also listed in Table 6-7.

With a more comprehensive investigation in Table 6-5 and Table 6-6, it is manifest that the objective function of the single operating point optimization (e.g. 47.8521 for optimization at point A) is higher than the objective function of the multi operating points optimization (i.e. 10.156), which at the first point of view shows that the single operating point optimization is

preferable. But based on this method, the constraints cannot be met for other operating points. As a result, the obtained result for single operating point optimization is not real and cannot provide a maximum power of 3.3kW by insuring all constraints.

*Table 6-7: Input parameters for optimization in step 4 when one of the discrete parameters in step3 is transferred into the real world as a fixed parameter*

<b>Parameter</b>	<b>Scenario I</b>		<b>Scenario II</b>		<b>Scenario III</b>	
<b>XL1</b>	47	55	free	free	free	free
<b>XL2</b>	47	55	free	free	free	free
<b>XT</b>	55	65	free	free	free	free
<b>NL1</b>	free	free	6	7	free	free
<b>NL2</b>	free	free	6	7	free	free
<b>NT</b>	free	free	7	8	free	free
<b>nL1</b>	free	free	free	free	1	2
<b>nL2</b>	free	free	free	free	1	2
<b>nT</b>	free	free	free	free	1	2

In step 4, the optimization runs again with the modified input parameters. The optimization results will be obtained as shown in Table 6-8.

In step 5, the second discrete value is considered as a fixed input. For this purpose, the aforementioned scenarios are included:

- *Scenario I:* for the lower value of core sizes, the turn numbers of each layer for  $L_1$ ,  $L_2$ , and transformer were obtained as 1, 0.8724, and 0.9938 in Table 6-8, respectively. Therefore, the turn numbers of each layer are 1 if we put a floor under them, and 2 if we set a ceiling on them. Furthermore and for the higher value of core sizes, the number of turns per layer was achieved as 1, 1.3379, and 1.1976, which can be considered as 1 by floor and 2 by ceiling.
- *Scenario II:* the core sizes were obtained higher than 55. Therefore, it can be discretized to 55 and 65 for step 5.

Table 6-8: The optimization results in step 4, when one of the parameters was in the real world and two of them were in the imaginary world

Parameter	Scenario I		Scenario II		Scenario III		Unit
	XL1=47 XL2=47 XT=55	XL1=55 XL2=55 XT=65	NL1=6 NL2=6 NT=7	NL1=7 NL2=7 NT=8	nL1=1 nL2=1 nT=1	nL1=2 nL2=2 nT=2	
<b>XL1</b>	-	-	55.319	55.319	50.268	63.999	-
<b>XL2</b>	-	-	55.233	55.233	50.044	63.199	-
<b>XT</b>	-	-	55.321	55.321	50.277	64.299	-
<b>NL1</b>	7.938	5.9908	-	-	3.247	4.3154	-
<b>NL2</b>	6.3479	6.7047	-	-	3.884	10.055	-
<b>NT</b>	7.691	7.7845	-	-	7.046	20.613	-
<b>nL1</b>	1.000	1.000	1.000	1.000	-	-	-
<b>nL2</b>	0.8724	1.3379	1.000	1.000	-	-	-
<b>nT</b>	0.9938	1.1976	1.000	1.000	-	-	-
<b>mL1</b>	7.938	5.9908	6	7	3.247	2.1577	-
<b>mL2</b>	7.276	5.0113	6	7	3.884	5.027	-
<b>mT</b>	7.7389	6.4998	7	8	7.046	10.306	-
<b>C1</b>	78.82	142.78	113.94	120.53	148.53	53.933	nF
<b>L1</b>	6.532	13.051	8.162	8.1578	7.3798	8.1655	μH
<b>KLm</b>	12.975	16.646	13.586	13.958	12.521	11.827	-
<b>Efficiency</b>	98.56	98.68	98.585	98.561	98.602	98.478	-
<b>PD(η/m)</b>	0.4303	0.2399	0.2984	0.2983	0.4249	0.1790	%/g

Scenario III: the turn numbers were determined 3.247, 3.884, and 7.046 for the turn numbers per layer equal 1. These values can be considered as 3, 3, and 7, for  $L_1$ ,  $L_2$ , and transformer, respectively. For the turn numbers per layer to equal 2, the total turn numbers can be selected as 4, 4, and 8.

The summary of selection in step 5 is listed in Table 6-9.



Table 6-9: Input parameters for optimization in step 6 when two discrete parameters in step5 are transferred into the real world as a fixed parameter and only one parameter is free

Parameter	Scenario I				Scenario II				Scenario III			
	XL1=47 XL2=47 XT=55		XL1=55 XL2=55 XT=65		NL1=6 NL2=6 NT=7		NL1=7 NL2=7 NT=8		nL1=1 nL2=1 nT=1		nL1=2 nL2=2 nT=2	
<b>XL1</b>	-	-	-	-	55	65	55	65	free	free	free	free
<b>XL2</b>	-	-	-	-	55	65	55	65	free	free	free	free
<b>XT</b>	-	-	-	-	55	65	55	65	free	free	free	free
<b>NL1</b>	free	free	free	free	-	-	-	-	3	4	3	4
<b>NL2</b>	free	free	free	free	-	-	-	-	3	4	3	4
<b>NT</b>	free	free	free	free	-	-	-	-	7	8	7	8
<b>nL1</b>	1	2	1	2	free	free	free	free	-	-	-	-
<b>nL2</b>	1	2	1	2	free	free	free	free	-	-	-	-
<b>nT</b>	1	2	1	2	free	free	free	free	-	-	-	-

Before starting step 6, two discrete values were considered as a fixed input parameter, and only one discrete parameter remains as a free parameter for each scenario. Now in step 6, the optimization is performed to find the value of the last discrete parameter. Table 6-10 shows the result of optimization done in step 6:

Table 6-10: The optimization results in step 6, when two parameters were in the real world and one of them was in the imaginary world

Parameter	Scenario I				Scenario II				Scenario III			
	XL1=47 XL2=47 XT=55		XL1=55 XL2=55 XT=65		NL1=6 NL2=6 NT=7		NL1=7 NL2=7 NT=8		nL1=1 nL2=1 nT=1		nL1=2 nL2=2 nT=2	
<b>XL1</b>	47	47	55	55	55	65	55	65	51.9	54.1	57.2	62.7
<b>XL2</b>	47	47	55	55	55	65	55	65	50.4	53.3	52.5	60.6
<b>XT</b>	55	55	65	65	55	65	55	65	64.9	55.7	64.9	64.0
<b>NL1</b>	6.37	6.08	5.32	5.12	6	6	7	7	3	4	3	4
<b>NL2</b>	6.49	6.10	5.62	5.13	6	6	7	7	3	4	3	4
<b>NT</b>	8.53	7.38	6.55	11.7	7	7	8	8	7	8	7	8
<b>nL1</b>	1	2	1	2	0.92	1.16	0.90	0.90	1	1	2	2
<b>nL2</b>	1	2	1	2	0.42	1.11	0.53	0.82	1	1	2	2
<b>nT</b>	1	2	1	2	0.90	0.92	0.90	1.01	1	1	2	2

Parameter	Scenario I				Scenario II				Scenario III			
	XL1=47 XL2=47 XT=55		XL1=55 XL2=55 XT=65		NL1=6 NL2=6 NT=7		NL1=7 NL2=7 NT=8		nL1=1 nL2=1 nT=1		nL1=2 nL2=2 nT=2	
<b>mL1</b>	6.36	3.04	5.32	2.56	6.52	5.17	7.78	7.78	3	4	1.5	2
<b>mL2</b>	6.49	3.05	5.62	2.57	14.3	5.40	13.2	8.53	3	4	1.5	2
<b>mT</b>	8.53	3.69	6.55	5.85	7.78	7.61	8.89	7.92	7	8	3.5	4
<b>C1 [nF]</b>	86.6	93.1	90.7	87.8	120	116	102	115	119	274	198	121
<b>L1 [<math>\mu</math>H]</b>	5.96	5.07	6.17	4.88	8.35	10.2	9.45	12.2	5.05	3.15	3.24	3.63
<b>KLM</b>	12.6	7.75	13.2	8.51	14.1	17.6	16.2	17.2	7.20	9.30	6.75	6.74
<b>Effi. (%)</b>	98.6	98.4	98.6	98.2	98.6	98.5	98.6	98.6	98.2	98.0	97.9	98.0
<b>PD. (%/g)</b>	0.43	0.43	0.24	0.24	0.30	0.17	0.30	0.17	0.27	0.31	0.24	0.19

According to the above table, the following conditions are discussed for moving into step 7:

- *Scenario I:* the total turn numbers for  $L_1$ ,  $L_2$ , and the transformer were obtained in scenario I as 6.37, 6.49, and 8.53 for the lower sizes and lower turns per layer, which will be 6, 6, and 8 if we put a floor under them, and 7, 7, 9 if we set a ceiling on them. For the lower sizes and higher turns per layer, the total turn numbers were obtained as 6.08, 6.10, and 7.38, which will be 6, 6, and 7 if we put a floor under them, and 7, 7, 8 if we set a ceiling on them. Also, the total turn numbers for  $L_1$ ,  $L_2$ , and the transformer were obtained 5.32, 5.62, and 6.55 for the higher sizes and lower turns per layer, which will be 5, 5, and 6 if we put a floor under them, and 6, 6, 7 if we set a ceiling on them. Finally, for the higher sizes and higher turns per layer, the total turn numbers were obtained as 5.12, 5.13, and 11.7, which will be 5, 5, and 11 if we put a floor under them, and 6, 6, 12 if we set a ceiling on them.
- *Scenario II:* the number of turns per layer for  $L_1$ ,  $L_2$ , and the transformer was obtained in scenario I as 0.92, 0.42, and 0.90 for the lower sizes and lower turn numbers, which will be 1 if we put a floor under them (0 is prohibited), and 2 if we set a ceiling on them. For the lower sizes and higher turn numbers, the number of turns per layer was obtained as 1.11, 1.16, and 0.92, which will be 1 if we put a floor under them, and 2 if we set a ceiling on them. Also, the number of turns per layer for  $L_1$ ,  $L_2$ , and the transformer was obtained at 0.90, 0.53, and 0.90 for the higher sizes and lower turn numbers, which will be 1 if we put a floor under them, and 2 if we set a ceiling on them. Finally, for the higher sizes and higher turn numbers, the number of turns

per layer was obtained as 0.90, 0.82, and 1.01, which will be 1 if we put a floor under them, and 2 if we set a ceiling on them.

- *Scenario III*: the core sizes for  $L_1$ ,  $L_2$ , and the transformer were obtained as 51.9, 50.4, and 64.9 for the lower turn numbers and lower turns per layer, which will be 47, 47, and 55 if we put a floor under them, and 55, 55, 65 if we set a ceiling on them. For the lower turn numbers and higher turns per layer, the core sizes were obtained as 54.1, 53.3, and 55.7, which will be 47, 47, and 55 if we put a floor under them, and 55, 55, 65 if we set a ceiling on them. Also, the core sizes for  $L_1$ ,  $L_2$ , and the transformer were obtained as 57.2, 52.5, and 64.9 for the higher turn numbers and lower turns per layer, which will be 55, 47, and 55 if we put a floor under them, and 65, 55, 65 if we set a ceiling on them. Finally, for the higher turn numbers and higher turns per layer, the core sizes were obtained as 62.7, 60.6, and 64.0, which will be 55, 55, and 55 if we put a floor under them, and 65, 65, 65 if we set a ceiling on them.

Therefore, we can conclude that the last non-integer parameter can be discretized in step 7 based on the corresponding scenarios as shown in Table 6-11 for better clarification.

*Table 6-11: Input parameters for optimization in step 8 when all the three discrete parameters in step 6 are transferred into the real world*

#Scenario	Discrete parameters								
	XL1	XL2	XT	NL1	NL2	NT	nL1	nL2	nT
<b>Scenario I</b>	47	47	55	6	6	8	1	1	1
	47	47	55	6	6	8	2	2	2
	47	47	55	7	7	9	1	1	1
	47	47	55	7	7	9	2	2	2
	55	55	65	6	6	8	1	1	1
	55	55	65	6	6	8	2	2	2
	55	55	65	7	7	9	1	1	1
	55	55	65	7	7	9	2	2	2
<b>Scenario II</b>	55	55	55	6	6	7	1	1	1
	55	55	55	6	6	7	2	2	2
	65	65	65	6	6	7	1	1	1
	65	65	65	6	6	7	2	2	2
	55	55	55	7	7	8	1	1	1
	55	55	55	7	7	8	2	2	2
	65	65	65	7	7	8	1	1	1
	65	65	65	7	7	8	2	2	2

#Scenario	Discrete parameters								
	XL1	XL2	XT	NL1	NL2	NT	nL1	nL2	nT
Scenario III	47	47	55	3	3	7	1	1	1
	55	55	65	3	3	7	1	1	1
	47	47	55	4	4	8	1	1	1
	55	55	65	4	4	8	1	1	1
	55	47	55	3	3	7	2	2	2
	65	55	65	3	3	7	2	2	2
	55	55	55	4	4	8	2	2	2
	65	65	65	4	4	8	2	2	2

where the last continuous variable is discretized by putting a floor under and a ceiling on it.

Consequently, the three discrete variables were considered as a fixed input parameter and now, all the variables are continuous and implementable. Therefore, the SQP algorithm can be performed in the real world. Hence, the last optimization is carried out in step 8 to find the airgap length while the efficiency and/or output power will be maximized. The result of this optimization is shown in Table 6-12:

*Table 6-12: The last optimization results (step 8), when all the three parameters were in the real world*

Scenario	Input parameters									Output parameters				
	XL1	XL2	XT	NL1	NL2	NT	nL1	nL2	nT	PD	eta	C1 [nF ]	L1 [μ H]	KL
I	47	47	55	6	6	8	1	1	1	Not feasible				
	47	47	55	6	6	8	2	2	2	Not feasible				
	47	47	55	7	7	9	1	1	1	Not feasible				
	47	47	55	7	7	9	2	2	2	Not feasible				
	55	55	65	6	6	8	1	1	1	0.2 40	98. 7	12 6	8.6	19. 3
	55	55	65	6	6	8	2	2	2	0.2 34	96. 4	70. 0	4.6	6.0
	55	55	65	7	7	9	1	1	1	0.2 39	98. 6	11 7	9.9	20. 0
	55	55	65	7	7	9	2	2	2	0.2 34	96. 3	70	4.6	6.0

Scenario	Input parameters									Output parameters				
	XL1	XL2	XT	NL1	NL2	NT	nL1	nL2	nT	PD	eta	C1 [nF]	L1 [ $\mu$ H]	KL
II	55	55	55	6	6	7	1	1	1	0.298	96.6	147	9.5	11.9
	55	55	55	6	6	7	2	2	2	0.297	96.2	70.1	4.6	6.0
	65	65	65	6	6	7	1	1	1	0.168	98.7	141	12	16.6
	65	65	65	6	6	7	2	2	2	0.164	96.2	60.0	5.34	6.0
	55	55	55	7	7	8	1	1	1	0.298	96.6	137	10	14.3
	55	55	55	7	7	8	2	2	2	0.297	96.3	85.0	3.77	6.1
	65	65	65	7	7	8	1	1	1	0.168	98.6	114	9.0	20.0
	65	65	65	7	7	8	2	2	2	0.168	98.2	87.7	4.0	8.1
III	47	47	55	3	3	7	1	1	1	Not feasible				
	55	55	65	3	3	7	1	1	1	0.240	98.5	132	11.3	19.0
	47	47	55	4	4	8	1	1	1	Not feasible				
	55	55	65	4	4	8	1	1	1	0.240	98.6	100	6.2	14.5
	55	47	55	3	3	7	2	2	2	Not feasible				
	65	55	65	3	3	7	2	2	2	0.193	96.3	110	2.9	6.2
	55	55	55	4	4	8	2	2	2	0.297	96.3	95.1	3.37	6.1
	65	65	65	4	4	8	2	2	2	0.164	96.2	144	2.22	6.0

The most obvious finding to emerge from Table 6-12 is that the optimum 3.3 kW bidirectional CLLC resonant converter in EV charging application is the sample with  $X_{L1}=55$ ,  $X_{L2}=55$ , and  $X_T=65$ , and  $C_1=C_2=100\text{nF}$ . It has also the minimum mass with the maximum efficiency and is selected as the optimum sample (step 9).

## 6.7. Comparison between the optimization results

The first comparison is the time for running the code for single operating point and multiple operating points optimizations, which is shown in Table 6-13. More information is also listed in Table 6-13.

*Table 6-13: Number of parameters and running time comparison for two optimization process*

Parameters	1 operating point	4 operating points
Number of input variables	30	62
Number of output constraints	16	64
Number of objective functions	1	1
Optimization running time	2.8 seconds	112 seconds

An important question is that what will be the optimization results when the FHA method is utilized to obtain the optimum result and meet the constraints. In this case, the FHA method is developed in Cades instead of SPA method. The peak value, RMS value, ZVS constraint, CCM operating condition, output voltage, required output current, and required switching frequency range are obtained based on the FHA method. The corresponding results in comparison with SPA method is summarize in Table 6-14, where the input parameters and the constraints are the same.

This table illustrates that the optimum result based on the proposed method (SPA) has a higher objective function in comparison with the result based on the FHA method, when all the constraints are met. The average efficiency of the proposed method is about 1.4% higher than FHA method, due to the fact that the value of the primary and secondary currents for FHA method is higher than SPA-based values and it causes higher losses. As a conclusion, the optimization result based on the proposed method has a higher average efficiency with lower mass.

Table 6-14: four operating points optimizations based on FHA and SPA methods

Parameter	FHA based optimization results	SPA based optimization results	unit
Objective function	0.158	0.240	%/g
Optimization time	47	70	s
Average efficiency	97.2	98.6	%
Core sizes [L <sub>1</sub> ,L <sub>2</sub> ,T]	[65,65,65]	[55,55,65]	-
Turn numbers [L <sub>1</sub> ,L <sub>2</sub> ,T]	[3,3,8]	[4,4,8]	-
C <sub>1</sub>	62	100	nF
L <sub>1</sub>	8.4	6.2	μH
K <sub>LM</sub>	13.8	14.5	-
Junction temperature constraints	OK	OK	-
Saturation constraints	OK	OK	-
Vertical fit constraints	OK	OK	-
Horizontal fit constraints	OK	OK	-

The last comparison is based on the selected methodology for the optimization process. The deterministic SQP method was adopted in this dissertation but it is better to compare it with the genetic algorithm (GA) which is a stochastic algorithm. In this case, the number of 100 populations is considered and 1000 generations are provided. The probability of mutation is selected as 10% to decrease the possibility of stuck in the local extremum. The optimization results based on the GA and SQP are demonstrated in Table 6-15. It should be mentioned that one of the advantages of the CADES software is the capability of changing the optimization method easily. In this case, before the input parameters, the optimization method is selected between sequential quadratic programming (SQP), genetic algorithm (GA), particle swarm optimization (PSO), DIviding RECTangles optimization (DIRECT), evolutionary optimization (EO), restricted tournament selection (RTS), and interior point optimizer (IPO).

Table 6-15: Optimization results based on the genetic algorithm (GA) and sequential quadratic programming (SQP) for 4 operating points optimizations

Parameter	Results based on GA	Results based on SQP	unit
Objective function	0.303	0.240	%/g
Optimization time	181.3	1.2	min
Average efficiency	95.4	98.6	%
Core sizes [L <sub>1</sub> ,L <sub>2</sub> ,T]	[55,55,55]	[55,55,65]	-
Turn numbers [L <sub>1</sub> ,L <sub>2</sub> ,T]	[2,2,6]	[4,4,8]	-
C <sub>1</sub>	36	100	nF
L <sub>1</sub>	13.8	6.2	μH
K <sub>LM</sub>	23.8	14.5	-
Junction temperature constraints	NOT OK	OK	-
Saturation constraints	NOT OK	OK	-
Vertical fit constraints	OK	OK	-
Horizontal fit constraints	OK	OK	-

The above tables indicates that the objective function is about 0.303 %/g for GA and 0.240 %/g for SPA method. The size of the magnetic cores is also less than for GA, but it is not possible to meet all constraints. In the other words, the optimum result with all constraints cannot be obtained by genetic algorithm. In this case, the junction temperature exceeds the defined limit and the magnetic cores operate in the saturation region due to the high frequency and high current operating.

## 6.8. Experimental Verification

The optimum result obtained in the previous part must be checked to physically verify that not only the obtained result can meet all the constraints, but also this converter can operate



correctly in different operating points with high efficiency in bidirectional power transfer. Two different samples are also built as case studies to compare the optimization data with other samples in the experimental environment to consider any probabilistic unobserved physical phenomenon. The main objectives of this part are as follows:

- Examining the objective function and constraints of different prototypes in multiple operating points;
- Comparing the proposed optimum result with two different scenarios to validate the proposed algorithm.

### 6.8.1. Specifications of the Experimental Prototype

Two experimental prototypes are considered to verify the proposed optimization algorithm. Table 6-16 shows the main specifications of the prototypes.

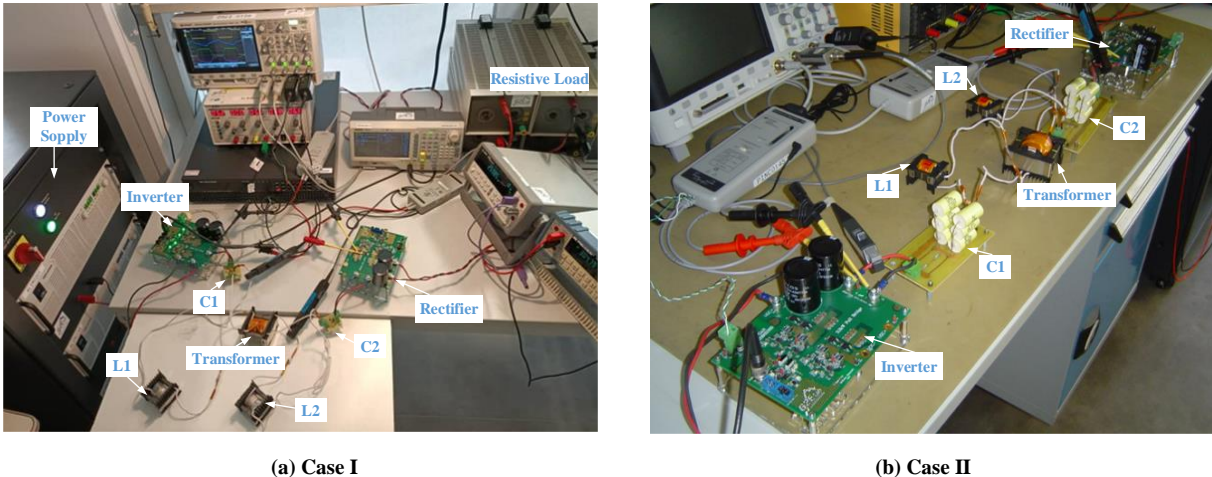


*Fig. 6-8: Two experimental prototypes. Case I is the optimum set up and Case II is the set up with a lower mass*

where *case I* is the optimum power density sample based on the proposed algorithm, and *case II* is a sample with lower mass and specifications obtained by the optimization algorithm. It should be mentioned that *case II* consists of a smaller standard size for magnetic components to demonstrate that *case I* is the optimum converter in size while all constraints are also met. There is no guarantee for *case II* to reach the maximum power in steady state conditions.

Table 6-16: Specifications of two experimental prototypes

<i>Parameter</i>	<i>Case I</i>	<i>Case II</i>
$S_1\sim S_8$	GS66508B GaN	GS66508B GaN
$D_1\sim D_8$	C4D10120 SiC	C4D10120 SiC
$C_1$	100 nF	99 nF
$C_2$	100 nF	99 nF
$C_0$	100 nF	220 $\mu$ F
$L_1$	6.2 $\mu$ H	25 $\mu$ H
$L_2$	6.2 $\mu$ H	25 $\mu$ H
$L_m$	90 $\mu$ H	125 $\mu$ H
$V_{OUT}$	250~400 V	250~400 V
$V_{IN}$	400 V	400 V
$f_{sw}$	100~350 kHz	90~350 kHz
$n$	1:1	1:1

### 6.8.2. Resonant tank

The resonant tank contains two parts: a magnetic part and resonant capacitors. The magnetic parts are made by EE-shape cores with 3C90 material. The value of leakage inductance and magnetizing inductance is measured by the impedance analyzer KEYSIGHT E4990A 20 Hz-120MHz with Keystone 16047E terminal for  $F \leq 100$ MHz (see Fig. 6-9).

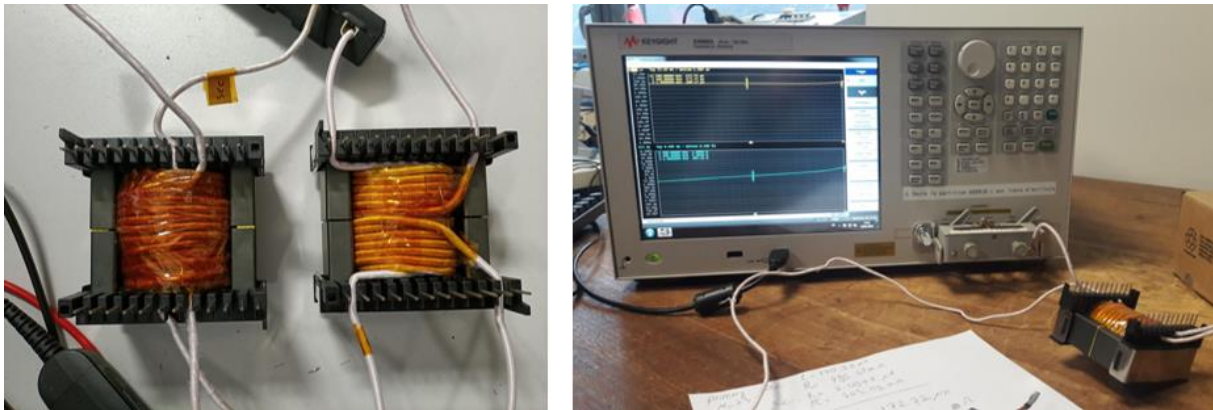
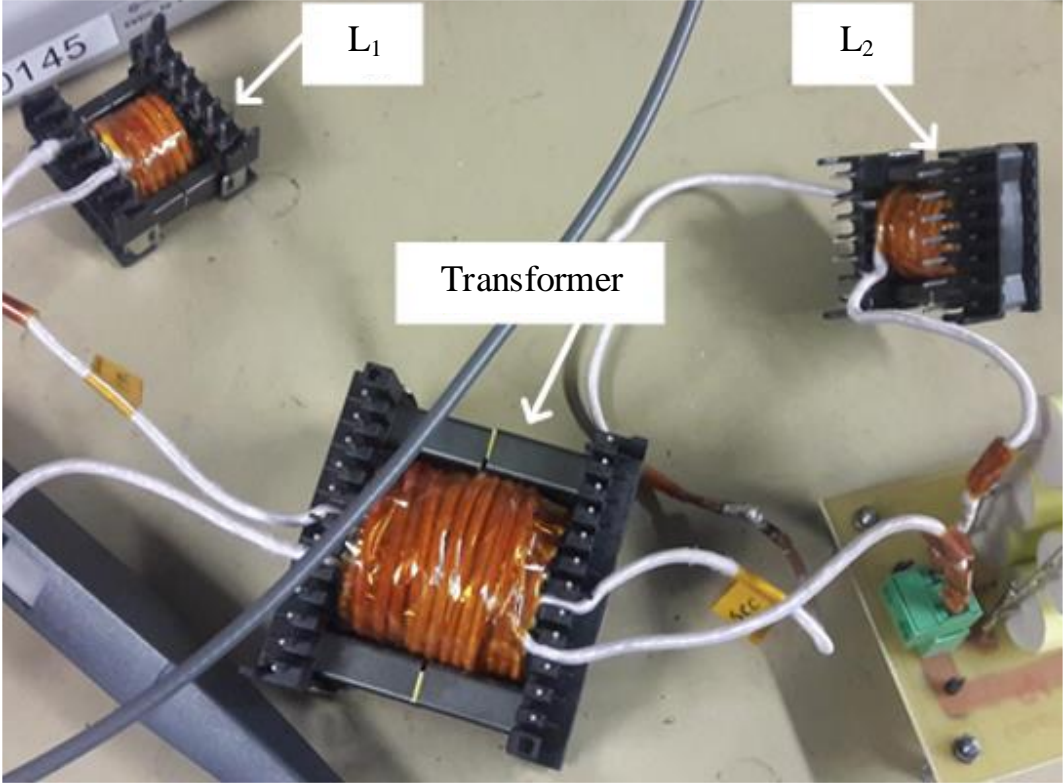


Fig. 6-9: The magnetic transformers (left figure) and impedance analyzer to measure leakage inductance and magnetizing inductance

The short circuit and open circuit tests are carried out to find the value of leakage and magnetizing inductance. For short circuit test, the secondary side is shorted and the value of inductance ( $L_{SC}$ ) is measured in the related frequencies. The inductance value in the open circuit

condition ( $L_{OC}$ ) is also measured when the secondary side is left as open circuit. These conditions were shown in Fig. 5-30.

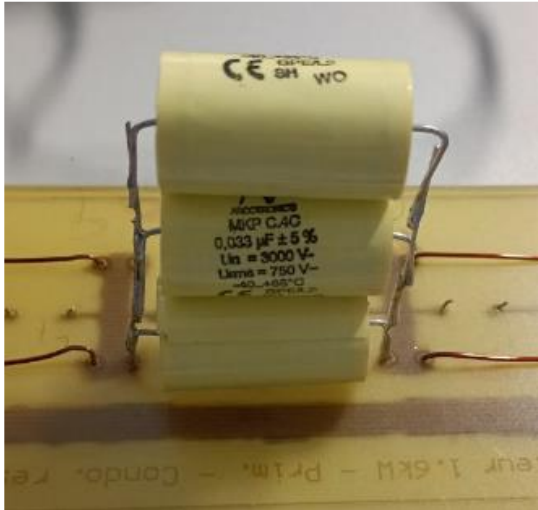
Also, the Litz wire 35819-D160 is also used for winding with 280 strands and a diameter of 0.15mm for each strand to reduce the skin effect. It should be mentioned that this selection is based on the maximum required current. The final magnetic part is shown in Fig. 6-10:



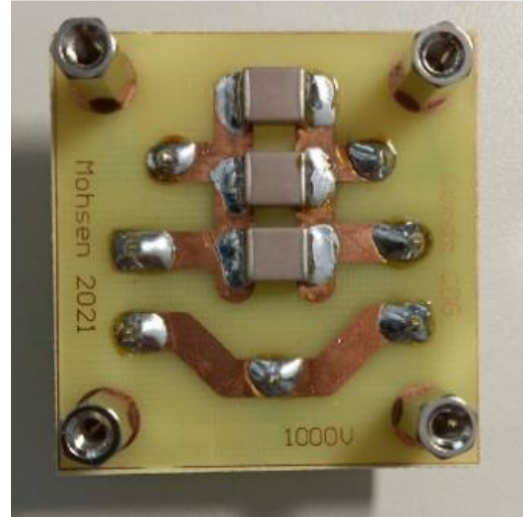
*Fig. 6-10: Physical implementation of the transformer, primary inductor ( $L_1$ ), and secondary inductor ( $L_2$ ) obtained by the initial design.*

The resonant capacitors are also shown in Fig. 6-11, where metalized polypropylene 33nF MKP capacitors are used for the smaller set up (Fig. 6-11-(a)) and three parallel MLCCs are used for the optimum set up to provide 100nF (Fig. 6-11-(b)). Due to the small mass of these capacitors, they are neglected in the total mass of the converter.

Also, the resonant capacitors and magnetic parts possess modularity, which means they can connect to the other part with a connector.



(a)



(b)

Fig. 6-11: The resonant capacitors for two experiments, (a) for the set up with lower size, and (b) for the optimum set up

The proposed optimization method can be verified easily, but it is better to consider a lower size magnetic core and evaluate the constraints.

### 6.8.3. Considering a Lower Size than the Optimum Setup

Let's consider an experimental setup with lower standard sizes for the magnetic cores to provide 3.3kW in the full-load conditions (however, there is no guarantee to reach 3.3kW with these magnetic cores). Fig. 6-12 shows the resonant elements of this setup. The parameters of this set up were listed in Table 6-16 case II.

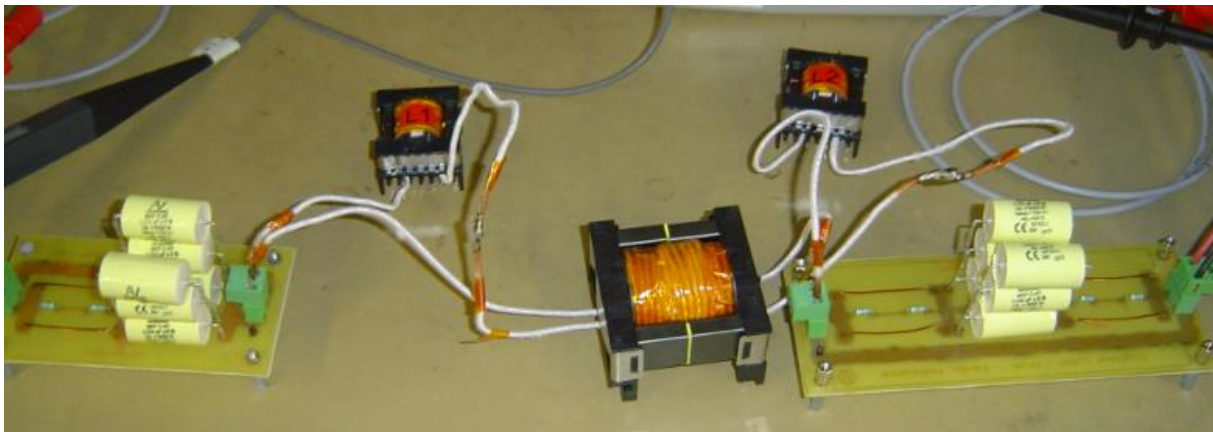


Fig. 6-12: Resonant tank of the experimental set up with a lower size

It is mandatory to consider different operating points to examine the converter with a lower size. Firstly, the switching frequency is considered as  $F=1.25$  and the load current is changed.

In this case, the maximum power is limited to 1.6kW. Fig. 6-13 illustrates the output current versus the output voltage at  $F=1.25$ :

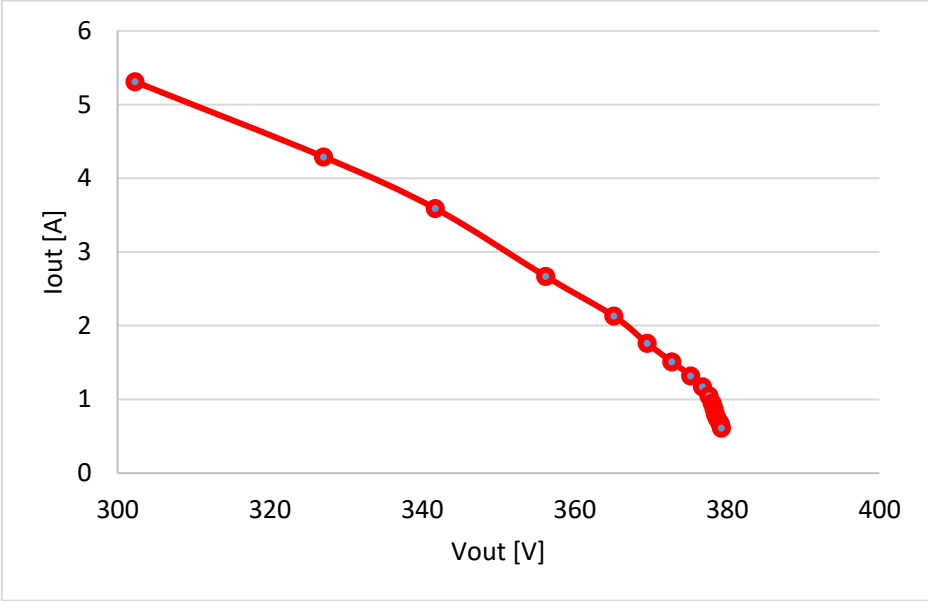


Fig. 6-13: The output current ( $I_{out}$ ) versus the output voltage ( $V_{out}$ ) of the smaller experimental set up

Secondly, the frequency is changed to obtain different power. Fig. 6-14 shows the M-F curve of this test set up.

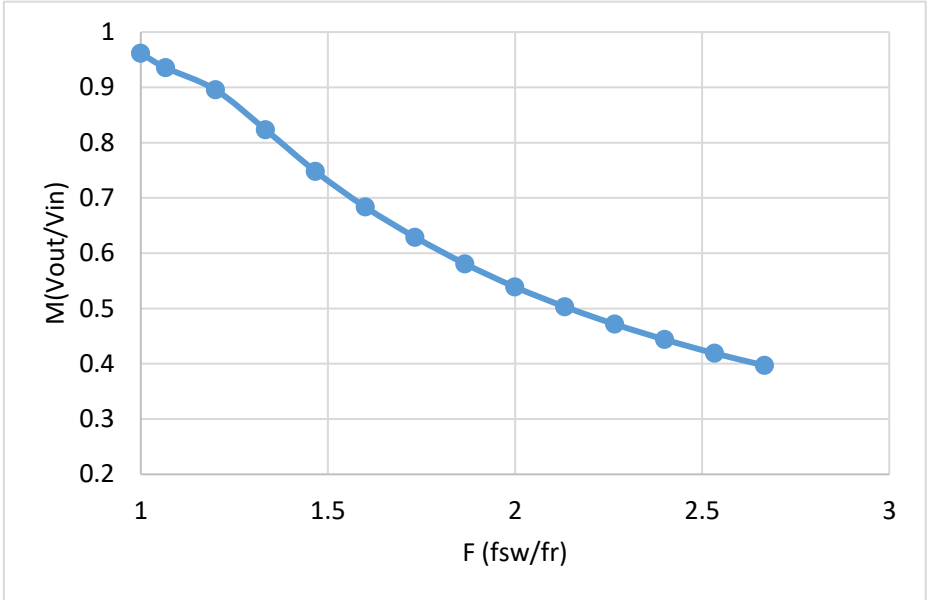


Fig. 6-14: M-F curve of the smaller experimental set up

However, the temperature of the primary inductor exceeds  $100^{\circ}\text{C}$  and contradicts the temperature constraints because the maximum junction temperature had been considered as

85°C in the optimization process. Furthermore, this overheating leads to the inductor behavior changes and directly varies the resonant frequency. As a result, the M-F curve shown in Fig. 6-15 was obtained in a short time and it is not valid for steady-state conditions.

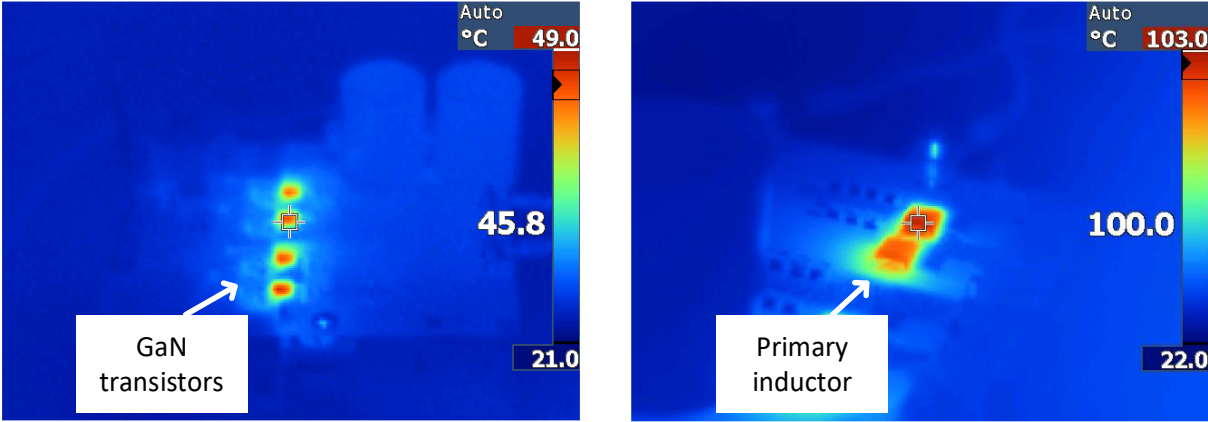


Fig. 6-15: The junction temperature of GaN transistors of the primary side (left curve), and the primary resonant inductor (right curve).

In this case, the resonant inductors current and capacitors voltage are shown in Fig. 6-16 which is captured immediately after the start-up condition.

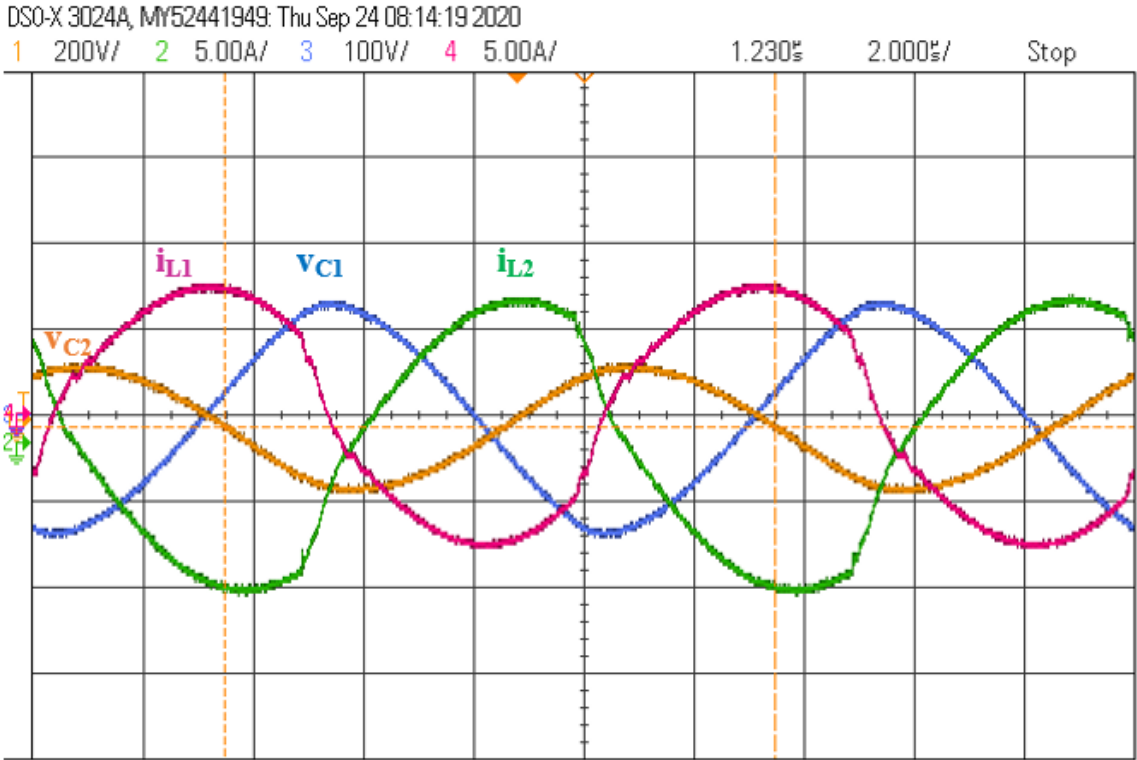


Fig. 6-16: The primary inductor current (red), the secondary inductor current (green), the primary capacitor voltage (blue), and the secondary capacitor voltage (orange) for the smaller in-size experimental set up

This experimental setup, which is lower than the optimum result in-size, expresses that it is not possible to reach the required power at  $F > 1$ , and also the temperature of components exceeds the constraint (i.e. reaches  $100^{\circ}\text{C}$ ) for  $F \approx 1$ . Therefore, this experimental setup cannot meet all the requirements and constraints.

### 6.8.4. Considering the Optimum Setup

Now, let's consider the 3.3 kW optimum experimental setup to evaluate it in the different operating points. The parameters of this set up were listed in Table 6-16 case I.

The first operating point is considered as  $F=1$ . The temperature distribution of the components is shown in Fig. 6-17-(a). Also, the placement of the component is shown in Fig. 6-17-(b). Furthermore, the corresponding waveforms of the resonant elements and semiconductors are shown in Fig. 6-17-(c) and (d), respectively.

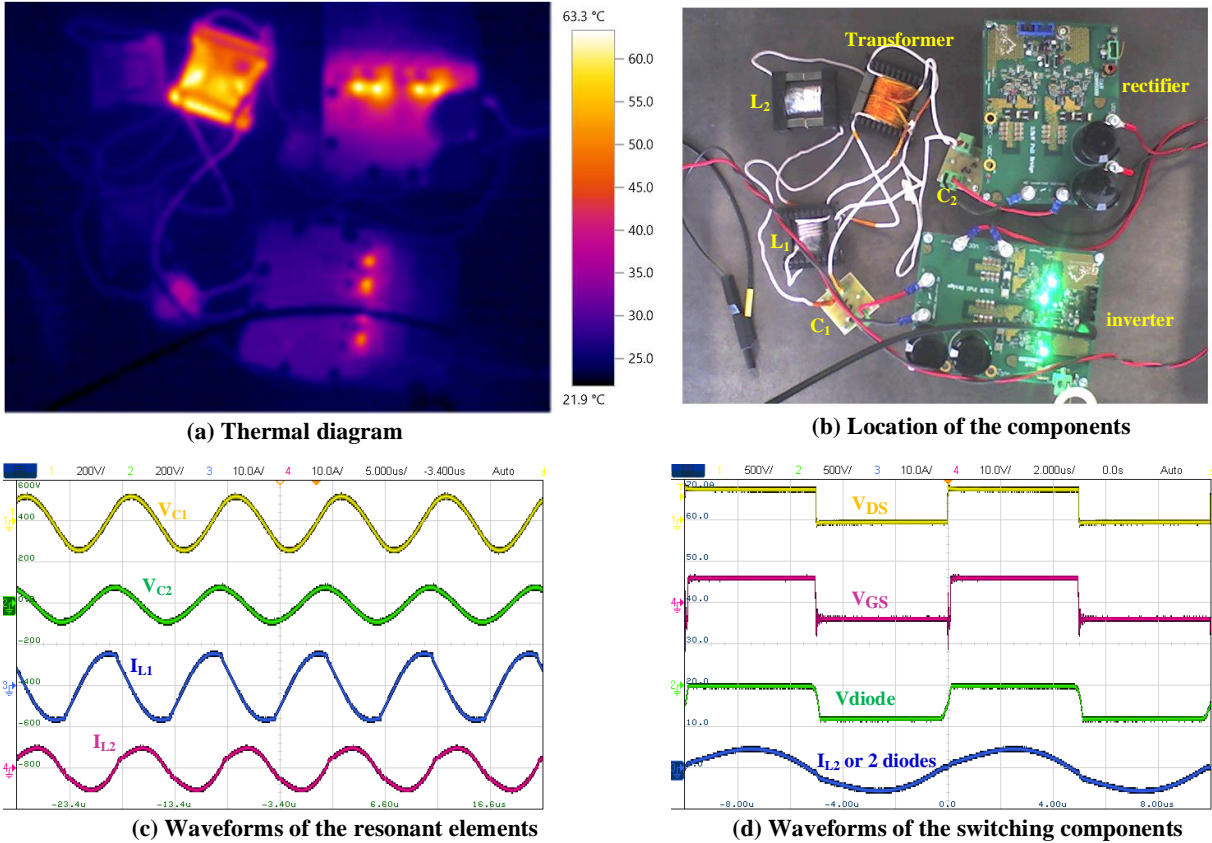


Fig. 6-17: Some important experimental results at  $F=1$ : (a) temperature distribution in a thermal diagram, (b) location of the components for better investigation of the thermal diagram, (c) voltage of resonant capacitors and current of resonant inductors, (d) drain-to-source and gate-to-source voltages of GaN transistor, and voltage and current of SiC diode.

According to Fig. 6-17, the maximum temperature is related to the transformer and it is 63.3°C. The temperatures of the GaN transistor and the SiC diode are 50.8°C and 62.8°C, respectively. The peak-to-peak voltages of  $C_1$  and  $C_2$  are 280V and 190V, and the peak-to-peak currents of  $L_1$  and  $L_2$  are 17.3A and 10.9, respectively.

The second operating point is considered as  $F=2$ . The temperature distribution of the components is shown in Fig. 6-18-(a). Also, the placement of the component is shown in Fig. 6-18-(b). Furthermore, the corresponding waveforms of the resonant elements and semiconductors are shown in Fig. 6-18-(c) and (d), respectively.

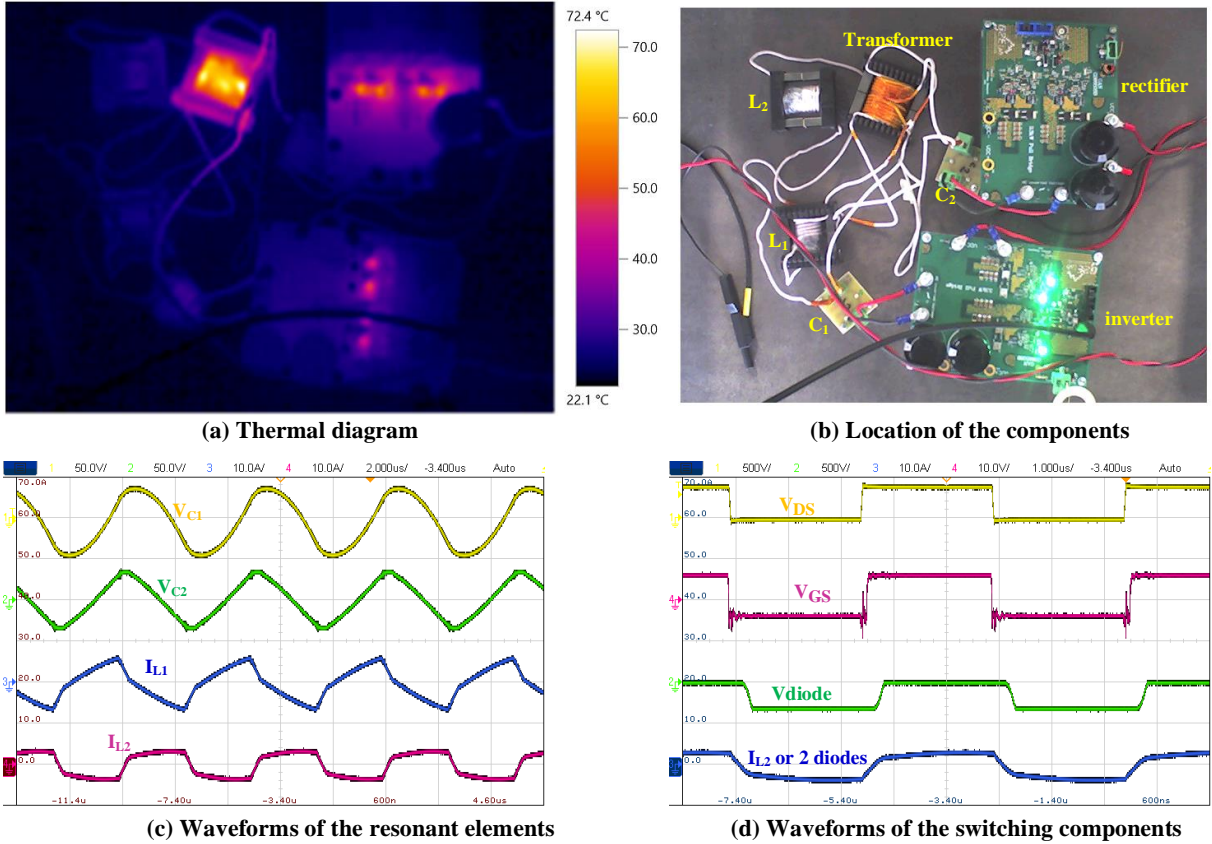


Fig. 6-18: Some important experimental results at  $F=2$ : (a) temperature distribution in a thermal diagram, (b) location of the components for better investigation of the thermal diagram, (c) voltage of resonant capacitors and current of resonant inductors, (d) drain-to-source and gate-to-source voltages of GaN transistor, and voltage and current of SiC diode.

According to Fig. 6-18, the maximum temperature is related to the transformer and it is 72.4°C. The temperatures of the GaN transistor and the SiC diode are 48.9°C and 54.6°C, respectively. The peak-to-peak voltages of  $C_1$  and  $C_2$  are 86V and 72V, and the peak-to-peak currents of  $L_1$  and  $L_2$  are 13.7A and 7.6, respectively.



The last operating point is considered as  $F=3$ . The temperature distribution of the components is shown in Fig. 6-19-(a). Also, the placement of the component is shown in Fig. 6-19-(b). Furthermore, the corresponding waveforms of the resonant elements and semiconductors are shown in Fig. 6-19-(c) and (d), respectively.

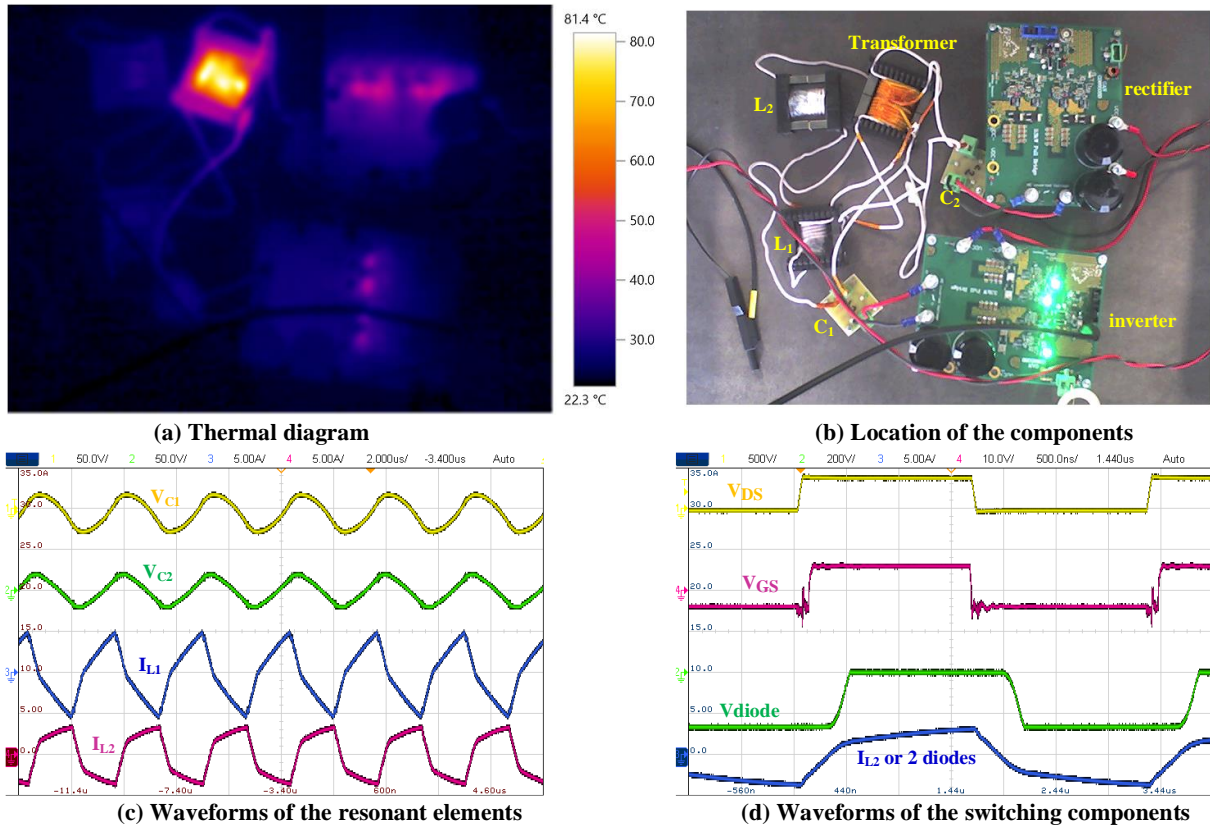


Fig. 6-19: Some important experimental results at  $F=3$ : (a) temperature distribution in a thermal diagram, (b) location of the components for better investigation of the thermal diagram, (c) voltage of resonant capacitors and current of resonant inductors, (d) drain-to-source and gate-to-source voltages of GaN transistor, and voltage and current of SiC diode.

According to Fig. 6-19, the maximum temperature is related to the transformer and it is  $81.4^{\circ}\text{C}$ . The temperatures of the GaN transistor and the SiC diode are  $41.5^{\circ}\text{C}$  and  $47.4^{\circ}\text{C}$ , respectively. The peak-to-peak voltages of  $C_1$  and  $C_2$  are 48V and 44V, and the peak-to-peak currents of  $L_1$  and  $L_2$  are 10.7A and 7.4, respectively.

As a result, the aforementioned results were shown that the temperature of all components is below  $85^{\circ}\text{C}$  and therefore the constraints related to the temperature are met. The electrical behavior of the components has a reasonable match with the results obtained by the state plane analysis shown in **Chapter 5**. Therefore, the proposed multi operating points optimization method is verified.

Table 6-17 is compared several important parameters of some references with the proposed method.

Table 6-17: General comparisons between some references and the proposed method

Ref.	Proposed	[18]	[35]	[42]	[167]	[168]	[169]	[170]
<b>Topology</b>	CLLC	CLLC	Flyback	CLLC	SRC	DAB	LLC	LLC
<b>Pout</b>	3.3kW	6.6kW	3.3kW	3.3kW	3.3kW	3.3kW	3.3kW	3.3kW
<b>Vout</b>	250V to 400V	0.975 to 1.025	250V to 420V	250V to 420V	250V to 400V	200V to 450V	230V to 430V	64.8V to 86.4V
<b>frequency</b>	100kHz to 350kHz	500kHz	100kHz	127kHz	200kHz	200kHz	86.6 kHz	300kHz
<b>Efficiency</b>	95.72%	97.85%	96.4%	98.2%	95%	96%	97.6%	-
<b>Optimization</b>	Multi	Single	Single	Single, GA	-	-	Single	-
<b>Mass/volume</b>	415gr for cores, V <sub>core</sub> = 167cm <sup>3</sup>	114 W/in <sup>3</sup>	V <sub>core</sub> = 170cm <sup>3</sup>	570gr, 90000 mm <sup>3</sup>	-	6.2 kg, 5.46 L	2540 cm <sup>3</sup> , 1.06 kW/L	-
<b>Transformer</b>	EE65, K <sub>LM</sub> = 14.52	Planar with 2 cores, K <sub>LM</sub> =10	EE65 core, K <sub>LM</sub> = 13.64	EE65 core, K <sub>LM</sub> = 16.2	-	-	K <sub>LM</sub> = 7.11	K <sub>LM</sub> = 2.86
<b>Inductors</b>	6.2μH	3.07μH	11μH	21μH	-	8 μH	45 μH	28μH
<b>Capacitors</b>	100nF	33nF	6μF	33nF	-	-	75nF	40nF
<b>Method</b>	SPA	FHA	-	FEM	FHA, FEM	TDA	TDA	FHA
<b>Application</b>	Bidirect. EV on-board charger	EV on-board charger	EV on-board charger	EV on-board charger	EV charger	EV on-board charger	EV on-board charger	EV on-board charger

## 6.9. Summary

In this chapter, an algorithm for the optimization of multi operating points problems in bidirectional EV charging applications was presented. The input parameters, output parameters, and constraints were expressed to use in an optimization algorithm. A single operating point optimization was implemented in *CADES* Software, and it was shown that the designed converter based on the single operating point cannot meet all the constraints for the other points. Therefore, the multi operating points optimization algorithm was proposed which can find an optimum converter through 9 steps, when all the constraints are met. It should be mentioned that a new version of the objective function (i.e. efficiency divided by mass) was considered

instead of typical power density (i.e. nominal output power divided by mass) since the maximum output power is fixed as 3.3kW, and cannot be maximized or minimized.

A 3.3-kW prototyping was built. Experimental results were used to verify the proposed method. Simulation and experimental results reveal the accuracy of the proposed analysis in the forward and the reverse power transfer modes for different power and voltage levels

# 7. Conclusions and Future Work

## 7.1. Conclusions

This dissertation focuses on the analysis and optimization of the full-bridge CLLC resonant converter for bidirectional EV charger applications. The outcomes of this dissertation are an exact method for analyzing the CLLC resonant converter and other high-order resonant converters as well as a multi operating points optimization algorithm for use in the EV charger applications and other wide-range applications.

Firstly, the types of EVs were introduced and the all-electric vehicle or battery electric vehicle (BEV) was selected due to the limitations of fossil fuels, increase in charging stations, advancement of lithium-ion battery technology, and price reduction of the batteries. Among the requirements of BEVs (i.e. electrical, placement, environmental, and safety requirements), only electrical requirements were considered. Secondly, the PWM-based converters and resonant-based converters were examined, and the resonant converters were selected due to their high efficiency, high power density, high switching frequency, bidirectional power transferring, and soft switching for a wide range of loads. Thirdly, the bidirectional capability was also considered for the selected converter because of beginning the consistent trends of the future, more using renewable energies capabilities, using as an uninterruptable power supply and avoiding blackouts, supplying appliances inside the vehicle, etc.

Among the different resonant converters, the CLLC resonant converter is a good candidate with excellent power density and efficiency bidirectionally and also a wide soft switching region. Nevertheless, none of the previous studies has provided any exact analyzing approach and general optimization method in terms of bidirectional power transferring and EV charging constraints.

Before presenting the proposed methods, it is needed to define the optimization problem and find an approach for its solving. The optimization algorithms can be classified into two categories: stochastic algorithms and deterministic algorithms, where sequential quadratic

programming (SQP) as one of the deterministic algorithms was selected in this dissertation. Because the SQP method is a gradient-based optimization technique, continuous variables are needed. But, in the power electronics converter, there are some discrete variables such as the total number of turns, core sizes, number of turns in each layer, etc. Therefore, a continuous model was presented to define each parameter as a continuous parameter.

Furthermore, the calculation of total power losses is important to obtain the total efficiency and power density. In this case, an interpolation-based method for the calculation of switching losses was presented to obtain the switching loss of different GaN transistors, with different voltages, currents, gate driver circuit parameters, temperatures, etc. For the conduction loss, another method was proposed to calculate conduction losses based on the datasheet's value of different GaN transistors. For comprehensive loss calculation, the diode loss, magnetic losses, copper losses in wires, capacitor loss, etc. were discussed. A method for magnetic design based on the magnetic circuit and reluctance was also considered. The objective function was evaluated based on the loss calculation of components, and the design procedure for the magnetic components and capacitors. Different constraints, e.g. operating region, maximum temperature, maximum RMS current of capacitors, maximum voltages, ZVS condition, and CCM operating, were also discussed to provide a global optimization problem with the correct objective function and constraints.

The common method for analyzing the resonant converters and also CLLC resonant converter is the first harmonic approximation (FHA) method. However, as it was shown in Table 3-4, the error reaches as high as 23.47% for  $i_{L1max}$ , 13.18% for  $i_{L2max}$ , 16.37% for  $v_{C1max}$ , and 19.09% for  $v_{C2max}$ . As a result, this method is not an appropriate method to design and optimize the CLLC resonant converter.

Therefore, a new formulation of state-space equations was presented and the fourth-order CLLC resonant converter was transformed into two second-order systems. Then using this mathematical method, the exact analysis of the converter in CCM and DCM, stresses of the components, voltage gain ratio, soft switching conditions, and the boundary between CCM/DCM were obtained. The accuracy of this method was compared with the simulation results, which implies that the proposed method can be considered as an exact method for the exact analysis of the CLLC resonant converter.

Having the proposed exact analysis method, it is better to use it in the optimization process to increase the accuracy of obtained results. At first, the proposed state-plane analysis was implemented into the *CADES* software by C++. This code was verified by Maxwell simulation.

As an example, the magnetizing inductance based on the *CADES* analysis was calculated as  $86.76\mu\text{H}$ , and it was obtained as  $84.3827\mu\text{H}$  using Maxwell simulation, which is shown the appropriate accuracy.

In the optimization process, it is obvious that an EV charger operates at different voltage and current levels based on the behavior of Lithium-Ion batteries. In this dissertation was shown that if only one operating point was considered and optimization was done based on that point, all the constraints could not be met for the other operating points. Therefore, a new approach was proposed for multi operating points optimization. Based on this method, the discrete variables were considered as continuous variables and optimization was done in the imaginary world. Then and each time for one discrete variable, the discrete variable will be continuous by putting a floor under it, and setting a ceiling on it. This process continued to find the continuous version of all variables, and finally, the best solution was considered as the optimum converter. It was EE55 core for the inductors and EE65 core for the transformer, and resonant capacitors equal to 100nF.

Two experimental setups were built to verify the optimization algorithm. One of them was the optimum 3.3 kW prototype obtained based on the proposed algorithm with  $X_{L1}=55$ ,  $X_{L2}=55$ , and  $X_T=65$ , and the other one was a prototype with a smaller-in-size converter (i.e.  $X_{L1}=47$ ,  $X_{L2}=47$ , and  $X_T=55$ ). It was attempted to the converters operated at same operating points and the constraints were evaluated.

Although the optimum converter has successfully operated in the defined operating points, the smaller converter has certain limitations in terms of the required power and high-frequency operating. It was not possible for the smaller converter to provide 3.3kW and this converter was limited to a lower power. Furthermore, the optimum converter run at 3.3kW and the maximum temperature of magnetic cores reached  $81.4^\circ\text{C}$ . But, for the smaller converter, the temperature of the primary inductor exceeds  $100^\circ\text{C}$  and contradicts the temperature constraints because the maximum junction temperature had been considered as  $85^\circ\text{C}$  in the optimization process. Furthermore, this overheating leads to the inductor behavior changes and directly varies the resonant frequency. Consequently, the designed converter has the minimum mass when 3.3kW is provided and it is not possible to achieve the output power of 3.3kW and the defined constraints with a smaller converter.

## 7.2. Future Work

Regarding future work on the analysis and optimization of bidirectional EV chargers based on the CLLC resonant converter, the following improvements are suggested:

1. The selected converter was a full-bridge CLLC resonant converter. Adding a half-bridge corresponding analysis can make the analysis detailed.
2. The common CLLC-based resonant converters are typically operated above the resonant frequency, similar to this dissertation. For a comprehensive analysis, it is better to add analysis below the resonant frequency.
3. In this dissertation, the resonant inductors were added externally to the transformer to provide the required leakage inductance. Including the resonant inductors and magnetizing inductor into one resonant network can result in finding the global maximum power density.
4. In the optimization process, transferring from one step to another step requires pre-examining by the designer and it is not done automatically. In the new version of this optimization algorithm, defining an automatic process is preferred.
5. The optimization algorithm can be implemented into Matlab for better data analysis.
6. The selected platform for the experimental setups is the conventional EE transformers. Using new technologies such as planar transformers can provide an integrated transformer with corresponding leakage inductors to reduce mass/volume significantly [42]. The CLLC implementation in an integrated magnetic part can be done in future work. Also, the anti-parallel junction capacitance of the main switches can be considered in the resonant tank as future work.

# References

- [1] M. Balat, "Status of Fossil Energy Resources: A Global Perspective," *Energy Sources, Part B: Economics, Planning, and Policy*, vol. 2, no. 1, pp. 31-47, 2007.
- [2] S. A. Neves and A. C. Marques, "The substitution of fossil fuels in the US transportation energy mix: Are emissions decoupling from economic growth?," *Research in Transportation Economics, Elsevier*, vol. 90, p. 101036, 2021.
- [3] P. Friedlingstein, M. W. Jones, M. O'Sullivan and e. al., "Global Carbon Project," 2021. [Online]. Available: [www.globalcarbonproject.org/carbonbudget](http://www.globalcarbonproject.org/carbonbudget). [Accessed 26 April 2022].
- [4] C. Marinescu and L. Barote, "Toward a practical solution for residential RES based EV charging system," in *International Conference on Optimization of Electrical and Electronic Equipment (OPTIM) & 2017 Intl Aegean Conference on Electrical Machines and Power Electronics (ACEMP)*, Brasov, Romania, 25-27 May 2017.
- [5] A. Chrisafis and A. Vaughan, "France to ban sales of petrol and diesel cars by 2040," [Online]. Available: [www.theguardian.com/business/2017/jul/06/france-ban-petrol-diesel-cars-2040-emmanuel-macron-volvo](http://www.theguardian.com/business/2017/jul/06/france-ban-petrol-diesel-cars-2040-emmanuel-macron-volvo). [Accessed 6 July 2017].
- [6] "Green Roadmap," [Online]. Available: [www.ft.dk/samling/20151/almdel/TRU/bilag/154/1594586.pdf](http://www.ft.dk/samling/20151/almdel/TRU/bilag/154/1594586.pdf).
- [7] "Global EV Outlook 2022: Securing supplies for an electric future," [Online]. Available: [www.iea.org/reports/global-ev-outlook-2022](http://www.iea.org/reports/global-ev-outlook-2022). [Accessed 23 May 2022].
- [8] R. Irle, "Global EV Sales for 2022 H1," 2022. [Online]. Available: [www.ev-volumes.com/country/total-world-plug-in-vehicle-volumes/](http://www.ev-volumes.com/country/total-world-plug-in-vehicle-volumes/). [Accessed 23 August 2022].
- [9] M. Dwyer, "EIA projects global conventional vehicle fleet will peak in 2038," [Online]. Available: [www.eia.gov/todayinenergy/detail.php?id=50096](http://www.eia.gov/todayinenergy/detail.php?id=50096). [Accessed 26 October 2021].
- [10] A. Emadi, *Advanced electric drive vehicles*, CRC Press, 2014.
- [11] S. Sawsan S. and A. M. Massoud, "Review on State-of-the-Art Unidirectional Non-Isolated Power Factor Correction Converters for Short-/Long-Distance Electric Vehicles," *IEEE Access*, vol. 10, pp. 11308-11340, 26 January 2022.
- [12] "The state of EV charging infrastructure in Europe by 2030," [Online]. Available: <https://www.virta.global/blog/ev-charging-infrastructure-development-statistics>. [Accessed 16 May 2022].
- [13] A. Syed Muhammad, T. T. Lie, B. C. Seet, S. Ayyadi and K. Jensen, "Review of Electric Vehicle Technologies, Charging Methods, Standards and Optimization Techniques," *Electronics*, vol. 10, no. 16, p. 1910, 9 August 2021.
- [14] [Online]. Available: [https://afdc.energy.gov/fuels/electricity\\_infrastructure.html](https://afdc.energy.gov/fuels/electricity_infrastructure.html).



- [15] [Online]. Available: <https://afdc.energy.gov/>.
- [16] [Online]. Available: <https://www.statista.com/statistics/932730/number-of-electric-vehicle-charging-stations-france/#statisticContainer>.
- [17] B. Albert G., A. C. Chu, S. Maxx and D. L. Waltz, "Vehicle Electrification: Status and Issues," *Proceedings of the IEEE*, vol. 99, no. 6, pp. 1116-1138, 2011.
- [18] Z. Zhang, C. Liu, M. Wang, Y. Si, Y. Liu and Q. Lei, "High-Efficiency High-Power-Density CLLC Resonant Converter With Low-Stray-Capacitance and Well-Heat-Dissipated Planar Transformer for EV On-Board Charger," *IEEE Transactions on Power Electronics*, vol. 35, no. 10, pp. 10831-10851, 2020.
- [19] J. Bigorra, C. Borrego, J. Fontanilles and J. Giró, "Innovative electrical and electronic architecture for vehicles with dual voltage power networks. In-vehicle application," *SAE transactions*, pp. 232-239, 2000.
- [20] A. Matallana, E. Ibarra, I. López, J. Andreu, J. Garate, X. Jordà and J. Rebollo, "Power module electronics in HEV/EV applications: New trends in wide-bandgap semiconductor technologies and design aspects," *Renewable and Sustainable Energy Reviews*, vol. 113, p. 109264, 2019.
- [21] V. Voora, S. Bermúdez and C. Larrea, "Global Market Insights report Inc. report," International Institute for Sustainable Development, 2019.
- [22] S. Grigory, X. Hu, N. Ilinskaya, A. Kumar, A. Koudymov, J. Zhang, M. Asif Khan, R. Gaska and M. S. Shur, "7.5 kW/mm<sup>2</sup> current switch using AlGa<sub>N</sub>/Ga<sub>N</sub> metal-oxide-semiconductor heterostructure field effect transistors on SiC substrates," *Electronics Letters*, vol. 36, no. 24, pp. 2043-2044, 2000.
- [23] V. T. Tran, D. Sutanto and K. M. Muttaqi, "The state of the art of battery charging infrastructure for electrical vehicles: Topologies, power control strategies, and future trend," in *Australasian Universities Power Engineering Conference (AUPEC)*, Melbourne, VIC, Australia, 19-22 November 2017.
- [24] M. Kwon and S. Choi, "An Electrolytic Capacitorless Bidirectional EV Charger for V2G and V2H Applications," *IEEE Transactions on Power Electronics*, vol. 32, no. 9, pp. 6792-6799, 2017.
- [25] X. Wang, Y. Liu, W. Qian, A. Janabi, B. Wang, X. Lu, K. Zou, C. Chen and F. Z. Peng, "Design, and Control of a SiC Isolated Bidirectional Power Converter for V2L Applications to both DC and AC Load," in *7th Workshop on Wide Bandgap Power Devices and Applications (WiPDA)*, IEEE, Raleigh, NC, USA, 29-31 October 2019.
- [26] S. N. Vaishnav and H. Krishnaswami, "Single-stage isolated bi-directional converter topology using high frequency AC link for charging and V2G applications of PHEV," in *IEEE Vehicle Power and Propulsion Conference*, Chicago, IL, USA, 06-09 September 2011.
- [27] M. Honarmand, A. Zakariazadeh and S. Jadid, "Optimal scheduling of electric vehicles in an intelligent parking lot considering vehicle-to-grid concept and battery condition," *Energy*, vol. 65, pp. 572-579, 2014.

- [28] H. S. Das, M. M. R. S. Li and C. W. Tan, "Electric vehicles standards, charging infrastructure, and impact on grid integration: A technological review," *Renewable and Sustainable Energy Reviews*, vol. 120, p. 109618, March 2020.
- [29] V. Monteiro, J. G. Pinto and J. L. Afonso, "Operation Modes for the Electric Vehicle in Smart Grids and Smart Homes: Present and Proposed Modes," *IEEE Transactions on Vehicular Technology*, vol. 65, no. 3, pp. 1007-1020, 2016.
- [30] S. Nazari, F. Borrelli and A. Stefanopoulou, "Electric vehicles for smart buildings: a survey on applications, energy management methods, and battery degradation," *Proceedings of the IEEE*, vol. 109, no. 6, pp. 1128-1144, 2021.
- [31] K. Bai, "Advanced Components for Electric Vehicle System: Vehicle-to-Grid Metering, Vehicle-to-Vehicle Charging, and High-Power Charge Circuit Interrupting Devices," PhD dissertation, University of Delaware, 2021.
- [32] S. Haghbin, S. Lundmark, M. Alakula and O. Carlson, "Grid-Connected Integrated Battery Chargers in Vehicle Applications: Review and New Solution," *IEEE Transactions on Industrial Electronics*, vol. 60, no. 2, pp. 459-473, 2013.
- [33] B. Plumer and H. Tabuchi, "6 Automakers and 30 Countries Say They'll Phase Out Gasoline Car Sales," *The New York Times*, [Online]. Available: <https://www.nytimes.com/2021/11/09/climate/cars-zero-emissions-cop26.html>. [Accessed 11 November 2021].
- [34] E. Gurpinar, Y. Yang, F. Iannuzzo, A. Castellazzi and F. Blaabjerg, "Reliability-Driven Assessment of GaN HEMTs and Si IGBTs in 3L-ANPC PV Inverters," *IEEE Journal of Emerging and Selected Topics in Power Electronics*, vol. 4, no. 3, pp. 956-969, 2016.
- [35] J.-H. Choi, H.-M. Kwon and J.-Y. Lee, "Design of a 3.3 kW 100 kHz EV Charger Based on Flyback Converter With Active Snubber," *IEEE Transactions on Vehicular Technology*, vol. 71, no. 7, pp. 7161-7170, 2022.
- [36] R. Bosshard and J. W. Kolar, "Multi-Objective Optimization of 50 kW/85 kHz IPT System for Public Transport," *IEEE Journal of Emerging and Selected Topics in Power Electronics*, vol. 4, no. 4, pp. 1370-1382, 2016.
- [37] Z. Ali, G. Putrus, M. Marzband, H. R. Gholinejad, K. Saleem and B. Subudhi, "Multiobjective Optimized Smart Charge Controller for Electric Vehicle Applications," *IEEE Transactions on Industry Applications*, vol. 58, no. 5, pp. 5602-5615, 2022.
- [38] S. K. Dube, R. Nair and P. Das, "Analysis and Design of an Integrated Bidirectional Three-Phase AC-DC Resonant Converter," *IEEE Transactions on Industrial Electronics*, pp. 1-10, (Early Access) 2022.
- [39] A. Ramezani and M. Narimani, "Optimal Design of Fully Integrated Magnetic Structure for Wireless Charging of Electric Vehicles," *IEEE Transactions on Transportation Electrification*, vol. 7, no. 4, pp. 2114-2127, 2021.
- [40] T. Amit Singh, Y. Naveen, P. AVJS, A. Vijay and K. Piyush, "Design of GaN based 72V,3.3KW LLC Resonant Converter for on-board EV Charger," in *IEEE Madras Section Conference (MASCAN)*, Chennai, India, 27-28 August 2021.

- [41] F. Qi, Z. Wang and Y. Wu, "650V GaN Based 3.3kW Bi-Directional DC-DC Converter for High Efficiency Battery Charger with Wide Battery Voltage Range," in *IEEE Applied Power Electronics Conference and Exposition (APEC)*, Anaheim, CA, USA, 17-21 March 2019.
- [42] S. Zou, J. Lu, A. Mallik and A. Khaligh, "Modeling and Optimization of an Integrated Transformer for Electric Vehicle On-Board Charger Applications," *IEEE Transactions on Transportation Electrification*, vol. 4, no. 2, pp. 355-363, 2018.
- [43] P. He and A. Khaligh, "Comprehensive Analyses and Comparison of 1 kW Isolated DC–DC Converters for Bidirectional EV Charging Systems," *IEEE Transactions on Transportation Electrification*, vol. 3, no. 1, pp. 147-156, 2017.
- [44] Z. Lv, X. Yan, Y. Fang and L. Sun, "Mode analysis and optimum design of bidirectional CLLC resonant converter for high-frequency isolation of DC distribution systems," in *Energy Conversion Congress and Exposition (ECCE)*, IEEE, Montreal, QC, Canada, 20-24 September 2015.
- [45] W. Chen, P. Rong and Z. Lu, "Snubberless Bidirectional DC–DC Converter With New CLLC Resonant Tank Featuring Minimized Switching Loss," *IEEE Transactions on Industrial Electronics*, vol. 57, no. 9, pp. 3075-3086, 2010.
- [46] J.-H. Jung, H.-S. Kim, M.-H. Ryu and J.-W. Baek, "Design Methodology of Bidirectional CLLC Resonant Converter for High-Frequency Isolation of DC Distribution Systems," *IEEE Transactions on Power Electronics*, vol. 28, no. 4, pp. 1741-1755, 2013.
- [47] Z. U. Zahid, Z. M. Dalala, R. Chen, B. Chen and J.-S. Lai, "Design of Bidirectional DC–DC Resonant Converter for Vehicle-to-Grid (V2G) Applications," *IEEE Transactions on Transportation Electrification*, vol. 1, no. 3, pp. 232-244, 2015.
- [48] W. L. Malan, D. M. Vilathgamuwa and G. R. Walker, "Modeling and Control of a Resonant Dual Active Bridge With a Tuned CLLC Network," *IEEE Transactions on Power Electronics*, vol. 31, no. 10, pp. 7297-7310, 2016.
- [49] B. Li, F. C. Lee, Q. Li and Z. Liu, "Bi-directional on-board charger architecture and control for achieving ultra-high efficiency with wide battery voltage range," in *IEEE Applied Power Electronics Conference and Exposition (APEC)*, Tampa, FL, USA, 26-30 March 2017.
- [50] H.-S. Kim, M.-H. Ryu, J.-W. Baek and J.-H. Jung, "High-Efficiency Isolated Bidirectional AC–DC Converter for a DC Distribution System," *IEEE Transactions on Power Electronics*, vol. 28, no. 4, pp. 1642-1654, 2013.
- [51] Z. Li, Y.-H. Hsieh, Q. Li, F. C. Lee and M. H. Ahmed, "High-Frequency Transformer Design with High-Voltage Insulation for Modular Power Conversion from Medium-Voltage AC to 400-V DC," in *IEEE Energy Conversion Congress and Exposition (ECCE)*, Detroit, MI, USA, 11-15 October 2020.
- [52] K. Sun, J. Wang, R. Burgos, D. Boroyevich, J. Stewart and N. Yan, "Design and Multi-Objective Optimization of an Auxiliary Wireless Power Transfer Converter in Medium-Voltage Modular Conversion Systems," *IEEE Transactions on Power Electronics*, vol. 37, no. 8, pp. 9944-9958, 2022.

- [53] M. Rezaayati, F. Tahami, J.-L. Schanen and B. Sarrazin, "Generalized State-Plane Analysis of Bidirectional CLLC Resonant Converter," *IEEE Transactions on Power Electronics*, vol. 37, no. 5, pp. 5773-5785, 2022.
- [54] P. He, A. Mallik, A. Sankar and A. Khaligh, "Design of a 1-MHz high-efficiency high-power-density bidirectional GaN-based CLLC converter for electric vehicles," *IEEE Transactions on Vehicular Technology*, vol. 68, no. 1, pp. 213-223, 2019.
- [55] M. Rezaayati, J.-L. Schanen, F. Tahami and B. Sarrazin, "Interpolation-Based Switching and Conduction Losses Model of GaN Transistors," in *IECON 2020 The 46th Annual Conference of the IEEE Industrial Electronics Society*, Singapore, 18-21 October 2020.
- [56] A. Safaee and K. Woronowicz, "Time-Domain Analysis of Voltage-Driven Series-Series Compensated Inductive Power Transfer Topology," *IEEE Transactions on Power Electronics*, vol. 32, no. 7, pp. 4981-5003, 2017.
- [57] J. Liu, J. Zhang, T. Q. Zheng and J. Yang, "A Modified Gain Model and the Corresponding Design Method for an LLC Resonant Converter," *IEEE Transactions on Power Electronics*, vol. 32, no. 9, pp. 6716-6727, 2017.
- [58] C.-Y. Oh, D.-H. Kim, D.-G. Woo, W.-Y. Sung, Y.-S. Kim and B.-K. Lee, "A High-Efficient Nonisolated Single-Stage On-Board Battery Charger for Electric Vehicles," *IEEE Transactions on Power Electronics*, vol. 28, no. 12, pp. 5746-5757, 2013.
- [59] U. R. Prasanna, A. K. Singh and K. Rajashekara, "Novel bidirectional single-phase single-stage isolated AC-DC converter with PFC for charging of electric vehicles," *IEEE Transactions on Transportation Electrification*, vol. 3, no. 3, pp. 536-544, 2017.
- [60] J. L. Russi, M. L. d. S. Martins and H. L. Hey, "Coupled-Filter-Inductor Soft-Switching Techniques: Principles and Topologies," *IEEE Transactions on Industrial Electronics*, vol. 55, no. 9, pp. 3361-3373, 2008.
- [61] D. Huang, F. C. Lee and D. Fu, "Classification and selection methodology for multi-element resonant converters," in *Twenty-Sixth Annual IEEE Applied Power Electronics Conference and Exposition (APEC)*, Fort Worth, TX, USA, 2011.
- [62] D. Fu, F. C. Lee, Y. Liu and M. Xu, "Novel Multi-Element Resonant Converters for Front-end DC/DC Converters," in *IEEE Power Electronics Specialists Conference*, Rhodes, Greece, 2008.
- [63] X. Li, J. Huang, Y. Ma, X. Wang, J. Yang and X. Wu, "Unified Modeling, Analysis, and Design of Isolated Bidirectional CLLC Resonant DC-DC Converters," *IEEE Journal of Emerging and Selected Topics in Power Electronics*, vol. 10, no. 2, pp. 2305-2318, 2022.
- [64] K.-K. Shyu, C.-M. Lai, K.-W. Jwo, M.-H. Pan and C.-P. Ku, "Using automatic frequency shifting techniques for LLC-SRC output voltage regulation," in *CES/IEEE 5th International Power Electronics and Motion Control Conference*, Shanghai, China, 14-16 August 2006.
- [65] H. Li, S. Wang, Z. Zhang, J. Zhang, W. Zhu, X. Ren and C. Hu, "A Bidirectional Synchronous/Asynchronous Rectifier Control for Wide Battery Voltage Range in SiC Bidirectional LLC Chargers," *IEEE Transactions on Power Electronics*, vol. 37, no. 5, pp. 6090-6101, 2022.

- [66] M.-H. Ryu, H.-S. Kim, J.-W. Baek, H.-G. Kim and J.-H. Jung, "Effective Test Bed of 380-V DC Distribution System Using Isolated Power Converters," *IEEE Transactions on Industrial Electronics*, vol. 62, no. 7, pp. 4525-4536, 2015.
- [67] L. Xue, Z. Shen, D. Boroyevich, P. Mattavelli and D. Diaz, "Dual Active Bridge-Based Battery Charger for Plug-in Hybrid Electric Vehicle With Charging Current Containing Low Frequency Ripple," *IEEE Transactions on Power Electronics*, vol. 30, no. 12, pp. 7299-7307, 2015.
- [68] C. Liu, J. Wang, K. Colomage, C. Gould and B. Sen, "A CLLC resonant converter based bidirectional EV charger with maximum efficiency tracking," in *8th IET International Conference on Power Electronics, Machines and Drives (PEMD 2016)*, Glasgow, UK, 19-21 April 2016.
- [69] E.-S. Kim, J.-S. Oh, M.-J. Kim, J.-H. Lee, J.-W. Woo and Y.-S. Jeon, "Enhancing Efficiency in Bidirectional Resonant DC-DC Converter," in *IEEE Applied Power Electronics Conference and Exposition (APEC)*, New Orleans, LA, USA, 15-19 March 2020.
- [70] Z. U. Zahid, "Design, Modeling and Control of Bidirectional Resonant Converter for Vehicle-to-Grid (V2G) Applications," *PhD Dissertation, Virginia Tech*, 2015.
- [71] C.-H. Lin, C.-Y. Hsieh and K.-H. Chen, "A Li-Ion Battery Charger With Smooth Control Circuit and Built-In Resistance Compensator for Achieving Stable and Fast Charging," *IEEE Transactions on Circuits and Systems I: Regular Papers*, vol. 57, no. 2, pp. 506-517, 2010.
- [72] K. Fahem, D. E. Chariag and L. Sbita, "On-board Bidirectional Battery Chargers Topologies for Plug-in Hybrid Electric Vehicles," in *International Conference on Green Energy Conversion Systems (GECS)*, Hammamet, Tunisia, 23-25 March 2017.
- [73] J. G. Pinto, V. Monteiro, H. Gonçalves and J. L. Afonso, "On-Board Reconfigurable Battery Charger for Electric Vehicles with Traction-to-Auxiliary Mode," *IEEE Transactions on Vehicular Technology*, vol. 63, no. 3, pp. 1104 - 1116, 2014.
- [74] S. Kim and F.-S. Kang, "Multi-Functional On-Board Battery Charger for Plug-in Electric Vehicles," *IEEE Transactions on Industrial Electronics*, vol. 62, no. 6, pp. 3460-3472, 2015.
- [75] Z. Zheng, K. Wang, L. Xu and Y. Li, "A Hybrid Cascaded Multilevel Converter for Battery Energy Management Applied in Electric Vehicles," *IEEE Transactions on Power Electronics*, vol. 29, no. 7, pp. 3537-3546, 2014.
- [76] S. Zhao, Q. Li, F. C. Lee and B. Li, "High-Frequency Transformer Design for Modular Power Conversion From Medium-Voltage AC to 400 VDC," *IEEE Transactions on Power Electronics*, vol. 33, no. 9, pp. 7545-7557, 2018.
- [77] M.-H. Ryu, H.-S. Kim, J.-H. Kim, J.-W. Baek and J.-H. Jung, "Test bed implementation of 380V DC distribution system using isolated bidirectional power converters," in *IEEE Energy Conversion Congress and Exposition*, Denver, CO, USA, 15-19 September 2013.
- [78] J. Min and M. Ordonez, "Bidirectional Resonant CLLC Charger for Wide Battery Voltage Range: Asymmetric Parameters Methodology," *IEEE Transactions on Power Electronics*, vol. 36, no. 6, pp. 6662-6673, 2021.

- [79] J. Huang, J. Xiao, C. Wen, P. Wang and A. Zhang, "Implementation of Bidirectional Resonant DC Transformer in Hybrid AC/DC Micro-Grid," *IEEE Transactions on Smart Grid*, vol. 10, no. 2, pp. 1532 - 1542, 2019.
- [80] S. Zou, J. Lu, A. Mallik and A. Khaligh, "Bi-Directional CLLC Converter With Synchronous Rectification for Plug-In Electric Vehicles," *IEEE Transactions on Industry Applications*, vol. 54, no. 2, pp. 998-1005, 2018.
- [81] S. Endres, C. Sessler, S. Zeltner, B. Eckardt and T. Morita, "6 kW Bidirectional, Insulated On-board Charger with Normally-Off GaN Gate Injection Transistors," in *PCIM Europe 2017; International Exhibition and Conference for Power Electronics, Intelligent Motion, Renewable Energy and Energy Management*, Nuremberg, Germany, 16-18 May 2017.
- [82] J. Huang, X. Zhang, A. Zhang and P. Wang, "Comprehensive Coordinated Frequency Control of Symmetrical CLLC-DC Transformer in Hybrid AC/DC Microgrids," *IEEE Transactions on Power Electronics*, vol. 35, no. 10, pp. 10374-10384, 2020.
- [83] J. Huang, X. Zhang, Z. Shuai, X. Zhang, P. Wang, L. H. Koh, J. Xiao and X. Tong, "Robust Circuit Parameters Design for the CLLC-Type DC Transformer in the Hybrid AC-DC Microgrid," *IEEE Transactions on Industrial Electronics*, vol. 66, no. 3, pp. 1906-1918, 2019.
- [84] P. He and A. Khaligh, "Design of 1 kW Bidirectional Half-bridge CLLC Converter for Electric Vehicle Charging Systems," in *IEEE International Conference on Power Electronics, Drives and Energy Systems (PEDES)*, Trivandrum, India, 14-17 December 2016.
- [85] J. Huang, X. Zhang and B. Zhao, "Simplified Resonant Parameter Design of the Asymmetrical CLLC-Type DC Transformer in the Renewable Energy System via Semi-Artificial Intelligent Optimal Scheme," *IEEE Transactions on Power Electronics*, vol. 35, no. 2, pp. 1548-1562, 2020.
- [86] C. Zhang, P. Li, Z. Kan, X. Chai and X. Guo, "Integrated Half-Bridge CLLC Bidirectional Converter for Energy Storage Systems," *IEEE Transactions on Industrial Electronics*, vol. 65, no. 5, pp. 3879 - 3889, 2018.
- [87] Y. Wei, Q. Luo, X. Du, N. Altin, J. M. Alonso and H. A. Mantooth, "Analysis and Design of the LLC Resonant Converter With Variable Inductor Control Based on Time-Domain Analysis," *IEEE Transactions on Industrial Electronics*, vol. 67, no. 7, pp. 5432 - 5443, 2020.
- [88] S. Ditze, "Steady-state analysis of the bidirectional CLLC resonant converter in time domain," in *IEEE 36th International Telecommunications Energy Conference (INTELEC)*, Vancouver, BC, Canada, 28 September - 02 October 2014.
- [89] J.-S. Lai, L. Zhang, Z. Zahid, N.-H. Tseng, C.-S. Lee and C.-H. Lin, "A high-efficiency 3.3-kW bidirectional on-board charger," in *IEEE 2nd International Future Energy Electronics Conference (IFEEEC)*, Taipei, Taiwan, 01-04 November 2015.
- [90] N. Radimov, R. Orr and T. Gachovska, "Bi-directional CLLC converter front-end for off-grid battery inverters," in *IEEE Canada International Humanitarian Technology Conference (IHTC2015)*, Ottawa, ON, Canada, 31 May-4 June 2015.
- [91] G. Liu, D. Li, J. Q. Zhang, B. Hu and M. L. Jia, "Bidirectional CLLC resonant DC-DC converter with integrated magnetic for OBCM application," in *IEEE International Conference on Industrial Technology (ICIT)*, Seville, Spain, 17-19 March 2015.

- [92] R. Oruganti and F. C. Lee, "Resonant Power Processors, Part I---State Plane Analysis," *IEEE Transactions on Industry Applications*, Vols. IA-21, no. 6, pp. 1453-1460, 1985.
- [93] H. Chen, E. Sng and K.-J. Tseng, "Generalized Optimal Trajectory Control for Closed Loop Control of Series-Parallel Resonant Converter," *IEEE Transactions on Power Electronics*, vol. 21, no. 5, pp. 1347-1355, 2006.
- [94] V. Anand A G, A. Pal, B. S. Kuchibhatla, R. Gurunathan and K. Basu, "An Unidirectional Single Stage Single Phase Soft-Switched Resonant High Frequency Link Inverter," *IEEE Transactions on Industry Applications*, vol. 57, no. 4, pp. 3238-3251, 2021.
- [95] T. N. Gücin, B. Fincan and M. Biberöglu, "A Series Resonant Converter-Based Multichannel LED Driver With Inherent Current Balancing and Dimming Capability," *IEEE Transactions on Power Electronics*, vol. 34, no. 3, pp. 2693-2703, 2019.
- [96] Y. Xu, C. Lu, Z. Yu, J. Chen, S. Xu, Y. Wang and X. He, "Multimode Constant Power Control Strategy for LCC Resonant Capacitor Charging Power Supply Based on State Plane Analysis," *IEEE Transactions on Power Electronics*, vol. 36, no. 7, pp. 8399-8412, 2021.
- [97] I. G. Zurbriggen, F. Degioanni and M. Ordonez, "Near-Time-Optimal Dynamics in PWM DC-DC Converters: Dual-Loop Geometric Control," *IEEE Journal of Emerging and Selected Topics in Power Electronics*, vol. 9, no. 1, pp. 167-182, 2021.
- [98] R. Barrero, O. Hegazy, J. V. Mierlo, P. Lataire and T. Coosemans, "A modified state-plane control of a bi-directional Series Resonant Converter for an EDLC Energy Storage System in Hybrid Electric Vehicles," in *16th European Conference on Power Electronics and Applications*, Lappeenranta, Finland, 26-28 August 2014.
- [99] R. Steigerwald, "A comparison of half-bridge resonant converter topologies," *IEEE Transactions on Power Electronics*, vol. 3, no. 2, pp. 174-182, 1988.
- [100] W. L. Malan, D. M. Vilathgamuwa, G. R. Walker and M. A. H. Broadmeadow, "Frequency modulation of a series resonant dual active bridge to minimize the circulating reactive currents in the high frequency link," in *IEEE 2nd Annual Southern Power Electronics Conference (SPEC)*, Auckland, New Zealand, 05-08 December 2016.
- [101] Y. Cai, C. Wang, F. Zhao and R. Dong, "Design of a high-frequency isolated DTHB CLLC bidirectional resonant DC-DC converter," in *IEEE Conference and Expo Transportation Electrification Asia-Pacific (ITEC Asia-Pacific)*, Beijing, 31 August 2014 - 03 September 2014.
- [102] J. Lu, A. Mallik, S. Zou and A. Khaligh, "Variable DC Link Control Loop Design for an Integrated Two-Stage AC/DC Converter," *IEEE Transactions on Transportation Electrification*, vol. 4, no. 1, pp. 99-107, 2018.
- [103] S. Ditze, T. Heckel and M. März, "Influence of the junction capacitance of the secondary rectifier diodes on output characteristics in multi-resonant converters," in *IEEE Applied Power Electronics Conference and Exposition (APEC)*, Long Beach, CA, USA, 20-24 March 2016.
- [104] L. Wang, Q. Luo and T. Luo, "A Time-Domain Optimization Design Methodology for CLLC Resonant Converter," in *IEEE 1st International Power Electronics and Application Symposium (PEAS)*, Shanghai, China, 13-15 November 2021.

- [105] Z. Zhao, Y. Wu, X. Du and Y. Zhao, "Design and Optimization of the High Frequency Transformer for 100kW CLLC Converter," in *IEEE Applied Power Electronics Conference and Exposition (APEC)*, Phoenix, AZ, USA, 14-17 June 2021.
- [106] Z. Zhang, C. Liu, Y. Si, Y. Liu, Q. Lei and S. Ai, "Investigation of Design Methodology of Planar Transformers for EV On Board Chargers," in *IEEE Energy Conversion Congress and Exposition (ECCE)*, Baltimore, MD, USA, 29 September 2019 - 03 October 2019.
- [107] B. Li, Q. Li, F. C. Lee and Y. Yang, "A symmetrical resonant converter and PCB transformer structure for common mode noise reduction," in *IEEE Energy Conversion Congress and Exposition (ECCE)*, Cincinnati, OH, USA, 01-05 October 2017.
- [108] J. Zhang, W. G. Hurley and W. H. Wölfle, "Gapped Transformer Design Methodology and Implementation for LLC Resonant Converters," *IEEE Transactions on Industry Applications*, vol. 52, no. 1, pp. 342 - 350, 2016.
- [109] F. Lin, X. Zhang, X. Li, H. Ma and C. Cai, "Design of Symmetrical CLLC-Resonant DC Transformer Considering Voltage Transfer Ratio and Cascaded System Stability," *IEEE Transactions on Industrial Electronics*, vol. 69, no. 1, pp. 463 - 474, 2022.
- [110] F. Lin, X. Zhang, X. Li, L. Chaohui and H. Ma, "Parameter Design for Symmetrical CLLC-Type DC Transformer Considering Cascaded System Stability and Power Efficiency," *IEEE Journal of Emerging and Selected Topics in Power Electronics*, vol. 9, no. 5, pp. 6219-6231, 2021.
- [111] J. Ge and H. Ma, "A Parameter Design Method of CLLC Resonant Converter Based On Time-Domain Model," in *IECON 2020 The 46th Annual Conference of the IEEE Industrial Electronics Society*, Singapore, 18-21 October 2020.
- [112] B. Zhao, X. Zhang and J. Huang, "AI Algorithm-Based Two-Stage Optimal Design Methodology of High-Efficiency CLLC Resonant Converters for the Hybrid AC–DC Microgrid Applications," *IEEE Transactions on Industrial Electronics*, vol. 66, no. 12, pp. 9756-9767, 2019.
- [113] R. W. Erickson and D. Maksimovic, *Fundamentals of power electronics, Principles of resonant power conversion*, Springer Science & Business Media, 2007.
- [114] M. Delhommais, «Méthode de pré-design par optimisation en électronique de puissance,» Doctoral dissertation,, Université Grenoble Alpes (ComUE), 2019.
- [115] S. Kirkpatrick, C. D. Gelatt Jr and M. P. Vecchi, "Optimization by simulated annealing," *Science*, vol. 220, no. 4598, pp. 671-680, 1983.
- [116] D. Teodorovic, P. Lucic, G. Markovic and M. Dell'Orco, "Bee colony optimization: principles and applications," in *8th IEEE Seminar on Neural Network Applications in Electrical Engineering*, pp. 151-156, 2006.
- [117] A. Rohan, M. Rabah, M. Talha and S.-H. Kim, "Development of intelligent drone battery charging system based on wireless power transmission using hill climbing algorithm," *Applied System Innovation*, vol. 4, no. 1, p. 44, 2018.
- [118] D. Weile and E. Michielssen, "Genetic algorithm optimization applied to electromagnetics: A review," *IEEE Transactions on Antennas and Propagation*, vol. 45, no. 3, pp. 343-353, 1997.



- [119] R. Poli, J. Kennedy and T. Blackwell, "Particle swarm optimization," *Swarm intelligence*, vol. 1, no. 1, pp. 33-57, 2007.
- [120] J. Barhen, V. Protopopescu and D. Reister, "TRUST: A deterministic algorithm for global optimization," *Science*, vol. 5315, no. 276, pp. 1094-1097, 1997.
- [121] D. a. M. Z. Bienstock, "Solving LP relaxations of large-scale precedence constrained problems," in *International Conference on Integer Programming and Combinatorial Optimization*, Springer, Berlin, Heidelberg, 2010.
- [122] W. Sun and Y.-X. Yuan, *Optimization theory and methods: nonlinear programming*, Vol. 1: Springer Science & Business Media, 2006.
- [123] S. Leyffer, "Integrating SQP and Branch-and-Bound for Mixed Integer Nonlinear Programming," *Computational optimization and applications*, vol. 18, no. 3, pp. 295-309, 2001.
- [124] J. M. X. Gablonsky, "Modifications of the DIRECT algorithm," PhD dissertation, North Carolina state university, 2001.
- [125] R. Fletcher and S. Leyffer, "Solving mixed integer nonlinear programs by outer approximation," *Mathematical programming*, vol. 1, no. 66, pp. 327-349, 1994.
- [126] T. Westerlund and F. Pettersson, "An Extended Cutting Plane Method for Solving Convex MINLP Problems," *Computers & chemical engineering*, vol. 19, pp. 131-136, 1995.
- [127] E. Babaei, H. Tarzamni, F. Tahami, H. Khoun Jahan and M. B. Bannae Sharifian, "Multi-input high step-up inverter with soft-switching capability, applicable in photovoltaic systems," *IET Power Electronics*, vol. 13, no. 1, pp. 133-143, 2020.
- [128] X. Huang, Q. Li, Z. Liu and F. C. Lee, "Analytical loss model of high voltage GaN HEMT in cascode configuration," *IEEE Transactions on Power Electronics*, vol. 29, no. 5, pp. 2208-2219, 2013.
- [129] J. Chen, Q. Luo, J. Huang, Q. He and X. Du, "A complete switching analytical model of low-voltage eGaN HEMTs and its application in loss analysis," *IEEE Transactions on Industrial Electronics*, vol. 67, no. 2, pp. 1615-1625, 2019.
- [130] Y. Xin, W. Chen, R. Sun, Y. Shi, C. Liu, Y. Xia, F. Wang, M. Li, J. Li, Q. Zhou and X. Deng, "Analytical switching loss model for GaN-based control switch and synchronous rectifier in low-voltage buck converters," *IEEE Journal of Emerging and Selected Topics in Power Electronics*, vol. 7, no. 3, pp. 1485-1495, 2019.
- [131] K. Wang, M. Tian, H. Li, F. Zhang, X. Yang and L. Wang, "An improved switching loss model for a 650V enhancement-mode GaN transistor," in *IEEE 2nd Annual Southern Power Electronics Conference (SPEC)*, 2016.
- [132] Q. Li, B. Liu, S. Duan, L. Wang, B. Xu and C. Luo, "Analytical Switching Loss Model of Cascode GaN HEMTs Based Totem-Pole PFC Converters Considering Stray Inductances," in *1st Workshop on Wide Bandgap Power Devices and Applications in Asia (WiPDA Asia)*, pp. 118-124, 2018.

- [133] N. Korada, Z. Yu and R. Ayyanar, "Loss characterization and analysis of high voltage e-mode GaN HEMT in soft-switching application," in *IEEE 6th Workshop on Wide Bandgap Power Devices and Applications (WiPDA)*, pp. 40-44, 2018.
- [134] X. Huang, T. Liu, B. Li, F. C. Lee and Q. Li, "Evaluation and applications of 600V/650V enhancement-mode GaN devices," in *IEEE 3rd Workshop on Wide Bandgap Power Devices and Applications (WiPDA)*, pp. 113-118, 2015.
- [135] N. Zhang, Z. Lin, L. Hong, Y. Tang and H. Ma, "An improved analytical model of GaN HEMT in cascode configuration during turn-on transition," in *IEEE 24th International Symposium on Industrial Electronics (ISIE)*, pp. 233-238, 2015.
- [136] G. Dadanema, F. Costa, Y. Avenas, J.-L. Schanen and C. Vollaie, "Analytical losses model for SiC semiconductors dedicated to optimization operations," in *In PCIM Europe 2016; International Exhibition and Conference for Power Electronics, Intelligent Motion, Renewable Energy and Energy Management*, pp. 1-9, 2016.
- [137] S. GaN, "GS66508B Bottom-side cooled 650 V E-mode GaN transistor Preliminary Datasheet, Rev 190502," 10 10 2022. [Online]. Available: <https://gansystems.com/wp-content/uploads/2019/05/GS66508B-DS-Rev-190502.pdf>.
- [138] T. Yao and R. Ayyanar, "A multifunctional double pulse tester for cascode GaN devices," *IEEE Transactions on Industrial Electronics*, vol. 64, no. 11, pp. 9023-9031, 2017.
- [139] K. Wang, X. Yang, H. Li, H. Ma, X. Zeng and W. Chen, "An analytical switching process model of low-voltage eGaN HEMTs for loss calculation," *IEEE Transactions on Power Electronics*, vol. 31, no. 1, pp. 635-647, 2015.
- [140] M. Mirjafari and R. S. Balog, "Survey of modelling techniques used in optimisation of power electronic components," *IET Power Electronics*, vol. 7, no. 5, pp. 1192-1203, 2014.
- [141] K. Wang, B. Li, H. Li, X. Yang and A. Qiu, "Characterization and modelling of frequency-dependent ON-resistance for GaN devices at high-frequencies," *IEEE Transactions on Power Electronics*, vol. 35, no. 5, pp. 4925-4933, 2019.
- [142] R. Li, X. Wu, S. Yang and K. Sheng, "Dynamic on-state resistance test and evaluation of GaN power devices under hard-and soft-switching conditions by double and multiple pulses," *IEEE Transactions on Power Electronics*, vol. 34, no. 2, pp. 1044-1053, 2018.
- [143] Z. Yan, L. Liu, C. Chen, H. Liu, W. Zhou and R. Mai, "Optimized Design of Integrated Planar Matrix Transformer for LLC Converter in Consumer Electronics," *IEEE Journal of Emerging and Selected Topics in Power Electronics*, vol. 10, no. 2, pp. 2254-2264, 2021.
- [144] J. Li, C. R. Sullivan and A. Schultz, "Coupled-inductor design optimization for fast-response low-voltage," in *In APEC. Seventeenth Annual IEEE Applied Power Electronics Conference and Exposition (Cat. No. 02CH37335)*, vol. 2, pp. 817-823, 2002.
- [145] E. Agheb, M. A. Bahmani, H. K. Høidalen and T. Thiringer, "Core loss behavior in high frequency high power transformers—II: Arbitrary excitation," *Journal of Renewable and Sustainable Energy*, vol. 4, no. 3, p. 033113, 2012.

- [146] J. Zhang, B. Gao, Z. He, L. Wang, R. Hou, Y. Liu, A. Luo, Y. Chen and R. Han, "Design and Optimization of a Magnetron DC–DC Isolated Power Supply With High Efficiency," *IEEE Transactions on Power Electronics*, vol. 37, no. 8, pp. 9392-9405, 2022.
- [147] G. R. Kalra, M. G. Pearce, S. Kim, D. J. Thrimawithana and G. A. Covic, "A Power Loss Measurement Technique for Inductive Power Transfer Magnetic Couplers," *IEEE Journal of Emerging and Selected Topics in Industrial Electronics*, vol. 1, no. 2, pp. 113-122, 2020.
- [148] M. K. Kazimierczuk, High-frequency magnetic components, John Wiley & Sons, 2009.
- [149] R. Chen, J. T. Strydom and J. D. v. Wyk, "Design of Planar Integrated Passive Module for Zero-Voltage-Switched Asymmetrical Half-Bridge PWM Converter," *IEEE transactions on industry applications*, vol. 39, no. 6, pp. 1648-1655, 2003.
- [150] J. Biela, U. Badstuebner and J. W. Kolar, "Impact of Power Density Maximization on Efficiency of DC–DC Converter Systems," *IEEE Transactions on Power Electronics*, vol. 24, no. 1, pp. 288-300, 2009.
- [151] A. Nawawi, C. Tong, S. Yin, A. Sakanova, Y. Liu, Y. Liu, M. Kai, K. See, K. Tseng, R. Simanjorang and C. Gajanayake, "Design and Demonstration of High Power Density Inverter for Aircraft Applications," *IEEE Transactions on Industry Applications*, vol. 53, no. 2, pp. 1168-1176, 2016.
- [152] Ferroxcube, "Datasheet, 3C90 Material Specification," 1 Sep. 2008. [Online]. Available: <http://www.ferroxcube.home.pl/prod/assets/3c90.pdf>.
- [153] Ferroxcube, "Datasheet, 3F4 Material Specifications," 1 Sep. 2008. [Online]. Available: <http://ferroxcube.home.pl/prod/assets/3F4.pdf>.
- [154] ANSI/IPC, ""IPC - 2221," in Generic Standard on Printed Board Design," ed. Northbrook, IL: IPC, 1998.
- [155] VISHAY, "Application Note, Power Dissipation in High Precision Vishay Sfernice Chip Resistors and Arrays (P Thin Film, PRA Arrays, CHP Thick Film)," VISHAY, 2009.
- [156] J. Kolar, T. Wolbank and M. SchrodL, "Analytical calculation of the RMS current stress on the DC link capacitor of voltage DC link PWM converter systems," in *Ninth International Conference on Electrical Machines and Drives (Conf. Publ. No. 468)*, Canterbury, UK, 03-01 September 1999.
- [157] D. S. Gautam, F. Musavi, W. Eberle and W. G. Dunford, "A Zero-Voltage Switching Full-Bridge DC–DC Converter With Capacitive Output Filter for Plug-In Hybrid Electric Vehicle Battery Charging," *IEEE Transactions on Power Electronics*, vol. 28, no. 12, pp. 5728-5735, 2013.
- [158] G. Datasheet, "On Board Charger (OBC), Valeo and Siemens, datasheet available in: <https://eveurope.eu/wp-content/uploads/20160719-GEN2.5-OBC-product-datasheet.pdf>," [Online]. Available: <https://eveurope.eu/en/product/new-siemens-valeo-ev-powercharger-360-3500-he-i/>.
- [159] OVARTECH, "3.3KW EV ON-BOARD CHARGER AIR-COOLED, datasheet available in: <http://www.ovartech.com/wp-content/uploads/2017/12/Ovartech-Air-cooled-3.3KW-OBC-CAD332DF-400A-Data-Sheet.pdf>," [Online]. Available: <http://www.ovartech.com/>. [Accessed 20 11 2019].

- [160] CISPR25:2021, "International Standard, CISPR/CIS/D - Electromagnetic disturbances related to electric/electronic equipment on vehicles and internal combustion engine powered devices," IEC, <https://webstore.iec.ch/publication/64645>, 2021.
- [161] R. Zheng, B. Liu and S. Duan, "Analysis and parameter optimization of start-up process for LLC resonant converter," *EEE Transactions on Power Electronics*, vol. 30, no. 12, pp. 7113-7122, 2015.
- [162] P. Enciu, F. Wurtz, L. Gerbaud and B. Delinchant, "Automatic differentiation for electromagnetic models used in optimization," *COMPEL-The international journal for computation and mathematics in electrical and electronic engineering*, vol. 28, no. 5, pp. 1313-1326, 2009.
- [163] B. Delinchant, D. Duret, L. Estrabaut, L. Gerbaud, H. Huu, B. Du Peloux, H. Rakotoarison, F. Verdière and F. Wurtz, "An optimizer using the software component paradigm for the optimization of engineering systems," *COMPEL-The international journal for computation and mathematics in electrical and electronic engineering*, vol. 26, no. 2, pp. 368-379, 2007.
- [164] V. System, "Vesta CADES," 2016. [Online]. Available: <https://www.vestasystem.fr/en/products/vestacades/vesta-cades.html>. [Accessed 3 Aug. 2018].
- [165] P. Enciu, L. Gerbaud and F. Wurtz, "Automatic differentiation for sensitivity calculation in electromagnetism: Application for optimization of a linear actuator," *IEEE transactions on magnetics*, vol. 47, no. 5, pp. 1238-1241, 2010.
- [166] Z. Fang, T. Cai, S. Duan and C. Chen, "Optimal Design Methodology for LLC Resonant Converter in Battery Charging Applications Based on Time-Weighted Average Efficiency," *IEEE Transactions on Power Electronics*, vol. 30, no. 10, pp. 5469-5483, 2014.
- [167] S.-H. Ryu, D.-H. Kim, M.-J. Kim, J.-S. Kim and B.-K. Lee, "Adjustable Frequency–Duty-Cycle Hybrid Control Strategy for Full-Bridge Series Resonant Converters in Electric Vehicle Chargers," *IEEE Transactions on Industrial Electronics*, vol. 61, no. 10, pp. 5354-5362, 2014.
- [168] D. Gautam, F. Musavi, M. Edington, W. Eberle and W. G. Dunford, "An automotive on-board 3.3 kW battery charger for PHEV application," in *IEEE Vehicle Power and Propulsion Conference*, Chicago, IL, USA, 06-09 September 2011.
- [169] H. Xu, Z. Yin, Y. Zhao and Y. Huang, "Accurate Design of High-Efficiency LLC Resonant Converter With Wide Output Voltage," *IEEE Access*, vol. 5, pp. 26653 - 26665, 2017.
- [170] A. S. Tandon, N. Yalla, A. Praneeth, V. Anand and P. Kumar, "Design of GaN based 72V,3.3KW LLC Resonant Converter for on-board EV Charger," in *IEEE Madras Section Conference (MASCON)*, pp. 1-6, 27 Aug. 2021.
- [171] A. Safaee and K. Woronowicz, "Time-Domain Analysis of Voltage-Driven Series–Series Compensated Inductive Power Transfer Topology," *IEEE Transactions on Power Electronics*, vol. 32, no. 7, pp. 4981-5003, 2017.
- [172] R. Oruganti and F. C. Lee, "Resonant power processors, Part I---State plane analysis," *IEEE Transactions on industry applications*, vol. 6, pp. 1453-1460, 1985.

# Appendix I

## Decoupling Method for the State Space Equations

By substituting  $i_{L1}$ ,  $i'_{L2}$ ,  $v_{C1}$ , and  $v'_{C2}$  as the function of  $i_{LP}$ ,  $i_{LN}$ ,  $v_{CP}$ , and  $v_{CN}$  according to (5.4) into (5.2) and rearranging them, the state space equations are recalculated as:

$$\frac{dv_{CP}}{dt} = \frac{1}{a_P + a_N} \left( \left( \frac{e_P}{C_1} + \frac{a_N}{C'_2} \right) i_{LP} + \left( \frac{e_P}{C_1} - \frac{a_P}{C'_2} \right) i_{LN} \right) \quad (\text{A.1})$$

$$\begin{aligned} \frac{di_{LP}}{dt} = & \frac{-1}{\Gamma(e_P + e_N)} \{ (a_P(L'_2 + L_m) + L_m + L_m e_N a_P + e_N(L_1 + L_m)) v_{CP} \\ & + (a_P(L'_2 + L_m) + L_m - L_m e_P a_P - e_P(L_1 + L_m)) v_{CN} \} \\ & - \frac{L_m + a_P L_m + a_P L'_2 v_1}{\Gamma} - \frac{L_m + a_P L_m + L_1 v'_2}{\Gamma} \end{aligned} \quad (\text{A.2})$$

$$\frac{dv_{CN}}{dt} = \frac{1}{a_P + a_N} \left( \left( \frac{e_N}{C_1} - \frac{a_N}{C'_2} \right) i_{LP} + \left( \frac{e_N}{C_1} + \frac{a_P}{C'_2} \right) i_{LN} \right) \quad (\text{A.3})$$

$$\begin{aligned} \frac{di_{LN}}{dt} = & \frac{-1}{\Gamma(e_P + e_N)} \{ (a_N(L'_2 + L_m) - L_m + L_m e_N a_N - e_N(L_1 + L_m)) v_{CP} \\ & + (a_N(L'_2 + L_m) - L_m - L_m e_P a_N + e_P(L_1 + L_m)) v_{CN} \} \\ & - \frac{a_N L'_2 + a_N L_m - L_m v_1}{\Gamma} - \frac{a_N L_m - L_m - L_1 v'_2}{\Gamma} \end{aligned} \quad (\text{A.4})$$

For decoupling the parameters P and N, it is mandatory to put the coefficients of unwanted parameters to zero. For (A.1) and (A.2), the coefficients of  $i_{LN}$  and  $v_{CN}$ , and for (A.3) and (A.4), the coefficients of  $i_{LP}$  and  $v_{CP}$  must be set equal to zero:

$$\begin{aligned} \frac{e_P}{C_1} - \frac{a_P}{C'_2} &= 0 \\ a_P(L'_2 + L_m) + L_m - L_m e_P a_P - e_P(L_1 + L_m) &= 0 \\ \frac{e_N}{C_1} - \frac{a_N}{C'_2} &= 0 \\ a_N(L'_2 + L_m) - L_m + L_m e_N a_N - e_N(L_1 + L_m) &= 0 \end{aligned} \quad (\text{A.5})$$

By solving (62), the parameters  $a_P$ ,  $a_N$ ,  $e_P$ , and  $e_N$  are obtained as shown in (5.5).

# Appendix II

## Initial Condition Calculation for the Proposed State Plane Analysis

Let's consider the secondary current of the CLLC resonant converter as the following circuit:

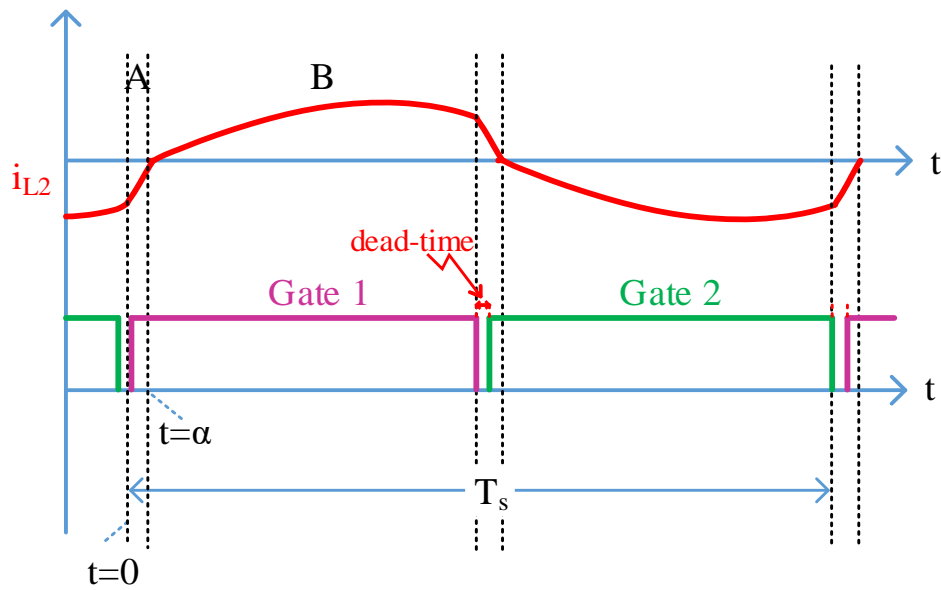


Fig. A-1: The waveform of secondary side current

Initially, the secondary current is negative, as the equivalent circuit was shown in Fig. 5-3 (d). Then this current becomes positive by a zero crossing, and the equivalent circuit becomes as shown in Fig. 5-3 (a).

In region A: the duration of this region is  $\alpha$ . Using Laplace transform, the primary current will be as the following equation for  $L_1=L_2$ , and  $C_1=C_2$ :

$$i_{L1} = \frac{ad + bf}{a^2 - b^2} \quad (0.1)$$

where

$$\begin{aligned}
d &= K_1 + K_2/S \\
f &= K_3 + K_4/S \\
a &= K_5 S + K_6/S \\
b &= K_7 S
\end{aligned} \tag{0.2}$$

and

$$\begin{aligned}
K_1 &= L_1 I_{L1_0} + L_m I_{Lm_0} \\
K_2 &= V_{DC} - V_{C1_0} \\
K_3 &= L_2 I_{L2_0} - L_m I_{Lm_0} \\
K_4 &= V_{out} - V_{C2_0} \\
K_5 &= L_1 + L_m \\
K_6 &= 1/C_1 \\
K_7 &= L_m
\end{aligned} \tag{0.3}$$

By simplifying, we can obtain the following equation in the Laplace domain as follows:

$$i_{L1}(S) = \frac{A S + B}{(K_5 - K_7)S^2 + K_6} + \frac{C S + D}{(K_5 + K_7)S^2 + K_6} \tag{0.4}$$

where

$$\begin{aligned}
A &= \frac{K_1 + K_3}{2} \\
B &= \frac{K_2 + K_4}{2} \\
C &= \frac{K_1 - K_3}{2} \\
D &= \frac{K_2 - K_4}{2}
\end{aligned} \tag{0.5}$$

Eq. (4) has always two complex poles, so its reverse of Laplace transform in the time domain can be written as the following equation:

$$i_{L1}(t) = I_{1pA} \sin(\omega_r t + \theta_{1pA}) + I_{2pA} \sin(q_1 \omega_r t + \theta_{2pA}) \tag{0.6}$$

where the index A represents the equation for state A.

where

$$\begin{aligned}
I_{1pA} &= \frac{\sqrt{P_{1A}^2 + P_{2A}^2}}{2} \\
\theta_{1pA} &= \text{tg}^{-1}(P_{1A}/P_{2A}) \quad \omega_r = \frac{1}{\sqrt{L_1 C_1}}, q_1 = \frac{1}{\sqrt{1+2k}}, k = \frac{L_m}{L_1} \\
I_{2pA} &= \frac{\sqrt{P_{3A}^2 + P_{4A}^2}}{2} \quad Z_1 = \sqrt{\frac{C_1}{L_1}} \\
\theta_{2pA} &= \text{tg}^{-1}(P_{3A}/P_{4A})
\end{aligned} \tag{0.7}$$

and

$$\begin{aligned}
P_{1A} &= \frac{K_1 + K_3}{K_5 - K_7} = \frac{L_1 I_{L1_0} + L_2 I_{L2_0}}{L_1} \\
P_{2A} &= \frac{K_2 + K_4}{\sqrt{K_6 (K_5 - K_7)}} = Z_1 (V_{DC} + V_{out} - V_{C1_0} - V_{C2_0}) \\
P_{3A} &= \frac{K_1 - K_3}{K_5 + K_7} = \frac{L_1 I_{L1_0} + 2L_m I_{Lm_0} - L_2 I_{L2_0}}{L_1 + 2L_m} \\
P_{4A} &= \frac{K_2 - K_4}{\sqrt{K_6 (K_5 + K_7)}} = q_1 Z_1 (V_{DC} - V_{out} - V_{C1_0} + V_{C2_0})
\end{aligned} \tag{0.8}$$

Also, for the secondary side current, the following equation in the Laplace domain is:

$$i_{L2}(S) = \frac{E S + F}{(K_5 - K_7)S^2 + K_6} + \frac{G S + H}{(K_5 + K_7)S^2 + K_6} \tag{0.9}$$

where

$$\begin{aligned}
E &= \frac{K_1 + K_3}{2} = A \\
F &= \frac{K_2 + K_4}{2} = B \\
G &= \frac{K_3 - K_1}{2} = -C \\
H &= \frac{K_4 - K_2}{2} = -D
\end{aligned} \tag{0.10}$$

In the time domain we have:



$$i_{L2}(t) = I_{1pA} \sin(\omega_r t + \theta_{1pA}) - I_{2pA} \sin(q_1 \omega_r t + \theta_{2pA}) \quad (0.11)$$

Finally, for all resonant elements, the following equations in the time domain are obtained:

$$\begin{aligned} i_{L1}(t) &= I_{1pA} \sin(\omega_r t + \theta_{1pA}) + I_{2pA} \sin(q_1 \omega_r t + \theta_{2pA}) \\ i_{L2}(t) &= I_{1pA} \sin(\omega_r t + \theta_{1pA}) - I_{2pA} \sin(q_1 \omega_r t + \theta_{2pA}) \\ i_{Lm}(t) &= 2I_{2pA} \sin(q_1 \omega_r t + \theta_{2pA}) \\ v_{C1}(t) &= 1/Z_1 \left( -I_{1pA} \cos(\omega_r t + \theta_{1pA}) - I_{2pA}/q_1 \cos(q_1 \omega_r t + \theta_{2pA}) \right) + V_{DC} \\ v_{C2}(t) &= 1/Z_1 \left( -I_{1pA} \cos(\omega_r t + \theta_{1pA}) + I_{2pA}/q_1 \cos(q_1 \omega_r t + \theta_{2pA}) \right) + V_{out} \end{aligned} \quad (0.12)$$

At the end of this region,  $i_{L2}$  will be zero, and  $i_{L1}=i_{Lm}$ .

In region **B**: using  $i_{L2}=0$  and  $i_{L1}=i_{Lm}$ , we have:

$$i_{L1} = \frac{ad + bf}{a^2 - b^2} \quad (0.13)$$

where

$$\begin{aligned} d &= K_1 + K_2/S \\ f &= K_3 + K_4/S \\ a &= K_5 S + K_6/S \\ b &= K_7 S \end{aligned} \quad (0.14)$$

and

$$\begin{aligned} K_1 &= L_1 I_{L1_0} + L_m I_{Lm_0} \\ K_2 &= V_{DC} - V_{C1_0} \\ K_3 &= L_2 I_{L2_0} - L_m I_{Lm_0} \\ K_4 &= -V_{out} - V_{C2_0} \\ K_5 &= L_1 + L_m \\ K_6 &= 1/C_1 \\ K_7 &= L_m \end{aligned} \quad (0.15)$$

The primary current is obtained as the following equation:

$$i_{L1}(S) = \frac{AS + B}{(K_5 - K_7)S^2 + K_6} + \frac{CS + D}{(K_5 + K_7)S^2 + K_6} \quad (0.16)$$

where

$$\begin{aligned}
 A &= \frac{K_1 + K_3}{2} \\
 B &= \frac{K_2 + K_4}{2} \\
 C &= \frac{K_1 - K_3}{2} \\
 D &= \frac{K_2 - K_4}{2}
 \end{aligned} \tag{0.17}$$

Eq. (16) has also two complex poles, so using the reverse Laplace transform we have:

$$i_{L1}(t) = I_{1pB} \sin(\omega_r t - \alpha + \theta_{1pB}) + I_{2pB} \sin(q_1(\omega_r t - \alpha) + \theta_{2pB}) \tag{0.18}$$

where

$$\begin{aligned}
 I_{1pB} &= \frac{\sqrt{P_{1B}^2 + P_{2B}^2}}{2} \\
 \theta_{1pB} &= \text{tg}^{-1}(P_{1B}/P_{2B}) \\
 I_{2pB} &= \frac{\sqrt{P_{3B}^2 + P_{4B}^2}}{2} \\
 \theta_{2pB} &= \text{tg}^{-1}(P_{3B}/P_{4B})
 \end{aligned} \tag{0.19}$$

For other resonant elements, the time domain equations in region B are obtained as:

$$\begin{aligned}
 i_{L1}(t) &= I_{1pB} \sin(\omega_r t - \alpha + \theta_{1pB}) + I_{2pB} \sin(q_1(\omega_r t - \alpha) + \theta_{2pB}) \\
 i_{L2}(t) &= I_{1pB} \sin(\omega_r t - \alpha + \theta_{1pB}) - I_{2pB} \sin(q_1(\omega_r t - \alpha) + \theta_{2pB}) \\
 i_{Lm}(t) &= 2I_{2pB} \sin(q_1(\omega_r t - \alpha) + \theta_{2pB}) \\
 v_{C1}(t) &= 1/Z_1 \left( -I_{1pB} \cos(\omega_r t - \alpha + \theta_{1pB}) - I_{2pB}/q_1 \cos(q_1(\omega_r t - \alpha) + \theta_{2pB}) \right) + V_{DC} \\
 v_{C2}(t) &= 1/Z_1 \left( -I_{1pB} \cos(\omega_r t - \alpha + \theta_{1pB}) + I_{2pB}/q_1 \cos(q_1(\omega_r t - \alpha) + \theta_{2pB}) \right) - V_{out}
 \end{aligned} \tag{0.20}$$

Now, it is needed to obtain  $P_{1A}$ ,  $P_{2A}$ ,  $P_{3A}$ ,  $P_{4A}$ ,  $P_{1B}$ ,  $P_{2B}$ ,  $P_{3B}$ , and  $P_{4B}$ . For this case, we know that the inductor current is a continuous parameter, i.e.:

$$X(\alpha^-)\Big|_A = X(\alpha^+)\Big|_B \quad (0.21)$$

For  $i_{L1}$ :

$$\begin{aligned} I_{L1}(\alpha^-) &= I_{L1}(\alpha^+) \\ \Rightarrow P_{1B} + P_{3B} &= P_{2A} \sin(\alpha) + P_{1A} \cos(\alpha) + P_{4A} \sin(q_1 \alpha) + P_{3A} \cos(q_1 \alpha) \end{aligned} \quad (0.22)$$

For  $i_{L2}$ :

$$\begin{aligned} I_{L2}(\alpha^-) &= I_{L2}(\alpha^+) \\ \Rightarrow P_{1B} - P_{3B} &= P_{2A} \sin(\alpha) + P_{1A} \cos(\alpha) - P_{4A} \sin(q_1 \alpha) - P_{3A} \cos(q_1 \alpha) \end{aligned} \quad (0.23)$$

For  $v_{C1}$ :

$$\begin{aligned} V_{C1}(\alpha^-) &= V_{C1}(\alpha^+) \\ \Rightarrow P_{2B} + \frac{P_{4B}}{q_1} &= P_{2A} \cos(\alpha) - P_{1A} \sin(\alpha) + \frac{P_{4A}}{q_1} \cos(q_1 \alpha) - \frac{P_{3A}}{q_1} \sin(q_1 \alpha) \end{aligned} \quad (0.24)$$

For  $v_{C2}$ :

$$\begin{aligned} V_{C2}(\alpha^-) &= V_{C2}(\alpha^+) \\ \Rightarrow -P_{2B} + \frac{P_{4B}}{q_1} &= -P_{2A} \cos(\alpha) + P_{1A} \sin(\alpha) \\ &+ \frac{P_{4A}}{q_1} \cos(q_1 \alpha) - \frac{P_{3A}}{q_1} \sin(q_1 \alpha) + 4Z_1 V_{out} \end{aligned} \quad (0.25)$$

By solving the above four equations, we have:

$$\begin{aligned} P_{1B} &= P_{2A} \sin(\alpha) + P_{1A} \cos(\alpha) \\ P_{2B} &= P_{2A} \cos(\alpha) - P_{1A} \sin(\alpha) - 2Z_1 V_{out} \\ P_{3B} &= P_{4A} \sin(q_1 \alpha) + P_{3A} \cos(q_1 \alpha) \\ P_{4B} &= P_{4A} \cos(q_1 \alpha) - P_{3A} \sin(q_1 \alpha) + 2q_1 Z_1 V_{out} \end{aligned} \quad (0.26)$$

Now, only  $P_{1A}$ ,  $P_{2A}$ ,  $P_{3A}$ , and  $P_{4A}$  remained. For this case, we know that the value of elements in the half of the switching period is negative of them, e.g. for  $i_{L1}$ :

$$I_{L1}(0) = -I_{L1}(\pi/\omega_s) \quad (0.27)$$

So, we have:

$$\begin{aligned}
-2I_{L1_0} &= P_{2B} \sin\left(\frac{\pi\omega_r}{\omega_s} - \alpha\right) + P_{1B} \cos\left(\frac{\pi\omega_r}{\omega_s} - \alpha\right) \\
&\quad + P_{4B} \sin\left(q_1\left(\frac{\pi\omega_r}{\omega_s} - \alpha\right)\right) + P_{3B} \cos\left(q_1\left(\frac{\pi\omega_r}{\omega_s} - \alpha\right)\right) \\
-2I_{L2_0} &= P_{2B} \sin\left(\frac{\pi\omega_r}{\omega_s} - \alpha\right) + P_{1B} \cos\left(\frac{\pi\omega_r}{\omega_s} - \alpha\right) \\
&\quad - P_{4B} \sin\left(q_1\left(\frac{\pi\omega_r}{\omega_s} - \alpha\right)\right) - P_{3B} \cos\left(q_1\left(\frac{\pi\omega_r}{\omega_s} - \alpha\right)\right) \\
-V_{C1_0} &= \frac{1}{2Z_1} \left( -P_{2B} \cos\left(\frac{\pi\omega_r}{\omega_s} - \alpha\right) + P_{1B} \sin\left(\frac{\pi\omega_r}{\omega_s} - \alpha\right) \right) \\
&\quad + \frac{1}{2q_1Z_1} \left( -P_{4B} \cos\left(q_1\left(\frac{\pi\omega_r}{\omega_s} - \alpha\right)\right) + P_{3B} \sin\left(q_1\left(\frac{\pi\omega_r}{\omega_s} - \alpha\right)\right) \right) + V_{DC} \\
-V_{C2_0} &= \frac{1}{2Z_1} \left( -P_{2B} \cos\left(\frac{\pi\omega_r}{\omega_s} - \alpha\right) + P_{1B} \sin\left(\frac{\pi\omega_r}{\omega_s} - \alpha\right) \right) \\
&\quad + \frac{1}{2q_1Z_1} \left( P_{4B} \cos\left(q_1\left(\frac{\pi\omega_r}{\omega_s} - \alpha\right)\right) - P_{3B} \sin\left(q_1\left(\frac{\pi\omega_r}{\omega_s} - \alpha\right)\right) \right) - V_{out}
\end{aligned} \tag{0.28}$$

For the sake of simplicity, we define:

$$\begin{aligned}
\sin\left(\frac{\pi\omega_r}{\omega_s}\right) &= S_r & \cos\left(\frac{\pi\omega_r}{\omega_s}\right) &= Y_r \\
\sin\left(\frac{\pi q_1 \omega_r}{\omega_s}\right) &= S_q & \cos\left(\frac{\pi q_1 \omega_r}{\omega_s}\right) &= Y_q
\end{aligned} \tag{0.29}$$

Now we have:

$$\begin{aligned}
a_1 I_{L1_0} + b_1 I_{L2_0} + c_1 V_{C1_0} + d_1 V_{C2_0} &= f_1 - f_1(\alpha) \\
a_2 I_{L1_0} + b_1 I_{L2_0} + c_2 V_{C1_0} + d_2 V_{C2_0} &= f_2 - f_2(\alpha) \\
a_3 I_{L1_0} + b_1 I_{L2_0} + c_3 V_{C1_0} + d_3 V_{C2_0} &= f_3 - f_3(\alpha) \\
a_4 I_{L1_0} + b_1 I_{L2_0} + c_4 V_{C1_0} + d_4 V_{C2_0} &= f_4 - f_4(\alpha)
\end{aligned} \tag{0.30}$$

where

$$\begin{aligned}
a_1 &= 2 + Y_r + Y_q & b_1 &= Y_r - Y_q \\
a_2 &= Y_r - Y_q & b_2 &= 2 + Y_r + Y_q \\
a_3 &= q_1 S_r + S_q & b_3 &= q_1 S_r - S_q \\
a_4 &= q_1 S_r - S_q & b_4 &= q_1 S_r + S_q \\
c_1 &= -Z_1 S_r - q_1 Z_1 S_q & d_1 &= -Z_1 S_r + q_1 Z_1 S_q \\
c_2 &= -Z_1 S_r + q_1 Z_1 S_q & d_2 &= -Z_1 S_r - q_1 Z_1 S_q \\
c_3 &= 2q_1 Z_1 + q_1 Z_1 Y_r + q_1 Z_1 Y_q & d_3 &= q_1 Z_1 Y_r - q_1 Z_1 Y_q \\
c_4 &= q_1 Z_1 Y_r - q_1 Z_1 Y_q & d_4 &= 2q_1 Z_1 + q_1 Z_1 Y_r + q_1 Z_1 Y_q
\end{aligned} \tag{0.31}$$

and

$$\begin{aligned}
f_1 &= -Z_1 S_r (V_{DC} + V_{out}) - q_1 Z_1 S_q (V_{DC} - V_{out}) \\
f_2 &= -Z_1 S_r (V_{DC} + V_{out}) + q_1 Z_1 S_q (V_{DC} - V_{out}) \\
f_3 &= q_1 Z_1 Y_r (V_{DC} + V_{out}) + q_1 Z_1 Y_q (V_{DC} - V_{out}) - 2q_1 Z_1 V_{DC} \\
f_4 &= q_1 Z_1 Y_r (V_{DC} + V_{out}) - q_1 Z_1 Y_q (V_{DC} - V_{out}) + 2q_1 Z_1 V_{out}
\end{aligned} \tag{0.32}$$

$$\begin{aligned}
f_1(\alpha) &= 2Z_1 V_{out} (Y_r \sin(\alpha) - S_r \cos(\alpha) + q_1 S_q \cos(q_1 \alpha) - q_1 Y_q \sin(q_1 \alpha)) \\
f_2(\alpha) &= 2Z_1 V_{out} (Y_r \sin(\alpha) - S_r \cos(\alpha) - q_1 S_q \cos(q_1 \alpha) + q_1 Y_q \sin(q_1 \alpha)) \\
f_3(\alpha) &= 2q_1 Z_1 V_{out} (Y_r \cos(\alpha) + S_r \sin(\alpha) - Y_q \cos(q_1 \alpha) - S_q \sin(q_1 \alpha)) \\
f_4(\alpha) &= 2q_1 Z_1 V_{out} (Y_r \cos(\alpha) + S_r \sin(\alpha) + Y_q \cos(q_1 \alpha) + S_q \sin(q_1 \alpha))
\end{aligned}$$

Now we have 4 equations with 5 unknown parameters. The fifth equation can be defined by knowing the fact that at  $t=\alpha$ ,  $i_{L2}=0$ . So,

$$\begin{aligned}
t = \alpha &\Rightarrow I_{L2} = 0 \Rightarrow P_{1B} = P_{3B} \\
&\Rightarrow P_{2A} \sin(\alpha) + P_{1A} \cos(\alpha) = P_{4A} \sin(q_1 \alpha) + P_{3A} \cos(q_1 \alpha)
\end{aligned} \tag{0.33}$$

or

$$\begin{aligned}
Z_1 (V_{DC} + V_{out} - V_{C1_0} - V_{C2_0}) \sin(\alpha) + (I_{L1_0} + I_{L2_0}) \cos(\alpha) = \\
q_1 Z_1 (V_{DC} - V_{out} - V_{C1_0} + V_{C2_0}) \sin(q_1 \alpha) + (I_{L1_0} - I_{L2_0}) \cos(q_1 \alpha)
\end{aligned} \tag{0.34}$$

As a result, the initial conditions of the resonant elements can be obtained by solving these 5 equations.

# Appendix III

## Optimization by Considering the Total Mass or Power Density as the Objective Function

If minimizing the total mass or maximizing the power density is considered as the objective function, the optimization results can be determined as:

*Table 0-1: Single operating point optimization results in the imaginary world when the maximum power density is selected for the objective function*

Optimization results at	Parameter	Selected point for optimization			
		Point A	Point B	Point C	Point D
General parameters	C <sub>1</sub> (nF)	56.37	62.47	20.00	20.01
	L <sub>1</sub> (μH)	3.76	5.13	16.01	16.00
	X [L <sub>1</sub> ,L <sub>2</sub> ,T]	20	20	20	20
		20	20	20	20
		20	20	20	20
	lg [L <sub>1</sub> ,L <sub>2</sub> ,T] (μm)	287.7	484.0	193.3	100
		262.3	325.1	202.4	100
		100	100	100	100
	N [L <sub>1</sub> ,L <sub>2</sub> ,T]	13.59	10.99	12.28	8.83
		12.98	9.01	12.56	8.83
		10.49	14.80	26.11	11.14
	m [L <sub>1</sub> ,L <sub>2</sub> ,T]	2	2	2	2
		2	2	2	2
2		2	2	2	
KLm	6.01	8.78	8.74	7.93	
Fit_H [L <sub>1</sub> ,L <sub>2</sub> ,T]	OK	OK	OK	OK	
Fit_V [L <sub>1</sub> ,L <sub>2</sub> ,T]	OK	OK	OK	OK	
Mass (g)	9.23	9.23	9.23	9.23	
Efficiency (%)	97.71	98.43	98.13	97.09	
Objective function (W/g)	233.24	322.48	168.38	88.98	
Optimization results at Point A	ZVS checker	OK	OK	OK	OK
	CCM checker	OK	OK	OK	OK
	Bmax checker	OK	NOK	NOK	NOK
	Efficiency	97.71	97.94	97.77	97.76
	Objective function W/g	233.24	285.30	91.13	89.99
	T <sub>j</sub> (°C)	84.999	79.92	59.08	59.07

Optimization results at	Parameter	Selected point for optimization			
		Point A	Point B	Point C	Point D
<b>Optimization results at Point B</b>	ZVS checker	OK	OK	OK	OK
	CCM checker	OK	OK	OK	OK
	Bmax checker	NOK	OK	NOK	NOK
	Efficiency	98.69	98.43	98.57	98.55
	Objective function W/g	223.85	322.48	94.09	90.85
	T <sub>j</sub> (°C)	54.26	84.999	46.11	46.05
<b>Optimization results at Point C</b>	ZVS checker	OK	OK	OK	OK
	CCM checker	NOK	OK	OK	OK
	Bmax checker	NOK	NOK	OK	NOK
	Efficiency	94.51	98.57	98.13	97.13
	Objective function W/g	14.89	90.28	168.33	23.41
	T <sub>j</sub> (°C)	44.33	45.10	84.999	41.27
<b>Optimization results at Point D</b>	ZVS checker	OK	OK	OK	OK
	CCM checker	NOK	OK	OK	OK
	Bmax checker	NOK	NOK	NOK	OK
	Efficiency	94.68	98.61	97.55	97.09
	Objective function W/g	13.26	80.28	25.25	88.98
	T <sub>j</sub> (°C)	41.71	42.32	39.32	84.999

According to the above table, it is manifest that the objective function converges to the minimum available mass (i.e. 9.23g) for any operating point, which is not true for a bidirectional 3.3kW battery charger. Therefore, this objective function is neglected in this dissertation.

# Appendix IV

## Transferring From the Imaginary World to the Real World for the Single Operating Point Optimization

The obtained results in part 6.4. were determined in the imaginary world. But, it is important to show the disadvantage of the single operating point in the real world, which is expressed in this part.

Firstly, a lower standard size for the magnetic parts is considered in the real world as shown in the following table:

*Table 0-1: Single operating point optimization results in the real world when a lower size is selected for the magnetic parts, by considering a different operating point and checking the objective function and constraints on all points*

Optimization results at	Parameter	Selected point for optimization			
		Point A	Point B	Point C	Point D
General parameters	C <sub>1</sub>	246.17nF	500nF	20nF	26.45nF
	L <sub>1</sub>	2.542uH	6.04uH	16uH	12.10uH
	X [L <sub>1</sub> ,L <sub>2</sub> ,T]	30	20	20	20
		25	20	20	20
		35	35	20	20
	lg [L <sub>1</sub> ,L <sub>2</sub> ,T]	290um	258um	304um	100um
		246um	180um	304um	345um
		100um	113um	100um	100um
	N [L <sub>1</sub> ,L <sub>2</sub> ,T]	4	4	2	2
		4	4	2	2
		4	4	2	2
m [L <sub>1</sub> ,L <sub>2</sub> ,T]	2	2	2	2	
	2	2	2	2	
	2	2	2	2	
KLm	10.01	20	8.744	9.693	
Fit_H [L <sub>1</sub> ,L <sub>2</sub> ,T]	OK	OK	OK	OK	
Fit_V [L <sub>1</sub> ,L <sub>2</sub> ,T]	OK	OK	OK	OK	
Power density	2.8519	3.905	10.6266	10.4973	



Optimization results at	Parameter	Selected point for optimization			
		Point A	Point B	Point C	Point D
Optimization results at Point A	ZVS checker	OK	OK	OK	OK
	CCM checker	OK	OK	OK	OK
	Bmax checker	OK	NOK	NOK	NOK
	Efficiency	97.796	92.36	97.76	97.929
	T <sub>j</sub>	84.999	377.7	59.07	62.258
Optimization results at Point B	ZVS checker	OK	OK	OK	OK
	CCM checker	OK	OK	OK	OK
	Bmax checker	NOK	OK	NOK	NOK
	Efficiency	97.933	98.408	98.55	98.681
	T <sub>j</sub>	115.46	84.999	46.11	47.809
Optimization results at Point C	ZVS checker	OK	OK	OK	OK
	CCM checker	OK	OK	OK	OK
	Bmax checker	NOK	NOK	OK	NOK
	Efficiency	98.635	98.217	98.126	98.319
	T <sub>j</sub>	62.43	37.87	84.999	108.557
Optimization results at Point D	ZVS checker	OK	OK	OK	OK
	CCM checker	OK	OK	OK	OK
	Bmax checker	NOK	NOK	NOK	OK
	Efficiency	98.706	98.277	97.54	96.932
	T <sub>j</sub>	55.98	87.38	39.32	84.999

Secondly, a higher standard size for the magnetic parts is considered in the real world as shown in the following table:

*Table 0-2: Single operating point optimization results in the real world when a higher size is selected for the magnetic parts, by considering a different operating point and checking the objective function and constraints on all points*

Optimization results at	Parameter	Selected point for optimization			
		Point A	Point B	Point C	Point D
General parameters	C <sub>1</sub>	110.0nF	200.5nF	20.1nF	34.16nF
	L <sub>1</sub>	2.911uH	1.59uH	15.9uH	9.37uH
	X [L <sub>1</sub> ,L <sub>2</sub> ,T]	35	25	25	25
		30	25	25	25
		42	42	25	25
	lg [L <sub>1</sub> ,L <sub>2</sub> ,T]	1mm	315um	100um	102um
		1mm	204um	100um	100um
		1mm	100um	100um	100um
	N [L <sub>1</sub> ,L <sub>2</sub> ,T]	8	4	4	4
		8	4	4	4
8		4	4	4	

Optimization results at	Parameter	Selected point for optimization			
		Point A	Point B	Point C	Point D
Optimization results at	m [L <sub>1</sub> ,L <sub>2</sub> ,T]	2	4	2	2
		2	4	2	2
		2	4	2	2
	KLm	6	8.795	7.295	7.290
	Fit_H [L <sub>1</sub> ,L <sub>2</sub> ,T]	OK	OK	OK	OK
	Fit_V [L <sub>1</sub> ,L <sub>2</sub> ,T]	OK	OK	OK	OK
	Power density	1.4166	3.8993	6.4157	6.3166
Optimization results at Point A	ZVS checker	OK	OK	OK	OK
	CCM checker	OK	OK	OK	OK
	Bmax checker	OK	NOK	OK	NOK
	Efficiency	97.11	96.94	97.73	97.973
	T <sub>j</sub>	84.999	172.02	59.12	65.99
Optimization results at Point B	ZVS checker	OK	OK	OK	OK
	CCM checker	OK	OK	OK	OK
	Bmax checker	OK	OK	NOK	NOK
	Efficiency	98.188	98.257	98.523	98.700
	T <sub>j</sub>	66.79	84.999	46.013	49.38
Optimization results at Point C	ZVS checker	OK	OK	OK	OK
	CCM checker	NOK	OK	OK	OK
	Bmax checker	OK	NOK	OK	NOK
	Efficiency	94.856	98.61	97.967	98.175
	T <sub>j</sub>	48.88	57.388	84.999	114.59
Optimization results at Point D	ZVS checker	OK	OK	OK	OK
	CCM checker	NOK	OK	OK	OK
	Bmax checker	OK	NOK	NOK	OK
	Efficiency	95.07	98.68	96.590	96.455
	T <sub>j</sub>	45.32	52.03	39.27	84.999

The two above tables demonstrate that by considering an operating point as the point of the optimization, all constraints cannot be met for the other operating points. Therefore, a single operating point is not a good candidate for optimizing a bidirectional EV charger for the wide range of voltages and currents. The proposed multi operating point optimization method solved this issue.